Indirect Galactic Dark Matter Search with JUNO: A Machine Learning-Enhanced Sensitivity Study from MeV to GeV

Dissertation

der Mathematisch-Naturwissenschaftlichen Fakultät
der Eberhard Karls Universität Tübingen
zur Erlangung des Grades eines
Doktors der Naturwissenschaften
(Dr. rer. nat.)

vorgelegt von
Jessica Eck
aus Stuttgart

Tübingen
2026

Gedruckt mit Genehmigung der Mathematisch-Naturwissenschaftlichen Fakultät
der Eberhard Karls Universität Tübingen.

Tag der mündlichen Qualifikation: 05.05.2026

Dekan:	Prof. Dr. Thilo Stehle
1. Berichterstatter:	Prof. Dr. Tobias Lachenmaier
2. Berichterstatter:	Prof. Dr. Josef Jochum

Abstract

The nature of Dark Matter (DM), which constitutes approximately 26 % of the energy content of the universe, remains one of the central open questions in modern physics. This work is dedicated to the indirect search for DM via monoenergetic neutrinos with the Jiangmen Underground Neutrino Observatory (JUNO) detector, covering the entire mass range from $m_\chi = 15\,\mathrm{MeV}$ to $10\,\mathrm{GeV}$. The analysis assumes DM self-annihilation via $\chi\chi \to \nu_\ell\bar{\nu}_\ell$ in the Milky Way, with a democratic neutrino flavor composition.
The primary goal of this work is to determine the exclusion sensitivity of JUNO on the thermally averaged annihilation cross section $\langle\sigma_\mathrm{A}v\rangle$ using a Bayesian framework with Markov Chain Monte Carlo (MCMC) sampling. Systematic uncertainties are accounted for through log-normal nuisance parameters, and the robustness against statistical fluctuations in real measurements is quantified through toy-Monte Carlo studies. To perform this analysis, precise Asimov-like predictions of signal and background spectra are essential.
Therefore, using extensive MC simulations based on GENIE and the full JUNO detector simulation, signal and background spectra are modeled across the entire energy range. The low-energy Diffuse Supernova Neutrino Background (DSNB) is incorporated considering different theoretical models, while atmospheric neutrino fluxes are propagated to the JUNO site assuming three-flavor oscillations including matter effects. Energy-dependent selection strategies are developed to optimize the signal-to-background (S2B) ratio in each regime.
In the MeV regime, a new machine learning (ML)-based vertex reconstruction achieving $\sim 18\,\mathrm{cm}$ resolution enables a topology-based selection of the inverse beta decay (IBD) combined with a subsequent pulse shape discrimination (PSD). In the sub-GeV regime, a flavor-based selection using ML-based particle identification as well as a topological zero-neutron selection are introduced to enhance characteristic spectral features of a monoenergetic neutrino source. In the GeV regime, directional selection around the Galactic Center (GC) suppresses the nearly isotropic atmospheric background while retaining a large fraction of the DM signal.
JUNO can improve existing Super-Kamiokande limits by approximately one order of magnitude in the mass range $m_\chi \sim 15\,\mathrm{MeV}$ to $1\,\mathrm{GeV}$ after $10\,\mathrm{yr}$ of data taking, with statistical uncertainty dominating systematic effects. For one-year scenarios, exclusion sensitivity is competitive with current limits in the MeV regime, while the sub-GeV range achieves 5σ discovery potential for masses above $\sim 0.2\,\mathrm{GeV}$. In the GeV regime, improvements are limited by angular resolution, but a competitive, independent verification of existing limits is achieved. The analysis extends to p-wave annihilation through $\mathcal{J}$-factor rescaling, and the model-independent flux limits determined in this work represent a general result applicable to any source of monoenergetic neutrino signals.
This work was carried out within the JUNO collaboration.

Zusammenfassung

Die Natur der Dunklen Materie (DM), die ungefähr 26 % des Energieinhalts des Universums ausmacht, bleibt eine der zentralen offenen Fragen der modernen Physik. Diese Arbeit widmet sich der indirekten Suche nach DM durch monoenergetische Neutrinos mit dem Jiangmen Underground Neutrino Observatory (JUNO)-Detektor, die den gesamten Massenbereich von $m_\chi = 15\,\mathrm{MeV}$ bis $10\,\mathrm{GeV}$ abdeckt. Die Analyse geht von DM-Selbstannihilation via $\chi\chi \to \nu_\ell\bar{\nu}_\ell$ in der Milchstraße mit einer demokratischen Neutrino-Flavor-Komposition aus.
Das Primärziel dieser Arbeit ist es, die Ausschlusssensitivität von JUNO auf den thermisch gemittelten Annihilationsquerschnitt $\langle\sigma_\mathrm{A}v\rangle$ unter Verwendung eines Bayes'schen Rahmens mit Markov Chain Monte Carlo (MCMC)-Sampling zu bestimmen. Systematische Unsicherheiten werden durch log-normale Störparameter berücksichtigt, und die Robustheit gegen statistische Schwankungen in realen Messungen wird durch Toy-Monte Carlo-Studien quantifiziert. Um diese Analyse durchzuführen, sind präzise Asimov-ähnliche Vorhersagen der Signal- und Hintergrundspektren essentiell.
Daher werden unter Verwendung umfangreicher Monte Carlo-Simulationen basierend auf GENIE und der vollständigen JUNO-Detektor-Simulation Signal- und Hintergrundspektren im gesamten Energiebereich modelliert. Der niederenergetische diffuse Supernova-Neutrino-Hintergrund (DSNB) wird unter Berücksichtigung verschiedener theoretischer Modelle einbezogen, während die atmosphärischen Neutrinoflüsse zum JUNO-Standort unter Annahme von Drei-Flavor-Oszillationen mit Materie-Effekten propagiert werden. Energieabhängige Selektionsstrategien werden entwickelt, um das Signal-zu-Hintergrund (S2B)-Verhältnis in jedem Regime zu optimieren.
Im MeV-Regime ermöglicht eine neue auf maschinellem Lernen (ML) basierte Vertex-Rekonstruktion mit einer Auflösung von $\sim 18\,\mathrm{cm}$ eine Topologie-basierte Selektion für den inversen Betazerfall (IBD) kombiniert mit einer anschließenden Pulsformdiskriminierung (PSD). Im sub-GeV-Regime werden eine Flavor-basierte Selektion unter Verwendung von ML-basierter Teilchenidentifikation (PID) sowie eine topologische Null-Neutronen-Selektion eingeführt, um charakteristische Spektralmerkmale einer monoenergetischen Neutrinoquelle zu verstärken. Im GeV-Regime unterdrückt die Richtungsselektion um das galaktische Zentrum (GC) den nahezu isotropen atmosphärischen Hintergrund, während ein großer Anteil des DM-Signals erhalten bleibt.
JUNO kann die bestehenden Super-Kamiokande-Grenzen in dem Massenbereich $m_\chi \sim 15\,\mathrm{MeV}$ bis $1\,\mathrm{GeV}$ nach $10\,\mathrm{yr}$ Datennahme um etwa eine Größenordnung verbessern, wobei statistische Unsicherheit systematische Effekte dominiert. Für Einjahres-Szenarien ist die Ausschlusssensitivität in dem MeV-Regime konkurrenzfähig mit aktuellen Grenzen, während der sub-GeV-Bereich ein 5σ-Entdeckungspotenzial für Massen oberhalb von $\sim 0.2\,\mathrm{GeV}$ erreicht. Im GeV-Regime sind Verbesserungen aufgrund der Winkelauflösung begrenzt, aber eine konkurrenzfähige, unabhängige Überprüfung bestehender Grenzen wird erreicht. Die Analyse wird auf das p-Wellen-Annihilation durch $\mathcal{J}$-Faktor-Reskalierung erweitert, und die in dieser Arbeit bestimmten modellunabhängigen Flussgrenzen stellen ein allgemeines Ergebnis dar, das auf jede Quelle monoenergetischer Neutrinosignale anwendbar ist.
Diese Arbeit wurde im Rahmen der JUNO-Kollaboration durchgeführt.

Contents

1 | Motivation and Overview

Dance first. Think later. It's the natural order.

– Samuel Beckett

The nature of Dark Matter (DM) has been one of the central open questions in modern physics since the 1930s [1]. A large number of independent observations provide evidence that the dominant fraction of matter in the universe consists of an unknown, non-luminous matter component, commonly referred to as Dark Matter (DM). Despite its enormous impact on cosmological phenomena, its nature on the level of particle physics has so far remained unexplained. To investigate DM experimentally, there are three different strategies: direct detection via scattering off standard model (SM) particles, the production of DM particles at accelerators, and indirect searches in which SM products are measured that originate from the annihilation or decay of DM particles (cf. Chap. 2). Since direct and accelerator-based experiments were able to set stringent limits, especially for the initially favored GeV DM masses, the experimental focus has increasingly shifted to the sub-GeV and MeV mass range in recent years [2]. In this low mass range, classical direct detection experiments are facing fundamental sensitivity limits. At the same time, many electromagnetic or hadronic indirect detection channels are strongly constrained for light DM. Neutrinos, however, play a special role among the possible end products of DM annihilations, as they represent one of the few remaining experimentally accessible channels due to their weak interaction [3]. They can escape almost unimpeded from the densest regions of the universe and carry spectral and directional information about their production processes (cf. Chap. 3).

Consequently, large-volume neutrino detectors offer a unique opportunity to study the self-annihilation or decay of light DM indirectly via a monoenergetic neutrino signature. Due to their high light yield, which enables both a low detection threshold and excellent energy resolution, scintillator detectors have a decisive advantage over water Cherenkov detectors for studying MeV and sub-GeV DM candidates. The Jiangmen Underground Neutrino Observatory (JUNO) detector has been operating since August 2025, and due to its large detector volume and excellent energy resolution, JUNO represents a highly promising experiment, particularly for neutrinos in the MeV and sub-GeV energy range [4, 5, 6] (cf. Chap. 4).

A sensitivity study has already demonstrated that JUNO will be able to set stringent limits on the self-annihilation of light DM into electron antineutrinos in the MeV mass range from 15 MeV to 100 MeV [7, 8]. Building on these results, the goal of this work is to systematically investigate the sensitivity of JUNO for the indirect search for DM by means of Monte Carlo (MC) simulations. On the one hand, the DM mass range considered so far is substantially extended from ≤ 100 MeV into the transition region to classical WIMP scenarios at around 10 GeV. This allows, for the first time, a continuous analysis across several orders of magnitude in energy within a consistent detector model. This extension requires going beyond the inverse beta decay (IBD) channel used in

previous studies. Instead, all charged current (CC) and neutral current (NC) interactions must be taken into account (cf. Chap. 5).
Due to significantly more complex event topologies of high-energy neutrino events and the subsequent final state interactions (FSIs), the expected measured energy spectrum of a monoenergetic neutrino signal is no longer determined solely by simple IBD kinematics, but has been modeled together with all relevant backgrounds using comprehensive MC simulations (cf. Chap. 6 and 7).
To enhance JUNO's sensitivity, energy-dependent background reduction methods are essential. Topology-based IBD selection cuts together with the pulse shape discrimination (PSD) method presented in [7, 8] are adopted in this work for the MeV energy range and improved using machine learning (ML)-based algorithms (cf. Chap. 8). In the sub-GeV regime, the signal-to-background (S2B) ratio is increased by means of reconstructed flavor information, while in the GeV range, the directional information of neutrinos is used for background reduction (cf. Chap. 9).
Finally, three Bayesian analyses are performed to determine the exclusion sensitivity of JUNO to an indirect DM signal over the full energy range considered in this work. The first analysis focuses on the IBD-dominated regime and extends previous studies [7, 8] up to $m_\chi = 300\,\mathrm{MeV}$. The second analysis addresses the sub-GeV regime $m_\chi \in [0.1\,\mathrm{GeV}, 1\,\mathrm{GeV}]$, while the third analysis covers the GeV regime from 1 GeV to 10 GeV. In all three cases, the energy-dependent efficiencies of the corresponding background reduction methods are incorporated consistently.
The resulting expected exclusion limits on the thermally averaged DM self-annihilation cross section are derived for 10 yr of data taking in JUNO, complemented by a one-year projection, an estimate of the discovery potential, and selected toy-MC studies to quantify the expected statistical spread. The results show that JUNO can improve the current best limits from Super-Kamiokande by roughly one order of magnitude for $m_\chi \simeq 15\,\mathrm{MeV}$ to $m_\chi \simeq 1\,\mathrm{GeV}$, with the transition from an IBD-based to a CC-based analysis occurring at $\sim 200\,\mathrm{MeV}$. In the GeV regime, directional selection can enhance the sensitivity for cuspy halo profiles, but JUNO is expected to primarily provide a competitive and independent cross-check of existing Super-Kamiokande limits. All exclusion limits are presented for both s-wave and p-wave dominated annihilation scenarios (cf. Chap. 10).

2 | Introduction to Dark Matter

Those who dance are considered insane by those who cannot hear the music.

– George Carlin

The standard model (SM) of particle physics provides an explanation of the underlying interactions of elementary particles. It includes the electromagnetic, strong, and weak interactions, thus describing three of the four fundamental forces of physics. Apart from gravity, which is currently best described by general relativity, the SM is a very successful predictive theory for baryonic matter. However, according to current knowledge, visible matter accounts for only about 15.6 % of the total mass of the universe [9].

2.1 Dark Matter Evidence

The existence of a new kind of matter was first postulated in 1933 by Zwicky [1] and has since been supported by numerous astrophysical and cosmological observations. Today, this new kind of matter is referred to as Dark Matter (DM).

2.1.1 Galactic Scale Observations

Strong evidence for the existence of DM on a galactic scale was first provided in 1978 by observations of the rotational curves of galaxies. The rotational velocities were inferred

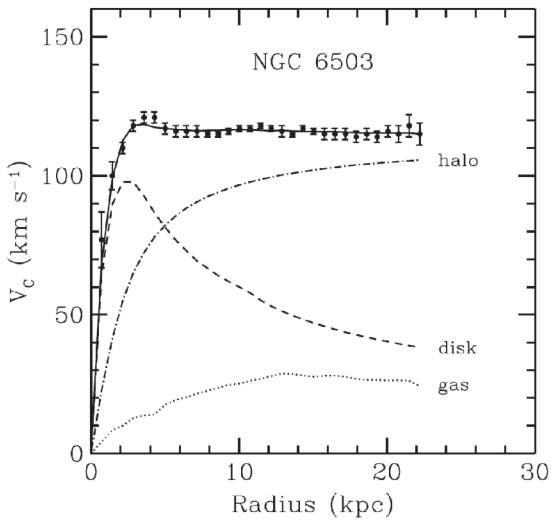

Figure 2.1: Rotational curve of NGC 6503, including the contributions of gas, disk and dark matter to the observed circular velocity v_c. Taken from [10].

from the Doppler shift of the 21 cm spin-flip transition hydrogen line, which measures the radial component of the velocity along the line of sight [11]. According to Newtonian theory, the rotational velocity $v(r)$ for objects orbiting the Galactic Center (GC) at a large distance r should be proportional to $1/\sqrt{r}$. However, the observations show a flat radial velocity distribution in the outer region of the galaxy [11, 12]. Fig. 2.1 shows an exemplary measurement of the circular velocity v_c in the galaxy NGC 6503. In addition to the contribution of baryonic matter (gas and luminous disk) to the total mass, the Galactic DM halo has been introduced with a density profile $\rho \propto 1/r^2$ [10], resulting in a flat velocity distribution for objects far from the GC. Most spiral galaxies, including the Milky Way, indicate the presence of a DM halo. The current models for possible DM density profiles in the Milky Way are discussed in section 3.2.
The rotational curves provide strong evidence for DM on the galactic scale, but there are also other indications, such as the gravitational lensing effects of distant galaxies and the velocity distribution of satellite galaxies, which imply a DM halo for spiral galaxies [10].

2.1.2 Galaxy Cluster Scale Observations

Assuming virial equilibrium, the velocity dispersion of galaxies in clusters, similar to the rotation curves at the galactic scale, also strongly suggests the existence of DM. The first evidence was provided by Zwicky in 1933 [13], when he deduced a mass-to-light ratio of ~ 400 (in units of solar mass to solar luminosity) from the velocity distribution in the Coma cluster. Current analyses estimate the DM content at the cluster scale to be about $0.7 - 0.8$, which is also confirmed by observations of gravitational lensing effects. In gravitational lensing, the light from a galaxy behind the cluster, as seen by the observer, is deflected by the mass in the cluster, producing characteristic ring-like signatures or weak lensing in the electromagnetic spectrum [14]. The mass distribution of the bending object can be determined without making any assumptions about the dynamical state of the cluster by reconstructing the geometric effect of the lens.
Studies of the Bullet Cluster, shown in Fig. 2.2, which consists of two colliding galaxy clusters, provide some of the strongest evidence for DM at the cluster scale. Gravitational

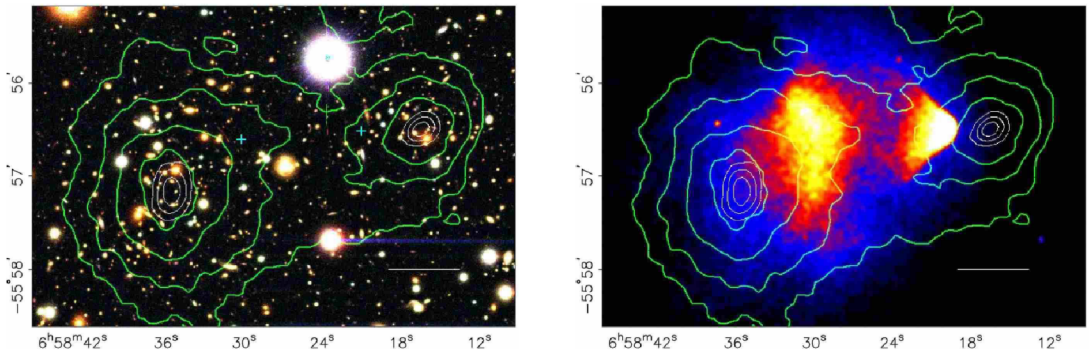

Figure 2.2: Observation of the Bullet Cluster 1E0657-558, demonstrating the spatial separation between the total mass and the baryonic matter. The left plot is a colored Magellan image (optical) and the right plot is a Chandra image (X-ray) indicating the density of the gas component. The green contours indicate the total mass distribution reconstructed from weak gravitational lensing, while the white contours show the uncertainty on the mass peak positions. The offset between the mass peaks and the gas demonstrates the presence of DM. Taken from [15].

lensing analyses have been used to determine the mass distribution in the two colliding

galaxy clusters, indicated by the green contours in Fig. 2.2. The white contours show the 1σ, 2σ and 3σ confidence levels for the position of the mass peaks [15]. On the other hand, the distribution of baryonic matter in the Bullet Cluster was obtained from X-ray observations of the hot gas, providing information about the gas density (see the blue "+" in the left plot and the colored area in the right plot of Fig. 2.2). The distinct spatial separation between the X-ray emitting plasma, which is slowed down after the collision, and the total mass distribution, which traces the collisionless components (galaxies and DM), provides strong evidence for an additional, invisible mass component [15, 16].

2.1.3 Cosmological Scale Observations

The most convincing evidence for DM is derived from measurements of the Cosmic Microwave Background (CMB) at cosmological scales. The CMB was formed about 380,000 years after the Big Bang when the universe cooled enough to form neutral hydrogen atoms through a process called recombination. During this process, the universe became transparent, and the associated photon decoupling is observed today as the CMB.

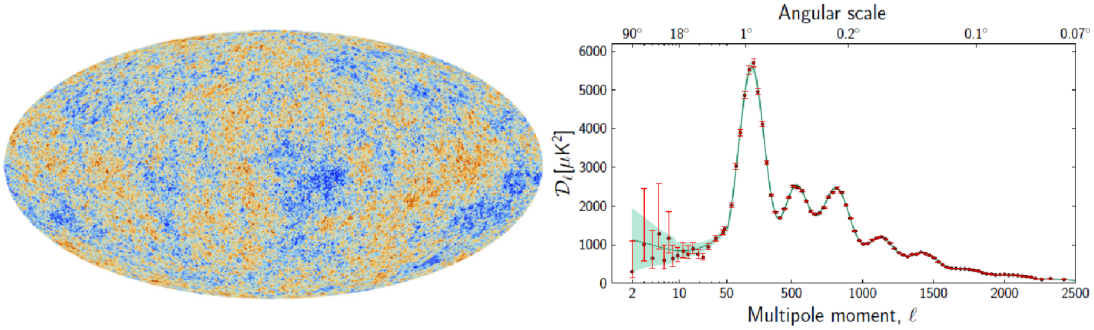

Figure 2.3: CMB fluctuations in the order of $\pm 300\,\mu$K from the mean temperature of 2.73 K (left panel) and the temperature power spectrum measured by Planck space observatory (right panel). Taken from [17].

The CMB was discovered accidentally in 1965 by Penzias and Wilson, who detected an isotropic microwave signal while calibrating a radio antenna [18]. This signal turned out to be a nearly perfect blackbody spectrum at a temperature of 2.73 K, providing an imprint of the hot state of the early universe. However, more detailed investigations have revealed temperature fluctuations on the order of $\delta T/T \sim 10^{-5}$, which are the result of primordial density variations caused by quantum fluctuations during inflation (cf. left panel of Fig. 2.3). The temperature fluctuations can be converted into an angular power spectrum using a spherical harmonic function representation, resulting in acoustic peaks that provide information about the energy composition of the universe (cf. right panel of Fig. 2.3). The observed temperature fluctuations are too small to explain the formation of cosmological structures in a purely baryonic universe, where fluctuations on the order of $\delta T/T \sim 10^{-2} - 10^{-3}$ would be required [9, 17]. This indicates the presence of non-baryonic DM, which could begin clustering before recombination. Numerical simulations of structure formation favor a Cold Dark Matter (CDM) dominated early universe, in which small halos form first, followed by the bottom-up formation of larger structures up to the scale of galaxy clusters. The majority of DM must therefore be non-relativistic, since Warm Dark Matter (WDM) and Hot Dark Matter (HDM) cannot fully explain the structures observed today. The results from the CMB observations led

to the SM of cosmology (ΛCDM), which describes the universe today as a composition of dark energy (69 %), CDM (26 %), baryonic matter (5 %) and radiation (<1 %).

2.1.4 Alternative Theory: MOND

All these observations indicate a much higher mass-to-light ratio than can be attributed to luminous matter alone. However, Modified Newtonian Dynamics (MOND) provides an alternative approach to DM by proposing a modification of the laws of gravity for very small accelerations [19]. For the galactic scale observations in section 2.1.1, MOND provides a successful explanation without the concept of DM. The rotational curves and the dynamics of dwarf galaxies can be explained by MOND. Furthermore, MOND does not lead to the so-called 'missing satellites problem', since it does not overestimate the number of dwarf galaxies, unlike the ΛCDM model, which requires a DM halo [20].
However, MOND cannot provide sufficient explanations for observations on larger scales, such as the total observed mass in clusters. MOND also provides no answer for the spatial separation between the baryonic and total mass in the Bullet Cluster (cf. Fig. 2.2) and is incompatible with the CMB observations in section 2.1.3, since the height of the third acoustic peak cannot be explained without the existence of DM (cf. Fig. 2.3) [9]. Thus, DM remains the most prominent explanation for the observations described in this section.

2.2 Dark Matter Properties and Candidates

From the various indications for DM, ranging from galactic to cosmological scales, it was possible to deduce certain fundamental properties. Based on these observations, many candidates have been proposed in the mass range from 10^{-22} eV to a few solar masses. Although Massive Astrophysical Compact Halo Objects (MACHOs) such as planets, white dwarfs, neutron stars, or black holes are possible DM candidates, it is clear today that baryonic matter does not account for a large fraction of the total DM. One exception to this are Primordial Black Holes (PBHs), which could have been formed by strong density fluctuations in the early universe shortly after cosmic inflation [21]. These could explain at least part of the CDM and have come back into the focus of the scientific community since LIGO's gravitational wave measurements in 2016, which could be an indication of PBH mergers [22]. But even PBHs cannot explain the total DM in the universe, which supports the existence of one or more new types of particles with specific properties.
Those DM particles are most likely non-baryonic matter that does not interact strongly or electromagnetically[1]. Since they can still be observed today, DM candidates must have a long lifetime compared to cosmological time scales. Observations in the Bullet Cluster also imply a small cross section, both for self-interactions and for interactions with baryonic matter. DM must interact gravitationally, but the mass is allowed to be in a wide range. The lower mass limit is constrained by quantum effects, which, based on phase space considerations, imply a limit of > 70 eV if DM is fermionic and $\gtrsim 10^{-22}$ eV if it is bosonic [23]. Since previous observations favor a CDM-dominated universe, a proposed DM candidate must have been non-relativistic in the early universe, and it should lead to the correct relic energy density $\Omega_\chi \approx 0.26$ observed today [9].

[1] Cosmological observations of the CMB provide strong constraints on the electric charge of DM, since this would lead to an interaction with the baryon-photon plasma during recombination. Depending on the DM mass, a maximum "milli-electric" charge is estimated to be on the order of $\sim 10^{-7}$ e [23].

In the SM of particle physics, only one particle has the necessary properties to be considered a candidate for DM: the neutrino. Neutrinos belong to the leptons in the SM and were already postulated by Pauli in 1930 [24]. They owe their name to the fact that they are electrically neutral, and for a long time, they were assumed to be massless. The discovery of neutrino oscillations, however, confirmed that neutrinos must have a small mass and can therefore interact gravitationally [25, 26]. Apart from that, neutrinos interact only weakly, and together with the fact that they are stable, this makes them unique among the SM particles. Because they are so light, neutrinos were highly relativistic in the early universe and would represent a form of Hot Dark Matter (HDM). Since the observational evidence clearly favors the CDM scenario, only a small fraction of the missing mass can be attributed to HDM, such as the SM neutrino.
Neutrinos and antineutrinos are created in the SM through the charged current (CC) and neutral current (NC) of the weak interaction in one of the three lepton flavors $\ell \in \{e, \mu, \tau\}$. However, there are theoretical extensions of the SM that propose so-called sterile neutrinos, which transform as singlets with respect to the weak interaction. These so far hypothetical right-handed neutrinos do not interact directly with the $W^{\pm}$ and Z bosons and have only very weak couplings to the active neutrinos, making them possible candidates for DM. In most theories, sterile neutrinos with masses in the keV range would have too high a thermal velocity to act as CDM. Instead, they would behave more like Warm Dark Matter (WDM) and could not alone explain the current observations of a CDM-dominated universe. Heavier sterile neutrinos in the GeV − TeV range could, in principle, be considered CDM candidates, but their production mechanisms face significant theoretical challenges and are strongly constrained by experiments [27]. Since the late 1980s, it has been widely accepted that DM most likely consists of previously unknown, cold, non-baryonic particles. Well-motivated candidates for such particles are axions, which were originally proposed to solve the strong CP problem in quantum chromodynamics and would be produced non-thermally in the early universe [28], as well as axion-like particles (ALP), which arise naturally in many extensions of the SM [29]. Another class of promising candidates are Weakly Interacting Massive Particles (WIMPs), which are discussed in detail in the following section.

2.2.1 The WIMP Miracle

Weakly Interacting Massive Particles (WIMPs) are hypothetical particles that are electrically neutral, stable, and interact only gravitationally and weakly. Classical WIMPs are assumed to participate in the weak interaction and are therefore mediated by the Z and $W^{\pm}$ bosons, with masses on the order of $\sim 100\,\mathrm{GeV}$ [30]. Based on the typical scaling of weak interaction cross sections ($\sigma \sim \alpha_{\mathrm{W}}^2/E^2$ with $\alpha_{\mathrm{W}} \sim 10^{-2}$), the annihilation cross section times velocity can be estimated as [30]

$$(\sigma v)_{\mathrm{WIMP}} \approx \alpha_{\mathrm{W}}^2 \cdot (100\,\mathrm{GeV})^{-2} \sim 10^{-25}\,\mathrm{cm}^3/\mathrm{s}\ . \tag{2.1}$$

Assuming SM thermodynamics, WIMPs would have been in a state of perpetual annihilation and pair production in thermal equilibrium with all other particles in the early universe. The time evolution of the WIMPs number density is described by the Boltzmann equation

$$\frac{\mathrm{d}n_\chi}{\mathrm{d}t} = -3Hn_\chi - \langle \sigma_{\mathrm{A}} v \rangle \left(n_\chi^2 - n_{\chi,\mathrm{eq}}^2 \right)\ , \tag{2.2}$$

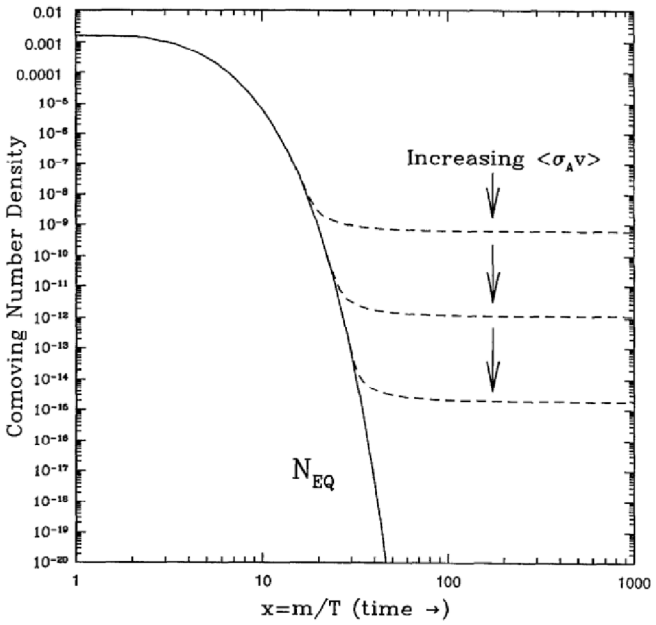

Figure 2.4: Comoving number density of WIMPs in the early universe as a function of $x = m_\chi/T$ assuming SM thermodynamics according to Eq. 2.2. The solid line describes the expected number density in thermal equilibrium and the dashed curves indicate the actual abundance dependent on the thermally averaged self-annihilation cross section $\langle \sigma_A v \rangle$. Taken from [31].

where $n_{\chi,\mathrm{eq}}$ is the number density in thermal equilibrium (cf. solid line in Fig. 2.4), and $\langle \sigma_A v \rangle$ is the thermally averaged self-annihilation cross section multiplied by the relative velocity v of two DM particles. At some point, the expansion rate H of the universe became greater than the annihilation rate $\Gamma = n_\chi \langle \sigma_A v \rangle$, which stopped the self-annihilation process (cf. dashed lines in Fig. 2.4) [32]. From the relic energy density of $\Omega_\chi h^2 = 0.1200 \pm 0.0012$ observed today [9], the canonical value of the annihilation cross section can be estimated by the condition $n_\chi \langle \sigma_A v \rangle_{\mathrm{can}} \approx H$. From the approximate solution of the Boltzmann equation (Eq. 2.2), the relic density can be expressed as[2] [30]

$$\Omega_\chi h^2 \approx \frac{3 \times 10^{-27}\,\mathrm{cm}^3/\mathrm{s}}{\langle \sigma_A v \rangle_{\mathrm{can}}} \ .$$

Solving for the annihilation cross section and inserting the energy density yields the mass-independent canonical value

$$\langle \sigma_A v \rangle_{\mathrm{can}} \approx \frac{3 \times 10^{-27}\,\mathrm{cm}^3/\mathrm{s}}{0.12} \approx 3 \times 10^{-26}\,\mathrm{cm}^3/\mathrm{s} \ .$$

Surprisingly, this value is very similar to that derived in Eq. 2.1, which is often referred to as the 'WIMP miracle'.
In this approximation, the thermally averaged self-annihilation cross section is assumed to be constant. However, since the freeze-out parameter $x_F = m_\chi/T$ is about $x_F \sim 20 - 30$ (cf. Fig. 2.4), the total velocity-dependent annihilation cross section $\sigma_A v$ can be described

[2] For this calculation, a self-conjugate Majorana WIMPs and constant annihilation (pure s-wave) are assumed [30].

in the non-relativistic regime in powers of the quadratic relative velocity [30, 33, 34]

$$\sigma_{\mathrm{A}} v = a + b \cdot v^2 + \mathcal{O}(v^4) \ . \tag{2.3}$$

The thermal average of the annihilation cross section during freeze-out is therefore approximated by

$$\langle \sigma_{\mathrm{A}} v \rangle = a_S + b_P \cdot x_F^{-1} + \mathcal{O}(x_F^{-2}) \tag{2.4}$$

where $a = a_S$ and $b_P = 6\, b$ due to the thermal average of $\langle v^2 \rangle = 6/x_F$ for a Maxwell-Boltzmann distribution[3] [30]. The velocity-independent contribution $\langle \sigma_{\mathrm{A}} v \rangle \approx a_S$ describes the s-wave annihilation of DM, which dominates in the present universe. However, in some WIMP scenarios, particularly those involving Majorana DM particles with vector or axial couplings, s-wave annihilations are either forbidden or at least strongly suppressed due to charge parity (CP) and helicity considerations [30]. In this case, the p-wave contribution $\langle \sigma_{\mathrm{A}} v \rangle \approx b_P \cdot x_F^{-1}$ becomes dominant, scaling quadratically with velocity. In the very early Universe, this contribution was significant, with typical velocities of $v \approx 0.3\ c$; whereas today, with $v \approx 10^{-3}\ c$, it is smaller by about six orders of magnitude [35, 36] (cf. Sec. 3.3.3).
The fact that WIMPs naturally explain the relic density and fulfill all the required DM properties makes them the leading candidate for non-baryonic CDM and resulted in a scientific focus on heavy DM particles in the GeV and TeV regimes. However, as no evidence has been found despite a large number of experiments, and instead even stricter limits have been set, the focus in recent years has shifted more towards lighter particles in the MeV and sub-GeV range, the so-called 'light DM'.

2.2.2 Light Dark Matter

Light DM poses a conceptual and phenomenological challenge. In the simplest thermal freeze-out picture, DM particles with masses below a few GeV would have decoupled too early, leading to a larger relic abundance when interacting with SM particles at the weak scale. From these considerations, the classical Lee–Weinberg limit provides a lower mass bound of roughly 2 GeV for conventional WIMPs [37]. Lighter particles would therefore require either an enhanced annihilation rate or an alternative production mechanism to match the observed relic density. However, more precise calculations of the thermodynamic equation of state in the early universe have shown that the reduction of relativistic degrees of freedom during the Quantum Chromodynamics (QCD) phase transition increases the annihilation rate for lighter DM masses [38]. As a consequence, thermally produced particles in the MeV–GeV range are not definitely excluded. This behavior is illustrated in Fig. 2.5, which shows the thermally averaged self-annihilation cross section required to produce the observed relic abundance for both s-wave (left) and p-wave dominated scenarios (right)[4]. The figure was produced using the data provided in [39] and considers the case of self-conjugate Majorana DM (red) and non self-conjugate Dirac DM (blue) in the energy range from MeV to GeV relevant for this work. The black line in the left panel of Fig. 2.5 reveals that the canonical cross section $\langle \sigma_{\mathrm{A}} v \rangle_{\mathrm{can}} = 3 \times 10^{-26}\,\mathrm{cm}^3/\mathrm{s}$ increasingly underestimates the required annihilation rate for light DM masses below the Lee–Weinberg limit.

[3] A factor of 3 arises from the three spatial dimensions, and the factor of 2 accounts for the relative velocity of two particles.

[4] Note that the values in the Dirac scenario are approximately twice as large as in the Majorana case.

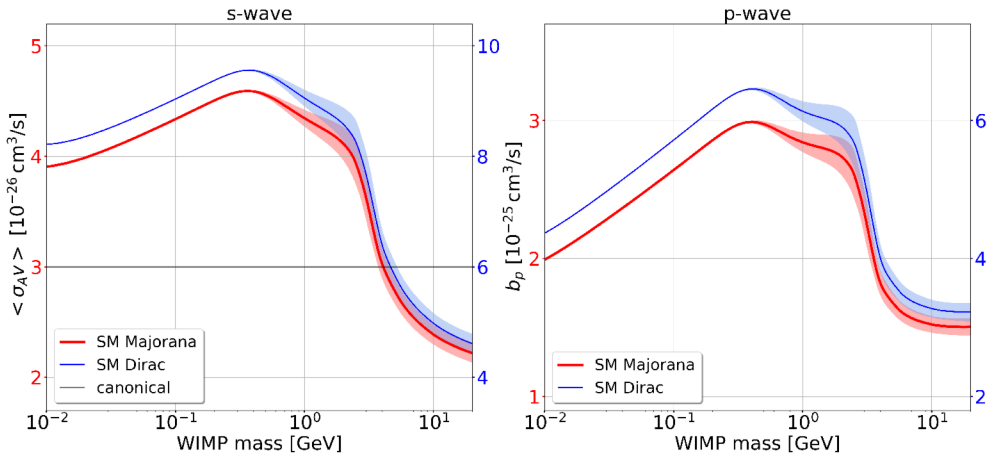

Figure 2.5: Thermally averaged annihilation cross section for s-waves (left panel) and for p-waves (right panel). The red curves describe the case of a self-conjugate Majorana WIMP and the blue plots correspond to a Dirac WIMP and have about twice the value. The annihilation cross sections are calculated from the data provided in [39] assuming SM thermodynamics, where the error band indicates the uncertainty in the equation of state used for the calculations [40]. The canonical value $\langle \sigma_{\mathrm{A}} v \rangle_{\mathrm{can}} = 3 \times 10^{-26}\,\mathrm{cm}^3/\mathrm{s}$ is indicated by the black line (left panel).

Despite this theoretical motivation, light DM candidates face stringent cosmological constraints, which are derived, in particular, from observations of Big Bang Nucleosynthesis (BBN) and the CMB. In particular, s-wave annihilations into visible final states, such as e^+e^- or photons, can disturb the formation of light elements and modify the photon–baryon plasma, leading to strong exclusions in the sub-GeV mass range [2, 41]. A promising way out lies, on the one hand, in scenarios with p-wave-dominated annihilation, where the cross section scales with velocity and is strongly suppressed at the time of the CMB. On the other hand, neutrinophilic DM, which annihilates preferentially or exclusively into neutrinos, is increasingly being discussed. The annihilation products evade the strict CMB and BBN bounds even in the MeV–sub-GeV regime [3, 42], while still producing a potentially detectable signal in large-volume neutrino detectors like JUNO.

2.3 Dark Matter Detection

Assuming DM consists of WIMPs, there are several possible approaches to detect these particles. A broad range of experiments has been developed to search for WIMPs across a wide mass range. While no discovery has been made so far, some experiments have established stringent exclusion limits, which will be presented in this section.

Detection through Production

One method to detect DM is through the production of WIMPs in proton-proton (pp) collisions at particle accelerators. Instead of observing WIMPs directly, the total momentum of the event is analyzed to search for missing energy [29]. This detection method is sensitive to WIMPs over a wide mass range, depending on the mediator mass, and is independent of astrophysical uncertainties. Producing WIMPs would also provide direct information about the coupling between DM and the SM, which is not

provided by indirect detection experiments. Prominent collider searches are the ATLAS and CMS experiments at the Large Hadron Collider (LHC), which set limits on the spin-independent (SI) and spin-dependent (SD) DM-nucleon interaction cross section in the GeV to TeV range [43]. So far, no significant excess has been observed in any collider experiment.

Direct Detection

Direct detection experiments aim to measure the recoil energy of atoms that result from elastic or inelastic scattering between the detector material and WIMPs. Since these recoil energies are expected to be in the order of a few keV, the detectors must have very low energy thresholds. This can be achieved by various detection techniques [29]. Experiments like XENONnT, LZ, DarkSide-50 or PandaX-4T use liquid noble gases

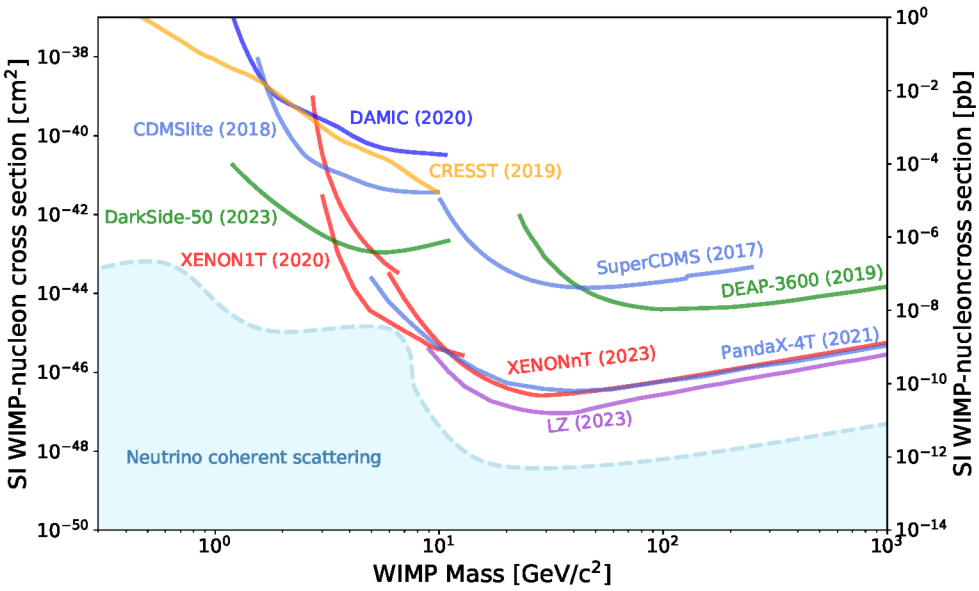

Figure 2.6: Upper limits on the SI DM-nucleon cross section depending on the WIMP mass. The irreducible *neutrino floor* (blue area) is caused by Coherent Elastic Neutrino-Nucleus Scattering (CEνNS) and is also added. Taken from [29].

like xenon or argon, which offer excellent background suppression. These noble liquid detectors have set the most stringent limits on the SI DM-nucleon interaction cross section, particularly in the GeV mass range (cf. Fig. 2.6). Other representatives of direct detection experiments are solid-state cryogenic detectors such as SuperCDMS, EDELWEISS or CRESST. These experiments use the calorimetric effect and are thus very sensitive to small temperature changes caused by the energy deposition of particles. These detector types are optimized to cover the spin-independent (SI) DM-nucleon interaction cross section in the low-mass DM range [29]. An important irreducible background for direct detection is the Coherent Elastic Neutrino-Nucleus Scattering (CEνNS). This background arises mainly from solar and atmospheric neutrinos, which scatter off entire nuclei. For very low spin-independent (SI) WIMP-nucleon interaction cross sections, the nuclear recoil spectra from CEνNS become indistinguishable from the ones expected from WIMPs [29] (cf. Sec. 5.1.2). This so-called *neutrino floor* is a fundamental sensitivity limit for present-day direct detection experiments and is included in Fig. 2.6.

Indirect Detection

Another approach for DM search is indirect detection. This method considers potential particle–antiparticle pairs produced through the self-annihilation or decay of WIMPs in objects like the Earth, the Sun or the Milky Way. In general, these processes can produce any particle–antiparticle pair, as long as the WIMP mass is sufficiently large to account for the corresponding rest masses of the SM particles. The preferred annihilation channel depends on the type of coupling as well as the DM mass, and the observable final-state products are typically gamma rays, charged cosmic rays (p or e^+), or neutrinos. Since the expected flux of such particles depends on both the annihilation or decay rate and the WIMP density distribution of the source, indirect detection is often subject to large systematic uncertainties. As long as the annihilation is not suppressed by symmetries such as CP or helicity, it is dominated today by s-wave processes (cf. Sec. 2.2.1). If s-waves are suppressed or forbidden, the annihilation would be dominated by the velocity-dependent p-wave according to Eq. 2.4. With an average velocity of $\sim 10^{-3}c$ in the present halo, the annihilation rate would be about six orders of magnitude smaller than for s-waves, and thus practically invisible to indirect searches from the Milky Way [36, 35].
However, experiments have set stringent limits on exclusive channels into gamma rays and charged cosmic rays in the MeV to sub-GeV range, effectively ruling them out as viable explanations for the thermal relic density observed today, for s-wave dominated annihilation [44, 45, 46, 47]. In contrast, annihilation channels into neutrinos remain much less constrained [36]. Due to their small interaction cross section with matter, neutrino interactions are rare and thus more challenging to detect. This leaves indirect DM searches with neutrinos as a promising method to probe DM models, which will be discussed in more detail in Section 3.

3 | Indirect Dark Matter Search with Neutrinos

Freedom to a dancer means discipline. That is what technique is for - liberation.

– Martha Graham

Indirect DM searches aim to detect the annihilation products of two DM particles, as explained in Sec. 2.3. In this work, the direct channel

$$\chi\chi \to \nu_\ell \, \bar{\nu}_\ell \quad \text{for} \quad \ell \in \{e, \mu, \tau\} \tag{3.1}$$

into neutrinos is considered dominant. Due to their small interaction probability, neutrinos are the least detectable particles in the SM. Consequently, any upper limit on the neutrino flux from DM annihilation translates into an upper bound on the self-annihilation cross section $\langle \sigma_{\mathrm{A}} v \rangle$. At the same time, their small interaction probability allows neutrinos to traverse dense environments in the universe undisturbed, making them highly valuable as messengers over large galactic scale distances, like the Milky Way [48]. In this analysis, a democratic ratio of $1:1:1$ is assumed for all three flavors ($\kappa_1 = 3$). This assumption remains valid even if one flavor is preferred in the self-annihilation process, since vacuum neutrino oscillations would still ensure a comparable flux of the other flavors at Earth [36] (cf. Section 4.5.1).

3.1 Expected Neutrino Flux

The expected neutrino flux from DM annihilations strongly depends on the underlying DM density distribution. Large DM densities can be found in particular at the centers of large gravitational potentials such as the Earth or the Sun, where DM can accumulate through gravitational capture [4]. In this work, however, the focus is on the expected neutrino signature from DM self-annihilation in the entire Milky Way, which is determined by the Galactic DM profile and thus requires certain astrophysical assumptions about the Galactic halo. There are also extragalactic components from galaxies or galaxy clusters that contribute an integrated neutrino flux considering annihilations from the entire cosmic DM distribution. However, this contribution is significantly smaller than the expected Galactic neutrino flux and is therefore not considered in this analysis [36]. The differential neutrino flux from DM self-annihilation in the Galactic halo, per unit energy and solid angle, can be written as

$$\frac{\mathrm{d}^2 \Phi^{\chi}_{\nu_\ell}}{\mathrm{d}E_{\nu_\ell} \, \mathrm{d}\Omega}(\psi, E_{\nu_\ell}) = \frac{1}{\kappa_1} \frac{1}{4\pi} \frac{\mathrm{d}N_{\nu_\ell}}{\mathrm{d}E_{\nu_\ell}} \int_{\mathrm{LOS}} \Gamma_A(s, \psi) \cdot \, \mathrm{d}s \tag{3.2}$$

for each neutrino flavor ν_ℓ. The local annihilation rate $\Gamma_A(s,\psi)$ per unit volume is integrated along the line of sight (LOS) distance coordinate s, where ψ is the angle between the direction of observation and the GC [49] (cf. Fig. 3.1). The annihilation rate depends on the one hand on the thermally averaged self-annihilation cross section $\langle\sigma_\mathrm{A} v\rangle$ (cf. Eq. 2.4) and on the other hand on the DM particle density $n_\chi = \rho(s,\psi)/m_\chi$. The annihilation rate can be expressed by

$$\Gamma_A(s,\psi) = \frac{1}{2}\,\langle\sigma_\mathrm{A} v\rangle\, n_\chi^2 \quad \text{for Majorana DM and} \tag{3.3}$$

$$\Gamma_A(s,\psi) = \langle\sigma_\mathrm{A} v\rangle\, n_\chi n_{\bar\chi} \quad \text{for Dirac DM.} \tag{3.4}$$

The factor 1/2 in Eq. 3.3 for the Majorana DM case ($\chi = \bar\chi$) prevents double counting of the particles, and in the Dirac case ($\chi \neq \bar\chi$) in Eq. 3.4, a factor 1/4 results from assuming symmetric number densities $n_\chi = n_{\bar\chi} = \rho(s,\psi)/(2\,m_\chi)$ when the number density is squared. Thus the annihilation rate can be expressed by

$$\Gamma_A(s,\psi) = \frac{1}{\kappa_2}\,\langle\sigma_\mathrm{A} v\rangle\,\frac{\rho^2(s,\psi)}{m_\chi^2}\ , \tag{3.5}$$

with $\kappa_2 = 2$ in the Majorana scenario and $\kappa_2 = 4$ in the Dirac case.

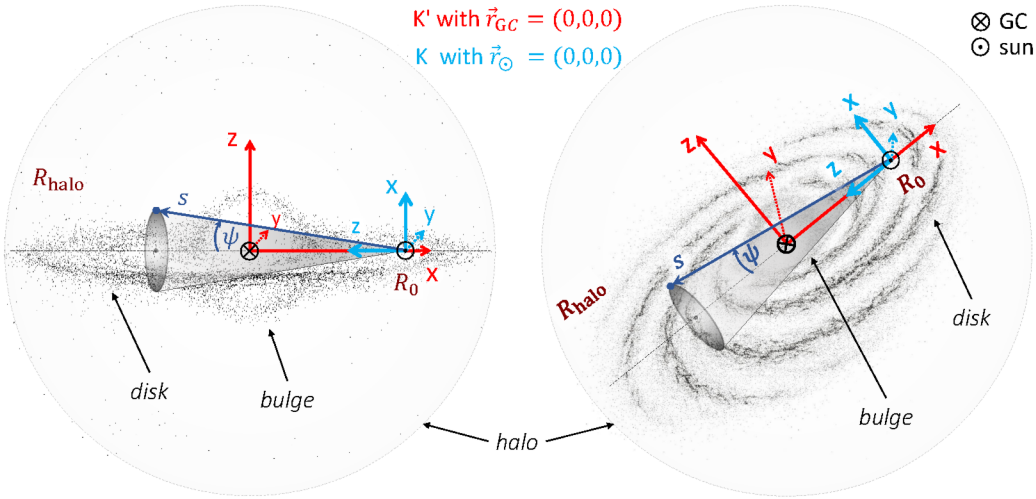

Figure 3.1: Schematic illustration of the Milky Way from two perspectives showing the baryonic bulge and disk, as well as the DM halo. The origin of the coordinate system K' is at the GC, while the coordinate system K is anchored at the Sun $\odot$. The x-z plane of K is tilted by 90° with respect to K', such that $\hat{e}'_x = -\hat{e}_z$. The LOS coordinate s and the angle ψ are given in K. The position of the Sun R_0 and the DM density profiles, however, are specified in K' with respect to the GC.

The neutrino spectrum per annihilation $\mathrm{d}N_{\nu_\ell}/\mathrm{d}E_{\nu_\ell}$ in Eq. 3.2 depends on the annihilation channel. Here, only the case of a 100 % branching fraction into neutrinos is considered, leading to a monoenergetic neutrino spectrum at the WIMP mass m_χ [36][1]

$$\frac{\mathrm{d}N_{\nu_\ell}}{\mathrm{d}E_{\nu_\ell}} = \delta(E_{\nu_\ell} - m_\chi)\ .$$

[1] Annihilations into hadronic, leptonic, or bosonic channels could also produce neutrinos via secondary processes; however, these would no longer exhibit a monoenergetic signature [50].

3.2 DM Distribution in the Galactic Halo

Since the expected differential neutrino flux in Eq. 3.2 depends on both particle-physics and astrophysical quantities, it is often more convenient to express the equation in terms of the astrophysical $\mathcal{J}$-factor

$$\mathcal{J}(\Delta\Omega) = \int \mathrm{d}\Omega \int_{LOS} \rho^2\big(r(s,\psi)\big) \cdot \mathrm{d}s \tag{3.6}$$

which for s-wave annihilation only includes the radial DM density profile and the LOS geometry and is typically given in units of $\mathrm{GeV}^2\,\mathrm{cm}^{-5}$. The distance $r(s,\psi) = \sqrt{R_0^2 + s^2 - 2R_0 s\cos\psi}$ from the GC depends on the LOS distance coordinate s and the enclosed angle ψ (cf. Fig. 3.1), while R_0 denotes the distance of the Sun from the GC.

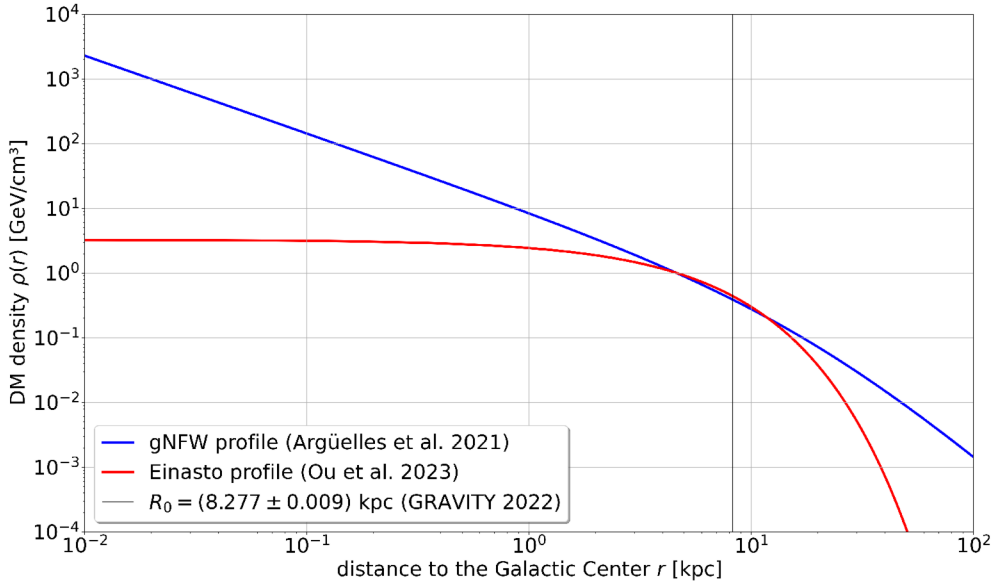

Figure 3.2: Radial DM density profile of the Galactic halo for different models. The parameters for the cuspy gNFW model (cf. Eq. 3.7) are adapted from [36] (blue curve) and the parameters for the cored Einasto model (cf. Eq. 3.8) can be found in [51] (red curve). The latest result for the distance R_0 between the Sun and the GC from GRAVITY [52] is also added in the plot (black line).

The DM density profile is commonly modeled using precise measurements of the Milky Way rotation curve (cf. Fig. 2.1) and must meet the local DM density $\rho(r = R_0) = \rho_0$. Historically, a local DM density of $\rho_0 = 0.3\,\mathrm{GeV/cm}^3$ and a solar distance to the GC of $R_0 = 8.5\,\mathrm{kpc}$ were assumed. However, these values have been excluded at the 4σ level by the latest studies [53]. Instead, the most recent results point to a distance of $R_0 = (8.277 \pm 0.009)\,\mathrm{kpc}$ to the GC [52], while the local DM density is estimated to be in the range $\rho_0 = (0.4 - 0.5)\,\mathrm{GeV/cm}^3$ [51, 54]. Despite these constraints on the density profile, substantial systematic uncertainties remain regarding the structure of the DM halo, depending on the assumed model. In particular, it remains unclear whether the DM halo in the GC is cuspy (steeply rising) or cored (flattened in the inner region). A widely used parametrization is the generalised Navarro-Frenk-White (gNFW) density

profile

$$\rho_{\mathrm{gNFW}}(r) = \frac{M_n}{4\pi r_s^3} \cdot \left(\frac{r}{r_s}\right)^{-\gamma} \left(1 + \frac{r}{r_s}\right)^{\gamma-3} \tag{3.7}$$

where M_n is the mass normalization, r_s is the scale radius, and $\gamma \approx 1$ leads to a steep density increase toward the GC [36, 51]. More recent studies, however, suggest a flatter DM distribution that is more accurately described by the Einasto profile [51]

$$\rho_{\mathrm{Ein}}(r) = \frac{M_n}{4\pi r_s^3} \cdot \exp\left(-\left[\frac{r}{r_s}\right]^{\alpha}\right) \ . \tag{3.8}$$

Fig. 3.2 shows both DM density profiles for the Galactic halo, where the parameters $(M_n, r_s, \gamma) = (6.64 \times 10^{11} M_\odot,\, 20\,\mathrm{kpc},\, 1.2)$ for the cuspy gNFW model are adapted from [36], while the parameters $(M_n, r_s, \alpha) = (0.62 \times 10^{11} M_\odot,\, 3.86\,\mathrm{kpc},\, 0.91)$ for the Einasto model are adapted from [51].

3.2.1 $\mathcal{J}$-Factor for Cone-Like ROI

To determine the percentage of the neutrino flux in Eq. 3.2 from a given region of interest (ROI), the $\mathcal{J}$-factor for this specific ROI with the solid angle $\Delta\Omega$ is compared to the full-sky (FS) $\mathcal{J}$-factor with $\Delta\Omega = 4\pi$. In this analysis, a cone with half-opening angle ψ_m around the GC is considered as ROI (cf. Fig. 3.1), where $\psi_m = \pi$ corresponds to the full-sky, thus the integral in Eq. 3.6 with the differential $d\Omega = \sin\psi \ \mathrm{d}\psi \ \mathrm{d}\varphi$ must be evaluated with the following limits [50]

$$\mathcal{J}_{\psi_m} = \int_0^{2\pi} \mathrm{d}\varphi \int_0^{\psi_m} \sin\psi \ \mathrm{d}\psi \int_0^{s_m(\psi)} \rho^2\big(r(s,\psi)\big) \ \mathrm{d}s \ , \tag{3.9}$$

where the LOS coordinate s is integrated up to

$$s_m(\psi) = \sqrt{R_{\mathrm{halo}}^2 - R_0^2 \sin^2\psi} + R_0 \cos\psi \ , \tag{3.10}$$

with R_{halo} denoting the halo radius[2]. When performing the integration, numerical divergences near the GC must be taken into account, especially for cuspy density profiles. Therefore, a Gauss–Legendre quadrature was applied for different sub-intervals, which is discussed in more detail in Appendix A. In Fig. 3.3, the ratio $\mathcal{J}_{\psi_m}/\mathcal{J}_{FS}$ is shown, which is identical to the fraction of the expected neutrino flux from the FS. As expected from the density profile in Fig. 3.2, the neutrino flux is significantly higher toward the GC. For the cuspy gNFW profile in Eq. 3.7, half of the total flux is expected within an opening angle of $2 \cdot \psi_m = 23.6°$ around the GC, whereas for the flattened, cored Einasto profile in Eq. 3.8, the same fraction is obtained from a much larger opening angle of $2 \cdot \psi_m = 73°$. Depending on the underlying density profile, a direction-dependent analysis can therefore substantially contribute to signal-to-background (S2B) optimization. In a cuspy profile scenario, a large fraction of the neutrino flux is expected to come from the GC, whereas a directional analysis would be less promising for a cored profile. This is discussed in detail in Section 9.2.

[2] In this work, $R_{\mathrm{halo}} = 100\,\mathrm{kpc}$ was chosen; however, $J(\psi_m)$ already converges for $R_{\mathrm{halo}} = 20\,\mathrm{kpc}$ due to the steep density fall-off (cf. Fig A.4).

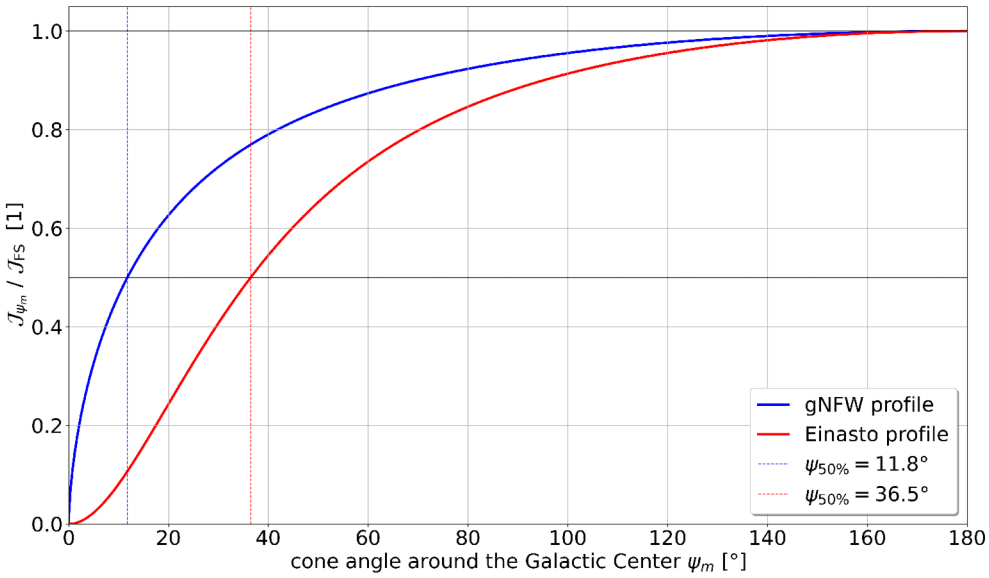

Figure 3.3: Fraction J_{ψ_m}/J_{FS} as a function of the cone angle around the GC. The curves show the cumulative flux contribution for the gNFW (blue) and the Einasto (red) density profiles. The vertical dashed lines mark the cone angle (half-opening angle) where 50 % of the total neutrino flux is expected from. For the cuspy gNFW profile $\psi_{50\,\%} \simeq 11.8°$ and for the cored Einasto profile $\psi_{50\,\%} \simeq 36.5°$ can be derived.

3.2.2 Dimensionless $\mathcal{J}$-Factor $\mathbf{J_{avg}}$

To cover the astrophysical uncertainties for different density profiles, the dimensionless

$$J_{\mathrm{avg}}(\psi_m) = \frac{\mathcal{J}_{\psi_m}}{\Delta\Omega(\psi_m) R_0 \rho_0^2} \tag{3.11}$$

is often introduced in sensitivity studies of indirect DM searches. The solid angle for a cone-like ROI around the GC is determined by

$$\Delta\Omega(\psi_m) = 2\pi \cdot (1 - \cos\psi_m) \ . \tag{3.12}$$

For FS observations ($\psi_m = \pi$), the gNFW profile yields $J_{\mathrm{avg}} \approx 4.3$, while the dimensionless $\mathcal{J}$-factor for the Einasto profile is about half as large as $J_{\mathrm{avg}} \approx 2.4$, which is visualized in Fig. A.5. For model-independent comparison of different experiments, the FS dimensionless $\mathcal{J}$-factor is assigned a canonical value of $J_{\mathrm{avg}} = 3$ for this work.

With these considerations, the differential neutrino flux for each neutrino or antineutrino flavor from DM self-annihilation via s-waves in the Galactic halo can be described by

$$\frac{\mathrm{d}\Phi^{\chi}_{\nu_\ell}(\psi_m)}{\mathrm{d}E_{\nu_\ell}} = \frac{1}{\kappa_1 \kappa_2} \cdot \frac{\langle \sigma_{\mathrm{A}} v \rangle}{m_\chi^2} \cdot \frac{\Delta\Omega(\psi_m)}{4\pi} \cdot R_0\, \rho_0^2\, J_{\mathrm{avg}}(\psi_m) \cdot \delta(E_{\nu_\ell} - m_\chi) \tag{3.13}$$

for a cone with a half-opening angle ψ_m around the GC[3]. In this work, $R_0 = 8.277\,\mathrm{kpc}$ is used for the distance between the Sun and the GC, while the local DM density is estimated to be $\rho_0 = 0.4\,\mathrm{GeV/cm^3}$ [36, 52].

[3]For FS observations, the solid angle $\Delta\Omega(180°) = 4\pi$ and the fraction become 1.

3.3 Velocity-Dependent Annihilation

In the previous section, only the velocity-independent s-wave annihilation of DM in the halo of the Milky Way was discussed. Since several DM models suppress this channel, the p-wave annihilation scenario is also considered here. In this case, the annihilation cross section $\langle \sigma_A v \rangle (v^2)$, according to Eq. 2.3, depends on the dimensionless average relative velocity $v \equiv v_{\mathrm{rel}}/c$ of the DM particles, which, in turn, varies with their distance r from the GC. Consequently, the annihilation rate in Eq. 3.5 yields an additional quadratic velocity term in the LOS integral in Eq. 3.2, which modifies the astrophysical $\mathcal{J}$-factor in Eq. 3.6 according to [36]

$$J^{(p)}(\Delta\Omega) = \int \mathrm{d}\Omega \int_{LOS} \rho^2\big(r(s,\psi)\big) \left\langle v^2\big(r(s,\psi)\big)\right\rangle \mathrm{d}s \ . \tag{3.14}$$

Unlike baryonic matter, the DM halo does not necessarily need to rotate around the GC. Instead, the velocity of the DM particles is locally approximated by a Maxwell distribution, whose width is characterized by the one-dimensional velocity dispersion $v_0(r)$ [36, 55]. This dispersion describes the mean squared velocity in one spatial direction and determines the average relative velocity via

$$\langle v^2(r)\rangle = 3\, v_0^2(r) \tag{3.15}$$

which is relevant for p-wave annihilation. The radial dependence of $v_0(r)$ is set by virial equilibrium in the Galactic potential and can be determined by solving the isotropic spherical Jeans equation [36]

$$\frac{\mathrm{d}\left(\rho_{\mathrm{DM}}(r)\, v_0^2(r)\right)}{\mathrm{d}r} = -\rho_{\mathrm{DM}}(r)\frac{\mathrm{d}\phi_{\mathrm{tot}}(r)}{\mathrm{d}r} \ . \tag{3.16}$$

In the following, the calculation of the effective $J^{(p)}$ factor is carried out explicitly by solving the Jeans equation for the gNFW and Einasto profiles, taking into account the total gravitational potential of the Milky Way. On the one hand, the gravitational potential is given by the baryonic contribution contained in the bulge and the disk, and on the other hand, the contribution of the DM distribution must also be taken into account.

3.3.1 Mass Contribution of Bulge, Disk and DM

The bulge potential is often parameterized by the radial Hernquist potential [36, 51]

$$\phi_{\mathrm{bulge}}(r) = -\frac{GM_b}{r + r_b}$$

which was adopted in this work with the parameters $(M_b, r_b) = (1.55 \times 10^{10} M_\odot, 0.7)$ from [51]. The mass enclosed within the radius r can be expressed as

$$M_{\mathrm{bulge}}(r) = \frac{r^2}{G}\frac{\mathrm{d}\phi_{\mathrm{bulge}}(r)}{\mathrm{d}r} = M_b \left(\frac{r}{r + r_b}\right)^2 \tag{3.17}$$

for spherically symmetric potentials. The potential of the disk, however, is axisymmetric and depends on the polar coordinates R and z in the coordinate system K' in Fig. 3.1[4].

[4]The polar coordinate R denotes the distance to the z axis of K'. The Sun is assumed at $z_\odot = 0\,\mathrm{kpc}$.

In this work, a finite thickness of the disk was assumed, which can be mathematically described by a double-exponential approach of the density [51, 56]

$$\rho_{\text{disk}}(R,z) = \frac{M_0}{4\pi z_d R_d^2} \cdot \exp\left(-\frac{R}{R_d} - \frac{|z|}{z_d}\right) \ . \tag{3.18}$$

Different baryonic contributions such as stars, dust, and gas were taken into account to calculate the total disk potential. The corresponding parameters are adopted from [51] and listed in Tab. 3.1, where M_0 denotes the normalization mass, while R_d and z_d represent the scale length and height, respectively. A detailed description of the individual components can be found in [57]. In order to obtain a radial total potential, the disk

Table 3.1: Parameters for the density of the individual disk components parameterized according to Eq. 3.18. The values used were taken from [51].

component	M_0 in $[M_\odot]$	R_d in [kpc]	z_d in [kpc]
Stellar	3.65×10^{10}	2.35	0.14
Warm Dust	2.20×10^{5}	3.30	0.09
Cold Dust	7.00×10^{7}	5.00	0.10
H I Gas	8.20×10^{9}	18.24	0.52
H_2 Gas	1.30×10^{9}	2.57	0.08

distribution is "spherized" by calculating the mass enclosed within a sphere of radius r for each disk component according to

$$\begin{aligned} M_{\text{disk}}^{(\text{sph})}(r) &= \frac{M_0}{4\pi z_d R_d^2} \int_0^{2\pi} \mathrm{d}\varphi \int_0^r R \exp\left(-\frac{R}{R_d}\right) \mathrm{d}R \int_{-z_r}^{+z_r} \exp\left(-\frac{|z|}{z_d}\right) \mathrm{d}z \\ &= \frac{M_0}{R_d^2} \int_0^r R \exp\left(-\frac{R}{R_d}\right) \cdot \left[1 - \exp\left(-\frac{\sqrt{r^2 - R^2}}{z_d}\right)\right] \mathrm{d}R \end{aligned} \tag{3.19}$$

which is numerically evaluated using the trapezoidal rule[5]. The z component is integrated to $z_r = \sqrt{r^2 - R^2}$ in order to account for the enclosed mass within the radius r considering the disk height.
The DM density is spherically distributed for both the gNFW profile in Eq. 3.7 and the Einasto profile in Eq. 3.8. Therefore, the mass enclosed within r can be calculated by the volume integral in spherical coordinates as

$$M_{\text{DM}}(r) = 4\pi \int_0^r \rho_{DM}(r')\ r'^2\, \mathrm{d}r' \ . \tag{3.20}$$

3.3.2 One-Dimensional DM Dispersion Velocity

Once the enclosed mass for all contributions of bulge, disk, and the DM component is known (cf. Eqs. 3.17, 3.19, and 3.20), the derivative of the total radial gravitational potential can be determined by

$$\frac{\mathrm{d}\phi_{\text{tot}}(r)}{\mathrm{d}r} = \frac{G\left[M_{\text{bulge}}(r) + M_{\text{disk}}(r) + M_{DM}(r)\right]}{r^2} \ , \tag{3.21}$$

[5]The spherical approximation for the disk potential has been validated in [58], who found sufficient agreement with N-body simulations including full multipole terms.

which is required for the Jeans equation in 3.16. With this, the one-dimensional velocity dispersion can be numerically integrated according to

$$v_0^2(r) = \frac{1}{\rho_{DM}(r)} \int_r^\infty \rho_{DM}(r') \frac{\mathrm{d}\phi_{\mathrm{tot}}(r')}{\mathrm{d}r'} \mathrm{d}r' \ . \tag{3.22}$$

To do this, the trapezoidal rule on a logarithmically spaced radial grid was used in a numerically backward integration. Fig. 3.4 shows the one-dimensional dispersion velocity

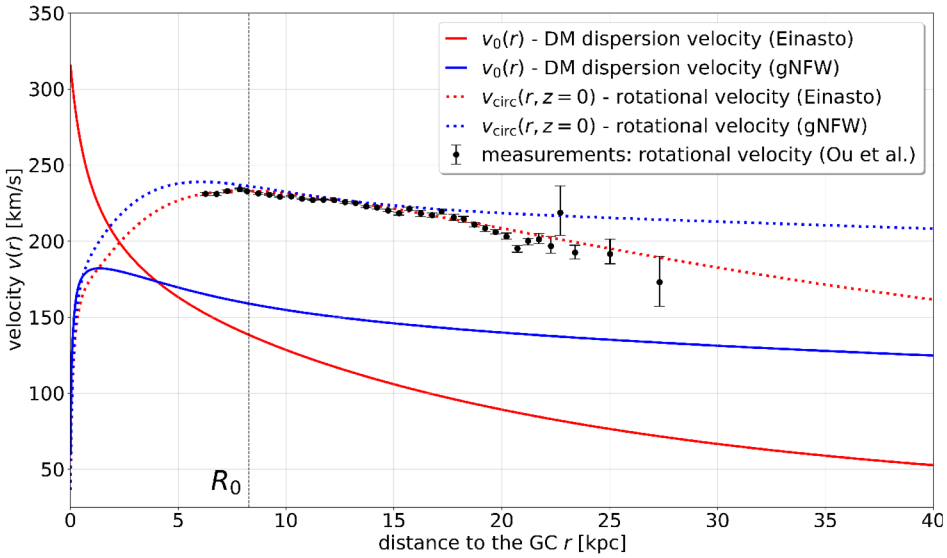

Figure 3.4: The solid curves show the one-dimensional velocity dispersion $v_0(r)$ from Eq. 3.22, considering the bulge, disk and DM gravitational potential for the gNFW (blue) and Einasto profile (red). In addition, the circular velocity $v_{\mathrm{circ}}(R = r)$ in the plane $z = 0$ was derived from the total potential according to Eq. 3.23 and compared to the measurements from [51].

$v_0(r)$ of the DM particles for the gNFW profile (solid blue curve) and the Einasto profile (solid red curve). For the cuspy gNFW model, $v_0(r) \to 0$ for $r \to 0$, due to the divergence in the density $\rho_{gNFW}(r)$ at the GC (cf. Eq. 3.7). In contrast, the Einasto density $\rho_{\mathrm{Ein}}(r)$ remains finite for small r, so that the bulge potential becomes dominant close to the GC, resulting in an increase of the dispersion velocity. According to Eq. 3.15 the average velocity of DM particles at the position of the Sun is $\langle v \rangle \approx 300\,\mathrm{km/s} \approx 10^{-3}\ c$.
For comparison, Fig. 3.4 also shows the rotational curves $v_{\mathrm{circ}}(R)$ in the plane $z = 0$, derived from the axisymmetric total potential $\phi_{\mathrm{tot}}(R, z)$, for the gNFW profile (dashed blue curve) and the Einasto profile (dashed red curve). For axisymmetric potentials with polar coordinates R and z, these can be computed as [59]

$$v_{\mathrm{circ}}^2(R) = R \left. \frac{\partial \phi_{\mathrm{tot}}(R, z)}{\partial R} \right|_{z=0} \ . \tag{3.23}$$

The individual components of the gravitational force in polar coordinates in the plane $z = 0$ can be expressed as

$$\left. \frac{\partial \phi_{\mathrm{tot}}(R, z)}{\partial R} \right|_{z=0} = \left. \frac{\mathrm{d}\phi_{\mathrm{bulge}}(r)}{\mathrm{d}r} \right|_{r=R} + \left. \frac{\partial \phi_{\mathrm{disc}}(R, z)}{\partial R} \right|_{z=0} + \left. \frac{\mathrm{d}\phi_{DM}(r)}{\mathrm{d}r} \right|_{r=R} \tag{3.24}$$

where the contributions from the bulge and the DM distribution can be determined analogously to Eq. 3.21. The contribution from the disk, on the other hand, is no longer trivial but can be computed for double-exponential disks using the Hankel-/Bessel integral [60]

$$\left.\frac{\partial\phi_{\text{disc}}(R,z)}{\partial R}\right|_{z=0} = 2\pi G\Sigma_0 \int_0^\infty kJ_1(kR)\cdot\frac{\alpha}{(\alpha^2+k^2)^{3/2}}\cdot\frac{1}{1+kz_d}\,\mathrm{d}k\ ,$$

$$\text{with}\quad \Sigma_0 = \frac{M_0}{2\pi R_d^2}\quad\text{and}\quad \alpha = \frac{1}{R_d}\ .$$

The circular velocities calculated in this way according to Eq. 3.23 were compared with the measured rotation curves from [51], which are shown as black dots in Fig. 3.4. For the assumed total potential, both profiles provide good agreement with the data, with the Einasto profile matching the measurements slightly better than the gNFW profile, since it was explicitly optimized for these data [51].

3.3.3 $\mathcal{J}$-Factor for p-Wave Annihilation

Due to the additional velocity term in the $\mathcal{J}_p$ factor in Eq. 3.14, both the magnitude of the expected neutrino flux and its directional dependence modify in the p-wave scenario. Similar to the $\mathcal{J}$-factor for s-wave annihilation, $\mathcal{J}^{(p)}$ was also integrated using

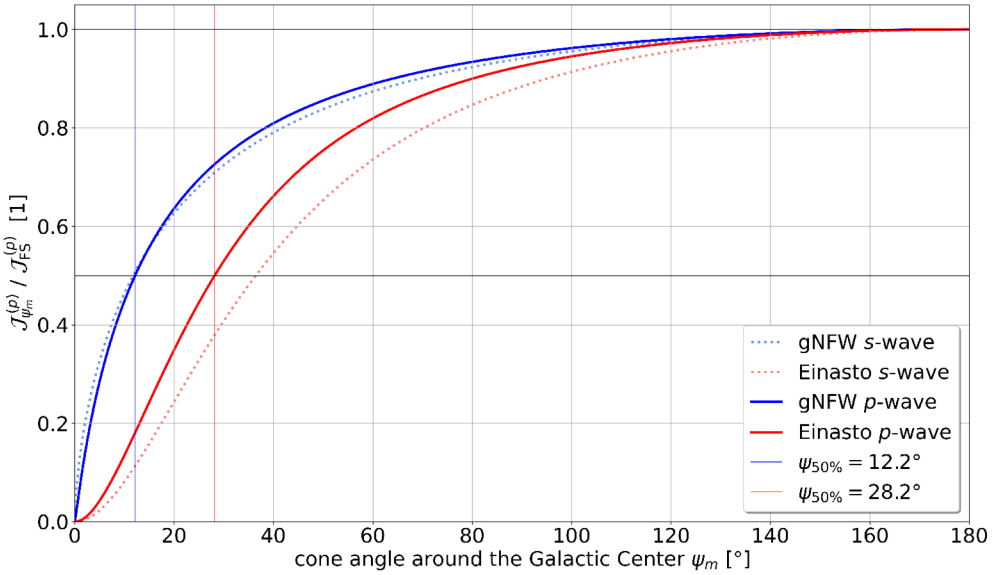

Figure 3.5: Fraction $J^{(p)}_{\psi_m}/J^{(p)}_{FS}$ for the gNFW (blue) and the Einasto (red) DM profiles in the p-wave annihilation scenario. For comparison also the curves for s-wave annihilation are added as dotted lines (cf. Fig. 3.3). The vertical lines mark the cone angle ψ_m where 50 % of the total neutrino flux is expected from, which for the cuspy gNFW profile $\psi_{50\,\%} \simeq 12.2°$ is comparable to the s-wave scenario. The cored Einasto profile $\psi_{50\,\%} \simeq 28.2°$ provides a more concentrated neutrino flux towards the GC compared to s-waves.

a Gauss–Legendre quadrature, which is explained in detail in Appendix A.2. Fig. 3.5 shows the ratio of $J^{(p)}_{\psi_m}/J^{(p)}_{FS}$, which corresponds to the fraction of the total neutrino flux

expected from a cone-like ROI (cf. Fig. 3.1)

$$\frac{\mathrm{d}\Phi^{\chi}_{\nu_\ell}(\psi_m)}{\mathrm{d}E_{\nu_\ell}} = \frac{1}{\kappa_1\kappa_2}\cdot\frac{b_P}{m_\chi^2}\cdot\frac{\Delta\Omega(\psi_m)}{4\pi}\cdot R_0\,\rho_0^2\,J^{(p)}_{\mathrm{avg}}(\psi_m)\cdot\delta(E_{\nu_\ell}-m_\chi)$$

to the FS flux for $\psi_m = \pi$. The parameter b_P is the annihilation constant in the dominant term of $\langle\sigma_{\mathrm{A}}v\rangle$ in Eq. 2.4 for the p-wave scenario with units [cm^3/s].
The blue curves in Fig. 3.5 show the result for the gNFW DM density profile, while the red curves correspond to the Einasto profile. The solid lines represent the p-wave scenario, and the dashed curves represent the s-wave scenario (from Fig. 3.3) for comparison. For cuspy profiles (gNFW) there is not a large difference between s and p-wave scenario, whereas for cored profiles (Einasto), the annihilation density is more concentrated towards the GC for p-waves, making a directional analysis more promising. This is in agreement with the results in [55]. However, the non-relativistic velocities of the DM particles lead to a suppression of the total flux for p-wave annihilations by a factor of about 10^{-6} compared to the s-wave scenario. This is illustrated in Fig. A.5 with the dimensionless $J^{(p)}_{\mathrm{avg}}(\psi_m)$ (defined analogously to Eq. 3.11). If s-waves are suppressed in reality, the expected annihilation rate is reduced by a factor of $\sim 10^{-6}$ due to the small average velocities of $\langle v\rangle \sim 10^{-3}\,c$ for DM particles in the Milky Way today, which makes indirect DM searches via neutrinos considerably more challenging.

3.4 Self-Annihilation Cross Section

After the astrophysical uncertainties have been summarized in the dimensionless J_{avg}, the remaining quantity that controls the expected neutrino flux in Eq. 3.13 is the thermally averaged self-annihilation cross section $\langle\sigma_{\mathrm{A}}v\rangle$, which has already been discussed in detail in Sections 2.2.1 and 2.2.2. In the following section, the results of previous indirect DM searches with neutrinos are translated into constraints on $\langle\sigma_{\mathrm{A}}v\rangle$, and are compared to the observations of the thermal relic density for s-wave annihilation in Fig. 2.5.
The most stringent limits on the thermally averaged self-annihilation cross section $\langle\sigma_{\mathrm{A}}v\rangle$ of DM into neutrinos in the MeV to GeV range have mainly been set by Super-Kamiokande (Super-K). Super-K is a 50 kton water Cherenkov neutrino detector that began operation in 1996 [61]. Since then, several sensitivity studies for indirect DM searches have been carried out with Super-K, and the results are shown in Fig. 3.6 and compared to the natural cross section from the thermal relic abundance in Fig. 2.5 [40].

The light blue curve shows the limit of Super-K in the MeV range, which is based on the data from the first three Super-K phases with a total of 7.8 yr data-taking [62]. For this χ^2 analysis, the event selection and background modeling developed for existing Diffuse Supernova Neutrino Background (DSNB) studies were used and adapted to the expected monoenergetic neutrino spectrum from DM annihilation according to $\chi\chi \to \nu_e\bar{\nu}_e$. Atmospheric electron (anti)neutrinos as well as Michel electrons were modeled as the dominant backgrounds and were taken into account in the analysis [62]. Since this study assumed a distance of $R_{0,[62]} = 8.5\,\mathrm{kpc}$ to the GC, a local DM density of $\rho_{0,[62]} = 0.3\,\mathrm{GeV/cm^3}$ and $J_{\mathrm{avg},[62]} = 5$, the results must be rescaled according to

$$\mathcal{F}_{(\mathrm{old})} = \frac{R_{0,(\mathrm{old})}}{R_{0,(\mathrm{new})}}\cdot\frac{\rho^2_{0,(\mathrm{old})}}{\rho^2_{0,(\mathrm{new})}}\cdot\frac{J_{\mathrm{avg},(\mathrm{old})}}{J_{\mathrm{avg},(\mathrm{new})}}\ ,$$

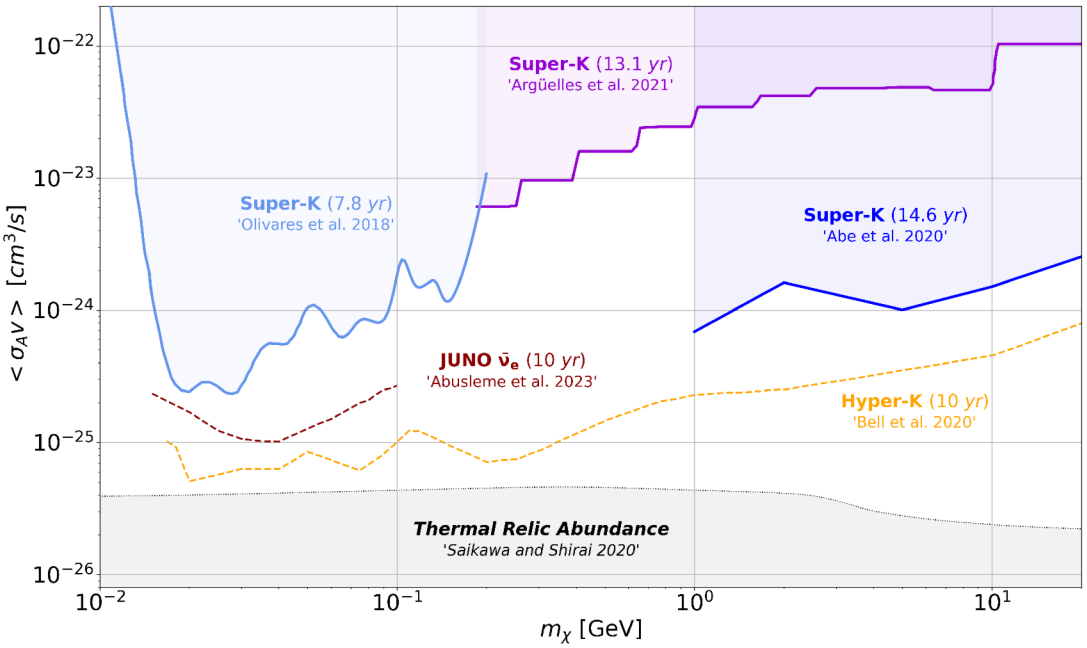

Figure 3.6: Best currently existing limits on the self-annihilation cross section $\langle \sigma_A v \rangle$ for DM s-wave annihilation in the MeV to GeV mass range, assuming a distance of $R_0 = 8.277\,\mathrm{kpc}$ to the GC, a local DM density of $\rho_0 = 0.4\,\mathrm{GeV/cm^3}$ and a dimensionless averaged $\mathcal{J}$-factor of $J_{\mathrm{avg}} = 3$. The Super-K limits are adapted from [62] (light blue), [36] (purple) and [63] (dark blue) and rescaled according to the chosen DM density parameters. The dashed lines indicate the rescaled estimated sensitivities for the next-generation experiments Hyper-K (yellow) and JUNO (red) after 10 yr of data taking (adapted from [8, 64]). In addition also the range from the natural DM abundance in Fig. 2.5 is included in the plot [39].

leading to a factor $\mathcal{F}_{[62]} = 8.5/8.277 \cdot 0.3^2/0.4^2 \cdot 5/3 \approx 0.96$.
The purple curve in Fig. 3.6 shows a conservative sensitivity estimate for 13.1 yr of Super-K data (Phase I-IV), adapted from [36]. In that analysis, a background-agnostic, likelihood-based approach was used, taking into account both galactic and extragalactic contributions to the neutrino flux, with the extragalactic component being subdominant [36]. Since $R_{0,[36]} = 8.127\,\mathrm{kpc}$ and $\rho_{0,[36]} = 0.4\,\mathrm{GeV/cm^3}$ were used in the analysis and the dimensionless factor $J_{\mathrm{avg},[36]} = 4.56$ can be calculated from the given DM density parametrization, the limits on $\langle \sigma_A v \rangle$ were rescaled by the factor $\mathcal{F}_{[36]} \approx 1.49$ [36].
The best existing limits in the GeV DM mass range (cf. dark blue curve in Fig. 3.6) were also set by Super-K, where a likelihood-based approach was employed to test the signal hypothesis of monoenergetic neutrinos against the known background spectrum [63]. For the DM density parametrization, a distance to the GC of $R_{0,[63]} = 8.5\,\mathrm{kpc}$ and a local density of $\rho_{0,[63]} = 0.3\,\mathrm{GeV/cm^3}$ were assumed. For the standard NFW profile, the averaged dimensionless FS $\mathcal{J}$-factor can be approximated as $J_{\mathrm{avg},[63]} \approx 3$, leading to a rescaling factor of $\mathcal{F}_{[63]} \approx 0.58$ for the blue curve. However, it should be noted that the analysis in [63] explicitly incorporates directional information relative to the GC. Consequently, the derived sensitivity does not depend solely on the FS normalization via the averaged J_{avg} factor, but also on the angular distribution of the signal (cf. Fig. 3.3), as well as on the angular resolution of the Super-K detector. The published limits are given for a NFW profile and would be reduced for a cored density distribution such as

the Einasto profile.
The dashed lines in Fig. 3.6 indicate the 90 % C.L. sensitivity of next-generation experiments after 10 yr of data-taking. The orange curve was adapted from [64], where extensive MC simulations of the Hyper-Kamiokande (Hyper-K) detector, the larger successor of Super-K [65], were performed. In this study, atmospheric neutrinos and spallation events were treated as the dominant backgrounds, and a likelihood-based analysis was employed to test the signal hypothesis under the same density parametrization as in [63]. The published results in [64] correspond to a 90 % C.L. sensitivity after 20 yr of data-taking. To obtain the results for 10 yr of data-taking, the factor $\mathcal{F}_{[64]} = \sqrt{2} \cdot \mathcal{F}_{[63]} \approx 0.82$ was applied[6].
The dashed red line in Fig. 3.6 shows the 90 % C.L. sensitivity to the self-annihilation cross section $\langle \sigma_{\mathrm{A}} v \rangle$ in JUNO after 10 yr of data-taking [8]. This study was published in 2023 and is based on detailed MC simulations of the expected signals and backgrounds in JUNO, where sophisticated background discrimination techniques are used to increase the S2B ratio. Both the χ^2-based likelihood-ratio test and the Bayesian analysis yielded consistent results. For this study in [8] the same astrophysical parameters as in [62] were assumed, and therefore the limits on $\langle \sigma_{\mathrm{A}} v \rangle$ were rescaled by the factor $\mathcal{F}_{\mathrm{avg},[62]} = 0.96$.

To derive the most stringent limits on b_P in the case of p-wave dominated annihilation, the curves in Fig. 3.6 must be rescaled by the factor $J^{(p)}_{\mathrm{avg}}/J_{\mathrm{avg}} = 10^{-6}$. This shifts the limits to the range $b_P \sim (10^{-17} - 10^{-19})\,\mathrm{cm}^3/\mathrm{s}$, which is approximately seven orders of magnitude above the natural annihilation cross section shown in Fig. 2.5 (left panel), which would be required to reproduce the observed relic abundance in the p-wave scenario.

[6] Since the significance criterion for a Poisson distribution scales as $\sim N_{\mathrm{sig}}/\sqrt{N_{\mathrm{bkg}}}$ where $N_{\mathrm{sig/bkg}} \propto T$, a factor of $\sqrt{2}$ must be included when halving the measurement time $T \to T/2$.

4 The Jiangmen Underground Neutrino Observatory

The one thing that can solve most of our problems is dancing.
– James Brown

The Jiangmen Underground Neutrino Observatory (JUNO) is a large-scale 20 kton liquid scintillator (LS) detector currently operating in Guangdong Province, China. The commissioning and filling of JUNO was completed in summer 2025, and physics data taking began on August 26, 2025 [6]. The main goal of JUNO is the determination of the neutrino mass ordering (NMO), which is to be achieved by detecting electron antineutrinos from two nearby nuclear power plants [4]. In order to determine the NMO, an energy resolution of 3% at 1 MeV is required, as well as effective background rejection [66]. In November 2025, initial performance results of JUNO were released based on a data set of 59.1 d, confirming that the designed requirements could be achieved [6, 67]. A data acquisition duty cycle of more than 97.8 % during this data-taking phase highlights the stability of the overall system. This section introduces all detector subsystems, the comprehensive simulation framework, and the physics potential of JUNO.

4.1 The JUNO Detector Systems

The central detector (CD) of JUNO consists of an acrylic sphere with a diameter of 35.4 m, filled with 20,000 tons of liquid scintillator (LS). The acrylic vessel is surrounded

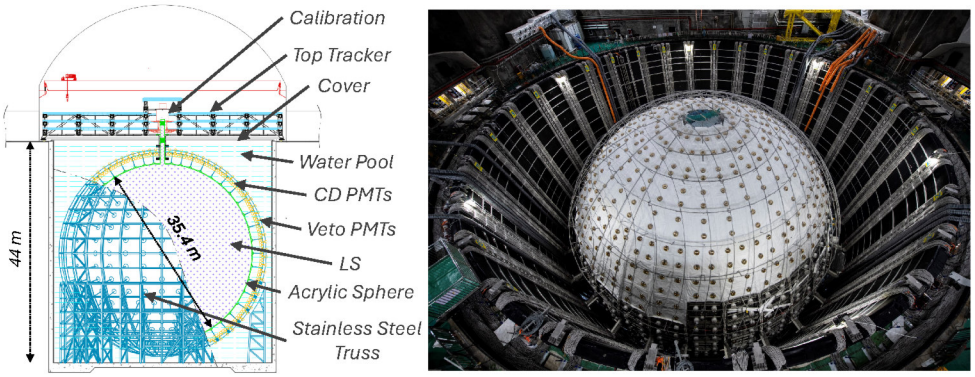

Figure 4.1: Schematic illustration of the detector systems in JUNO on the left and a picture of the CD on the right, showing the acrylic sphere mounted inside the cylindrical water pool. The picture was taken in 2024 before commissioning started and was provided by JUNO collaboration.

by 17,612 20-inch photomultiplier tubes (PMTs) which are supplemented by a further 25,587 3-inch PMTs to increase the optical coverage to 88 % [6, 5]. In order to suppress background events, the CD is located 650 m underground in the middle of a cylindrical water pool with a diameter of 43.5 m (cf. illustration in the left panel of Fig. 4.1). This 35 kton water Cherenkov detector acts, on the one hand, as an active muon veto and shields the CD, on the other hand, from particles generated in the surrounding rocks by natural radioactivity or cosmic rays [5]. In addition, a Top Tracker consisting of plastic scintillator modules is positioned above the water tank, which provides further tracking information for cosmic muons from above. Two months of data taking demonstrated an excellent muon-tagging efficiency of more than 99.9 % using JUNO 's water Cherenkov detector, further supported by the Top Tracker system [6].

4.2 The Liquid Scintillator in JUNO

The liquid scintillator (LS) used in JUNO mainly consists of long hydrocarbon chains, which can be described by the chemical formula $C_6H_5C_nH_{2n+1}$ with $10 \leq n \leq 16$, called linear alkyl benzene (LAB) [68]. In addition, the LAB is mixed with 2.5 g/l of 2,5-Diphenyloxazole (PPO), acting as a fluor and with 3 mg/l of the wavelength shifter 1,4-Bis (2-methylstyryl) benzene (Bis-MSB) to avoid self-absorption and to shift the scintillation light to a wavelength that matches the highest sensitivity of the PMTs. The LS is optimized to have a large light yield (1500 PE/MeV) and a long attenuation length ($L_{\text{att}} > 20$ m at 430 nm) [66, 69]. At the same time, it must meet the contamination limits for the concentration of radioactive isotopes, such as ^{238}U, ^{232}Th, and ^{40}K whose natural decay products pose a significant background challenge in the low energy region [5]. To fulfill the criteria for both optical and radio-purity, the LS undergoes a series of complex, multi-stage purification steps before it is filled into the CD [69, 70]. The behavior of the optical properties after different purification stages is regularly checked using suitable monitoring systems. A very successful system for determining the attenuation length and group velocity of light in the LS with high precision has been developed in recent years at the Eberhard Karls University in Tübingen and was also used to check the optical quality of the JUNO LS [71].
First measurements of the optical properties in the LS show that the requirements were even exceeded. During the six-month filling phase of JUNO, an average attenuation length of $L_{\text{att}} = 20.6$ m was measured, and a light yield of 1785 PE/MeV was reconstructed at the center of the CD. Although the currently determined energy resolution for two 0.511 MeV γ rays is slightly above the specified target value at about 3.4 %, it still seems realistic to achieve the planned resolution, as the causes are mainly due to systematic effects that have not yet been fully addressed [6]. However, since the underlying performance parameters such as detector volume, optical coverage, light yield, and transparency of the LS meet or even exceed the specified expectations, improved reconstruction and calibration methods should enable reaching the 3 % target at 1 MeV.

4.3 The Detection Principle in JUNO

The detection principle in JUNO is based on the production of scintillation light by different particles through their interactions with the LS. The energy deposited by a charged particle leads to excitation and ionization of the LAB molecules, and the excitation energy is transferred non-radiatively to the PPO molecules. While de-exciting, the PPO molecules emit photons at ~ 380 nm, which will be shifted by the Bis-MSB

to a wavelength of $\sim 430\,\mathrm{nm}$ before being detected by the surrounding PMTs [69]. In first order, the number of produced photons is proportional to the deposited energy and depends on the light yield of the LS. However, this proportionality is not perfect due to the quenching effect, which causes a reduced light yield per MeV for highly ionizing particles, such as α-particles or protons. This effect needs to be considered when reconstructing the energy of an event in JUNO.
While the ionizing particle propagates through the LS, its energy is deposited according to Birks' Law at a rate of $\mathrm{d}E/\,\mathrm{d}x$ [72]. The scintillation light produced in an event is not emitted instantaneously but follows a characteristic time profile, which consists of multiple components accounting for the de-excitation processes from different molecular energy states (e.g., singlet and triplet states). The resulting pulse can be described by a weighted sum of exponential functions

$$P(t) = \sum_i \frac{\omega_i}{\tau_i} \cdot e^{-\frac{t}{\tau_i}} \tag{4.1}$$

considering the decay time constants τ_i and their weights ω_i [73]. The JUNO LS emission profile is best described using four components, with the first prompt component of a few ns, dominating. Heavier particles, such as alpha particles and hadrons, are more ionizing and therefore often produce higher excited states which decay more slowly [68]. Consequently, the ratio of fast to slow emission components for these particles is significantly smaller than that for lighter particles, such as betas and gammas[1], which predominantly excite fast singlet states. This feature is used in JUNO for separating different particle types via pulse shape discrimination (PSD), which is an important tool for background reduction and will be discussed in more detail in Section 8.3.
After the scintillation photons reach the PMT cathode, they can be converted into photoelectrons (PEs) with a probability given by the quantum efficiency of the photocathode. The final signal reflects a convolution of the hit-time profile of the scintillation photons and the characteristic time response of the PMTs. The signal is also distorted by the transit time spread (TTS) of the PMTs and superimposed by their dark count rate (DCR). Additionally, interference from possible pre- and after-pulses also affects the actual physical signal. Therefore, suitable methods must be found to reconstruct the waveforms output after passing through the flash analog-to-digital converters [74].

4.4 The JUNO Simulation Framework

Since data taking in JUNO started in August 2025, the analyses presented in this work were performed using Monte Carlo (MC) simulated data generated with the JUNO software framework version J24.1.2 [75]. The JUNO software includes four steps that are based on Geant4 and the SNiPER framework (Software for Non-collider Physics Experiment) and take into account all detector systems introduced in Section 4.1.
The first step `DetSim` of the JUNO simulation framework describes all relevant processes from event generation to the detection of the scintillation light by the PMTs. The events for all datasets used in this work were generated with the GENIE MC neutrino generator (v3.2 `G18_10b_02_11b` model tuning), which simulates neutrino interactions and their final-state particles for a given neutrino flux based on the corresponding cross sections [76, 77]. After generation, the events are randomly distributed within the geometry of the CD

[1] Gamma rays do not produce scintillation light by ionization but through scattering off electrons, which ionize the medium.

volume, and the resulting particles are propagated step-by-step using a Geant4-based MC simulation. To accurately simulate the signature of an event, a wide range of possible interactions for various particles is implemented, including electromagnetic interactions and decays, as well as elastic and inelastic scattering of hadrons. The behavior of excited isotopes, which de-excite by emitting different particles and thereby deposit additional energy in the detector, is also considered in the JUNO software according to the cross sections of the TALYS database [78]. The resulting scintillation light, as well as Cherenkov radiation, is propagated through the LS, considering the optical parameters of the CD, until the optical photons reach the photocathode of a PMT. With a sophisticated optical model, also considering the geometry of the PMTs as well as boundary effects such as reflections, the hitting photons are converted into photoelectrons (PEs).
After the `DetSim` stage in the JUNO software framework, the hit-times of the photons can be further processed in the electronics simulation `ElecSim`. Here, all PMT effects, such as the transit time spread (TTS), the dark count rate (DCR), and possible pre- and after-pulses, are simulated. The digitization by flash analog-to-digital converters is also simulated, and `ElecSim` provides final digitized waveforms for all PMTs. At this simulation stage, the threshold and trigger conditions are also taken into account, and the final ROOT file stores the electronic MC truths for all trigger windows.
The next step `Calib` of the simulation framework involves several methods of waveform reconstruction. The method used for the data in this analysis is the deconvolution method. After performing a Fourier transform of the digital waveform, high-frequency noise can be suppressed by applying appropriate filters, while the low-frequency physical signals are reconstructed as individual T-Q pairs (Time–Charge) using the single PE waveform responses of the PMTs as a calibration [79].
In the final step of the JUNO simulation framework called `Reco`, various algorithms are implemented, in order to reconstruct the vertex and energy of the events, as well as several features from the deconvoluted waveform, such as the first hit time (FHT), the total charge, and the slope of the waveform within the first 4 ns after the FHT [79]. These features are extracted for each PMT and provide relevant information for more complex reconstruction methods, such as particle identification (PID) or the directional reconstruction of neutrinos, which will be discussed in more detail in Section 9.2 [79].
Processing the simulation through all stages ensures that the MC data undergoes the same processing chain as real detector data, thereby providing more realistic predictions for the detector response and event reconstruction. The simulations used in this work are based on the design parameters of the detector. Initial comparisons with the data recorded since August 2025 show that key characteristics, such as light yield, energy resolution, and radio-purity, are consistent with or even surpass the assumptions of the simulations [6].

4.5 Physics Potential in JUNO

JUNO was designed as a multi-purpose neutrino experiment with excellent performance across a wide energy range. While its primary goal is the determination of the neutrino mass ordering (NMO) with reactor antineutrinos in the MeV regime (cf. Sec. 4.5.1), JUNO also provides significant sensitivity to neutrinos with energies up to several tens of GeV, thereby enabling a broad physics potential. This section provides an overview of the most relevant physics programs in JUNO, categorized by energy. It starts with the low-energy MeV region, for which the detector was optimized.

4.5.1 Neutrino Mass Ordering and Reactor Antineutrinos

The main goal of JUNO is the determination of the neutrino mass ordering (NMO), which is to be achieved by the detection of reactor antineutrinos with high energy resolution [4]. In the standard model (SM), neutrinos are assumed to be massless. However, after the so-called *solar neutrino problem* was observed in the late 1960s during the Homestake experiment, where only about one third of the expected solar neutrino flux of ν_e was measured, the idea of neutrino oscillations arose. According to this theory, the three neutrino generations must have different masses, where the mass eigenstates $|\nu_i\rangle$ with $i \in \{1,2,3\}$ are rotated with respect to the flavor eigenstates $|\nu_\ell\rangle$, with $l \in \{e,\mu,\tau\}$, by specific mixing angles θ_{ij}. The connection between flavor and mass eigenstates is expressed as

$$|\nu_\ell\rangle = \mathbf{U}_{\ell i}\,|\nu_i\rangle \quad \text{and} \quad |\nu_i\rangle = \mathbf{U}^*_{i\ell}\,|\nu_\ell\rangle \ ,$$

where $\mathbf{U}_{\ell i} \in \mathbb{C}$ describes the elements of the Pontecorvo-Maki-Nakagawa-Sakata (PMNS) matrix

$$\mathbf{U} = \underbrace{\begin{pmatrix} 1 & 0 & 0 \\ 0 & c_{23} & s_{23} \\ 0 & -s_{23} & c_{23} \end{pmatrix} \cdot \begin{pmatrix} c_{13} & 0 & s_{13}e^{-i\delta} \\ 0 & 1 & 0 \\ -s_{13}e^{i\delta} & 0 & c_{13} \end{pmatrix} \cdot \begin{pmatrix} c_{12} & s_{12} & 0 \\ -s_{12} & c_{12} & 0 \\ 0 & 0 & 1 \end{pmatrix}}_{\text{rotation matrices in (23), (13) and (12) with CP violating phase } \delta} \cdot \underbrace{\begin{pmatrix} e^{i\alpha_1/2} & 0 & 0 \\ 0 & e^{i\alpha_2/2} & 0 \\ 0 & 0 & 1 \end{pmatrix}}_{\text{Majorana phases } \alpha_1,\, \alpha_2} \tag{4.2}$$

with $s_{ij} = \sin\theta_{ij}$ and $c_{ij} = \cos\theta_{ij}$. The phase δ describes the possible charge parity (CP) violation and is conventionally assigned to the mixing matrix of the eigenstates (13). The Majorana phases α_1 and α_2, in contrast, do not affect the oscillation but only influence lepton-number-violating processes like the neutrinoless double beta decay ($0\nu\beta\beta$).

Neutrinos are produced and absorbed in their flavor eigenstates $|\nu_\ell\rangle$, but they propagate through space in their mass eigenstates $|\nu_i\rangle$. With the Hamiltonian $\mathcal{H}$, their state can be expressed as a function of the propagation length L and their energy E_{ν_i} according to

$$|\nu_i(L)\rangle = |\nu_i(0)\rangle \exp\left(-\mathrm{i}\,\mathcal{H}L\right) = |\nu_i(0)\rangle \exp\left(-\mathrm{i}\frac{m_i^2 L}{2E_{\nu_i}}\right) \ . \tag{4.3}$$

For example, the probability of detecting an electron antineutrino of energy E as an electron antineutrino again after traveling a distance L is given by [4]

$$\begin{aligned} P_{\bar\nu_e\to\bar\nu_e}\left(\frac{L}{E_{\bar\nu_e}}\right) = 1 &- c_{13}^4\,\sin^2(2\theta_{12})\,\sin^2\left(\frac{\Delta m^2_{12}\,L}{4E_{\bar\nu_e}}\right) \\ &- \sin^2(2\theta_{13})\left[c_{12}^2\,\sin^2\left(\frac{\Delta m^2_{31}\,L}{4E_{\bar\nu_e}}\right) + s_{12}^2\,\sin^2\left(\frac{\Delta m^2_{32}\,L}{4E_{\bar\nu_e}}\right)\right] \ . \end{aligned} \tag{4.4}$$

The lower plot in Fig. 4.3 illustrates the survival probability for electron antineutrinos $P_{\bar\nu_e\to\bar\nu_e}(E_{\bar\nu_e})$ at the JUNO site after traveling a baseline of $L = 52.5\,\mathrm{km}$, which depends on the mass-squared differences $\Delta m^2_{ij} = m_i^2 - m_j^2$ (cf. Eq. 4.4).

Several of the oscillation parameters have been determined with considerable precision, and the best-fit values from NuFIT 6.0 are listed in Tab. 4.1 [80]. While Δm^2_{21} is known with an uncertainty of less than 3 %, for $\left|\Delta m^2_{31}\right|$, only the magnitude is known, but not the sign. This leaves two possible mass hierarchies, which are schematically illustrated

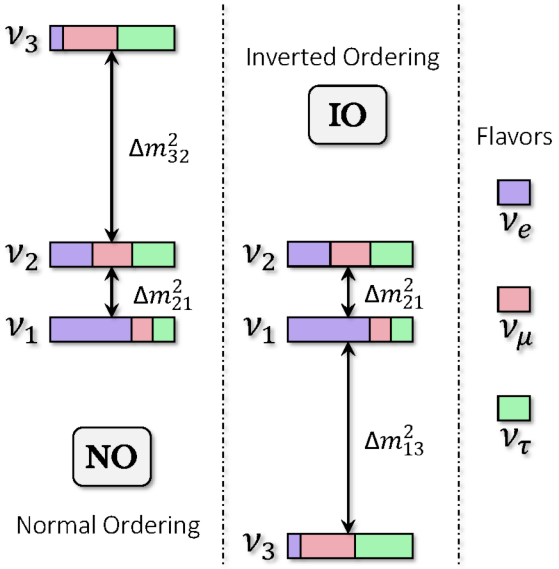

Figure 4.2: Possible realizations of the NMO, showing the NO where m_1^2 is the smallest mass and the IO where m_3^2 is the smallest mass. The colors denote the three different neutrino flavors ν_ℓ with $l \in \{e, \mu, \tau\}$ and their contribution to the mass eigenstates ν_i with $i \in \{1, 2, 3\}$.

in Fig. 4.2. In the case of the Normal Ordering (NO) (left), m_3 is the heaviest mass state, while in the Inverted Ordering (IO) (right), it is the lightest. In addition to the NMO, there are several other open questions:

- The absolute neutrino masses are still unknown and can be probed experimentally by endpoint spectroscopy of a β spectrum by looking for neutrinoless double beta decay ($0\nu\beta\beta$). One representative is the KATRIN experiment in Karlsruhe, Germany, which provided the most stringent limits on the neutrino mass of $\nu < 0.45\,\text{eV}$ with 90 % C.L. [81].

- It is not yet established whether neutrinos are Dirac or Majorana particles. This question can likewise be addressed by $0\nu\beta\beta$ experiments. The LEGEND experiment, for example, uses ultrapure Germanium detectors to look for $0\nu\beta\beta$. First physics results from LEGEND-200 have not observed a signal but set leading lower limits on the ^{76}Ge half-life at the level of $T^{0\nu}_{1/2} \geq 10^{26}\,\text{yr}$ with 90 % C.L. [82]. A planned large-scale phase, LEGEND-1000, aims to achieve full coverage of the IO band with very high probability [83].

- The CP phase δ also remains undetermined. While CP-conserving phases are strongly disfavored in the case of IO, they are still allowed for NO. Updated global fits from a combined analysis of Super-K and T2K still prefer values of δ close to maximal CP violation, but CP-conserving solutions remain allowed, and a definitive discovery has not yet been achieved [84].

- The octant of the atmospheric mixing angle is still unknown, since θ_{23} could lie below or above 45°. Determining the correct octant is essential for the proper interpretation of the CP phase δ and also addresses the question of possible symmetries in the neutrino sector.

To determine the NMO, JUNO aims to detect the oscillated spectrum of electron antineutrinos, which are produced from fission products in two nearby nuclear power plants. Both reactors are located 52.5 km away from the central detector on the Chinese coast in Taishan and Yangjiang [66]. The unoscillated emitted reactor antineutrino flux is defined by the respective antineutrino spectra per fission of the four main isotopes ^{235}U, ^{238}U, ^{239}Pu, and ^{241}Pu in nuclear power plants, and it can be modeled using different theoretical approaches [66]. Experiments such as Daya Bay [85], Double Chooz [86] and RENO [87] have measured electron antineutrino spectra from nuclear power plants and observed deviations from the theoretical predictions. To obtain a direct measurement of the unoscillated reactor antineutrino flux for JUNO and thus support model-independent NMO analyses, the satellite detector Taishan Antineutrino Observatory (TAO) was developed [88]. Located at a distance of 30 m from one of the Taishan reactor cores, TAO aims to measure the spectral shape of the reactor antineutrino flux with sub-percent accuracy. This reference spectrum can then be compared to the oscillated spectrum measured in JUNO, significantly reducing model-dependent systematic uncertainties.

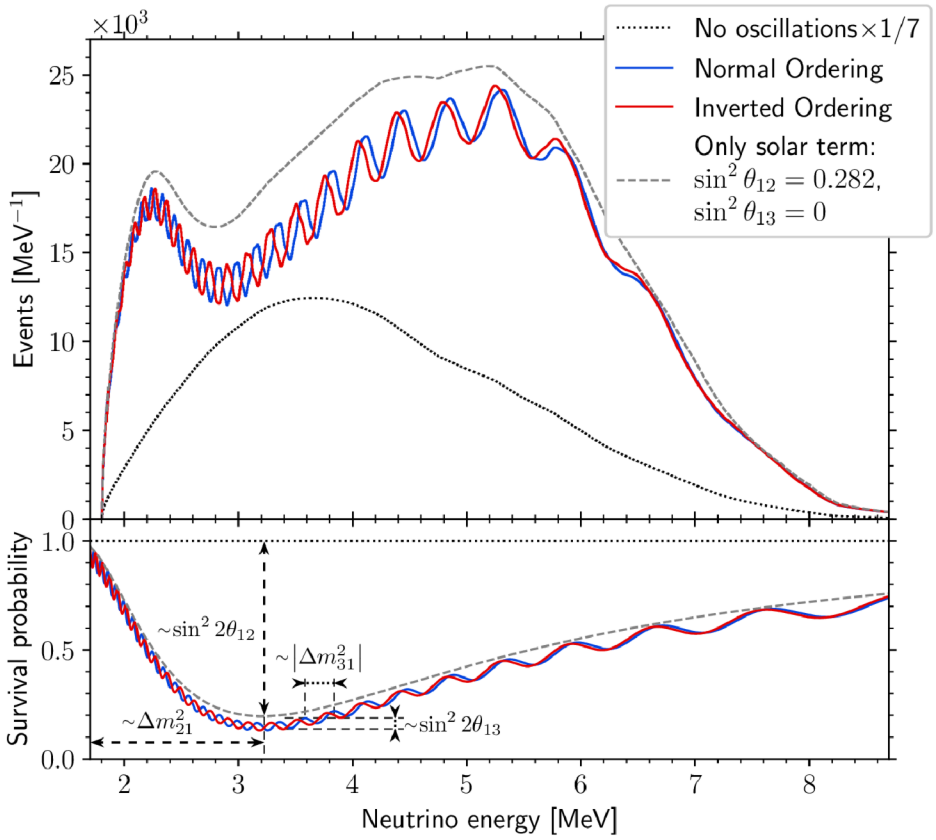

Figure 4.3: The upper plot shows the expected reactor electron antineutrino spectrum in JUNO after 6 yr of data taking, assuming perfect energy resolution. In the lower panel the corresponding survival probability $P_{\bar{\nu}_e \to \bar{\nu}_e}(E_{\bar{\nu}_e})$ at a baseline of $L = 52.5$ km is plotted. The blue and red lines illustrate the NO and IO, respectively, while the dotted line in the upper panel indicates the case of no oscillation. The dashed line considers only the NMO-independent solar term for oscillation, using a value of $\sin^2\theta_{12} = 0.282$ to avoid overlap with the red and blue curves. In the lower panel the oscillation parameters from Tab. 4.1 are associated with the respective oscillation lengths and amplitudes. Plot taken from [66].

The detection of the oscillated reactor antineutrino spectrum in JUNO is directly related to the survival probability $P_{\bar{\nu}_e \to \bar{\nu}_e}(E_{\bar{\nu}_e})$ in Eq. 4.4, which depends on whether normal (NO) or inverted mass ordering (IO) is realized in nature. The upper plot of Fig. 4.3 illustrates the expected electron antineutrino energy spectrum after 6 yr of data taking in the absence of oscillations (black dotted line) and the case where only the hierarchy-independent solar oscillation term with a mixing angle θ_{12} is included (black dashed line). If all oscillation terms are taken into account, the NO (blue) and IO (red) scenarios would produce slightly different spectral shapes [66]. Resolving these spectral differences with a high energy resolution of at least 3 % at 1 MeV allows for the determination of the NMO.

4.5.2 Precision Measurements of the Oscillation Parameters

Beyond the determination of the NMO, JUNO will provide world-leading precision measurements of the solar and atmospheric oscillation parameters, which can be related to the respective oscillation lengths and amplitudes in the reactor antineutrino spectrum. Tab. 4.1 summarizes the best-fit values for the mixing parameters, which are visually illustrated in the lower panel of Fig. 4.3. According to JUNO's design

Table 4.1: Summary of the best-fit values and 1σ uncertainties of the standard three-flavor neutrino oscillation parameters from global fits (NuFIT 6.0) [80]. $\Delta m^2_{3\ell}$ denotes Δm^2_{31} in NO and Δm^2_{32} in IO.

Parameter	Normal Ordering (NO)	Inverted Ordering (IO)
$\sin^2\theta_{12}$	$0.308^{+0.012}_{-0.011}$	$0.308^{+0.012}_{-0.011}$
$\sin^2\theta_{23}$	$0.470^{+0.017}_{-0.013}$	$0.550^{+0.012}_{-0.015}$
$\sin^2\theta_{13}$	$0.02215^{+0.00056}_{-0.00058}$	$0.02231^{+0.00056}_{-0.00056}$
δ_{CP} [°]	212^{+26}_{-41}	274^{+22}_{-25}
Δm^2_{21} [10^{-5} eV^2]	$7.49^{+0.19}_{-0.19}$	$7.49^{+0.19}_{-0.19}$
$\Delta m^2_{3\ell}$ [10^{-3} eV^2]	$+2.513^{+0.021}_{-0.019}$	$-2.484^{+0.020}_{-0.020}$

report, approximately $\mathcal{O}(10^5)$ IBD events collected over 6 yr of data taking will enable sub-percent precision on the oscillation parameters $\sin^2\theta_{12}$, Δm^2_{21}, and $\left|\Delta m^2_{ee}\right|$ [4][2]. The experiment's potential has already been demonstrated by the first results obtained after only 59.1 d of data taking, where, despite limited statistics, a precise measurement of the solar parameters

$$\begin{aligned} \sin^2\theta_{12} &= 0.3092 \pm 0.0087 \ , \\ \Delta m^2_{21} &= (7.50 \pm 0.12) \times 10^{-5}\ \mathrm{eV}^2 \ , \end{aligned} \tag{4.5}$$

was achieved under the NO hypothesis. This result is fully consistent with global fits and improves the previous world precision by a factor of 1.6 [67]. With increasing exposure and further reduction of systematics, JUNO is expected to reach sub-percent sensitivity and provide critical input for precision studies of the three-flavor neutrino framework.

[2] The effective mass-squared difference $\Delta m^2_{ee} = \cos^2\theta_{12}\,\Delta m^2_{31} + \sin^2\theta_{12}\,\Delta m^2_{32}$ describes the oscillation frequency observed in reactor antineutrino disappearance experiments.

4.5.3 Geo-Neutrinos

Another low-energy antineutrino source in the MeV range is the Earth itself. In particular, electron antineutrinos with energies up to $\sim 3.5\,\text{MeV}$ are produced in the β^- decays of various daughter isotopes within the decay chains of ^{238}U and ^{232}Th [89]. Since

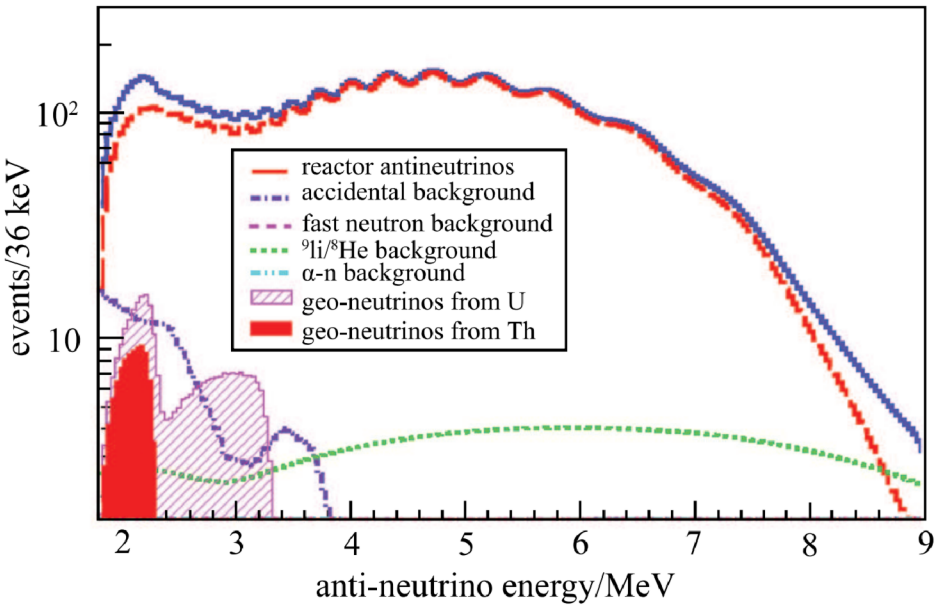

Figure 4.4: Expected geo-neutrino energy spectrum from ^{238}U (pink hatched area) and ^{232}Th (red hatched area) as well as the reactor antineutrino spectrum in JUNO. The blue solid line denoted the total expected number of events after 1 yr of data taking, and the dashed lines different background contributions. Plot was taken from [89].

geo-neutrinos are detected in JUNO by the same channel as reactor antineutrinos, they have to be statistically separated from the dominant reactor background (cf. Fig. 4.4). Depending on the power output of the two nuclear power plants, the signal-to-background ratio can vary between only 8 % (at full power) and 46 % (during shutdown) [89].
While the composition of the Earth's crust is well understood, there is little information about the distribution of radioactive elements in the mantle. A precise reconstruction of the geo-neutrino flux can provide insights into the radiogenic heat produced by the Earth, as well as the $^{232}\text{Th}/^{238}\text{U}$ ratio in the mantle, since neutrinos can pass through the Earth unimpeded.

4.5.4 Solar Neutrinos

Solar electron neutrinos ν_e are produced in various reactions of the dominant proton-proton (pp) fusion chain and the Carbon-Nitrogen-Oxygen (CNO) cycle in the Sun and represent a measurable signal in the sub-MeV and MeV energy range. These neutrinos are detected in JUNO via eleastic scattering (ES) with electrons and, in contrast to reactor or geo-antineutrinos $\bar{\nu}_e$, solar neutrinos do not produce a characteristic delayed coincidence signal, which makes it much more difficult to distinguish them from background events. For this reason, excellent radio-purity in JUNO is essential, which will be determined by the Online Scintillator Internal Radioactivity Investigation System (OSIRIS) pre-detector and JUNO itself [90]. Given sufficiently low radioactive contamination ($\leq 10^{-16}\,\text{g/g}$

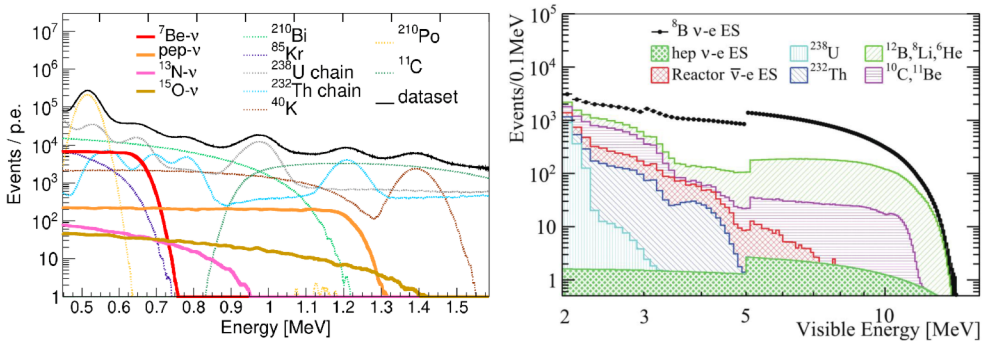

Figure 4.5: Expected solar neutrino spectrum in JUNO mainly from different reactions in the pp-chain in the Sun. The left plot shows the lower energy region including the ^{7}Be, pep, ^{13}N and ^{15}O solar neutrino contributions via ES as well as the relevant radio backgrounds after 6 yr of data taking. The right plot shows the solar ES neutrino contribution of ^{8}B in the larger energy region after 10 yr of data taking. The relevant backgrounds due to cosmogenic and radioactive isotopes are also considered, as well as the ES background of the reactor antineutrinos. The left plot was taken from [91] and the right plot from [92].

for ^{238}U and ^{232}Th) [4, 69], solar neutrinos can be used to study the transition from the vacuum-dominated to the matter-enhanced regime, where the MSW effect becomes dominant. In particular, measurements of the ^{7}Be neutrino flux in the sub-MeV range (left plot in Fig. 4.5) and the ^{8}B neutrino flux in the MeV range (right plot in Fig. 4.5) are of great physical interest. These measurements not only allow investigations of the MSW effect but also provide valuable and independent insights into the oscillation parameters in addition to the reactor neutrino analyses [4, 92].

4.5.5 Core Collapse Supernovae Neutrinos

A Core Collapse Supernova (CCSN) marks the final stage of a massive star and is one of the most powerful events in the universe, releasing around 10^{53} ergs of energy. About 99 % of the total energy is emitted in the form of neutrinos, which are released much earlier compared to the electromagnetic signal of a CCSN. So far, only one SN has been observed in which a neutrino signal was detected several hours before the visible light. The SN *1987A* occurred at a distance of approximately 50 kpc in the Large Magellanic Cloud and led to a total of $\sim$ 30 neutrino detections in the energy range of 7-40 MeV, in agreement with theoretical predictions [93, 94, 95, 96].
The expected time profile for the neutrino luminosity, flavor and energy is directly related to the different CCSN phases and is illustrated in Fig. 4.6 for a CCSN in a typical distance of 10 kpc [4]. During the bounce and shock propagation phase, a powerful burst of electron neutrinos ν_e with mean energies $\sim$ 12 MeV is emitted within a few milliseconds [4, 97]. In the subsequent post-bounce accretion phase, which occurs several hundred milliseconds after the bounce, neutrinos of all flavors are produced, with electron neutrinos ν_e and electron antineutrinos $\bar{\nu}_e$ being the dominant components. The average neutrino energies range from 10-20 MeV and increase until the explosion. The third phase describes the cooling of the proto-neutron star around 10 s after the bounce, during which neutrinos of all flavors are emitted and gradually lose energy over time [4].
Due to its large detector volume, JUNO will detect several thousand events via different channels from a future CCSN [4, 97]. As a real-time monitor, JUNO can therefore

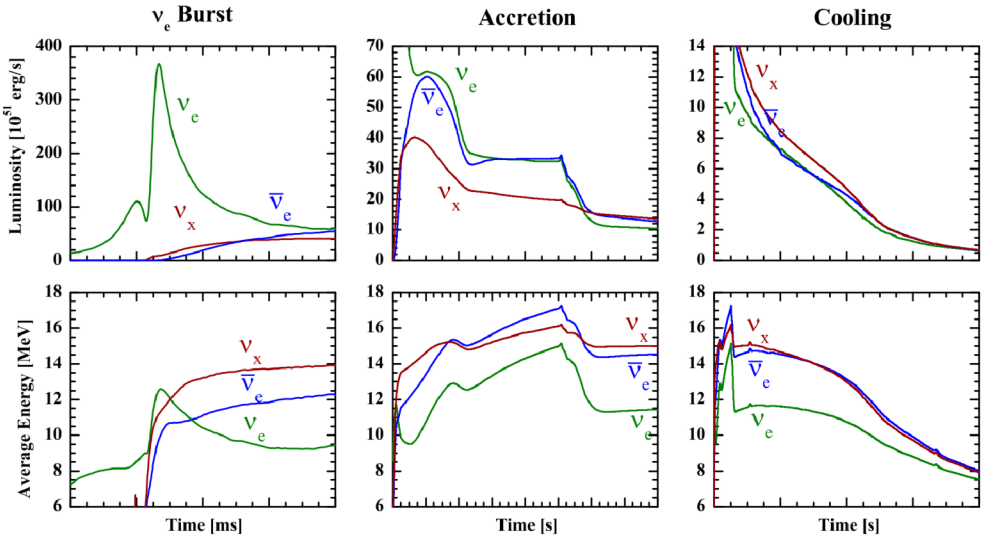

Figure 4.6: Luminosity and average energy of the emitted neutrinos during the three CCSN stages at a distance of 10 kpc. The first column shows the ν_e neutrino burst during the bounce and the shock propagation. The second stage illustrated the accretion phase, which predominantly emits ν_e and $\bar{\nu}_e$ neutrinos. Finally, in the last phase, the remaining proto-neutron is cooling down while the luminosity and energy of the neutrinos decrease continuously. Figure adapted from [4].

contribute to a multi-messenger warning system and even support CCSN pointing [97].

4.5.6 Diffuse Supernova Neutrino Background

While type II CCSNs are rare events that occur only once every few decades in the Milky Way, a vast number of such explosions have taken place since the beginning of the universe. Each of these SNs emitted, on average, 10^{57} neutrinos of all flavors, which collectively overlap and form an isotropic and nearly constant flux, known as the Diffuse Supernova Neutrino Background (DSNB) [98]. Although the DSNB has not yet been detected, theoretical models predict a measurable flux, which is accessible to JUNO in the energy range of 12-30 MeV [98]. Since JUNO provides strong background discrimination techniques for electron antineutrinos $\bar{\nu}_e$ in this energy region, it has the potential to reach a 3σ significance, assuming the reference model after 3 yr of data taking, and would significantly improve current upper limits in the case that no observation can be made [98]. In this work, the DSNB is treated as a background for indirect DM search in the MeV region and is therefore discussed in more detail in Sec. 7.3.

4.5.7 Atmospheric Neutrinos

Cosmic radiation interacting with the atmosphere continuously produces mesons, such as kaons and pions, which subsequently undergo weak decays. In these processes, neutrinos and antineutrinos of all flavors are produced over a broad energy range from 10 MeV to 10 TeV, reaching the JUNO detector with baselines ranging from 15 km to 13000 km [4]. The dominant production channels in the sub-GeV and GeV energy regions are the decay chains

$$\begin{aligned} &\pi^+ \to \mu^+ + \nu_\mu \ , \quad \mu^+ \to e^+ + \bar{\nu}_\mu + \nu_e \quad \text{and} \\ &\pi^- \to \mu^- + \bar{\nu}_\mu \ , \quad \mu^- \to e^- + \nu_\mu + \bar{\nu}_e \ . \end{aligned} \tag{4.6}$$

Therefore, the flux of ν_μ and $\bar{\nu}_\mu$ is approximately twice as large as that of ν_e and $\bar{\nu}_e$ for energies below $\sim 1\,\text{GeV}$, and neutrinos and antineutrinos occur in roughly equal proportions.
Atmospheric neutrinos are an important source because they are produced throughout the atmosphere. Depending on their zenith angle, they traverse different path lengths through the Earth before reaching the detector. Since the resonance energy of the MSW effect lies in the range of 3-10 GeV, it is possible to investigate hierarchy-dependent matter effects with atmospheric neutrinos by analyzing the survival probability in the zenith angle θ - neutrino energy E_ν plane illustrated in Fig. 4.7 (for calculations cf. Sec. 7.4.2). Although the targeted NMO sensitivity of $3\,\sigma$ is primarily achieved through

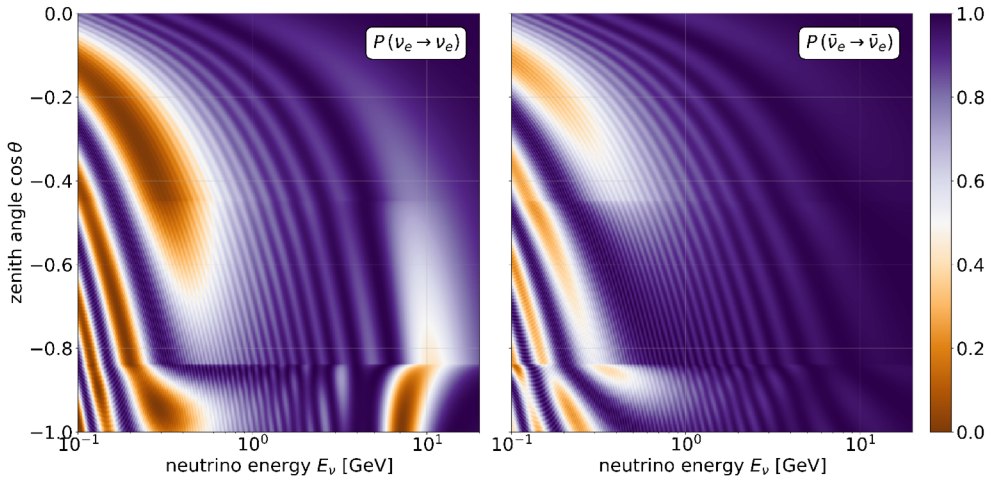

Figure 4.7: Two oscillograms of the survival probabilities $P_{\nu_e \to \nu_e}$ and $P_{\bar{\nu}_e \to \bar{\nu}_e}$ for up-going atmospheric neutrinos at a zenith angle θ, assuming NO and a mean production height of 18 km. The probabilities were calculated assuming a simplified PREM Earth model with three layers (cf. Tab. 7.1). The MSW resonance effect appearing for ν_e in the left plot would appear in the right plot when IO is assumed.

the observation of vacuum oscillations of reactor antineutrinos, it can be enhanced by analyzing the oscillation of atmospheric neutrinos with an independent 1-1.8 σ sensitivity after 10 yr data taking [4].
In addition to the NMO analysis, JUNO can also contribute to the determination of other oscillation parameters. As discussed in Sec. 4.5.1, the octant of the atmospheric mixing angle θ_{23} remains unresolved. Assuming the NMO is known, JUNO can help to exclude the wrong octant with a sensitivity of 0.9-1.8 σ [4]. The CP-violating phase δ also remains unknown. Since it only affects appearance channels such as $P_{\nu_e \to \nu_\mu}$, while JUNO is primarily sensitive to disappearance channels like $P_{\bar{\nu}_e \to \bar{\nu}_e}$, measuring the CP phase poses a significant challenge. The sub-GeV region for upward-going neutrinos offers the most promising opportunities for analyzing CP violation [4]. However, in this energy range, directional reconstruction is difficult, and kinematic smearing further limits JUNO's sensitivity to the CP phase [4]. The sensitivity can be enhanced if the neutrino flavor is identified, which has already been demonstrated using ML methods [99]. Furthermore, there are proposals to make increased use of disappearance channels for an indirect determination of the CP phase [100]. Another approach involves the use of an external cyclotron source in the future to study the appearance channel $P_{\bar{\nu}_\mu \to \bar{\nu}_e}$ in JUNO, to which the detector is very sensitive. Depending on the cyclotron power, this method could achieve a sensitivity of up to $3\,\sigma$ for specific values of the CP phase [101].

In this work, the atmospheric neutrinos are treated as a background over a broad energy range, and the expected neutrino fluxes and events are discussed in more detail in Sec. 7.4.

4.5.8 Physics Beyond Standard Neutrino Physics

In addition to the major physics programs discussed above, JUNO also offers the potential to explore physics beyond the SM of neutrino physics. One such example is the ability of JUNO to set new limits on possible proton decay modes [102]. Proton decay is predicted by many GUT models, with the channel $p \to K^+ + \bar{\nu}$ being among the most likely channels. In this two-body decay, the K^+ is produced with a kinetic energy of about $\sim 105\,\mathrm{MeV}$, generating a prompt signal in the LS. The kaon subsequently decays with a lifetime of $\sim 12.4\,\mathrm{ns}$, predominantly (63 %) into $K^+ \to \mu^+ + \nu_\mu$ [29]. The resulting μ^+ then decays into a positron e^+. Consequently, a proton decay event in JUNO would produce a characteristic triple-coincidence signal, which can be effectively distinguished from background through temporal and energy-based selection criteria. Moreover, JUNO can contribute to the search for sterile neutrinos on an eV scale. A fourth sterile component would affect neutrino oscillations, particularly manifesting in the electron antineutrino disappearance channel $P_{\bar{\nu}_e \to \bar{\nu}_e}$ through an additional $\sin^2(2\theta_{14})$ driven term [4]. For this reason, reactor neutrino experiments like JUNO are especially well suited to search for such light sterile neutrinos on a $\mathcal{O}(10^{-5}\,\mathrm{eV}^2)$ [103].
The analysis presented in this work on the indirect DM search also falls into the category of physics beyond the SM. A detailed sensitivity study has already been published for MeV DM [8]. In this work, the analysis is extended to higher WIMP energies, and the expected neutrino signal in the MeV, sub-GeV, and GeV regions is discussed (cf. Chap. 6).

5 | Neutrino Interactions and Visible Energy in JUNO

Let us read and let us dance - two amusements that will never do any harm to the world.

– Voltaire

The sensitivity of JUNO for indirect DM searches fundamentally depends on how well a monoenergetic neutrino signal can be distinguished from continuous background spectra. This distinction is not straightforward since multiple physical processes at the interaction vertex, subsequent final state interactions (FSIs) and ionization quenching in the LS, affect the correlation between the initial neutrino energy E_ν and the experimentally accessible visible energy E_{vis}. To predict the spectral shape of a potential DM signal and accurately model the background contributions that undergo the same processes, it is necessary to understand the detector response for different neutrino interaction channels. Sec. 5.1 introduces the relevant charged current (CC) and neutral current (NC) neutrino interactions, as well as the inverse beta decay (IBD), and clarifies the terminology, distinguishing vertex configurations from final-state topologies. Sec. 5.2 examines how these interactions manifest in the JUNO LS, using MC simulations to map the correlation between the neutrino energy E_ν and the quenched deposited energy E_{Qdep} for each channel. To transform the quenched deposited energy to the reconstructed visible energy E_{vis}, Sec. 5.3 derives a global parametrization of the energy resolution in JUNO from 12 MeV to 10 GeV.

5.1 Neutrino Interactions with Matter

Neutrino interactions are mediated by the weak force through the exchange of heavy gauge bosons. In a charged current (CC) interaction, a charged $W^\pm$ boson is exchanged, coupling leptonic and hadronic currents with pure vector–axial (V–A) structure. In a neutral current (NC) interaction, mediated by the neutral Z^0 boson, the coupling involves a mixture of vector and axial-vector components. CC currents couple only to left-chiral fermions (and right-chiral antifermions), while NC currents also possess a right-chiral component which, however, does not couple to neutrinos. Therefore, in the SM of particle physics, there are only left-chiral active neutrinos and right-chiral active antineutrinos. Consequently, for neutrinos, the weak interaction is maximally parity-violating [24]. Neutrinos can interact with SM particles in a variety of ways. In this work, the focus is on CC and NC interactions with nucleons, which may be either free or bound in a nucleus. Neutrinos can also scatter elastically off atomic electrons; however, the interaction probability for these processes in JUNO becomes dominant only for energies < 4 MeV [7].

5.1.1 Neutrino-Nucleon Interaction

Depending on the energy transfer ω of the interaction, neutrinos interact via quasieleastic scattering (QES), resonant scattering (RES), or deeply inelastic scattering (DIS) interactions with free nucleons. For small ω, the neutrino typically scatters off the entire nucleon, which is called a QES interaction. In CC interactions

$$\nu_\ell + n \to \ell^- + p \quad \text{and} \quad \bar{\nu}_\ell + p \to \ell^+ + n$$

a $W^\pm$ boson is exchanged, converting the neutrino into a charged lepton $\ell^\pm$ (cf. red box in Fig. 5.1), whereas in NC interactions

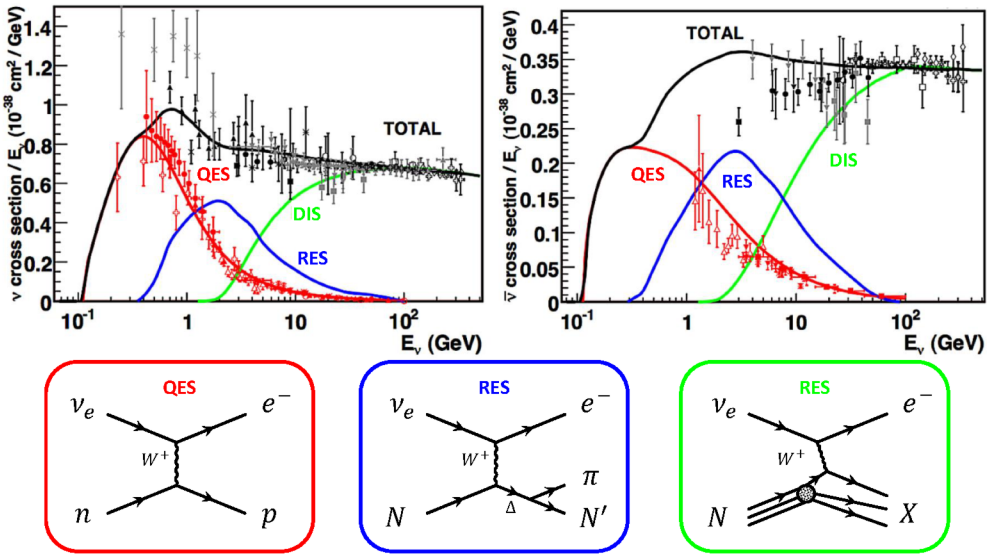

Figure 5.1: Upper panel: CC interaction cross section per nucleon for neutrinos (left) and antineutrinos (right), divided by the neutrino energy E_ν. Adapted from [104]. Lower panel: Feynman diagrams for QES, RES and DIS CC interactions exemplarily illustrated for ν_e.

$$\nu_\ell + N \to \nu_\ell + N \quad \text{and} \quad \bar{\nu}_\ell + N \to \bar{\nu}_\ell + N \ , \quad \text{with } N \in \{p, n\}$$

the exchanged particle is the Z^0 boson, which does not carry any electric charge. Therefore, the incoming neutrino remains a neutrino in the final state [104]. As illustrated in the upper panel of Fig. 5.1, QES interactions (red) dominate for neutrino energies up to $E_\nu \approx 1\,\text{GeV}$. However, already in the sub-GeV regime, the energy transfer in the neutrino interaction is sufficient to excite the nucleons N to a resonant Δ or other higher N^* resonances (cf. blue curve in Fig. 5.1). In this case, a so-called resonant scattering (RES) interaction occurs, with a pion in the final state [104]. At very large energy transfer ω, neutrinos no longer scatter off the entire nucleon but off one of its partons (quarks). In this process, the nucleon is destroyed, and a hadronic shower is initiated (indicated with X in Fig. 5.1), enabling studies of the internal structure of hadrons. These deeply inelastic scattering (DIS) interactions become dominant only in the several GeV regime (cf. green curve in Fig. 5.1) and are therefore not of primary importance for this work [104].

5.1.2 Neutrino-Nucleus Interaction

For nucleons bound in a nucleus, additional collective effects occur in neutrino interactions besides QES, RES and DIS. In Fig. 5.2, the response of a nucleus (blue) is qualitatively compared with that of a single nucleon (red) as a function of the energy transfer ω. The

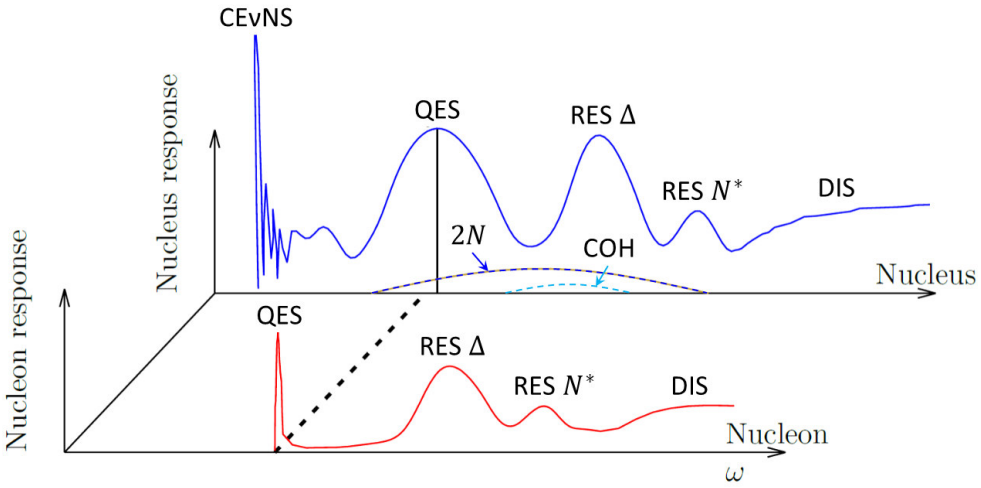

Figure 5.2: Schematic response function of a nucleon (red) and a nucleus (blue) in a neutrino interaction, including the QES, RES (excitation of Δ or N-baryons) and DIS interactions. In addition, collective effects in a nuclear environment such as CEνNS, COH and two-body currents ($2N$) are considered for the interaction of bound nucleons. Adapted from [105].

Coherent Elastic Neutrino-Nucleus Scattering (CEνNS) peak describes the interaction of the neutrino with the entire nucleus A according to $\nu_\ell + A \to \nu_\ell + A$. CEνNS is a pure NC interaction and is not to be confused with the coherent π production, which is referred to as COH in Fig. 5.2, where CC and NC currents are involved [104, 105]. In a COH interaction, the neutrino also scatters off the entire nucleus, but a forward-directed pion is produced in the process according to

$$\nu_\ell/\bar{\nu}_\ell + A \to \begin{cases} \ell^\mp + \pi^\pm + A & \text{(CC)} \\ \nu_\ell/\bar{\nu}_\ell + \pi^0 + A & \text{(NC)} \end{cases} .$$

QES neutrino interactions with bound nucleons almost always produce a 1-particle 1-hole (1p1h) excitation, with the nucleon lifted above the Fermi surface. Usually, this nucleon will subsequently leave the nucleus, resulting in a $1N$ knockout [24, 104]. In this case, the QES CC interactions can be written as [105]

$$\begin{aligned} \nu_\ell + (A, Z) &\to \ell^- + p + (A-1, Z)^* \\ \bar{\nu}_\ell + (A, Z) &\to \ell^+ + n + (A-1, Z-1)^* \ , \end{aligned} \tag{5.1}$$

while in NC interactions, the neutrino remains in place of the charged lepton $\ell^\pm$, and no conversion of $p \leftrightarrow n$ occurs. Since the separation energy of the nucleon must be taken into account for the $1N$ knockout, the QES peak in Fig. 5.2 is shifted to larger energy transfers ω compared to free nucleons, and the peak is broadened due to the Fermi motion of the nucleons [104, 106]. Another important contribution to neutrino–nucleus interactions is the two-body currents at the vertex, in which the bosons of the weak

interaction couple to a pair of nucleons and lift both above the Fermi surface (2-particle 2-hole (2p2h) excitation) [24]. This can proceed either via short-range nucleon–nucleon correlations or via so-called meson exchange currents (MEC). Typically, both nucleons are emitted from the parent nucleus in a $2N$ knockout, therefore, these processes are collectively labeled as $2N$ in Fig. 5.2 (dashed dark-blue line).

5.1.3 Terminology of the Vertex Mechanism and Final Topology

To avoid confusion, especially when distinguishing QES from MEC interactions on nuclei, the relevant terminology is defined here. QES interactions are one-body currents in which the weak gauge boson couples to a single nucleon. In contrast, MEC, together with nucleon–nucleon correlations, belongs to the class of two-body currents which, in the sub-GeV regime, provide a relevant contribution to QE-like events [107]. The labels 1p1h and 2p2h describe the nucleonic configuration at the vertex; the number specifies how many nucleons are lifted above the Fermi surface, leaving the corresponding number of holes below it. In the sub-GeV region, QES interactions almost always lead to a 1p1h state, whereas in the MeV regime, exclusive Fermi/Gamow–Teller transitions can occur [104]. In contrast, MEC interactions typically produce a 2p2h state and contribute only marginally to 1p1h [105].
The final event topology, however, is not determined by the vertex configuration but rather by the subsequent final state interactions (FSIs). Nucleons lifted above the Fermi surface may leave the nucleus (knockout) or be reabsorbed. They can also scatter off and eject additional nucleons that were not involved at the vertex. As a result, the detector signature depends strongly on the FSI. For this reason, the topology of QES and MEC events is often denoted as CC0πNp, which specifies the number of pions and the proton multiplicity[1]. A CC0π1p topology can arise either from a genuine QES process or from a MEC interaction followed by FSI that reabsorbs one of the nucleons; hence, events that are not genuine QES are also counted in the QE-like sample. Since the analyses in this work will focus on CC0π with no pions in the final state, the event topology is classified according to CCNpNn, which specifies the proton and neutron multiplicities (e.g. CC0p1n denotes no protons and one neutron in the final state).

5.2 Neutrino Interactions in the JUNO Simulation

The probability of a neutrino interaction in the JUNO LS depends on the target composition and on the corresponding cross sections of the interactions, which are discussed in Sec. 5.1. Tab. 5.1 lists the main target isotopes present in the JUNO LS, as implemented in the MC simulation. As described in Sec. 4.2, approximately $\sim 99\,\%$ of the LS mass is composed of carbon ^{12}C and hydrogen ^{1}H atoms. In addition, the fluor PPO contributes some isotopes to the LS, along with the presence of naturally occurring isotopes, although their fractions are very small.
For the MC datasets produced in this work (cf. Tab. C.1), the GENIE generator version 3.2.0 with tune `G18_10b_02_11b` was used. To describe nuclear effects, the Local Fermi Gas model is used for all nuclei listed in Tab. 5.1. The QES interactions and the 2p2h contributions (MEC) are described using the Valencia model, whereas for the RES processes and the COH π production, the Berger-Sehgal model is used [77]. Tune `G18_10b_02_11b` uses the hN model, which is a full intranuclear data-driven cascade

[1] For RES or COH events, the topology is labeled CCNπ according to the number N of pions in the final state.

Table 5.1: Isotopic mass composition of the main constituents of the JUNO LS, as implemented in the JUNO simulation framework version J24.1.2. The values of ^{1}H and ^{12}C were calculated, assuming $n = 11$ in the chemical formula (cf. Sec. 4.2).

target nuclei	mass fraction [%]	origin
^{12}C	86.98	LS
^{1}H	12.01	LS
^{13}C	0.941	natural isotope
^{16}O	0.034	PPO
^{14}N	0.027	PPO

model, where the hadrons produced after an interaction are propagated step by step inside the nucleus until they either exit the nucleus or are reabsorbed [76, 108]. The de-excitations of the residual daughter nuclei after the FSI are modeled using the TALYS database [78], while all final-state particles are propagated through the detector in step-by-step MC simulations using Geant4. In order to obtain the final visible energy

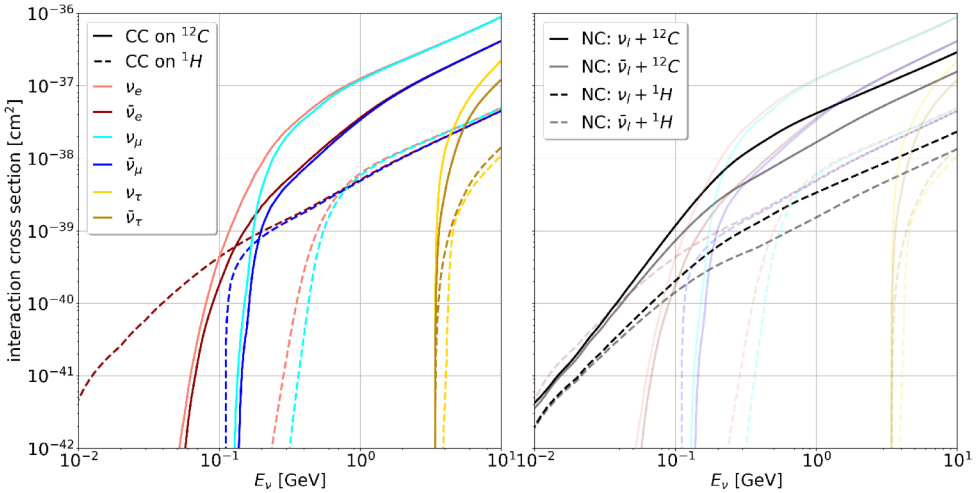

Figure 5.3: Total CC (left and right colored curves) and NC (right black curves) neutrino interaction cross sections for different neutrino and antineutrino flavors on ^{12}C (solid lines) and ^{1}H (dashed lines). The cross sections where taken from the GENIE generator framework version 3.2.0 [76].

spectrum in JUNO, the quenched energy deposition from CC and NC events of all neutrinos and antineutrinos with the targets in Tab. 5.1 must be considered. Focusing on the main target isotopes, Fig. 5.3 shows the total neutrino interaction cross sections for CC (left) and NC interactions (right) on ^{12}C (solid lines) and ^{1}H (dashed lines). For neutrino energies in the MeV range $E_\nu \lesssim 100\,\text{MeV}$, the CC QES interaction of $\bar{\nu}_e$ with hydrogen ^{1}H dominates (cf. dashed dark-red line in the left panel). This so-called inverse beta decay (IBD) is discussed in detail in Sec. 5.2.1. In the sub-GeV range between $E_\nu \sim 0.1 - 1.0\,\text{GeV}$, QES, RES, and MEC interactions of electron and muon neutrinos on ^{12}C are dominant (solid lines). In the GeV range between $E_\nu \sim 1 - 10\,\text{GeV}$, CC, RES and DIS interactions on ^{12}C dominate. Due to the large $\tau^{\pm}$-lepton rest mass of $m_\tau = 1.78\,\text{GeV}$, CC interactions of tau neutrinos become relevant only in the GeV regime [29]. For NC interactions (cf. right panel of Fig. 5.3), all neutrino flavors

contribute across the entire energy range, since no charged lepton needs to be produced in the interaction. The NC interaction cross section depends only on whether it is a neutrino ν_ℓ or an antineutrino $\bar{\nu}_\ell$, since due to parity violation of the weak interaction, the coupling to left-handed neutrinos at high energies $\gtrsim 0.5\,\text{GeV}$ is about a factor of two stronger than to right-handed antineutrinos [109].
The relation between the initial neutrino energy E_ν and the quenched deposited energy E_{Qdep} of the interaction depends on the primary particles produced at the vertex of the interaction, as well as on the FSI, which can produce further secondary particles. All final-state particles produced in an event will deposit their energy in the LS, but are subject to ionization quenching as described by Birks' Law [72], which reduces the scintillation light yield for heavily ionizing particles (cf. Sec. 4.3). To calculate the quenched deposited energy E_{Qdep}, effects such as the nonlinearity of the scintillator due to quenching and Cherenkov radiation, as well as the non-uniformity at the outer part of the CD, must be taken into account. In addition, instrumental effects that impact the energy scale must be understood in detail and corrected using sophisticated calibration methods. To achieve this, JUNO employs a multiple-source calibration strategy in combination with two independent PMT and readout systems [110]. Detailed MC studies show that the non-linearity, as well as the non-uniformity, can be controlled to $< 1\,\%$ [110, 111], which has also been confirmed by the first calibration data of JUNO [6]. Based on MC datasets $D1$ and $D2$ in Tab. C.1, the true and quenched deposited energy of all relevant interaction channels (IBD, CC, and NC) in JUNO are studied in Secs. 5.2.1 and 5.2.2. All relevant detector effects, such as light yield and non-linearity, are included in these simulations.

5.2.1 Inverse Beta Decay

For neutrino energies up to approximately 100 MeV, CC interactions of electron antineutrinos $\bar{\nu}_e$ on hydrogen ^{1}H dominate, as can be deduced from the left plot of Fig. 5.3. This interaction, illustrated in Fig. 5.4, is known as the inverse beta decay (IBD)

$$\bar{\nu}_e + p \rightarrow e^+ + n \ . \tag{5.2}$$

In this QES interaction, the neutrino energy is distributed between the resulting positron e^+ and neutron n according to the kinematics of the IBD process, which has an energy threshold of $E_{\text{IBD,th}} = 1.806\,\text{MeV}$ corresponding to the mass difference between the neutron and positron (right side of Eq. 5.2) and the proton (left side of Eq. 5.2) [66]. The positron deposits its energy in the LS and subsequently annihilates with an electron, emitting two 511 keV photons. The signal generated by the positron occurs within the

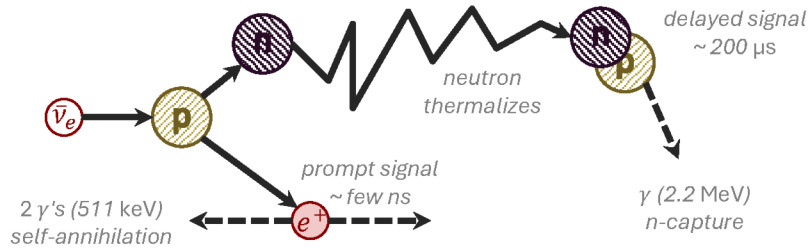

Figure 5.4: Schematic illustration of an IBD interaction in the JUNO LS, including the prompt signal caused by the energy deposition and annihilation of the positron e^+ and the delayed n-capture signal on ^{1}H after the neutron has thermalized.

first few hundred nanoseconds and is referred to as the prompt signal. The neutron first thermalizes through elastic scattering with the nuclei in the detector material, depositing its kinetic energy via nuclear recoils. Once thermalized, it is captured by a nucleus, most likely ^{1}H, resulting in the emission of a characteristic 2.2 MeV photon. Only about 1 % of the neutrons are captured by a ^{12}C nucleus instead, resulting in the emission of a characteristic energy of 4.9 MeV [112]. The n-capture time follows an exponential decay with a typical time constant $\tau \approx 215\,\mu$s and is therefore referred to as the delayed signal [4, 112]. The temporal and spatial coincidence between the prompt and delayed signal of an IBD event allows for very effective background suppression. To achieve this, specific selection cuts are applied to the measured events in order to efficiently reject background events as IBD candidates, which are discussed in detail in Sec. 8.2.
In Fig. 5.5, the relation between the initial neutrino energy $E_{\bar{\nu}_e}$ and the prompt deposited energy is shown for approximately 800,000 simulated IBD events[2]. The upper panel displays the true deposited energy E_{dep} before quenching, while the lower panel shows the quenched deposited energy E_{Qdep} after applying Birks' law to model the non-linear scintillation response. Since most of the neutrino energy is transferred to the positron due to the kinematics of the reaction, a clear correlation between E_{dep} and $E_{\bar{\nu}_e}$ is observed. For the dominant class of events, the prompt deposited energy can be expressed as

$$E_{\text{dep}} \approx E_{\bar{\nu}_e} - E_{\text{IBD,th}} + 2\,m_e = E_{\bar{\nu}_e} - 0.78\,\text{MeV}\ , \tag{5.3}$$

where the neutron's kinetic energy is fully deposited through elastic scattering during thermalization, and the positron annihilation contributes $2\,m_e = 1.022\,\text{MeV}$. This corresponds to the main correlation band in the upper panel of Fig. 5.5 and the dominant peak in the inset histogram at $E_{\bar{\nu}_e} - E_{\text{dep}} \approx 0.78\,\text{MeV}$ (cf. dashed black line). In addition to the main correlation band, several parallel sub-bands shifted to lower deposited energies are visible in Fig. 5.5. These arise from sub-dominant inelastic interactions of the neutron with ^{12}C nuclei. The most prominent secondary processes are [113]

$$^{12}\text{C}(n,\alpha)^{9}\text{Be}: \quad n + {}^{12}\text{C} \to \alpha + {}^{9}\text{Be}\ , \qquad Q = -5.7\,\text{MeV and} \tag{5.4}$$

$$^{12}\text{C}(n,n+3\alpha): \quad n + {}^{12}\text{C} \to n + \alpha + {}^{8}\text{Be} \to n + 3\alpha\ , \qquad Q = -7.3\,\text{MeV}\ , \tag{5.5}$$

which occur in $\sim 10\,\%$ of all IBD events. Since in the ^{12}C$(n,\alpha)^{9}$Be process ($\sim 2.5\,\%$), the neutron is absorbed by the ^{12}C nucleus, the delayed signal is absent for these events[3]. In the unquenched E_{dep} plot, the energy shift of IBD events, which undergo sub-dominant inelastic neutron processes, corresponds to the Q-values of the interactions and the visible energy threshold of 0.78 MeV for IBD events. The most prominent classes of inelastic neutron processes are indicated by the colored dashed lines in the upper left inset histogram of Fig. 5.5. These secondary interactions are the reason for the parallel sub-band structure in the E_{dep} plot. The lower panel of Fig. 5.5 shows the quenched deposited energy E_{Qdep} after applying Birks' law. At higher positron energies, ionization quenching becomes more pronounced due to the increased ionization density along the particle track. This leads to a systematic deviation from the ideal linear correlation and broadens the energy response. Since the α particles, which are produced by inelastic neutron interactions on carbon (e.g. Eq. 5.4 and 5.5), experience strong ionization

[2]The events were generated by GENIE in a detector volume with $r \leq 16\,\text{m}$, assuming a flat neutrino energy distribution $E_{\bar{\nu}_e} \in [10 - 300]\text{MeV}$ and a prompt time window of $2\,\mu$s (cf. $D1$ in Tab. C.1).

[3]Further sub-bands correspond to additional inelastic channels involving nuclear breakup and multiple α emissions (cf. colored dashed lines in the inset upper left plot in Fig. 5.5).

quenching, the sub-bands from secondary neutron processes are less distinct in the quenched energy spectrum. Despite these effects, the overall correlation between $E_{\bar{\nu}_e}$ and E_{Qdep} remains strong over the entire energy range considered. This tight correlation makes the IBD channel particularly well suited for searches for monoenergetic $\bar{\nu}_e$ signals. Combined with the characteristic delayed n-capture signal and the resulting powerful background suppression, the IBD channel is very well suited for the sensitivity study of DM annihilation for masses below $\sim 300\,\mathrm{MeV}$ (cf. Sec. 10.2).

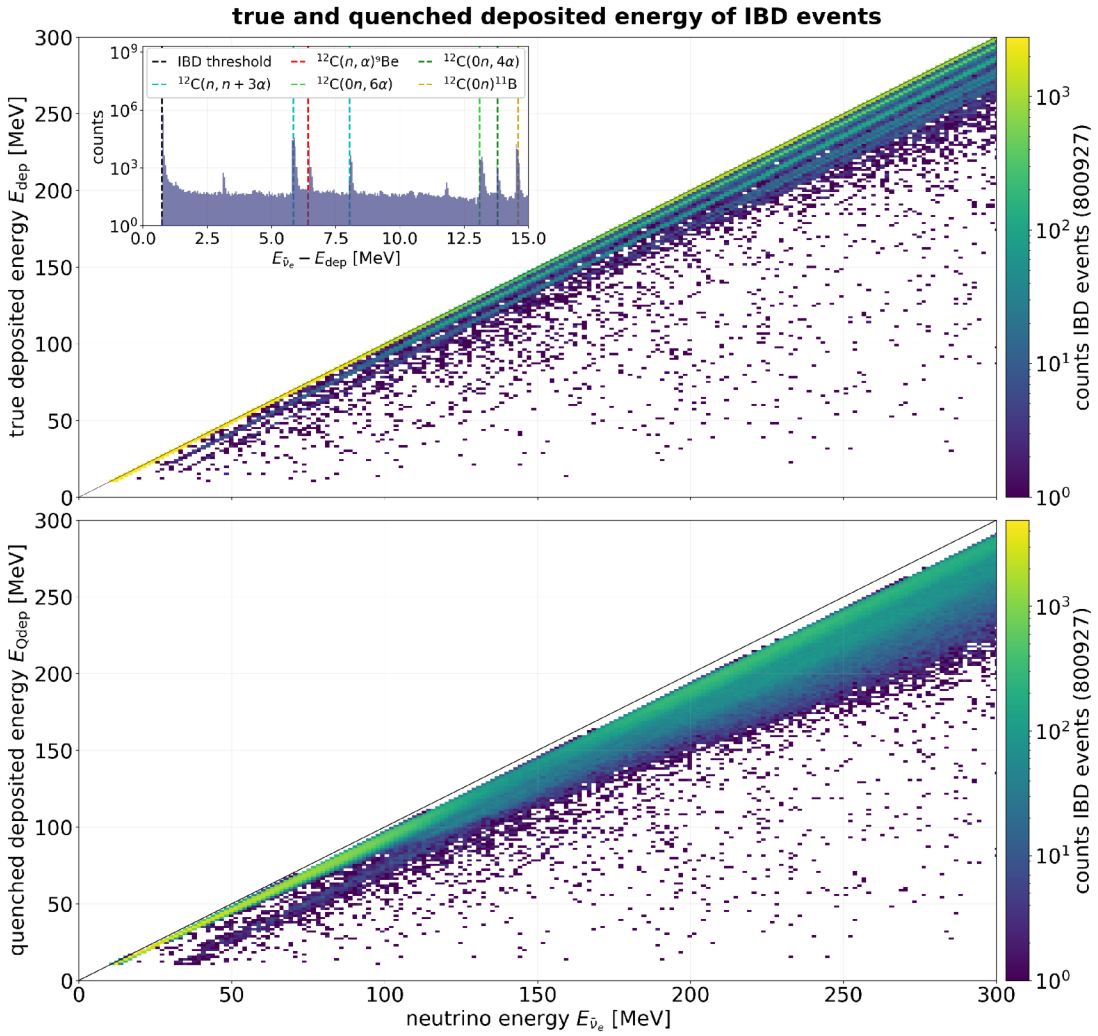

Figure 5.5: Correlation between the initial neutrino energy $E_{\bar{\nu}_e}$ and the prompt energy deposition for approximately 800,000 IBD events isotropically distributed in the CD. *Top:* True deposited energy E_{dep} before quenching, showing a nearly ideal correlation with discrete parallel sub-bands arising from secondary neutron interaction processes. The inset shows the distribution of the energy difference $E_{\bar{\nu}_e} - E_{\mathrm{dep}}$, with the prominent peak at $E_{\mathrm{IBD,th}} - 2\,m_e \approx 0.78\,\mathrm{MeV}$ (dashed black line) corresponding to the main class of IBD events. The sub-dominant peaks between $5.5 - 8.0\,\mathrm{MeV}$ (dashed blue and red lines) arise from the inelastic neutron processes in Eq. 5.4 and 5.5. *Bottom:* Quenched deposited energy E_{Qdep} after applying Birks' law. The deviation from the diagonal demonstrates the reduced scintillation light yield due to ionization quenching, particularly at higher energies.

5.2.2 CC and NC Channels

For the indirect DM search with masses in the sub-GeV and GeV range, the IBD channel is no longer optimally suited, since, despite excellent background reduction methods, it yields only a small number of events compared to all CC events (cf. Fig. 5.3). Therefore, in this work, the CC channel is chosen for the sensitivity study in the sub-GeV and GeV range. Although this channel promises a significantly larger number of events (cf. Sec. 6.1), it simultaneously offers less effective background reduction methods due to the significantly more complex event topology compared to IBD interactions. The greatest challenge arises from the background due to atmospheric neutrinos, whose spectrum extends continuously over a wide energy range (cf. Sec. 7.4). In addition to CC events, NC events also constitute a relevant background. Since in these events the neutrino carries away a large fraction of its energy from the detector, they represent a critical background in the MeV region. In order to distinguish a potential monoenergetic DM signal from this broad background, a precise understanding of the detector response to CC and NC interactions is essential. In Fig. 5.6, the correlation between the quenched deposited energy E_{Qdep} and the neutrino energy E_ν is shown for CC events (upper panel) and NC events (lower panel). Approximate 400,000 simulated events (cf. $D2$ in Tab. C.1) with uniformly distributed neutrino energies $E_\nu \in [0.01, 10]\,\mathrm{GeV}$ are evaluated for both channels and will be discussed in the following sections.

CC Events

Compared to the IBD channel in Fig. 5.5, the correlation for CC events in the upper panel of Fig. 5.6 is more smeared. Nevertheless, the quenched deposited energy still shows a reasonably strong correlation with the neutrino energy, as the charged lepton deposits the majority of the neutrino energy promptly in the detector. The smearing of the deposited energy arises mainly from additional nucleon knockouts, where the neutrino energy must account not only for the Q-value of the interaction but also for the nucleon separation energy. For ^{12}C, the proton separation energy is $S_p = 15.96\,\mathrm{MeV}$ and the neutron separation energy is $S_n = 18.72\,\mathrm{MeV}$ [114]. In particular, in the case of neutron knockouts, the neutron carries away part of the neutrino energy and deposits only a part of it via elastic scattering, mainly with the protons in the LS. It is, however, later observed during the n-capture after its thermalization, producing a delayed signal in the form of a characteristic 2.2 MeV photon, which is not included in the plot.For neutrino energies larger than $E_\nu = m_\mu = 105.7\,\mathrm{MeV}$, muon neutrinos ν_μ and antineutrinos $\bar{\nu}_\mu$ can also participate in CC interactions, resulting in the production of a charged muon $\mu^\pm$ in the final state. Similar to an electron, the muon deposits its energy while propagating through the LS, producing scintillation light along the track. While anti-muons μ^+ will always decay with a life-time of $\tau_\mu = 2.197\,\mu\mathrm{s}$, muons μ^- will first form myonic atoms by being captured in the shell. Afterwards, the process of muon capture on the nucleus $\mu^- + p \to n + \nu_\mu$ competes with μ^- decay in the atomic shell. The probability for μ^- capture on the nucleus depends on the isotope and is about $\sim 8\,\%$ for ^{12}C [115]. If the muons or anti-muons do not escape the detector volume, they will decay according to[4]

$$\mu^- \to e^- + \bar{\nu}_e + \nu_\mu \quad \text{and} \quad \mu^+ \to e^+ + \nu_e + \bar{\nu}_\mu \,. \tag{5.6}$$

[4]For neutrino energies of $(0.1 - 10)\,\mathrm{GeV}$, approximately 97 % of the CC events are fully contained, which means that the leptons will not leave the CD but deposit their energy fully in the LS [116].

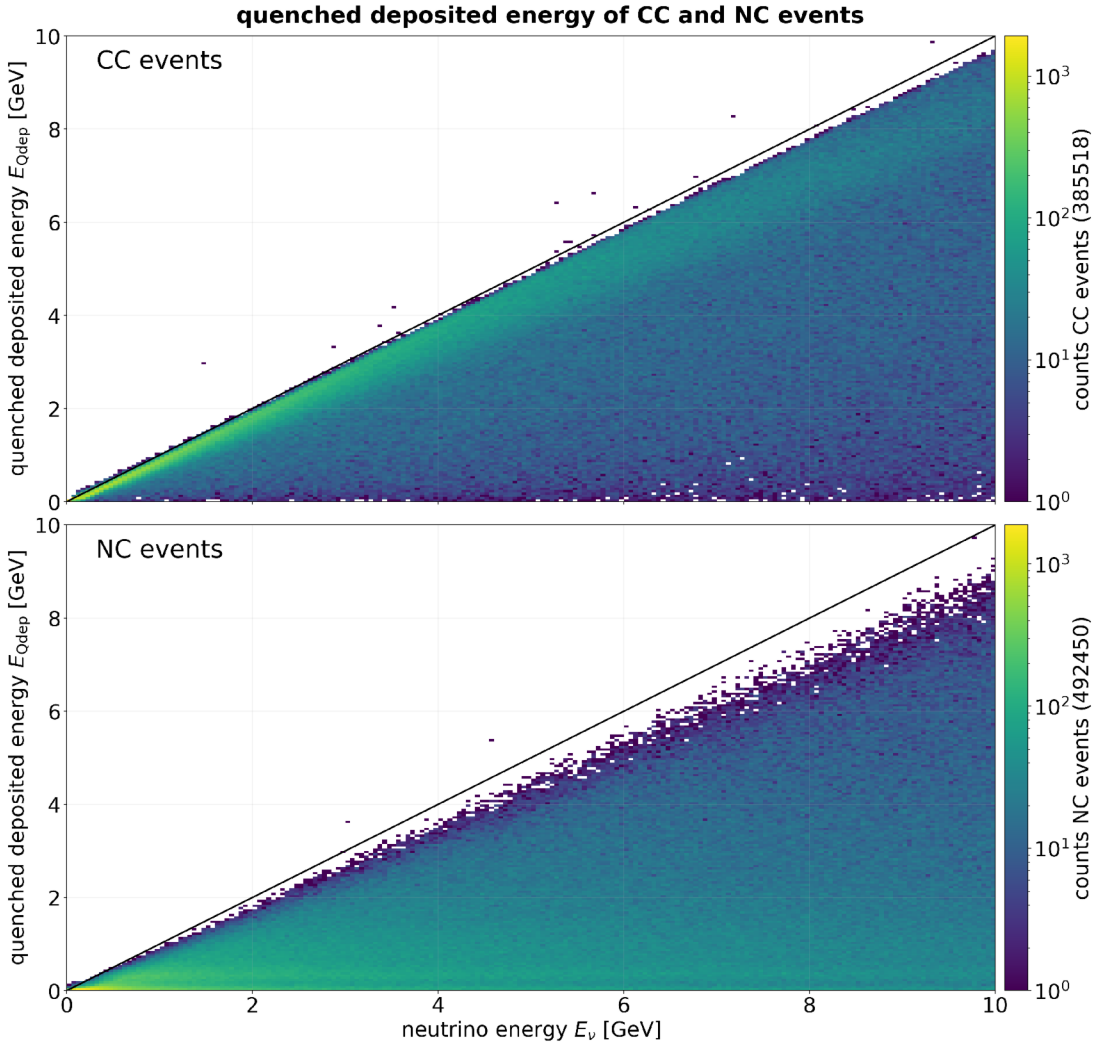

Figure 5.6: Quenched deposited energy E_{Qdep} distribution of CC events (upper panel) and NC events (lower panel) in JUNO, considering a flat neutrino energy distribution $E_\nu \in [0.01, 10]$GeV. The deviation from the diagonal black line demonstrates the reduced scintillation light yield due to ionization quenching, which is larger for NC events due to primarily hadronic energy deposition.

The resulting electron or positron $e^{\pm}$, known as a Michel electron, produces another delayed scintillation signal with a characteristic spectral shape, while part of the muon energy is carried away by neutrinos escaping the detector, which leads to additional smearing of the CC signal [115, 117].

In Tab. 5.2, the most frequent CC channels in the sub-GeV range are listed, including the subsequent decay of the remaining isotopes[5]. These interactions were either produced in a QES or a MEC process. The relative appearance of the most probable listed interactions with respect to all CC interactions is shown in Fig. 5.7 in the sub-GeV range. In addition, the IBD contribution is shown for comparison. The most frequent interaction is no. (1) with the topology CC1p0n at the primary vertex. In this case,

[5]Due to their long lifetime, many decays are irrelevant for the DM signal. However, during these decays, energy is deposited in the detector, causing additional single events that need to be considered for the atmospheric neutrino background.

Table 5.2: List of the most probable CC interactions on ^{12}C in the sub-GeV range generated by GENIE version 3.2.0 with `G18_10b_02_11b` model tuning. The interactions are produced either in an QES or a MEC event. Some of the residual isotopes created in the interactions are unstable and will decay accordingly [118].

no.	full CC interaction	topology	decay of the residual isotope
(1)	$\nu_{e/\mu} + {}^{12}\mathrm{C} \to e/\mu^- + {}^{11}\mathrm{C} + p$	CC1p0n	β^+ decay ($t_{1/2} = 20.34\,\mathrm{min}$)
(2)	$\bar{\nu}_{e/\mu} + {}^{12}\mathrm{C} \to e/\mu^+ + {}^{11}\mathrm{B} + n$	CC0p1n	stable
(3)	$\nu_{e/\mu} + {}^{12}\mathrm{C} \to e/\mu^- + {}^{10}\mathrm{C} + p + n$	CC1p1n	β^+ decay ($t_{1/2} = 19.30\,\mathrm{s}$)
(4)	$\bar{\nu}_{e/\mu} + {}^{12}\mathrm{C} \to e/\mu^+ + {}^{10}\mathrm{Be} + n + p$	CC1p1n	β^- decay ($t_{1/2} = 1.38 \times 10^6\,\mathrm{yr}$)
(5)	$\nu_{e/\mu} + {}^{12}\mathrm{C} \to e/\mu^- + {}^{10}\mathrm{B} + 2p$	CC2p0n	stable
(6)	$\nu_{e/\mu} + {}^{12}\mathrm{C} \to e/\mu^- + {}^{9}\mathrm{B} + 2p + n$	CC2p1n	proton emission ($t_{1/2} \sim \mathrm{zs}$)
(7)	$\bar{\nu}_{e/\mu} + {}^{12}\mathrm{C} \to e/\mu^+ + {}^{10}\mathrm{B} + 2n$	CC0p2n	stable

the neutrino energy is shared between the lepton e/μ^- and the ejected proton p. Since both charged particles promptly deposit their energy via scintillation in the detector, the interaction preserves the monoenergetic neutrino signature particularly well, which is discussed in more detail in Sec. 6.2.2. Depending on whether the event is produced by ν_e or ν_μ, the deposited energy of interaction (1) is shifted by

$$Q(\nu_e) = m_e + m_p + M(^{11}\mathrm{C}) - M(^{12}\mathrm{C}) + \Delta E_{\mathrm{ex}}(^{11}\mathrm{C}) \approx 17.9\,\mathrm{MeV} + \Delta E_{\mathrm{ex}}(^{11}\mathrm{C}) \quad (5.7)$$

$$Q(\nu_\mu) = m_\mu + m_p + M(^{11}\mathrm{C}) - M(^{12}\mathrm{C}) + \Delta E_{\mathrm{ex}}(^{11}\mathrm{C}) \approx 123.1\,\mathrm{MeV} + \Delta E_{\mathrm{ex}}(^{11}\mathrm{C}) \quad (5.8)$$

relative to the neutrino energy E_{ν_e}, where $\Delta E_{\mathrm{ex}}(^{11}\mathrm{C})$ denotes the excitation energy of the residual isotope[6] [114, 119]. The interactions (2), (3), (4) and (6) listed in Tab. 5.2 produce a neutron in the final state and can thus mimic the IBD signature. Atmospheric neutrinos that will produce these topologies must be treated as potential background events for the IBD dominated MeV analysis. In the sub-GeV range, the probability of proton knockouts is generally higher than that of neutron knockouts. As a result, the linear correlation between the deposited energy and the neutrino energy E_ν remains relatively well preserved, particularly in this energy regime (cf. upper panel in Fig. 5.6).

NC Events

In contrast to CC events, NC interactions do not produce charged leptons. Therefore, all neutrino and antineutrino flavors participate in NC interactions (cf. right panel of Fig. 5.3). Since no charged lepton is created, the energy deposition is dominated by hadronic interactions in the LS. In particular, nucleon knockout, as well as pion production (depending on E_ν), determines the event topology. In principle, many of the hadronic topologies encountered in CC interactions (cf. third column of Tab.5.2) can also occur in NC events; however, the absence of a charged lepton implies that the visible energy is almost entirely hadronic. This has two important consequences for the detector response. On the one hand, the scintillation light yield is strongly affected by ionization quenching, since protons and other heavy secondaries have a much higher ionization

[6]The isotope ^{11}C is unstable and decays with a half-life of $t_{1/2} = 20.34\,\mathrm{min}$ via β^+ decay. Due to the long half-life, it is irrelevant for the DM signal

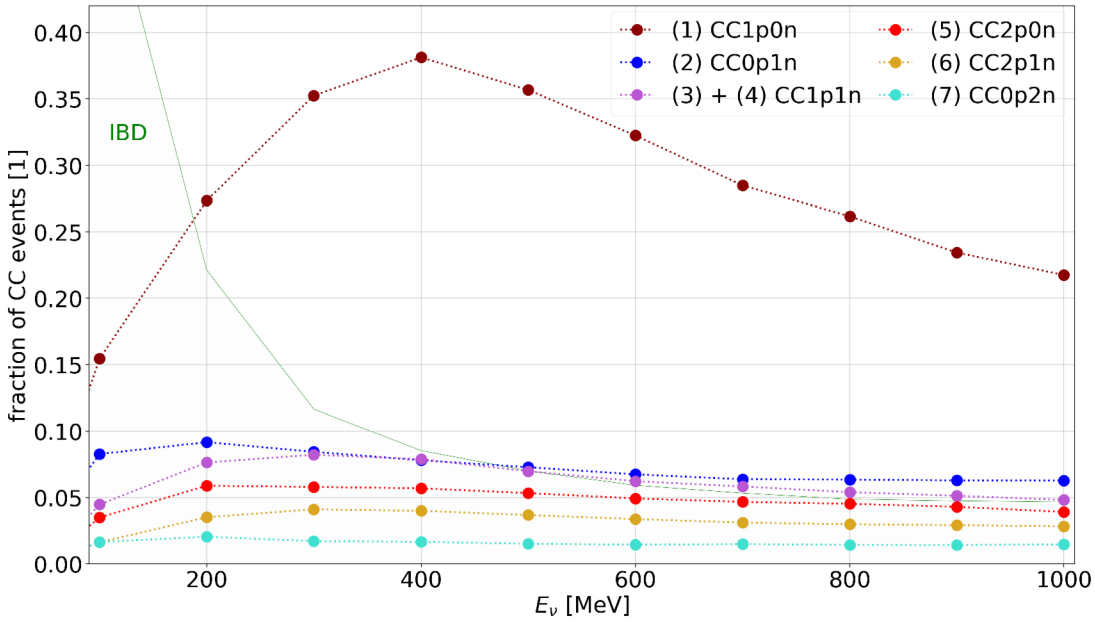

Figure 5.7: Relative appearance of the most probable CC interactions on ^{12}C listed in Tab. 5.2 with respect to all CC interactions (obtained from dataset $D5$ in Tab. C.1). The contribution of IBD interactions is added for comparison.

density than charged leptons. Therefore, the quenching effect is significantly larger for NC events than for CC events, which is reflected by the stronger deviation from the diagonal in the lower panel of Fig. 5.6. On the other hand, the outgoing neutrino carries away a large fraction of its initial energy, thus only a part of the energy is deposited in the detector. As a result, the correlation between E_ν and the quenched deposited energy E_{Qdep} is much weaker than that for CC events, and the NC distribution is shifted to lower visible energies. In the MC sample shown in Fig. 5.6, more than 50 % of all NC events in the neutrino energy range from $\sim 100\,\mathrm{MeV}$ to $10\,\mathrm{GeV}$ yield a quenched deposited energy below $\sim 1\,\mathrm{GeV}$.
Due to the combination of the large quenching of hadronic energy depositions and the undetected outgoing neutrino, NC interactions do not preserve a monoenergetic neutrino signature and are therefore not well suited to search for a monoenergetic signal. Instead, NC events can cause a broad region of low E_{Qdep} events and thus mainly contribute as background. This is particularly relevant for the MeV analysis, where the IBD channel dominates the signal spectrum, but where NC interactions can produce one or more neutrons in the final state, e.g.

$$\nu_x + {}^{12}\mathrm{C} \rightarrow \nu_x + {}^{11}\mathrm{C} + n \ . \tag{5.9}$$

While the prompt energy spectrum of such events is typically more quenched than that of positrons and is often shifted to lower visible energies, they can survive the IBD selection cuts and thus constitute an atmospheric neutrino induced background (cf. Sec. 7.4.3).

5.2.3 Exclusive CC Channels on ^{12}C

GENIE is well tested in the sub-GeV and GeV regimes and, in that domain, includes all relevant neutrino interactions discussed in Sec. 5.1. In the MeV range, however, nuclear effects are not fully covered. For example, QES interactions are modeled as pure 1p1h

processes (cf. Eq. 5.1), in which a nucleon at the vertex is always lifted above the Fermi surface and usually results in a $1N$ knockout. Consequently, the exclusive interactions

$$\begin{aligned} \nu_e + {}^{12}\mathrm{C} &\rightarrow e^- + {}^{12}\mathrm{N}_{g.s.} \quad (Q = -17.3\,\mathrm{MeV}) \quad \text{and} \\ \bar{\nu}_e + {}^{12}\mathrm{C} &\rightarrow e^+ + {}^{12}\mathrm{B}_{g.s.} \quad (Q = -13.4\,\mathrm{MeV}) \end{aligned} \tag{5.10}$$

which describe transitions between discrete nuclear states, are not included, even though they are expected to occur in JUNO [104, 120]. The solid curves in Fig. 5.8 show the CC

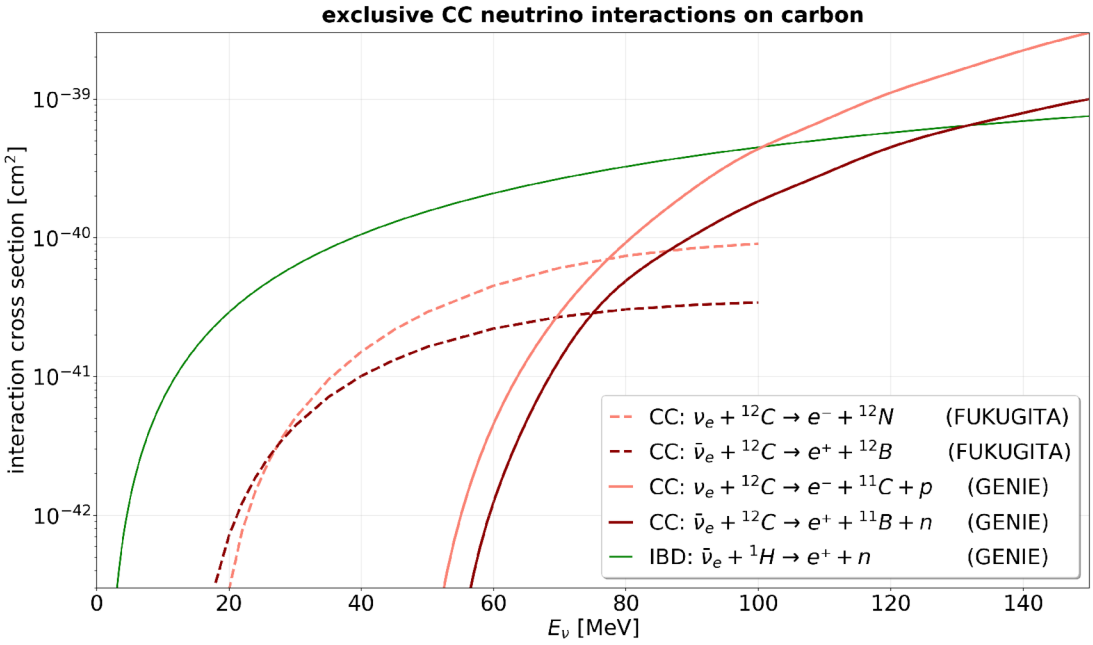

Figure 5.8: CC neutrino interaction cross sections of ν_e and $\bar{\nu}_e$ on ^{12}C (red lines) compared with the IBD cross section (green line). The solid lines represent the cross sections implemented in GENIE version 3.2.0. The dashed lines mark the calculated cross sections of the exclusive channels in Eq. 5.10, that were calculated in [120] and confirmed by the KARMEN measurements in 1996 [121].

interaction cross sections implemented in GENIE version 3.2.0. Fukugita *et al.* computed the cross sections for the exclusive channels in Eq. 5.10, which were confirmed by the KARMEN measurements in 1996 and are shown as dashed lines in Fig. 5.8 [104, 121]. These exclusive interactions begin at the corresponding Q-values of Eq. 5.10, whereas the 1p1h (solid red lines) processes must additionally overcome the nucleon separation energy [114].
Since both isotopes $^{12}\mathrm{N}_{g.s.}$ and $^{12}\mathrm{B}_{g.s.}$ are unstable and emit another lepton $e^\pm$ during the subsequent beta decay after half-lives of $t_{1/2} = 11.0\,\mathrm{ms}$ and $t_{1/2} = 20.2\,\mathrm{ms}$, these channels also provide a coincidence signature [118]. In contrast to the IBD channel, however, the energy of the delayed decay is not monoenergetic but follows a beta spectrum with endpoint energies of $Q(^{12}\mathrm{N}_{g.s.}) = 16.3\,\mathrm{MeV}$ and $Q(^{12}\mathrm{B}_{g.s.}) = 13.4\,\mathrm{MeV}$, respectively [121, 118]. In addition, the relatively long half-lives compared to that of n-capture for IBD events complicate the event reconstruction. Since the IBD channel is considerably more promising for MeV events, the exclusive channels of ν_e and $\bar{\nu}_e$ on ^{12}C are not considered in this work.

5.3 Energy Resolution in JUNO

In Sec. 5.2, the quenched deposited energy for various channels was studied using MC simulations. All relevant detector effects, such as light yield, nonlinearity, and quenching, are already included in these simulations. However, to obtain the expected visible energy spectrum of a signal in JUNO, the detector's energy resolution must also be taken into account. This resolution additionally depends on the PMT characteristics, the readout electronics, and the reconstruction algorithms. Since, for some MC datasets used in this work, only the detector simulation was performed (cf. Tab. C.1), these additional effects are included in the energy resolution for simplicity. As the reconstruction algorithms are energy-dependent, the results of the relative energy resolution $f_{\text{res}}(E) \equiv \sigma_E(E)/E$ from several studies were combined in Fig. 5.9, and a global fit was performed over the energy range relevant to this work, from 12 MeV to 10 GeV.

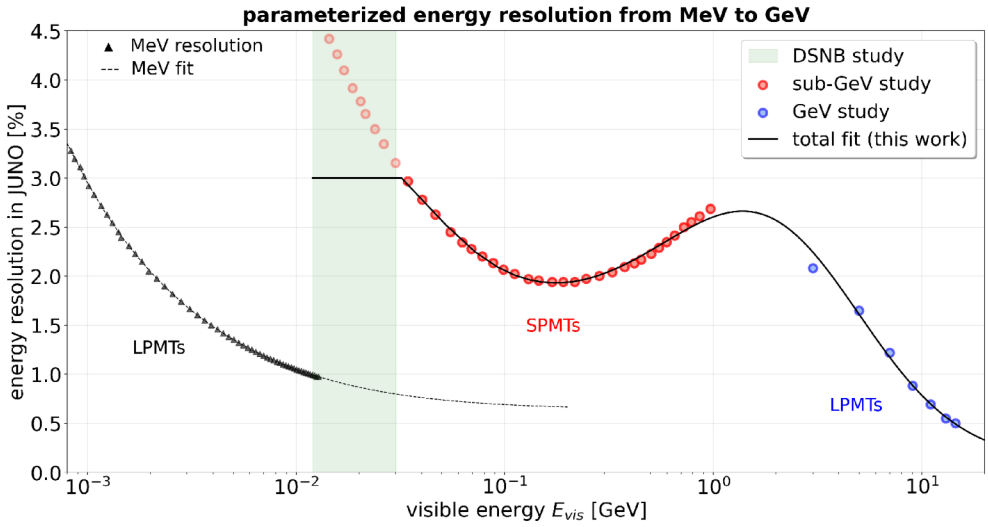

Figure 5.9: Relative energy resolution $f_{\text{res}}(E) \equiv \sigma_E(E_{\text{vis}})/E_{\text{vis}}$ in JUNO throughout the energy scales. The DSNB study (green hatched area) assumes a constant value of 3 % [98]. The red points mark the estimated resolution in the sub-GeV range [111] and the blue dots are the results in the GeV range [122, 123]. The black curve shows the global parametrization in Eq. 5.12, used in this work. For comparison the MeV parametrization (cf. Eq. 5.11) is included as black dashed line [124].

The energy resolution has been studied in detail in the low-energy MeV range for $E_{\text{vis}} \leq 12\,\text{MeV}$, since determining the NMO after 6 yr data taking requires an energy resolution of at least $3\,\%/\sqrt{E}$ in JUNO. In this energy range, the absolute energy resolution can be approximated by

$$\sigma_E(E) = \sqrt{\left(\frac{a}{\sqrt{E}}\right)^2 + b^2 + \left(\frac{c}{E}\right)^2} \tag{5.11}$$

as given in Ref. [4]. Recent analyses using fully simulated MC data (including electronics and reconstruction) in [124] report the best-fit parameters $a = 0.02614$, $b = 0.00640$, and $c = 0.01205$, which lead to the targeted resolution of 3 % at $E = 1\,\text{MeV}$. This result is also confirmed by first calibration measurements in JUNO [6]. The results from [124] are shown in Fig. 5.9 as black triangles, and the fit from Eq. 5.11 is added as a dashed black line. Since the analyses of this work start at $E_{\text{vis}} = 12\,\text{MeV}$, the parametrization

in Eq. 5.11 cannot be used[7]. Instead, the energy resolution of events up to 10 GeV has to be considered. Some studies apply the parametrization given in Eq. 5.11 to the entire sub-GeV range up to $E_{\text{vis}} = 1\,\text{GeV}$ [99]. However, since the results presented in [124] were obtained exclusively for positron events with $E_{\text{vis}} < 13\,\text{MeV}$, they cannot be directly applied to higher-energy events, which often produce a non-point-like energy deposition.

A detailed analysis of the energy reconstruction in the sub-GeV range is presented in [111], with results that account for both the electronics and vertex reconstruction shown as red points in Fig. 5.9. This reconstruction method relies only on the firing status of the small PMTs, rather than on precise charge measurements from the large 20-inch PMTs. The energy resolution can be improved using the double-calorimetry method, which combines both PMT systems [125]. In this approach, the nonlinear charge response of the LPMTs can be calibrated using the firing status of the SPMTs, while still taking advantage of the high photon statistics provided by the LPMTs. However, since no detailed study of this method exists in the sub-GeV range, the pessimistic scenario for energy reconstruction, considering only the SPMTs, was adopted in this work for $E_{\text{vis}} \geq 30\,\text{MeV}$. For the energy range $E_{\text{vis}} = 12 - 30\,\text{MeV}$ (green hatched region in Fig. 5.9), this work follows the energy resolution assumed in DSNB studies for JUNO, which adopt a constant relative energy resolution of $f_{\text{res}}(E) = 3\,\%$ [4, 98]. This assumption is more optimistic than the results presented in [111] (red points), but more conservative than the energy resolution given in Eq. 5.11 for IBD events in the MeV range (dashed black line). For the energy resolution in the GeV range, the results from the machine learning (ML) approach presented in [122] were used, where PMT-by-PMT waveform features from MC-simulated CC and muon events served as input for various neural network (NN) architectures. Similar results are presented in the dissertation in [123]. To account for the energy resolution over the entire energy range from 12 MeV to 10 GeV in the analyses presented in this work, a global fit was performed according to

$$f_{\text{res}}(x \equiv \ln(E_{\text{vis}}/\text{MeV})) \;=\; \begin{cases} 0.03, & E \leq 30\,\text{MeV}, \\ \exp\left(\sum_{k=0}^{5} A_k\, x^k\right), & E > 30\,\text{MeV}, \end{cases} \tag{5.12}$$

using the least-squares method. The result is shown in Fig. 5.9 as the solid black line, and the best-fit results for the parameters A_k, together with their $1\,\sigma$ uncertainties, are listed in Tab. 5.3.

Table 5.3: Best fit values and 1σ uncertainties for the parameterized energy-resolution.

parameter	best fit value
A_5	0.00306 ± 0.00036
A_4	-0.101 ± 0.012
A_3	1.24 ± 0.15
A_2	-7.09 ± 0.93
A_1	18.83 ± 2.82
A_0	-22.10 ± 3.310

[7] Following previous DM studies [7, 8], the lower limit of $E_{\text{vis}} \geq 12\,\text{MeV}$ was chosen such that the contribution from reactor neutrinos becomes negligible (cf. Sec. 7.1).

Summary of Neutrino Interactions and Visible Energy in JUNO

This chapter establishes how neutrino energy E_ν translates into visible energy E_{vis} in JUNO, providing the foundation for signal and background modeling in the DM sensitivity analysis. In the MeV range, IBD interactions on free protons provide an almost linear correlation between $E_{\bar{\nu}_e}$ and E_{Qdep}, while the prompt–delayed coincidence from n-capture enables powerful background suppression. This makes IBD the optimal channel for DM masses below $\sim 300\,\text{MeV}$. At higher energies, CC interactions on ^{12}C dominate. Among all CC topologies, the CC1p0n channel best preserves the monoenergetic signature, since the neutrino energy is shared between a charged lepton and a knocked-out proton, both of which promptly deposit their energy in the LS. NC events, in contrast, primarily deposit energy through hadrons and lose significant energy to the outgoing neutrino. They do not preserve monoenergetic signatures and contribute mainly as background. Particularly NC topologies with neutrons that can mimic IBD events pose a challenging background in the MeV range. Finally, a global parametrization of the energy resolution from 12 MeV to 10 GeV completes the detector response model, enabling the translation from simulated E_{Qdep} to expected E_{vis} distributions. These results are reflected in the signal modeling in Chap. 6 and the background estimation in Chap. 7.

6 | Neutrino Signature from DM Annihilation in JUNO

There are shortcuts to happiness, and dancing is one of them.
– Vicki Baum

The previous chapter established how neutrino energy E_ν translates into visible energy E_{vis} in JUNO. Building on these results, this chapter analyzes the expected visible energy spectrum for a monoenergetic neutrino source $E_\nu = m_\chi$ from DM self-annihilation. The sensitivity of JUNO to such a signal depends not only on the total number of expected events but also on how well the resulting spectral signature can be distinguished from the background. Sec. 6.1 calculates the expected event rates from DM annihilation, explicitly separating IBD, CC, and NC contributions. Sec. 6.2 applies the detector response established in Chap. 5 to determine how the monoenergetic neutrino energy is mapped onto the visible energy spectrum for different DM masses, ranging from the MeV to the GeV regime.

6.1 Expected Event Number from DM Annihilation

The expected number of neutrino events in JUNO from a source with a differential flux $\mathrm{d}\Phi_\nu/\,\mathrm{d}E_\nu$ is calculated for a given interaction channel (ch) according to

$$\frac{\mathrm{d}N_{\text{ch}}}{\mathrm{d}E_\nu}(E_\nu) = \frac{\mathrm{d}\Phi_\nu(E_\nu)}{\mathrm{d}E_\nu} \cdot \sigma_{\text{ch}}(E_\nu) \cdot N_{\text{target}} \cdot t \cdot \varepsilon \ . \tag{6.1}$$

The neutrino flux from DM self-annihilation $\mathrm{d}\Phi_\nu^\chi/\,\mathrm{d}E_\nu$ was discussed in detail in Sec. 3.1, where, to avoid the large uncertainties associated with different DM distribution models, a canonical value of $J_{\text{avg}} = 3$ for s-wave annihilation was assumed. Consequently, the neutrino flux only scales with the thermally averaged self-annihilation cross section $\langle\sigma_{\text{A}} v\rangle$. In order to reach sufficient statistics, the time of data taking was set to $t = 10\,\text{yr}$ for this analysis. The factor ε covers all relevant detection efficiencies and was set to one in this chapter. The final efficiencies for each channel are discussed in more detail in Chap. 8 and 9. The other factors in Eq. 6.1 account for the interaction probability of the respective interaction. Depending on the channel (ch), the cross-section $\sigma_{\text{ch}}(E_\nu)$ of CC and NC interactions, as well as all participating target nuclei N_{target}, must be considered (cf. Tab. 5.1). In the MeV range, the IBD channel is dominant with a well-known interaction cross section $\sigma_{\text{IBD}}(E_{\bar{\nu}_e})$ (cf. green line in Fig. 5.8). Thus, the number of expected IBD events can be calculated with the number N_p of hydrogen ^{1}H (free protons p) according to

$$\frac{\mathrm{d}N_{\text{IBD}}^\chi}{\mathrm{d}E_{\bar{\nu}_e}}(E_{\bar{\nu}_e}) = \frac{\mathrm{d}\Phi_{\bar{\nu}_e}^\chi}{\mathrm{d}E_{\bar{\nu}_e}} \cdot \sigma_{\text{IBD}}(E_{\bar{\nu}_e}) \cdot N_p \cdot t \ .$$

In the sub-GeV region, all CC and NC interactions need to be taken into account. To calculate the number of expected events, all relevant interactions on ^{1}H (p) and ^{12}C are considered. For CC interactions, the number of expected events for the neutrino flavors $\nu_\ell \in \{\nu_e, \bar{\nu}_e, \nu_\mu, \bar{\nu}_\mu\}$ is calculated by GENIE according to

$$\frac{\mathrm{d}N^{\chi}_{\mathrm{CC}}}{\mathrm{d}E_\nu}(E_\nu) = \sum \frac{\mathrm{d}\Phi^{\chi}_{\nu_\ell}}{\mathrm{d}E_{\nu_\ell}} \cdot x_{\mathrm{CC},\nu_\ell} \cdot t \quad \text{with}$$

$$x_{\mathrm{CC},\nu_\ell} = \sigma^{p}_{\mathrm{CC},\nu_\ell}(E_{\nu_\ell}) \cdot N_p + \sigma^{^{12}\mathrm{C}}_{\mathrm{CC},\nu_\ell}(E_{\nu_\ell}) \cdot N_{^{12}\mathrm{C}}$$

where $\sigma_{\mathrm{CC},\nu_\ell}$ includes all relevant CC interactions (QES, MEC, RES, DIS and COH) on ^{1}H and ^{12}C. The calculation of the expected NC events by GENIE is performed analogously, but here the neutrino flavors ν_τ and $\bar{\nu}_\tau$ are also considered for the total number of events.

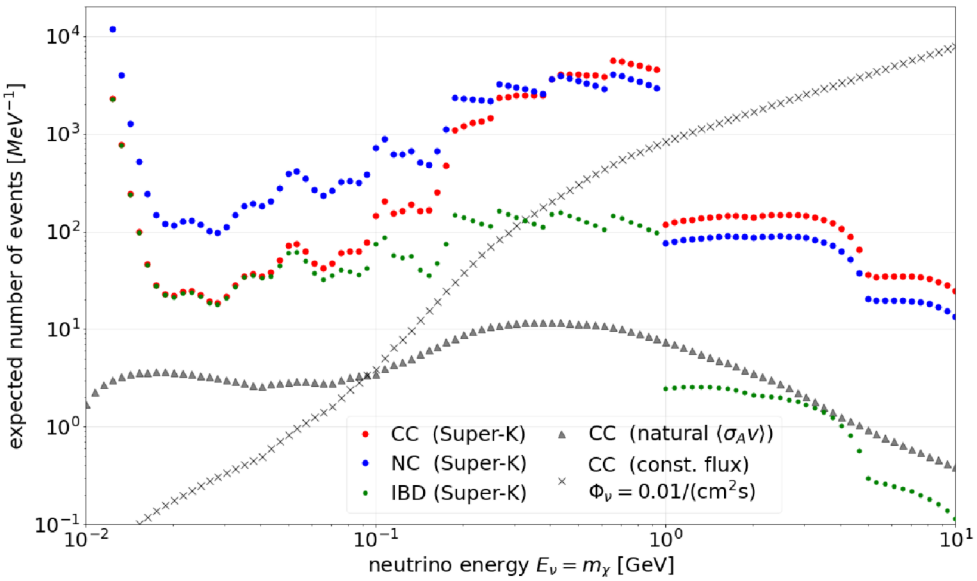

Figure 6.1: Expected event number of neutrinos originating from DM self-annihilation in the Milky Way after 10 yr and a fiducial volume of 20 ktons in JUNO. The individual contributions from the IBD (green), the CC (red) and the NC (blue) channel are shown separately. The dots were calculated assuming the best limits on the self-annihilation cross section $\langle\sigma_\mathrm{A} v\rangle_\mathrm{SK}$ set by Super-K (cf. Fig. 3.6), while the gray triangle show the comparison for CC events if the natural annihilation cross section $\langle\sigma_\mathrm{A} v\rangle$ in Fig. 2.5 is assumed. For comparison, the gray crosses indicate the expected number of CC events for a constant neutrino flux of $\Phi_\nu = 0.01\,\mathrm{cm}^{-2}\,\mathrm{s}^{-1}$, corresponding approximately to the flux of a 100 MeV WIMP with natural annihilation cross section. This reference curve isolates the energy dependence for CC events arising purely from the interaction cross sections and target composition in JUNO, independent of DM model assumptions.

In Fig. 6.1, the number of expected neutrino events from DM annihilation for different DM masses in the Milky Way after $t = 10\,\mathrm{yr}$ data taking in JUNO is presented. For an optimistic estimate of the event number, the upper limit on the thermally averaged self-annihilation cross section $\langle\sigma_\mathrm{A} v\rangle_\mathrm{SK}$ set by Super-K can be used (cf. Fig. 3.6). The colored dots show the number of events for the CC (red), the NC (blue) and the IBD channel (green) under this assumption. For a conservative estimate on the opposite, the

thermally averaged self-annihilation cross section $\langle \sigma_A v \rangle$ derived from observations of the natural relic density, as discussed in Fig. 2.5, can be applied. For comparison, the expected number of CC events in this scenario is added as black triangles. As expected, in the MeV range, the IBD channel is the dominant CC interaction. Since for energies above 105.7 MeV, the CC interactions of ν_μ and $\bar{\nu}_\mu$ contribute, and in addition, the interaction probabilities on ^{12}C become dominant (cf. 5.3), the CC channel promises significantly more events in the sub-GeV region compared to only considering the IBD channel. However, since CC events lack the characteristic prompt-delayed coincidence signature that makes IBD events effective for background suppression, the increased event rate comes with higher background contamination. It is therefore important to determine in the overlap region where an IBD-based analysis should be replaced by a CC-based approach to obtain the best sensitivity to DM annihilation signals in JUNO, which is a central goal of this work. To isolate the energy-dependent detector response, Fig. 6.1 also shows the expected number of CC events for a constant neutrino flux of $\Phi_\nu = 0.01\,\mathrm{cm}^{-2}\mathrm{s}^{-1}$ (gray crosses), corresponding to the flux expected for a $m_\chi \approx 100\,\mathrm{MeV}$ WIMP with a natural annihilation cross section. Since this reference curve assumes an energy-independent flux, it highlights the contribution to the CC event rate arising solely from the energy dependence of the interaction cross sections and the target composition in JUNO. The comparison demonstrates that the structure seen in the colored curves originates from the DM model-dependent neutrino flux.
The number of NC events (blue points in Fig. 6.1) is approximately comparable to the number of CC events in the sub-GeV and GeV regimes. In the MeV range, however, the number of NC events is significantly larger than that of CC interactions, since all neutrino flavors contribute to NC processes, whereas CC interactions are mainly limited to $\bar{\nu}_e$ (IBD channel). However, due to the escaping neutrino and the strong quenching of NC events, a large fraction falls below the analysis threshold of $E_{\mathrm{vis}} = 12\,\mathrm{MeV}$ and therefore does not contribute to the signal region (cf. Sec. 5.2.2).

6.2 Expected Spectral Shape of DM Neutrinos

While Sec. 6.1 quantified the total number of expected events, the sensitivity to a DM signal depends critically on how these events translate in visible energy. A sharp spectral feature is easier to distinguish from the continuous atmospheric neutrino background than a broad distribution. In the following, the visible energy spectra for six representative DM masses in the MeV, sub-GeV, and GeV regimes are presented, based on full JUNO detector simulations that include all relevant interaction channels and the energy resolution derived in Sec. 5.3. The analysis reveals how the initially monoenergetic neutrino line at $E_\nu = m_\chi$ is transformed into characteristic spectral shapes that vary across the three energy regimes.
Fig. 6.2 shows the resulting visible energy spectra for six DM masses (cf. dataset $D5$ in Tab. C.1). The upper subplots represent the MeV range with $m_\chi = 50\,\mathrm{MeV}$ and $m_\chi = 80\,\mathrm{MeV}$, which is discussed in Sec. 6.2.1. The middle subplots illustrate the expected signals for sub-GeV DM masses $m_\chi = 300\,\mathrm{MeV}$ and $m_\chi = 500\,\mathrm{MeV}$ (cf. Sec. 6.2.2), while the two lower subplots with $m_\chi = 2\,\mathrm{GeV}$ and $m_\chi = 5\,\mathrm{GeV}$ represent signals from DM annihilations in the GeV range (cf. Sec. 6.2.3). The original neutrino energy $E_\nu = m_\chi$ is indicated by a vertical black dotted line in each subplot. The black curve represents the total number of events, while the individual contributions from CC (red), NC (blue), and IBD interactions (green hatched) are shown separately. The event numbers in parentheses correspond to events above the analysis threshold

of $E_{\mathrm{vis}} \geq 12\,\mathrm{MeV}$. The spectra are generated assuming 10 yr of data taking, a fiducial volume of 20 kton, the current best limits on $\langle \sigma_{\mathrm{A}} v \rangle$ from Super-K, and the canonical value $J_{\mathrm{avg}} = 3$. All CC and NC interactions are simulated with GENIE, including de-excitation processes modeled by the TALYS database (cf. Sec. 4.4). For each neutrino flavor, more than 10,000 CC and NC events were isotropically generated within the detector volume, followed by full Geant4 detector propagation of all final state particles. The quenched deposited energy E_{Qdep} was smeared according to the energy resolution parametrization in Eq. 5.12 to derive the final visible energy spectrum E_{vis}.

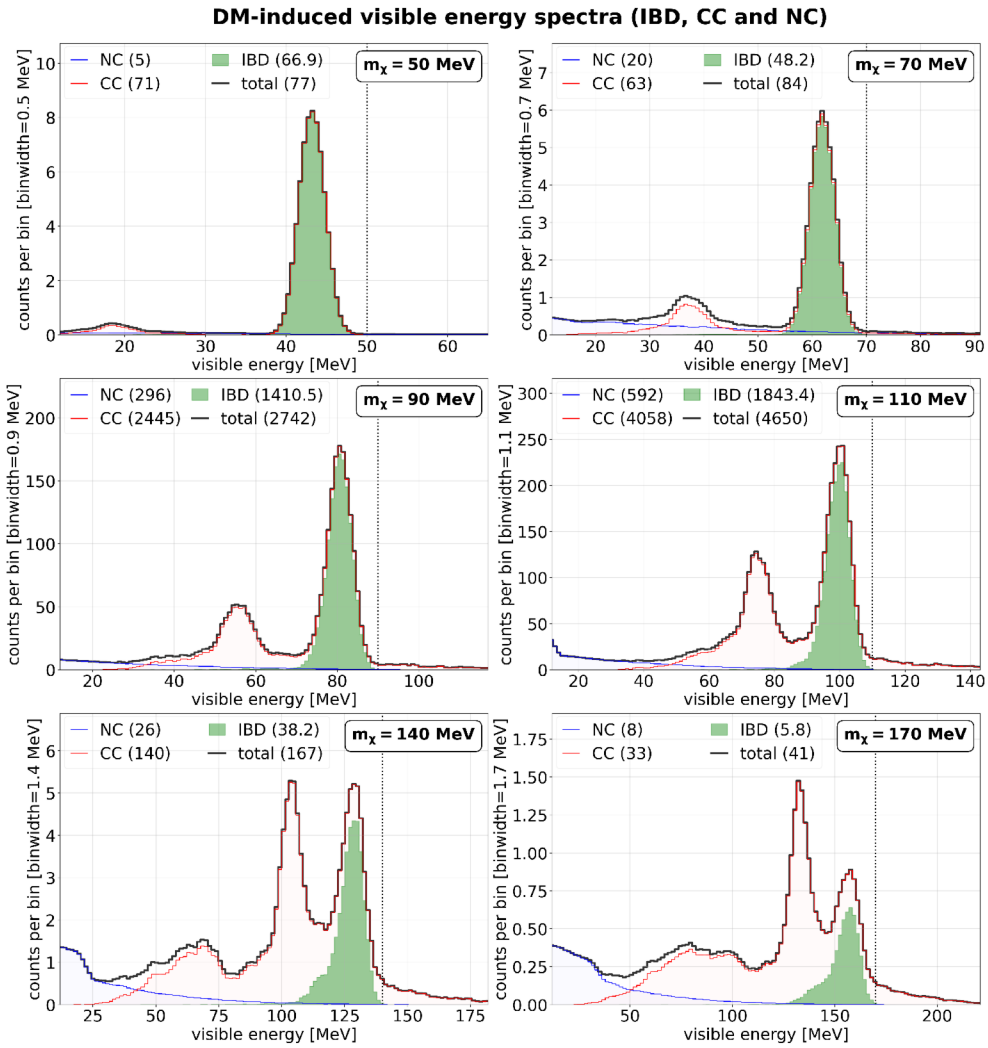

Figure 6.2: Expected visible energy spectra for a monoenergetic neutrino signal with $E_\nu = m_\chi$ from DM annihilation in the Milky Way, assuming 10 yr of data taking and a fiducial volume of 20 kton in JUNO. The spectra are shown for DM masses in the MeV range (upper panels), the sub-GeV range (middle panels), and the GeV regime (lower panels). The vertical dotted line indicates the original neutrino energy $E_\nu = m_\chi$. The individual contributions from NC (blue), CC (red), and IBD (green hatched) interactions are shown separately, and the black curve shows the total events. The numbers in parentheses denote the number of events for each channel above the analysis threshold of $E_{\mathrm{vis}} \geq 12\,\mathrm{MeV}$.

6.2.1 Neutrinos from MeV DM Annihilation

In the MeV region, the expected measured DM spectrum is dominated by the IBD kinematics, as can be deduced from the green hatched contributions in the upper subplots of Fig. 6.2. As discussed in Sec. 5.2.1, in IBD interactions, the neutrino energy is split between the positron and the neutron. However, due to the mass ratios, the majority of the neutrino energy is transferred to the positron, which deposits the energy as the prompt signal in the detector. As a result, the monoenergetic nature of the IBD signal is relatively well preserved. In addition to the IBD channel, there are also contributions from other CC interactions (red curve in the upper panel of Fig. 6.2), which are mainly due to QES interactions of ν_e on ^{12}C according to interaction (1) in Tab. 5.2. Due to the Q-value of this interaction in Eq. 5.7, the red peak is shifted with respect to the neutrino energy $E_\nu = m_\chi$. According to Fig. 6.1, many NC events are expected in the MeV region as well; however, since the visible energy of NC events is shifted to smaller energies, most NC events will produce signals outside the energy window of $E_{\text{vis}} \geq 12\,\text{MeV}$. The

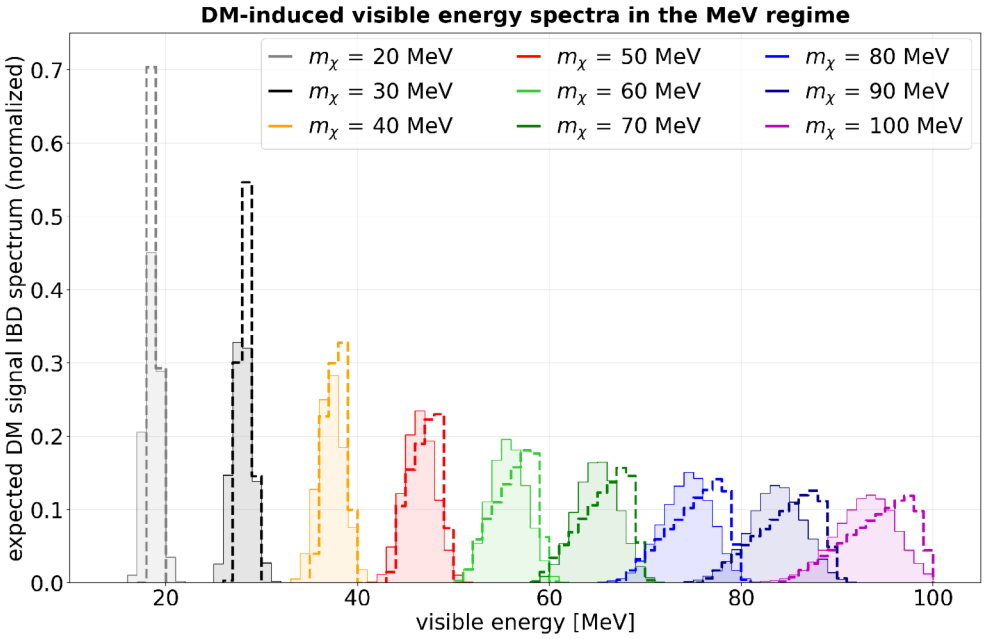

Figure 6.3: Normalized IBD signal spectra for neutrinos from DM annihilation of different DM masses in the MeV regime. Dashed: results from a previous study [7] using positron energy only and the parametric energy resolution in Eq. 5.11. Filled: full detector simulation of this work (cf. dataset $D5$ in Tab. C.1) including neutron thermalization and the parametrized energy resolution (cf. Fig. 5.9).

expected neutrino signal from MeV DM annihilation has already been discussed in detail in [7, 8]. In these studies, the visible energy spectrum was modeled using IBD kinematics and the parametric energy resolution in Eq. 5.11, assuming E_{vis} exclusively based on the positron energy. This approach neglects the energy deposited by the neutron during its thermalization through elastic scattering on protons in the LS. In Fig. 6.3, the normalized spectra from [7] (dashed lines) are compared to the results of this work (filled histograms), which are based on a full detector simulation, and consider the energy resolution parametrized in Eq. 5.12. The spectra from this work exhibit a systematic shift toward lower visible energies. This shift arises because the recoil protons produced during neutron thermalization are strongly quenched.

6.2.2 Neutrinos from sub-GeV DM Annihilation

As illustrated in Fig. 6.1, IBD interactions become subdominant in the sub-GeV regime, which is also reflected in the middle subplots of Fig. 6.2. Instead, the CC contribution exhibits a characteristic spectral shape, while the NC events contribute in the lower energy range. In order to understand the shape of the CC signal, Fig. 6.4 shows, as an

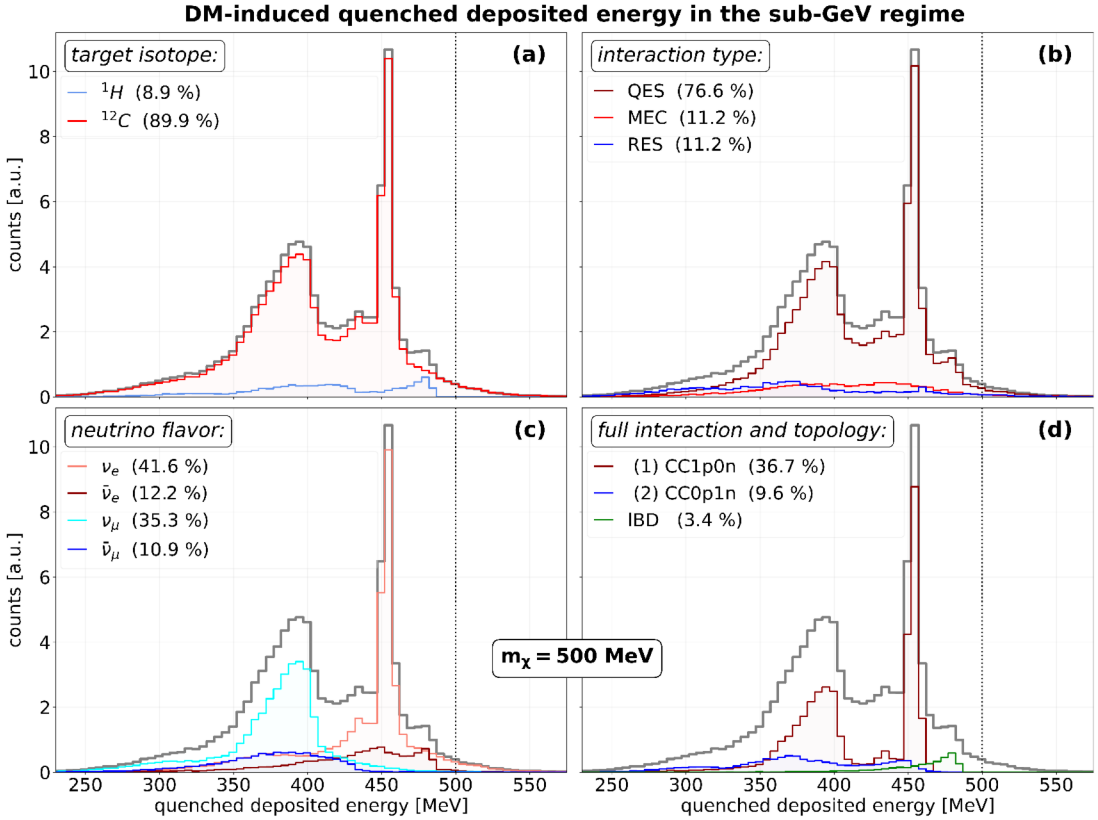

Figure 6.4: Quenched deposited energy spectrum considering all CC interactions of a monoenergetic neutrino signal with $E_\nu = 500\,\text{MeV}$. Unlike Fig. 6.2 the energy resolution of JUNO was not considered for this spectrum. The four subplots show the contribution of different targets (a), interaction types (b), neutrino flavors (c) and full interaction (d) to the signal.

example, the quenched deposited energy of all CC events for a monoenergetic neutrino signal with $E_\nu = 500\,\text{MeV}$ at the `DetSim` level of the JUNO simulation (cf. dataset $D5$ in Tab. C.1). For this figure, the energy resolution in JUNO was not taken into account, so the actual quenched deposited energy E_{Qdep} can be discussed. For this reason, the spectral shape differs from that in Fig. 6.2 (center right), where the energy resolution is included. The bin width in both figures is 5 MeV. Subplot (a) shows the interactions with different target isotopes. As expected, CC interactions on ^{12}C (red) dominate, while those on ^{1}H (blue) occur much less frequently, with only $\sim 9\,\%$. Subplot (b) illustrates the contributions from different interaction types. In the sub-GeV region, QES events (purple) dominate with $\sim 77\,\%$, while RES and MEC contributions are more evenly distributed across the spectrum, each with about $\sim 11\,\%$. Subplot (c) shows the contributions of different neutrino flavors. Since CC cross sections for neutrinos in this energy range are significantly larger than for antineutrinos, ν_e and ν_μ events dominate the signal (cf. Fig. 5.3). The characteristic peaks can be attributed to these

two flavors, whereas the antineutrinos $\bar{\nu}_e$ and $\bar{\nu}_\mu$ contribute more smoothly distributed components. As the neutrino energy is not sufficient to produce charged $\tau^\pm$ leptons, ν_τ and $\bar{\nu}_\tau$ do not contribute. To understand the structure of the quenched deposited energy in detail, subplot (d) shows the most relevant interactions listed in Tab. 5.2 (cf. Fig. 5.7). Interaction (1) provides the largest contribution with $\sim 37\,\%$ (red curve) and, due to the CC1p0n topology, shapes the characteristic peak structure.
The narrow peak at $\sim 455\,\mathrm{MeV}$ originates from interaction (1) with ν_e and is produced by the prompt energy deposition of the electron e^- and the proton p. Its position is shifted with respect to the neutrino energy $E_\nu = 500\,\mathrm{MeV}$ by the Q-value of the reaction $Q_{(1)}(\nu_e) \approx 18\,\mathrm{MeV}$ (cf. Eq. 5.7), as well as by the quenching of the proton. The second characteristic region between 350 MeV and 405 MeV arises from ν_μ events of interaction (1), which exhibit a significantly larger shift of the deposited energy with respect to the neutrino energy E_ν due to $Q_{(1)}(\nu_\mu) \approx 123\,\mathrm{MeV}$ (cf. Eq. 5.8). However, because of muon decay, part of the muon mass still contributes to the visible spectrum in the form of a characteristic Michel electron spectrum, such that the endpoint of this second peak starts at $\sim E_{\nu_\mu} - Q_{(1)}(\nu_\mu) + m_\mu/2$ (without quenching) [117]. Since, in muon decay, part of the energy is carried away by neutrinos escaping the detector, the monoenergetic structure present in the first peak of interaction (1) with ν_e is reduced.
Contributions from interaction (2) in Tab. 5.2 are shown in Fig. 6.4 (d) as the blue curve. Due to the CC0p1n topology, no monoenergetic structure is visible for this interaction, since the energy is shared between the charged lepton e/μ^+ and the neutron, which is hardly visible in the prompt signal but produces a delayed event during the neutron capture. This topology corresponds to that of the IBD reactions (green curve), which also contribute with $\sim 3.4\,\%$. In contrast to the CC1p0n topology, IBD yields a narrow energy maximum close to the neutrino energy, with only small shifts. However, since its contribution remains below $4\,\%$ in the sub-GeV region, the overall CC channel is more dominant and thus more promising for the signal. Due to the finite energy resolution of the JUNO detector (cf. Sec. 5.3), the characteristic ν_e CC1p0n peak is smeared, resulting in two peaks of approximately the same height for $m_\chi = 500\,\mathrm{MeV}$, as shown in the middle right subplot in Fig. 6.2.
In summary, the CC channel in the sub-GeV regime offers significant potential for DM searches due to the characteristic double-peak structure arising from the CC1p0n topology. The distinct peaks from ν_e and ν_μ QES interactions on ^{12}C provide a spectral signature that can be distinguished from the continuous atmospheric neutrino background. This sensitivity can be further enhanced if ν_μ and ν_e flavor events can be separated experimentally. Recent studies have demonstrated that such flavor identification is achievable in JUNO using ML-based pulse shape analysis, making use of the different event topologies of electron showers and muon tracks in the LS [126]. In addition, a topological restriction of events that do not produce delayed signals from muon decays or n-captures could be used to extract the ν_e-induced CC1p0n signature, while simultaneously reducing the background by excluding all other topologies. Both, the flavor-based selection and a topology-based method are presented in more detail in Chap. 9.

6.2.3 Neutrinos from GeV DM Annihilation

NC and CC interactions of neutrinos with energies in the GeV range produce significantly more complex final states, leading to the disappearance of the double-peak structure in the visible energy spectrum that is observed in the sub-GeV region (cf. Fig. 6.2). Figure 6.5 shows, as an example, the quenched deposited energy of the CC events for

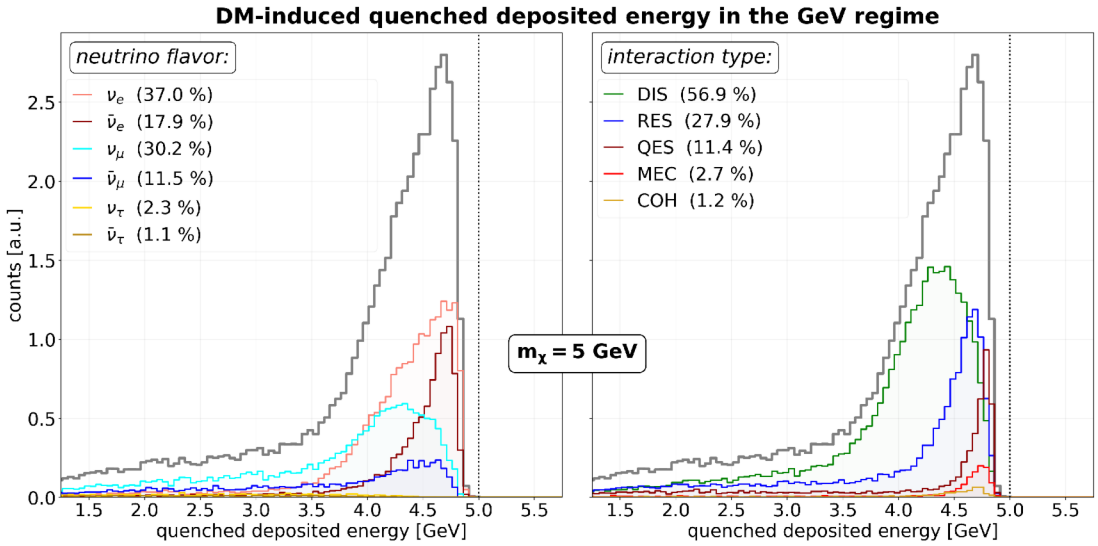

Figure 6.5: Quenched deposited energy spectrum for CC events of a monoenergetic neutrino signal with $E_\nu = 5\,\text{GeV}$. Unlike Fig. 6.2 the energy resolution of JUNO was not considered for this spectrum. The two subplots show the contribution of different neutrino flavors (left) and interaction types (right) to the signal.

a monoenergetic neutrino flux with $E_\nu = 5\,\text{GeV}$. The spectrum corresponds to that shown in Fig. 6.2 (lower right subplot) but does not account for the energy resolution in JUNO. The left panel illustrates the contributions of the different neutrino flavors. Since the neutrino energy is sufficient to produce charged tau leptons $\tau^\pm$, contributions from ν_τ and $\bar{\nu}_\tau$ are also included. However, due to their comparatively small cross section (cf. Fig. 5.3), they contribute only a few percent to the total signal. The dominant contributions still arise from ν_e and ν_μ interactions, which together account for more than two thirds of the signal. The right panel of Fig. 6.5 shows different interaction types. Unlike in the sub-GeV region, QES interactions no longer dominate CC interactions. Instead, DIS and RES processes comprise the majority of the interaction types. The final-state particles in these interactions are considerably more complex, as the primary hadron production is significantly stronger. In RES interactions, at least one pion is produced, while in DIS processes, the neutrino interacts directly with quarks (cf. Sec. 5.1.1), resulting in a hadronic jet.

Despite the significantly broader signal distribution compared to the MeV and sub-GeV regimes, the monoenergetic nature of the DM neutrino signal remains a characteristic feature in the GeV range. Since the dominant background from atmospheric neutrinos follows a smooth distribution (cf. Sec. 7.4), the characteristic accumulation of DM neutrino events below the DM mass shown in the lower panels of Fig. 6.2 provides a spectral feature that can be used in the sensitivity analysis. In addition, the reconstructed neutrino direction can be exploited in the GeV regime by applying an energy-dependent cone selection around the GC, since DM-induced neutrinos are expected to originate preferentially from this direction (cf. Sec. 3.2), whereas the background events exhibit an isotropic distribution. The potential of such a direction-dependent selection is investigated in detail in Sec. 9.2.

6.3 Summary of DM Signals and Analysis Strategy

In this chapter, the expected neutrino signature from DM self-annihilation in the Milky Way was derived for JUNO after 10 yr of data taking. Starting from the differential neutrino flux, the expected event rates in JUNO were calculated for all relevant interaction channels, explicitly separating IBD, CC, and NC contributions and including interactions on both ^{1}H and ^{12}C as modeled by GENIE. Using the full JUNO detector simulation, the chapter investigated how an initially monoenergetic neutrino line at $E_\nu = m_\chi$ is mapped onto the visible energy spectrum for different DM masses and energy regimes. The results reveal distinct CC-induced spectral characteristics across three energy regimes that are illustrated in Fig. 6.6 (cf. dataset $D5$ in Tab. C.1). In the MeV range, the IBD kinematics preserve a narrow, nearly monoenergetic peak (dark red $\bar{\nu}_e$), which is mainly defined by the energy deposition of the positron. In the transition region from the IBD- to the CC-dominated regime between $m_\chi \simeq 100\,\text{MeV}$ and $m_\chi \simeq 200\,\text{MeV}$, the IBD peak (dark red) is continuously replaced by the ν_e-induced CC1p0n peak (light red), such that the spectral features in this region are dominated mainly by $\nu_e/\bar{\nu}_e$ contributions. In the sub-GeV region for $m_\chi > 200\,\text{MeV}$, CC interactions give rise to the characteristic double-peak structure driven by CC1p0n topologies of ν_e (light red) and ν_μ (light blue), whereas IBD becomes subdominant. In the GeV regime, increasingly complex CC and NC final states from RES and DIS processes broaden the spectrum and wash out distinct spectral features. Based on these spectral characteristics, three separate Bayesian analyses are performed in this work, using the advantages of the respective interaction channels:

- **MeV regime ($m_\chi = 12 - 300\,\text{MeV}$):** The analysis is based on the IBD channel, exploiting its characteristic prompt-delayed coincidence signature for efficient background suppression. Additional pulse shape discrimination (PSD) techniques are applied to further optimize the signal-to-background (S2B) ratio (cf. Chap. 8). Compared to previous analyses [7, 8], the IBD-based analysis is extended from 100 MeV up to 300 MeV to cover the transition region from an IBD- to a CC-dominated DM-induced signal.
- **Sub-GeV regime ($m_\chi = 0.1 - 1\,\text{GeV}$):** The analysis uses the CC channel, which dominates this energy range. A flavor identification technique based on ML methods can be employed to separate ν_e and $\bar{\nu}_e$ contributions and optimize the S2B ratio specifically in the transition region from an IBD- to a CC-dominated signal. In addition, a topology-based selection strategy is investigated with the goal to enhance the ν_e and ν_μ-induced CC1p0n double-peak structure, which is characterized by a zero-neutron event topology (cf. Sec. 9.1).
- **GeV regime ($m_\chi = 1 - 10\,\text{GeV}$):** The analysis relies on the CC channel with a direction-dependent approach. Since DM annihilation in the galactic halo produces an enhanced neutrino flux from the direction of the GC (cf. Fig. 3.3), directional reconstruction of DM-induced events can be used to reduce the isotropic atmospheric neutrino background and improve sensitivity (cf. Sec. 9.2).

The optimization of these analysis strategies requires a comprehensive understanding of all relevant background contributions. In the following chapter, the individual background sources are discussed in detail, and the final expected visible energy spectrum in JUNO is derived.

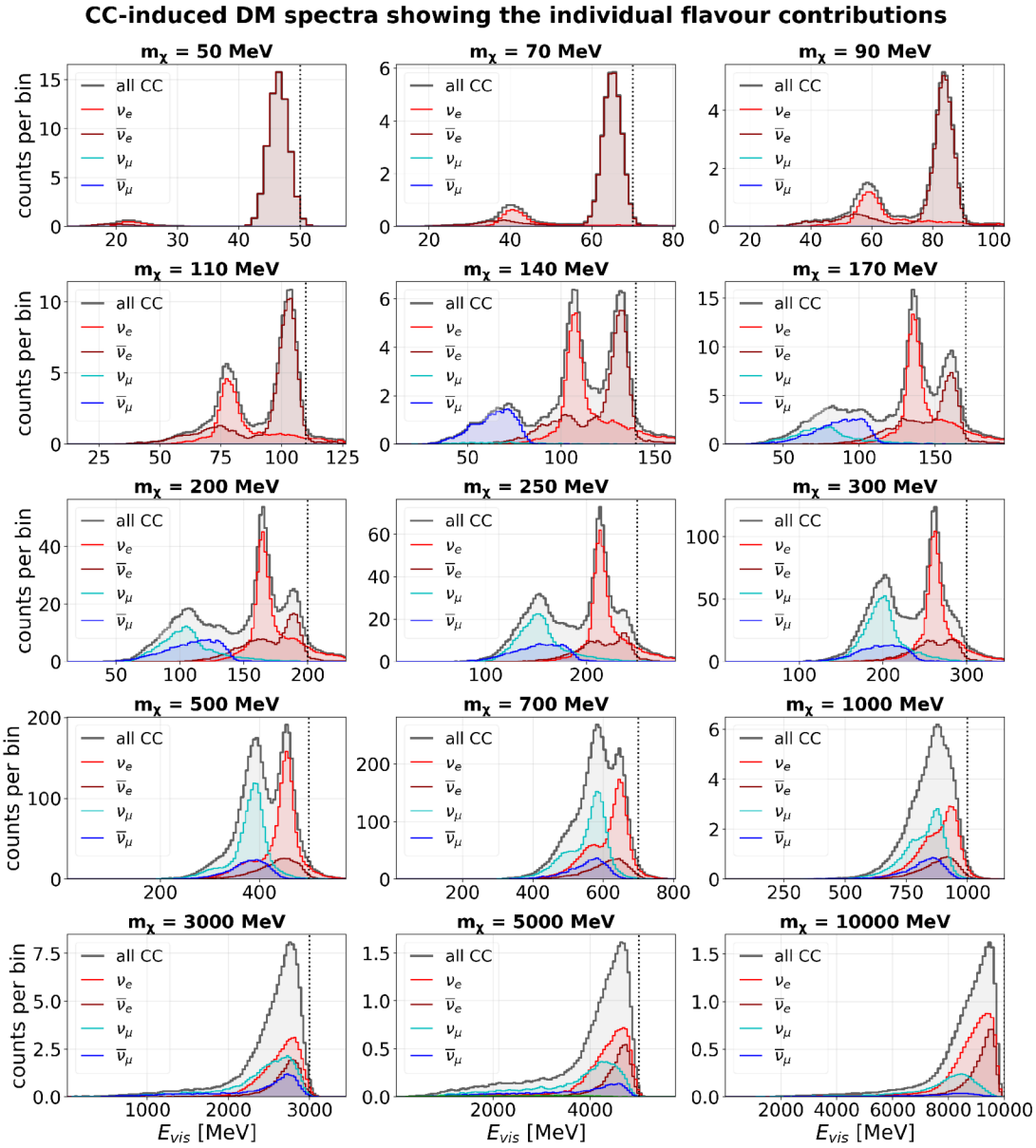

Figure 6.6: CC-induced DM signal spectra in JUNO, showing the flavor composition of the energy-smeared visible energy distribution for selected DM masses $m_\chi = 50\,\text{MeV}$ to $m_\chi = 10\,\text{GeV}$. The black histogram denotes the total CC contribution, while the vertical dotted line marks $E_\nu = m_\chi$ in each panel.

7 | Background Contributions in JUNO

Dance is the hidden language of the soul, of the body.
– Martha Graham

In Chap. 6, the expected visible energy spectrum of a DM-induced neutrino signal was analyzed. For a comprehensive sensitivity analysis, all background contributions must also be taken into account. In this chapter, the individual background contributions are discussed, and the final expected visible energy spectrum in JUNO is presented.

7.1 Low Energy Background

At low energies, several background sources contribute to the expected event rate in JUNO. Understanding these contributions is essential to define an appropriate energy threshold for the indirect DM search. The dominant contribution of this low-energy background arises from reactor antineutrinos, which are used as the primary signal for the NMO analysis. As shown in Fig. 4.3, the reactor antineutrino flux extends up to $\sim 12\,\mathrm{MeV}$, producing a large number of IBD events that would overwhelm any potential DM signal in this energy range. Events from natural radioactivity also contribute at low energies. JUNO employs a sophisticated purification system as part of a strict radioactivity control strategy to reduce the contamination of radioactive isotopes such as ^{238}U, ^{232}Th, ^{40}K, and ^{222}Rn in the LS [127]. Nevertheless, residual contaminations in the acrylic sphere or the PMTs give rise to single events. However, since these events with deposited energies mostly below 6 MeV are predominantly located near the detector edge, they can be effectively suppressed by applying a fiducial volume cut.
Additional contributions arise from geo-neutrinos and solar neutrinos. While geo-neutrinos have a maximum energy of $\sim 3.3\,\mathrm{MeV}$ (cf. Fig. 4.4), solar neutrinos from the ^{8}B decay reach energies up to 18 MeV [128]. However, since the sun does not produce antineutrinos, solar neutrinos do not constitute a background for the IBD channel. The situation is different for cosmogenic isotopes, which are produced by muon-induced spallation on ^{12}C nuclei. In particular, ^{9}Li and ^{8}He represent a significant background for the IBD channel, as their β-decays are often accompanied by the emission of a neutron and can thus mimic an IBD signal [129]. The endpoint energies of the β decays are $Q(^{9}\mathrm{Li}) = 13.6\,\mathrm{MeV}$ and $Q(^{8}\mathrm{He}) = 10.7\,\mathrm{MeV}$, respectively [118].
Based on these considerations, a lower energy threshold of $E_{\mathrm{vis}} \geq 12\,\mathrm{MeV}$ is adopted for the sensitivity analysis presented in this work, following the approach of the DSNB study in [4, 98] and previous DM studies [7, 8]. This choice ensures that the reactor antineutrino background becomes negligible, while simultaneously suppressing the contributions from natural radioactivity, geo-neutrinos, and the dominant fraction of cosmogenic isotope decays.

7.2 Fast Neutrons

Fast neutrons (FNs) are mainly produced by muon-induced spallation in the surrounding rock and water and represent a critical background for the IBD channel, as they can produce a prompt proton recoil signal followed by a delayed neutron capture signal. The flux of muon-induced FNs follows a falling spectrum, which can be described by an approximate power law of $E^{-0.5}$ in the range $\sim 10 - 100\,\mathrm{MeV}$ and E^{-2} at higher energies [130, 131]. Despite JUNO's muon veto system, which includes the water Cherenkov detector and the top tracker, this process can mimic a genuine IBD event. An efficient suppression can be achieved by applying a fiducial volume cut, considering only events inside a radius of $R \leq 16\,\mathrm{m}$ from the center of the CD. With this cut, the fiducial volume is reduced to $V = 14.77\,\mathrm{kton}$, leading to a volume cut efficiency of $\varepsilon_V = 0.739$. However, with this cut, the FN rate is reduced to $\sim 7.1\,\%$ [7, 8], and by applying pulse shape discrimination (PSD) techniques (cf. Sec. 8.3), the FNs background can be further reduced to $2\,\%$ of the remaining events after the fiducial volume cut [8]. With these methods, 0.6 ± 0.1 events are expected after $10\,\mathrm{yr}$ of data taking [7], making FNs a negligible background for this analysis.

7.3 Diffuse Supernova Neutrino Background

Since the beginning of the universe, massive stars have continuously formed and ended their lives as type II Core Collapse Supernova (CCSN). In each of these explosions, approximately $99\,\%$ of the total released energy is emitted in the form of around 10^{57} neutrinos of all flavors [98]. The overall neutrino emission from all past CCSNs throughout cosmic history is expected to result in an isotropic and nearly constant flux observed today, known as the Diffuse Supernova Neutrino Background (DSNB). Although this background has not yet been detected, the differential neutrino flux

$$\frac{\mathrm{d}\Phi^{\mathrm{DSNB}}(E_\nu)}{\mathrm{d}E_\nu} = \int_0^\infty R_{\mathrm{SN}}(z) \cdot \frac{\mathrm{d}N(E'_\nu)}{\mathrm{d}E'_\nu} \cdot \frac{\mathrm{d}E'_\nu}{\mathrm{d}E_\nu} \cdot \left| \frac{c\,\mathrm{d}t}{\mathrm{d}z} \right| \mathrm{d}z$$

can be calculated by integrating over all past CCSNs in the visible universe, taking into account the evolution of the universe. The supernova (SN) rate $R_{SN}(z)$ depends on the star formation rate and considers the fraction of those stars with masses larger than $8\,\mathrm{M}_\odot$, which will end up in CCSN explosions. The redshift-dependent parametrization of the star formation rate is taken from [98].
To determine the average differential neutrino spectrum $\mathrm{d}N(E'_\nu)/\,\mathrm{d}E'_\nu$ of an individual SN, the fraction f_{BH} of so-called failed SNs, which directly collapse into a Black Hole (BH), must be taken into account. Since the neutrino spectrum of failed SNs differs from that of CCSNs, the averaged neutrino spectrum is given by

$$\frac{\mathrm{d}N(E'_\nu)}{\mathrm{d}E'_\nu} = (1 - f_{BH}) \frac{\mathrm{d}N_{CCSN}(E'_\nu)}{\mathrm{d}E'_\nu} + f_{BH} \frac{\mathrm{d}N_{BH}(E'_\nu)}{\mathrm{d}E'_\nu} \ . \tag{7.1}$$

The relationship between the emitted neutrino energy E'_ν and the neutrino energy detected today E_ν depends on the redshift z and is given by $\mathrm{d}E'_\nu/\,\mathrm{d}E_\nu = (1+z)$ and the connection between cosmic time t and redshift z is determined by the Friedmann equation [98]. Large uncertainties in the calculation of the DSNB flux arise from the limited knowledge of several astrophysical inputs. These include the present-day supernova rate $R_{\mathrm{SN}}(0)$, which is uncertain by at least a factor of two [98], the redshift

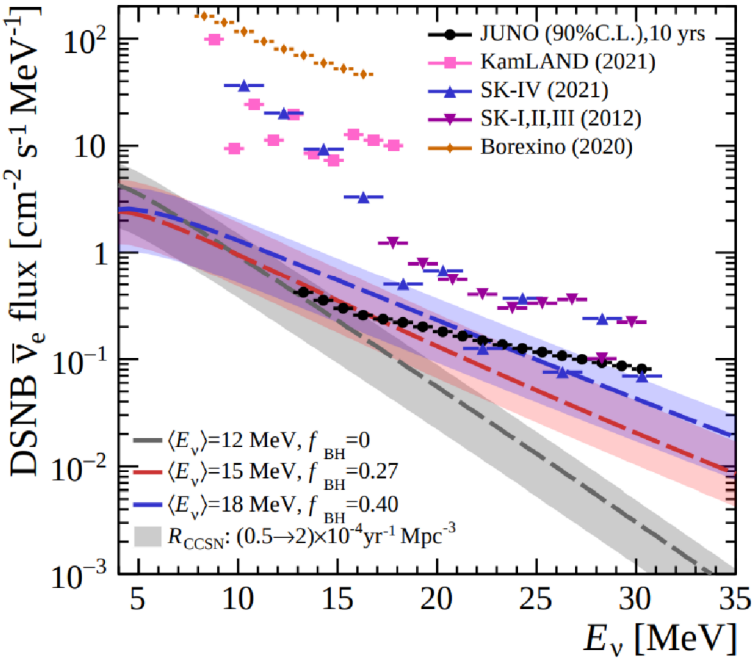

Figure 7.1: Expected DSNB $\bar{\nu}_e$ flux. The gray, red and blue dashed lines indicate the DSNB flux predictions for different model parameters, while the colored hatched area indicate the present supernova rate $R_{\mathrm{SN}}(z = 0)$ ranging from 0.5 to 2 $\times$ $10^{-4}\,\mathrm{yr}^{-1}\mathrm{Mpc}^{-3}$. The currently existing DSNB flux limits from Super-K, KamLAND and Borexino are included in the plot as well as the estimated 90 % confidence level upper limit in JUNO from 12 to 30 MeV after 10 yr of data taking. Taken from [98].

dependence of the star formation history, and the average neutrino spectra of both successful and failed SNs (cf. Eq.7.1). In particular, the fraction of failed supernovae f_{BH} and the average emitted neutrino energy $\langle E'_\nu \rangle$ have a significant impact on the spectral shape of the predicted flux. As discussed in [98], variations of these parameters cause a broad spread in the DSNB spectra, leading to differences of more than an order of magnitude in the predictions at energies above $\sim$25 MeV, as shown in Fig. 7.1. The expected visible DSNB spectrum is modeled with the JUNO simulation framework (cf. dataset *D*3 in Tab. C.1). Since the IBD channel is dominant for these energies, the number of expected events can be calculated according to[1]

$$\frac{\mathrm{d}N^{\mathrm{DSNB}}_{\mathrm{IBD}}}{\mathrm{d}E_{\bar{\nu}_e}}(E_{\bar{\nu}_e}) = \frac{\mathrm{d}\Phi^{\mathrm{DSNB}}_{\bar{\nu}_e}}{\mathrm{d}E_{\bar{\nu}_e}} \cdot \sigma_{\mathrm{IBD}}(E_{\bar{\nu}_e}) \cdot N_p \cdot t \cdot \varepsilon \ .$$

For the sensitivity study presented in this work, the three DSNB flux predictions (min, mid and max) from [98] are adopted, which are displayed in Fig. 7.1. This choice ensures that the DSNB background is modeled comprehensively, covering its large systematic uncertainties as realistically as possible. Whenever the DSNB contribution is referred to without further specification, the maximum-flux scenario (blue curve) is implied.

[1] The efficiency ε is set to 1 in this section.

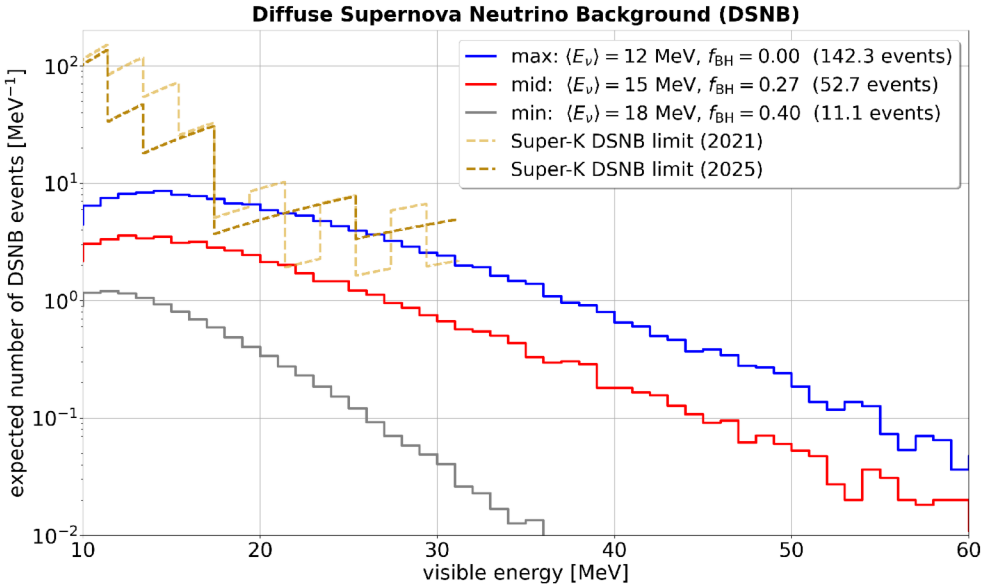

Figure 7.2: Expected visible energy spectrum of the DSNB background after 10 yr of data taking and a fiducial volume of 20 kton in JUNO (cf. dataset *D*3 in Tab. C.1). Three theoretical predictions are considered (cf. Fig. 7.1) and the latest upper limits from Super-K are added for comparison [132, 133].

7.4 Atmospheric Neutrino Background

Atmospheric neutrinos represent the dominant background for the indirect DM search in JUNO across the entire visible energy range from 12 MeV to 10 GeV. As discussed in Sec. 4.5.7, they are produced when high-energy cosmic rays interact with atomic nuclei in the Earth's atmosphere. These interactions initiate air showers in which pions and kaons are produced, which subsequently decay, producing a continuous flux of ν_e, $\bar{\nu}_e$, ν_μ, and $\bar{\nu}_\mu$ (cf. Eq. 4.6). In contrast to the monoenergetic neutrino signal expected from DM annihilation, atmospheric neutrinos follow a steeply falling power-law spectrum and interact with the detector material via CC and NC processes, producing a broad distribution of visible energies. Since the atmospheric CC and NC spectra overlap with the DM signals considered in this work, accurate modeling of this background is essential for the sensitivity analysis. This requires a detailed understanding of the initial atmospheric neutrino flux at the production site, the modification of the flavor composition through neutrino oscillations during propagation to the detector, and the translation of neutrino energy into visible energy through the various interaction channels discussed in Chap. 5. In the following subsections, each of these aspects is discussed in detail.

7.4.1 Atmospheric Neutrino Flux

Since there is no single model that covers the entire relevant energy range from a few MeV to the GeV range with equal reliability, the models Honda–Athar–Kajita–Kasahara–Midorikawa (HAKKM14) and FLUKA for the emitted atmospheric neutrino flux are used in this work [134, 135]. To model the atmospheric background, however, the oscillated flux arriving at the JUNO detector must be considered (cf. Sec. 7.4.2).

Honda–Athar–Kajita–Kasahara–Midorikawa (HAKKM14) Model

For energies above $E_\nu \geq 100\,\text{MeV}$, the expected flux is best described by the HAKKM14 model [134]. This model is based on a three-dimensional MC simulation of cosmic showers in the atmosphere. The differential flux per energy and solid angle was explicitly calculated for the location of JUNO and takes into account cosmic primary spectra, hadronic interactions in the atmosphere, as well as the geomagnetic cutoff [136]. Seasonal variations, which arise due to different atmospheric densities, were taken into account by calculating the flux as a one-year average[2].

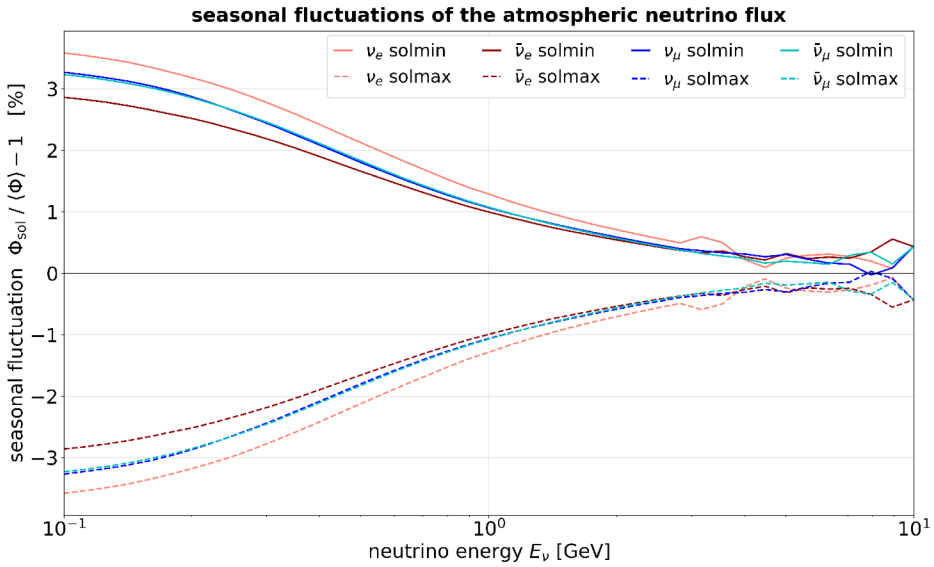

Figure 7.3: Fluctuations of the expected atmospheric neutrino flux at JUNO for minimum (`solmin`) and maximum solar activity (`solmax`). The flux is calculated with the HAKKM14 model for ν_e, $\bar{\nu}_e$, ν_μ, and $\bar{\nu}_\mu$ [134]. The y axis shows the deviations in [%] from the average flux $\langle\Phi\rangle$ in one solar activity cycle of $\sim 11\,\text{yr}$. The expected neutrino flux is larger for `solmin` and the relative fluctuations are larger for smaller neutrino energies. At $E_\nu = 100\,\text{MeV}$ the deviation for the ν flux (light red curve) is at $\sim 7\,\%$ and they become negligible for $E_\nu > 10\,\text{GeV}$.

In addition to seasonal fluctuations, modulations of cosmic radiation also influence the atmospheric neutrino flux. These depend on the current solar activity, which follows an approximately 11-year cycle [137]. Cosmic rays are at their maximum when solar activity is at its minimum (`solmin`), since the heliospheric magnetic field is weak during this phase. At solar maximum (`solmax`), on the other hand, the strong, turbulent magnetic field, together with the solar wind, causes cosmic rays to be deflected and decelerated. As shown in Fig. 7.3, the atmospheric neutrino flux calculated for JUNO at $E_\nu = 100\,\text{MeV}$ fluctuates by $\sim 6 - 7\,\%$ between `solmin` and `solmax` [134]. Since the analyses in this work were performed for 10 yr of data taking, the averaged `solmin`/`solmax` profile can be used as the nominal flux for a solar activity cycle of $\sim 11\,\text{yr}$.

[2]The seasonal variations are not explicitly calculated for JUNO, but were estimated in Fig. B.1 using the flux calculated for Kamioka at a latitude of about $\sim 36°$ [136]. Since the seasonal variations are smallest near the equator and increase toward the poles, the variations expected at JUNO with a latitude of $\sim 22°$ lie below the $< 1.5\,\%$ calculated for Kamioka.

FLUKA Model

In the low-energy region $E_\nu \leq 100\,\text{MeV}$, the atmospheric neutrino flux is no longer reliably described by the HAKKM14 model due to increasing uncertainties from hadron production and complex muon processes. Instead, the FLUKA model is used for the energy range 10-100 MeV, which is also based on MC simulations of cosmic air showers but covers low-energy processes better. Since the FLUKA flux in [135] was calculated for the location of Super-K, it was normalized for each flavor in the overlap region of $100 - 944\,\text{MeV}$ to the HAKKM14 flux calculated for JUNO. Figure 7.4 shows the differential atmospheric neutrino flux $\mathrm{d}\Phi_{atmo}/\,\mathrm{d}E_\nu$ multiplied by the squared neutrino energy E_ν^2, averaged over the solar activity cycle and normalized in the overlap region[3].

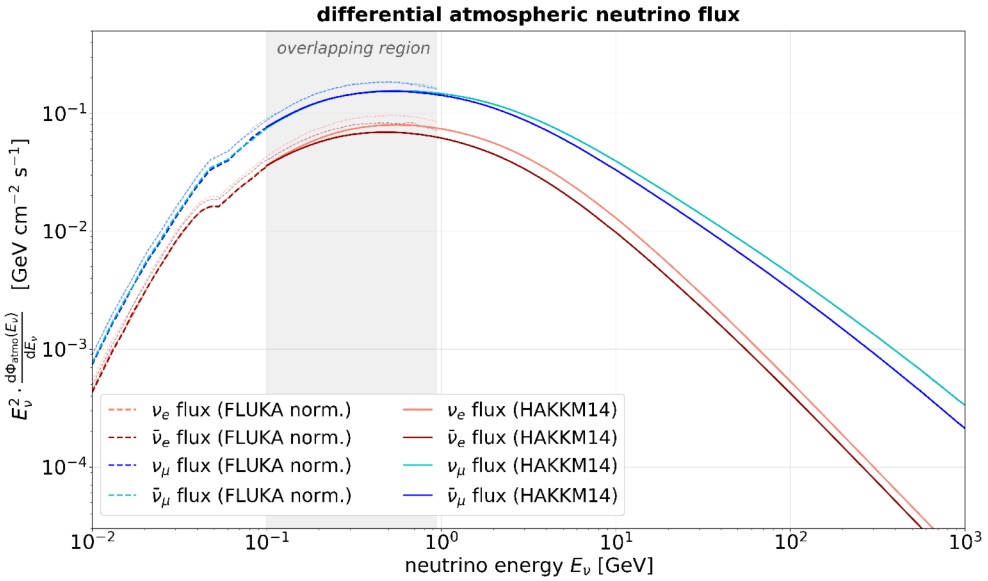

Figure 7.4: Differential atmospheric neutrino flux at the location of JUNO. The flux for energies $> 100\,\text{MeV}$ is calculated with the HAKKM14 model (solid curves) and is averaged over one cycle of solar activity [134]. Below 100 MeV the flux is originally calculated with the FLUKA model for the location of Super-K (bright dashed curves). For this reason the FLUKA flux is normalized to the HAKKM14 in the overlapping region to match the calculated flux for JUNO (dashed curves).

7.4.2 Neutrino Oscillation in Matter

The atmospheric neutrino flux from HAKKM14 and FLUKA model is provided as unoscillated flux at the point of production in the atmosphere and thus describes the generated spectra of ν_e, $\bar{\nu}_e$, ν_μ, and $\bar{\nu}_\mu$ prior to propagation to the detector. However, the fluxes arriving at JUNO differ significantly from these initial spectra, since the neutrinos undergo non-trivial three-flavor oscillations along their path to the Earth, particularly when traversing the Earth's core (cf. Fig. 4.7). These oscillations modify both the expected energy spectra and the flavor composition. For a realistic description of the atmospheric background in the JUNO detector, it is therefore necessary to calculate the oscillated atmospheric neutrino flux at the detector.

[3]This representation highlights differences between models and flavors over a wide energy range by partially compensating for the steeply falling neutrino flux. It is well established in the literature and adopted here for comparability [99, 138].

Oscillated HAKKM14 Flux

For neutrino energies $E_\nu \geq 100\,\mathrm{MeV}$, the unoscillated differential HAKKM14 fluxes

$$\frac{\mathrm{d}\Phi^0_{\nu_i}(E_{\nu_i}, \cos\theta, \phi)}{\mathrm{d}E_{\nu_i} \cdot \mathrm{d}(\cos\theta) \cdot \mathrm{d}\phi} \quad \text{for } \nu_i \in \{\nu_e, \bar{\nu}_e, \nu_\mu, \bar{\nu}_\mu\}$$

are used as input, which are calculated for the geographical location of the JUNO detector. The fluxes are tabulated in neutrino energy E_{ν_i}, zenith angle $\cos\theta$, and azimuth angle ϕ [136]. For each combination of neutrino flavor, energy, and solid angle, a production height h calculated by the HAKKM14 authors is provided in the form of a quantile function [136]. From this, a mean height $\bar{h}(E_{\nu_i}, \cos\theta_i, \phi_i)$ is determined for each bin and each flavor, which is used as the effective production height.

The neutrino oscillations are calculated in the three-flavor framework using the PMNS matrix $\mathbf{U}$ (cf. Eq. 4.2). Taking into account the influence of matter, the effective Hamiltonian in the flavor basis is given by [139]

$$\mathcal{H} = \frac{1}{2E_\nu}\,\mathbf{U}\begin{pmatrix}0 & 0 & 0\\ 0 & \Delta m^2_{21} & 0\\ 0 & 0 & \Delta m^2_{31}\end{pmatrix}\mathbf{U}^\dagger + \begin{pmatrix}V & 0 & 0\\ 0 & 0 & 0\\ 0 & 0 & 0\end{pmatrix} \tag{7.2}$$

Here, the potential $V = \sqrt{2}\,G_F\,N_e$ with the Fermi coupling constant G_F accounts for the influence of matter, which depends primarily on the electron density N_e [139][4]. Since, according to Eq. 4.3, the oscillation probabilities depend on the path length L of the traversed medium, the geometric baseline from the production point of the neutrinos to the JUNO detector must be determined[5]. For upward-going neutrinos ($\cos\theta_z < 0$), the trajectory passes through the Earth's interior, while for downward-going neutrinos ($\cos\theta_z \geq 0$), the propagation proceeds exclusively via vacuum oscillations in the atmosphere. To describe matter effects, a simplified, radially symmetric Earth model based on the Preliminary Reference Earth Model (PREM) is used [140]. For this purpose, the Earth is divided into three layers: the crust and upper mantle, the lower mantle, and the core. The radius ranges were chosen based on [140], and for each layer, the corresponding averaged mass densities ρ_i are calculated from the tables provided in the paper. To determine the electron density $N_{e,i}$, the elemental composition of each

Table 7.1: Simplified PREM Earth model for the description of matter effects in the oscillation calculation. The geometric dimensions as well as the mass density ρ are calculated from the tables provided in [140], while the averaged electron fraction Y_e is calculated from the composition of elements in each layer [141].

layer i	radius range [km]	ρ_i [g/cm^3]	$Y_{e,i}$
core	$0 - 3480$	10.838	0.460
lower mantle	$3480 - 5701$	4.907	0.493
upper mantle / crust	$5701 - 6371$	3.561	0.493

layer i must be considered. From the baryon density $N_{b,i} = \rho_i / m_p$, the number of

[4] For antineutrinos, the matter potential changes its sign ($V \to -V$).
[5] For simplicity, JUNO is assumed to be located on the Earth's surface for this calculation.

electrons per unit volume can be derived according to

$$N_{e,i} = Y_{e,i} \cdot N_{b,i} = Y_{e,i} \cdot \frac{\rho_i}{m_p} \ ,$$

where, for each layer, averaged electron fractions are calculated according to

$$Y_{e,i} = \sum_n w_n \frac{Z_n}{A_n} \ .$$

The weight w_n for all present elements with atomic number Z_n and mass number A_n was taken from [141]. The final values for the radius range, mass density, and electron fraction are summarized in Tab. 7.1. With this, the potential V can now be determined according to

$$V_i = \sqrt{2}\, G_F\, N_{e,i} \approx 7.568 \times 10^{-14}\,\text{eV} \left(\frac{\rho_i}{\text{g/cm}^3}\right) Y_{e,i}$$

and the Hamiltonian operator $\mathcal{H}_i$ in Eq. 7.2 can be derived for each shell. For the mixing parameters, the values provided by NuFIT 6.0 in Tab. 4.1 were used [80], with the exception of $\sin^2\theta_{12}$ and Δm^2_{21}, which were replaced by the best-fit values from JUNO in Eq. 4.5 [67]. Depending on the production point of a neutrino in the atmosphere and its arrival direction at the JUNO detector, each trajectory results in a sequence of propagation segments in the various layers with different lengths L_j . Each of these segments is described by an effective evolution operator

$$S_j(E_\nu) = \exp(-\mathrm{i}\,\mathcal{H}_j\, L_j) \ ,$$

while the full evolution operator from the point of production to the detector is obtained as the product of all individual segments[6]

$$S(E_\nu, \cos\theta, \bar{h}) = S_n \cdots S_2\, S_1 \ .$$

The transition amplitude for a flavor change $\nu_\alpha \to \nu_\beta$ is given by the corresponding matrix element of the evolution operator

$$\mathcal{A}_{\alpha\to\beta}(E_\nu, \cos\theta, \bar{h}_\alpha) = \langle \nu_\beta | S(E_\nu, \cos\theta, \bar{h}_\alpha) | \nu_\alpha \rangle = S_{\beta\alpha} \ ,$$

from which the transition probability $P_{\nu_\alpha\to\nu_\beta}(E_\nu, \cos\theta, \bar{h}_\alpha) = |S_{\beta\alpha}|^2$ can be derived. The oscillated differential atmospheric neutrino flux is then obtained by folding the unoscillated flux with the corresponding transition probabilities

$$\Phi^{\text{osc}}_\beta(E_\nu, \cos\theta, \phi) = \sum_{\alpha=e,\mu} \Phi^0_\alpha(E_\nu, \cos\theta, \phi)\, P_{\nu_\alpha\to\nu_\beta}(E_\nu, \cos\theta, \bar{h}_\alpha) \ .$$

Before the results of this approach are discussed, the oscillation calculation for the low-energy atmospheric neutrino flux provided by FLUKA is presented, allowing both contributions to be analyzed consistently in the following sections.

[6] Here, $\bar{h}_\alpha$ denotes the mean production height of the respective initial flavor ν_α. For antineutrinos, the calculation is performed analogously, but with the opposite sign of the potential V in the Hamiltonian.

Oscillated FLUKA Flux

The atmospheric neutrino fluxes provided by FLUKA in the low-energy region $E_\nu \leq 100\,\text{MeV}$ are available only as direction-integrated spectra without explicit angular differentiation, therefore the approach from Sec. 7.4.2 is not applicable. However, the characteristic oscillation lengths in this energy range differ significantly from those in the GeV-range, as shown in Fig. B.2[7]. Due to the small neutrino energies and the large effective propagation distances between the point of production and the detector, these atmospheric neutrinos undergo a large number of oscillation periods. Consequently, the oscillation phases can be treated as fully averaged, such that all interference terms effectively vanish [142]. In this case, the flavor transition probability can be described by

$$P_{\alpha\beta} = \sum_{i=1}^{3} |U_{\alpha i}|^2 |U_{\beta i}|^2 \ ,$$

depending only on the absolute squares of the PMNS matrix elements. For antineutrinos, the same probability matrix is used in this approximation, since both matter effects and the influence of the CP phase no longer play a relevant role in this energy range. The FLUKA flux can therefore be converted into an oscillated flux at the JUNO detector for each flavor according to

$$\Phi_\beta^{\text{osc}}(E_\nu) = \sum_{\alpha=e,\mu} \Phi_\alpha^0(E_\nu)\, \bar{P}_{\alpha\beta} \ .$$

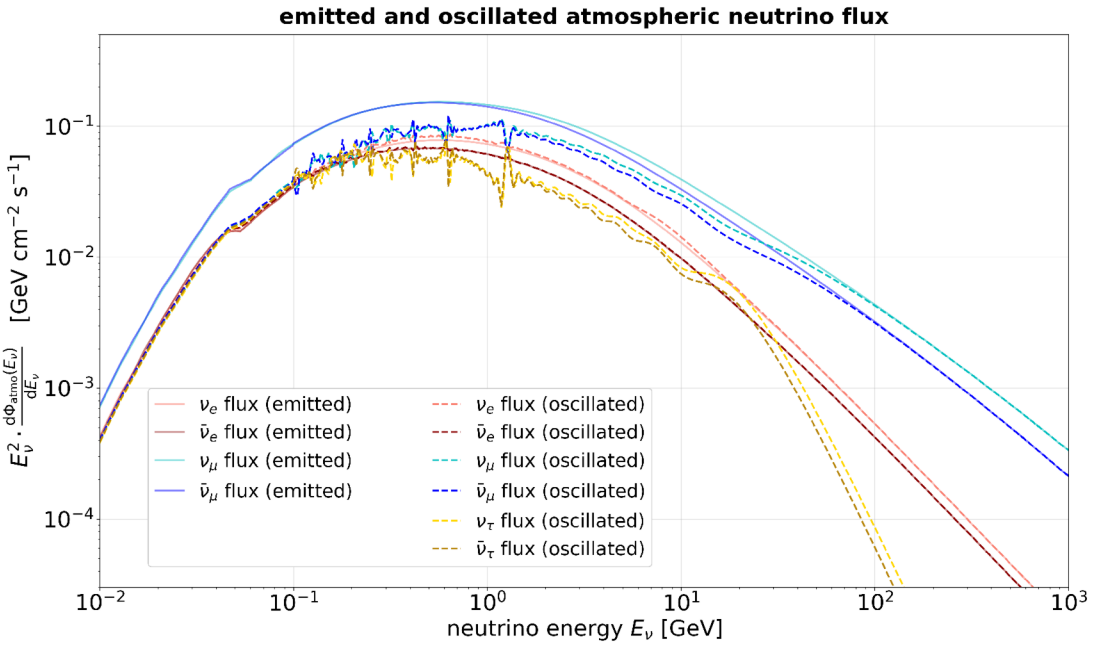

Figure 7.5: Total emitted (unoscillated) and oscillated differential atmospheric neutrino flux multiplied by the squared neutrino energy for each neutrino flavor at the location of JUNO. For τ neutrinos the initial flux is zero. The contribution in the oscillated flux is mainly due to the appearance channels $\nu_\mu \to \nu_\tau$ and $\bar{\nu}_\mu \to \bar{\nu}_\tau$.

[7] The oscillation probabilities $P(\nu_e \to \nu_\alpha)$ and $P(\nu_\mu \to \nu_\alpha)$ in Fig. B.2 were calculated for the PREM layers presented in Sec. 7.4.2 and a mean production height of 18 km.

Total Oscillated Flux

The total oscillated flux per neutrino flavor from the FLUKA model ($E_\nu \leq 100\,\text{MeV}$) and the HAKKM14 model ($E_\nu > 100\,\text{MeV}$) is shown as a dashed line in Fig. 7.5 and is compared with the corresponding unoscillated flux (solid line). The oscillations are particularly dominant in the sub-GeV to GeV range and lead to a significant modification of the flavor ratios. While the disappearance channel for ν_e and $\bar{\nu}_e$ (cf. Fig. B.2 upper left panel) is compensated by the appearance channels $\nu_\mu \to \nu_e$ and $\bar{\nu}_\mu \to \bar{\nu}_e$, the μ neutrino flux is significantly reduced. This is largely due to the dominant appearance channel $\nu_\mu \to \nu_\tau$ ($\bar{\nu}_\mu \to \bar{\nu}_\tau$), which converts a substantial fraction of the original muon neutrino flux into tau neutrinos (cf. Fig. B.2 lower right panel). The result of the oscillated flux is consistent with other studies [99, 138]. Figure 7.6 shows the ratio

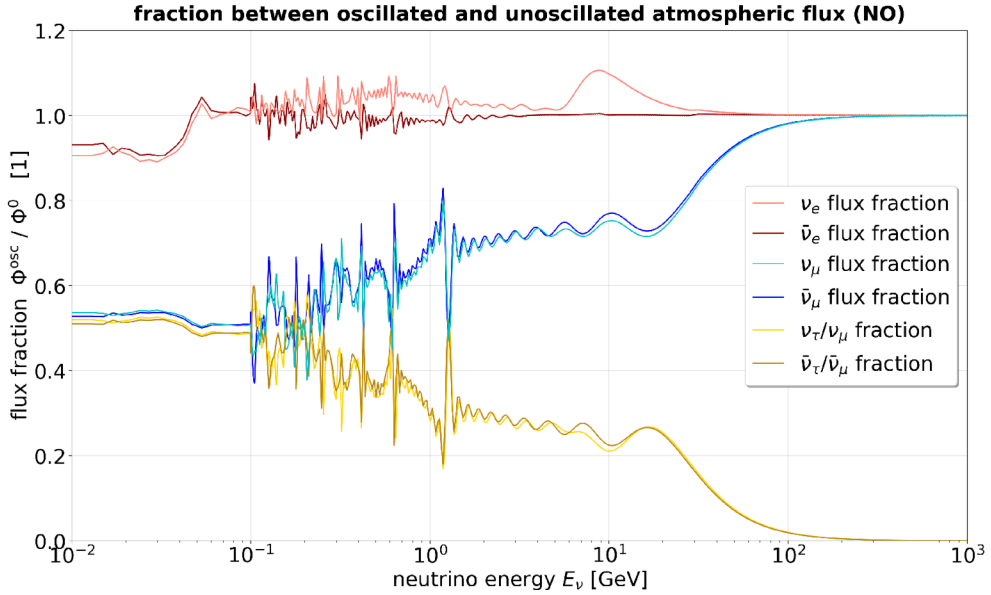

Figure 7.6: Fraction between unoscillated and oscillated atmospheric neutrino flux per neutrino flavor in JUNO. Since there is no unoscillated τ neutrino flux, the fractions for ν_τ and $\bar{\nu}_\tau$ are given with respect to the unoscillated ν_μ and $\bar{\nu}_\mu$ flux.

between the oscillated and unoscillated flux per flavor for NO[8]. For electron neutrinos, this ratio remains close to one over a wide energy range. In contrast, the ν_μ and $\bar{\nu}_\mu$ fluxes are significantly reduced in the energy range below $\sim 50\,\text{GeV}$ and approach a constant value of $\sim 54\,\%$ in the MeV range. At high energies $E_\nu > 100\,\text{GeV}$, all flux ratios converge back to one (for ν_τ and $\bar{\nu}_\tau$ to zero), marking a nearly oscillation-free regime. To ensure a realistic description of the dominant background for indirect DM search in JUNO, the final atmospheric neutrino flux is modeled in this work over the entire relevant energy range by taking into account

- the HAKKM14 model for $E_\nu > 100\,\text{MeV}$ calculated for JUNO,
- the FLUKA-based flux model for Super-K in the range $10\,\text{MeV} \leq E_\nu \leq 100\,\text{MeV}$ (with normalization to HAKKM14 in the overlap region),
- averaged seasonal and solar modulations (`solmin`/`solmax`),
- as well as three-flavor neutrino oscillations, including matter effects.

[8] Since there is no initial $\nu_\tau/\bar{\nu}_\tau$ flux, the fraction is given with respect to the unoscillated $\nu_\mu/\bar{\nu}_\mu$ flux.

7.4.3 Atmospheric CC and NC Background

Since atmospheric neutrinos are distributed over a broad energy range, they can interact with the detector material via CC or NC interactions. Depending on the neutrino energy E_ν, this can lead to complex event topologies, which are discussed in detail in Chap. 5. In order to comprehensively estimate the spectral shape of atmospheric CC and NC background in the different energy regimes, large MC data sets for neutrino energies from 10 MeV to 20 GeV are analyzed for all flavors. For this purpose, the neutrino interactions, including the final state interactions (FSIs), are generated with the GENIE framework version 3.2.0 (cf. Sec. 5.2), and the JUNO simulation version J24.1.2 is used at the `DetSim` level to derive the deposited energy, which is then folded with the energy resolution in JUNO (cf. Sec. 5.3). The oscillated flux illustrated in Fig. 7.5 is used as input for each flavor in order to model the measured spectral shape of the atmospheric background in JUNO. The derived visible spectrum was normalized to the expected number of total events per energy bin, which is calculated according to[9]

$$\frac{\mathrm{d}N^{\mathrm{atmo}}_{\mathrm{CC/NC}}}{\mathrm{d}E_\nu}(E_\nu) = \frac{\mathrm{d}\Phi^{\mathrm{osc}}_{\nu}}{\mathrm{d}E_\nu} \cdot x_{\mathrm{CC}}(E_\nu) \cdot t \cdot \varepsilon \ ,$$

with the effective cross section of CC interactions in JUNO

$$x_{\mathrm{CC}}(E_\nu) = x^{p}_{\mathrm{CC}}(E_\nu) + x^{^{12}\mathrm{C}}_{\mathrm{CC}}(E_\nu) = \sum_{\nu_\ell} \sigma^{\nu_\ell,p}_{\mathrm{CC}}(E_{\nu_\ell}) \cdot N_p + \sum_{\nu_\ell} \sigma^{\nu_\ell,^{12}\mathrm{C}}_{\mathrm{CC}}(E_{\nu_\ell}) \cdot N_{^{12}\mathrm{C}} \ ,$$

where the total cross sections $\sigma^{\nu_\ell,p}_{\mathrm{CC}}(E_{\nu_\ell})$ and $\sigma^{\nu_\ell,^{12}\mathrm{C}}_{\mathrm{CC}}(E_{\nu_\ell})$ for each flavor $\nu_\ell \in \{\nu_e, \bar{\nu}_e, \nu_\mu, \bar{\nu}_\mu\}$ include all interaction types described in Sec. 5.2 (QES, MEC, RES, DIS, COH). Analogously, the effective cross section $x_{\mathrm{NC}}(E_\nu)$ can be determined, where ν_τ and $\bar{\nu}_\tau$ are also taken into account.

Atmospheric CC Background

The expected visible energy spectrum of atmospheric CC events in JUNO after 10 yr of data taking is shown in Fig. 7.7 (obtained with dataset $D4$ in Tab. C.1). The deposited energy was determined from more than 5 million MC simulated events of the flavors ν, $\bar{\nu}_e$, ν_μ and $\bar{\nu}_\mu$, which were convolved with the energy resolution in JUNO (cf. Fig. 5.9). The contribution of τ-neutrinos was neglected since they occur only above $m_\tau \approx 1.8\,\mathrm{GeV}$ and play a subdominant role in the energy range of this analysis. As discussed in Sec. 5.2.2, the neutrino energy is usually distributed among several final state particles in CC interactions. Therefore, the correlation between neutrino energy E_ν and visible energy E_{vis} in the detector is smeared (cf. upper panel of Fig. 5.6), resulting in the disappearance of the oscillation structure in Fig. 7.5.
Instead, atmospheric CC events produce a smooth, continuous distribution in the final visible energy spectrum, which constitutes a significant background across all energy regimes. In the sub-GeV to GeV range, they represent the dominant background due to the large atmospheric neutrino flux and increasing CC cross sections. The ratio of neutrino to antineutrino events for both flavors is approximately 2:1 for $E_{\mathrm{vis}} > 0.3\,\mathrm{GeV}$, which can be attributed to the higher interaction probability of neutrinos (cf. Fig. 5.3). In the MeV range, however, antineutrino events dominate the spectrum, since interactions on ^{1}H become more dominant there. Especially atmospheric IBD events in Fig. 7.7(cf. dark red curve) constitute an irreducible background.

[9] The efficiency ε was set to one in this section.

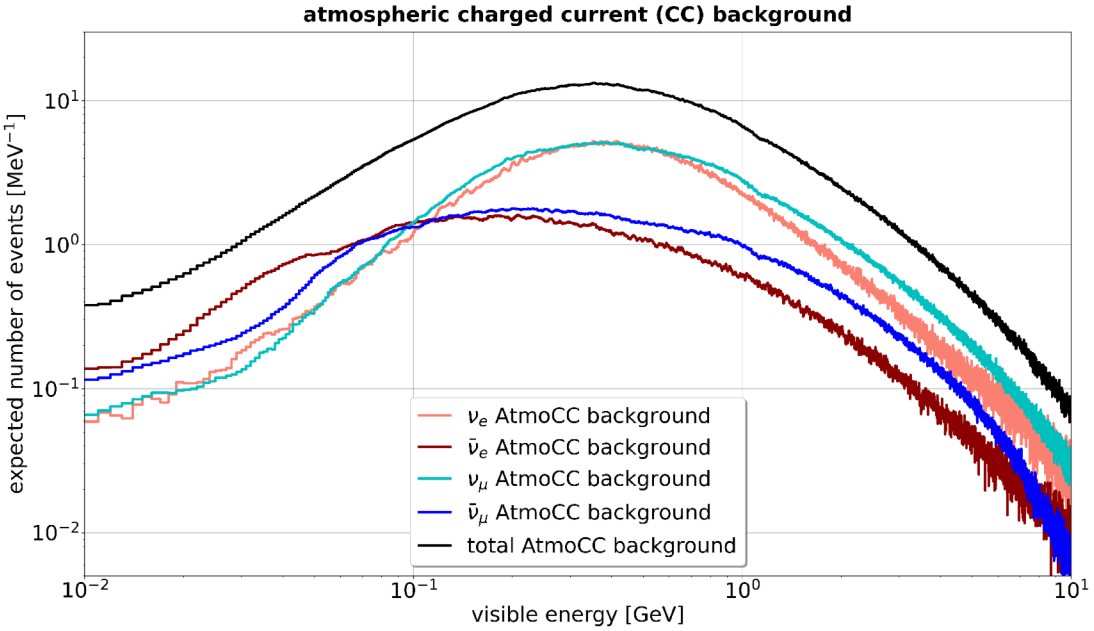

Figure 7.7: Expected visible energy spectrum of the atmospheric CC background after 10 yr of data taking and a fiducial volume of 20 kton in JUNO. The contribution of τ neutrinos was not considered, due to the large rest mass of the τ lepton, the contribution is negligible for CC events in the relevant energy range.

Atmospheric NC Background

The expected visible energy spectrum of atmospheric NC events in JUNO after 10 yr of data taking is shown in Fig. 7.8. In contrast to CC interactions, for modeling the atmospheric NC background, all neutrino flavors (including ν_τ and $\bar{\nu}_\tau$ from oscillations) are considered, and more than 9 million MC events are simulated according to their oscillated fluxes in Fig. 7.5 (cf. dataset *D*4 in Tab. C.1). As discussed in Sec. 5.2.2, in NC interactions, the outgoing neutrino carries away a large fraction of its initial energy, resulting in significantly lower visible energies compared to E_ν (cf. lower panel of Fig. 5.6). Consequently, atmospheric NC events are the dominant background in the MeV range. In contrast to CC, approximately twice as many neutrino events as antineutrino events are expected due to the higher interaction probability over the entire visible energy window. The spectrum exhibits a characteristic plateau for all flavors around $E_{\text{vis}} \sim 0.3\,\text{GeV}$, which is mainly produced by RES and MEC processes, as illustrated in Fig. B.3. The MEC contribution arises from 2p2h interactions as implemented in the Valencia model in GENIE, while the RES peak reflects the production of the $\Delta(1232)$ resonance [143, 144].
Although there is no charged lepton produced in NC events, they can mimic the IBD signature if the final state topology contains one or more neutrons. In such events, the prompt energy deposition from hadronic recoils, combined with a delayed n-capture signal, can survive the IBD selection cuts (cf. Sec. 8.2.1). This makes atmospheric NC events with final-state neutrons a critical background for the IBD-based DM search in the MeV regime. To suppress this background, pulse shape discrimination (PSD) techniques are applied, making use of the different time profiles of proton and positron signals, which are discussed in detail in Sec. 8.3.

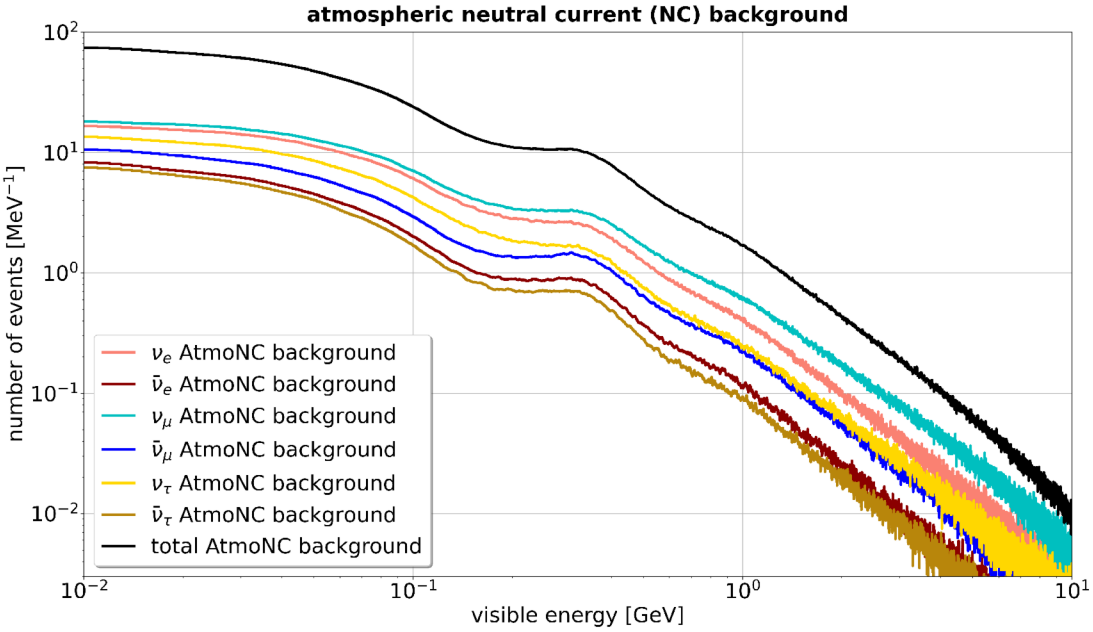

Figure 7.8: Expected visible energy spectrum of the atmospheric NC background after 10 yr of data taking and a fiducial volume of 20 kton in JUNO. For the atmospheric NC backgrounds all neutrinos flavors are considered, including ν_τ and $\bar{\nu}_\tau$ from oscillations.

7.5 Final Visible Energy Spectrum in JUNO

To determine the final visible spectrum of all signal and background contributions in JUNO, the fiducial volume cut discussed in Sec. 7.2 and the muon veto strategy must be considered. To suppress the fast neutron background, only events within a radius of $R \leq 16$ m are considered, which simultaneously enables better pulse shape analysis since reflections at the acrylic are avoided. Thus, the fiducial volume cut efficiency is $\varepsilon_V = 0.739$ compared to the full 20 kton at a radius of 17.7 m. The muon veto strategy applied in this work follows the approach validated with the first JUNO data [6, 67]. After each identified muon[10], a detector-wide veto of 5 ms is applied, resulting in an efficiency of $\varepsilon_{\text{veto}} = 0.956$. The additional spallation-neutron veto applied in the reactor neutrino analysis [67] to suppress ^{9}Li and ^{8}He backgrounds is not required in this work since the energy threshold of $E_{\text{vis}} \geq 12$ MeV already excludes these low energy contributions (cf. Sec. 7.1). Fig. 7.9 shows the expected visible energy spectrum in JUNO after 10 yr of data taking for a fiducial mass of 14.77 kton in the energy range from 10 MeV to 10 GeV. The number of events for each contribution is calculated according to Eq. 6.1 for a given flux Φ_ν, where $\varepsilon = \varepsilon_V \cdot \varepsilon_{\text{veto}} \approx 0.706$ accounts for the fiducial volume cut and the muon veto efficiency. The gray shaded area indicates the visible energy threshold of $E_{\text{vis}} \geq 12$ MeV, which allows the reactor antineutrino background (cyan) to be neglected in this work (cf. Sec. 7.1). The event numbers for each contribution in the visible energy window are added in parentheses. Atmospheric NC events (yellow) constitute the dominant background in the MeV range, with $\sim$ 7300 expected events due to the large fraction of energy carried away by the outgoing neutrinos. At higher energies in the sub-GeV to GeV range, atmospheric CC interactions (green) become

[10]The muon tagging efficiency is larger than 99.9 % [6].

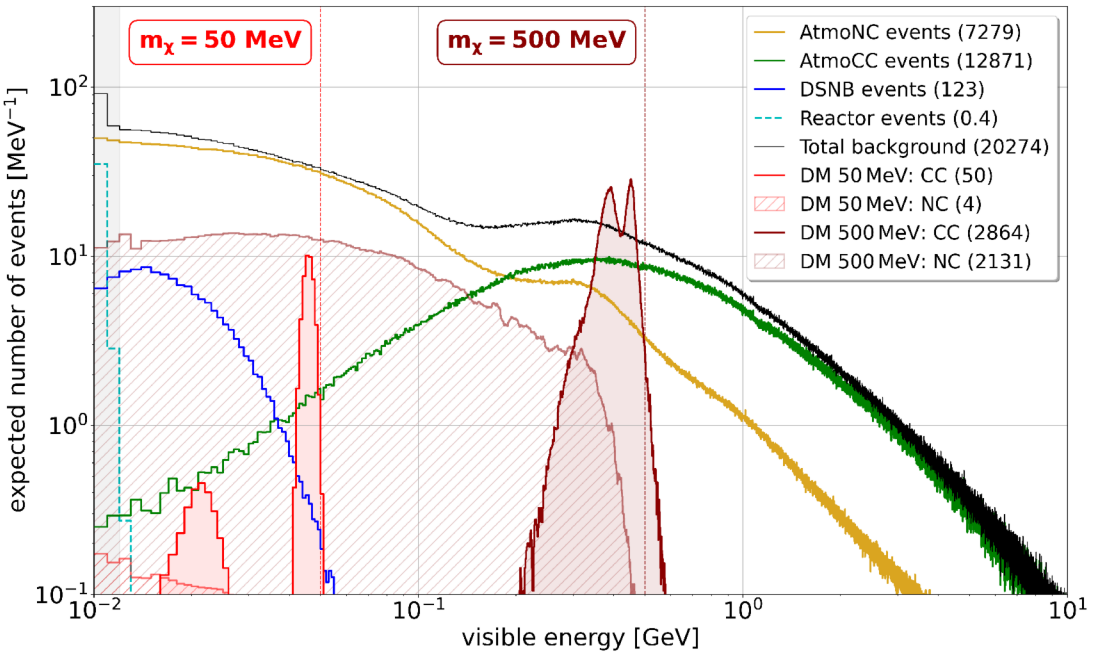

Figure 7.9: Expected visible energy spectrum in JUNO for a fiducial mass of 14.77 kton after 10 yr of data taking. In order to neglect the reactor antineutrino background (cyan dashed line), the visible energy range starts from $E_{\text{vis}} \geq 12$ MeV. The DSNB background is illustrated in blue, considering the max flux model displayed in Fig. 7.1. The atmospheric NC and CC backgrounds are displayed in yellow and green, respectively and constitute the dominant backgrounds in the whole visible energy range and the black curve shows the total background contribution. The expected DM-induced signal for $m_\chi = 50$ MeV (light red) and $m_\chi = 500$ MeV (dark red) is added including the CC (filled) and NC (hatched) contribution. The expected number of events in the visible energy range from 12 MeV to 10 GeV for each contribution is added in parentheses.

the dominant background component, contributing around $\sim$ 12,900 events in total. The DSNB (blue) adds a subdominant but relevant hypothetical IBD background of $\sim$ 120 events, predominantly in the energy range below 50 MeV (cf. Sec. 7.3). In total, approximately $\sim$ 20,300 background events are expected in the visible energy window after 10 yr of data taking.
For comparison, two DM-induced signals are added in red, considering the CC (filled) and NC (hatched) interactions: the signal of DM neutrinos with $m_\chi = E_\nu = 50$ MeV (light red) represents the MeV regime and shows the characteristic IBD peak close to the DM mass (light red vertical line) and the second shifted peak driven by CC1p0n interactions of ν_e on ^{12}C (cf. Eq. 5.7). The signal for $m_\chi = 500$ MeV (dark red) represents sub-GeV DM annihilation and shows the characteristic double-peaked structure, extensively discussed in Sec. 6.2.2. In contrast to all background contributions, which exhibit continuous spectra, the neutrino flux from DM self-annihilation is expected to be monoenergetic. Although the signal is smeared due to the interaction kinematics in the LS (cf. Sec. 5.2), the characteristic spectral shape can be used to derive a sensitivity for the indirect DM search in JUNO. To further improve the signal-to-background (S2B) ratio, various energy-dependent background reduction techniques are discussed in detail in Chap. 8 for the MeV range and Chap. 9 for the sub-GeV and GeV range.

8 | Signal-to-Background Optimization for MeV DM

You've gotta dance like there's nobody watching.
– William W. Purkey

After the expected neutrino signal from DM annihilations was analyzed in Chap. 6, and all relevant backgrounds were discussed in Chap. 7, various background reduction methods can be introduced to increase the signal-to-background (S2B) ratio. To this end, targeted techniques are applied that preserve the expected DM signal to a large extent while simultaneously reducing the background contributions. Since both the spectral features of the DM-induced signal and the background reduction methods depend strongly on the energy range, the MeV, sub-GeV, and GeV energy ranges are discussed separately. This chapter focuses on the background reduction techniques in the MeV range.

Up to $E_\nu \approx 200\,\text{MeV}$, the inverse beta decay (IBD) is the dominant CC channel, as shown in Fig. 5.7. In previous sensitivity studies for indirect DM searches in JUNO, only the energy range 12-100 MeV has been investigated [7, 8]. This work extends the sensitivity study for the IBD channel up to visible energies of 300 MeV. For this purpose, extensive MC datasets were generated and analyzed using the JUNO simulation framework (cf. Sec. 4.4). To obtain the final event topology, all final state interactions (FSIs) were taken into account. While DSNB neutrinos mainly produce IBD events and thus constitute an irreducible background to the IBD DM signal, atmospheric NC events and CC events (excluding IBD) can be suppressed using suitable techniques[1]. On the one hand, the temporal and spatial coincidence between the prompt signal of the positron and the delayed neutron capture can be exploited to exclude other event topologies [67]. For this purpose, targeted IBD selection cuts are introduced in Sec. 8.2 and the IBD detection efficiency is derived. On the other hand, especially NC events and partially also CC events (excluding IBD) can be distinguished from genuine IBD events by pulse shape analysis. Based on different time components of the LS for different particle types, which allow a pulse shape discrimination (PSD), a classical and a machine learning (ML) approach is presented in Sec. 8.3 that enables event classification of IBD, NC, and CC (excluding IBD) interactions and therefore increases the S2B ratio.

For both the event topology selection and the PSD methods, a reliable reconstruction of the prompt vertex is required. In the first case, the reconstructed vertex enters the spatial coincidence criterion between prompt and delayed signal, while in the second case it determines the time of flight (TOF) correction of the photon arrival times and thus the reconstructed pulse shapes. Therefore, vertex reconstruction is a key technical prerequisite for the background suppression of atmospheric CC and NC events discussed in this chapter.

[1] In this chapter, the term CC (excluding IBD) refers to all charged current interactions that are not true IBD events.

8.1 Machine Learning Approach for Vertex Reconstruction

Similar to the energy reconstruction methods discussed in Sec. 5.3, vertex reconstruction techniques also depend strongly on the relevant energy regime. In the reactor-antineutrino range ($E_{\text{vis}} < 12\,\text{MeV}$), JUNO typically uses the classical Optical Maximum-likelihood Reconstruction (OMILREC) algorithm, which reconstructs the energy and vertex of point-like events by maximizing a combined time-and-charge likelihood [145]. In contrast, high-energy atmospheric neutrino events $> 1\,\text{GeV}$ produce extended tracks. For these events, dedicated track reconstruction methods have been developed [146]. However, the intermediate energy range $E_{\text{vis}} \in [12, 300]\,\text{MeV}$, which is central to the IBD-based analysis presented in this work, has received limited attention so far. A sensitivity study for low-energy atmospheric neutrinos in the range 100 MeV to 10 GeV assumes a vertex uncertainty of 1 m, although this value lacks detailed justification [99]. An internal technical note on DSNB sensitivity in JUNO reports a vertex uncertainty below 15 cm for 'most' events between 10 MeV and 40 MeV, using the OMILREC method, which appears consistent with the performance in the reactor neutrino regime [145]. However, the fundamental limitation of OMILREC is the assumption of a single emission point, which applies only to point-like events [145]. Since positron track lengths exceed 50 cm for $E_{\text{vis}} > 150\,\text{MeV}$ (cf. Fig. 8.1), the point-like approximation becomes insufficient in this energy region. To estimate the vertex resolution for IBD-like events across the

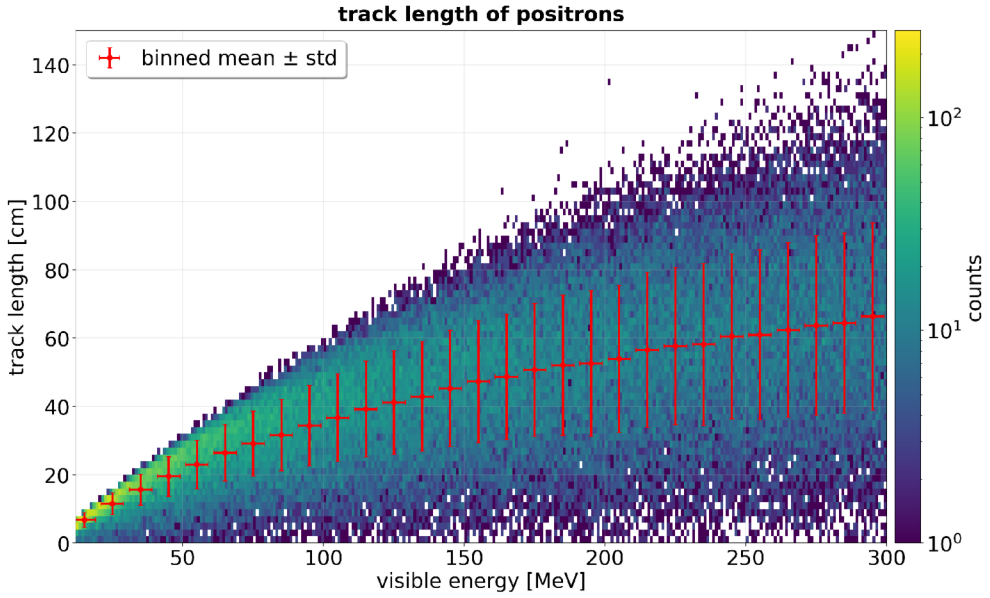

Figure 8.1: Distribution of positron track lengths for 120,000 MC simulated IBD events with visible energies between 12 MeV and 300 MeV. The red crosses indicate the mean value and standard deviation in 10 MeV energy bins.

extended energy range $E_{\text{vis}} \in [12, 300]\,\text{MeV}$, a data-driven ML approach was developed in this work. From the time and charge patterns of the waveforms measured by each PMT, the three-dimensional vertex position $\vec{r}_{\text{Qdep}}$ of the prompt event, weighted by the quenched deposited energy E_{Qdep} along the track is determined. This energy-weighted vertex definition is chosen to ensure a well-defined vertex assignment, even for events that are no longer point-like. The neural network (NN) architecture and results are presented in this section as a function of visible energy and vertex position.

8.1.1 Input Features and Dataset Preparation

In the JUNO LS detector, scintillation photons produced during a particle interaction propagate isotropically through the detector volume and are detected by 17,612 surrounding large PMTs (20-inch diameter). Each photon produces a photoelectron at the PMT photocathode, which are amplified through an avalanche process in the subsequent dynode chain. The resulting signal is recorded as a characteristic waveform for each PMT, which carries time and voltage charge information of the detected light. The waveforms of all PMTs together therefore provide implicit information about the topology of the event. To suppress high-frequency noise and to improve the temporal resolution, the waveform is deconvoluted in the first 1.25 μs by unfolding the response of a single photoelectron for each PMT [5]. From these improved waveforms, characteristic features can be extracted, which contain information about the temporal and charge-based structure of the scintillation light [79]. The underlying idea for the definition of suitable features is to preserve as much relevant physical information per PMT as possible while drastically reducing the number of input parameters compared to the entire waveforms. In this approach, for each event a set of four characteristic waveform features f_i is extracted for all PMTs, which are used as input parameters for the NN.

- The **first hit time (FHT)** (f_1) corresponds to the time of the earliest hit for each PMT and is determined using a fraction discriminator with a threshold of 20 % of the maximum charge (amplitude of the deconvoluted waveform). Since PMT closest to the interaction vertex detect a signal earlier than distant ones, the FHT carries direct information about the interaction vertex.
- The **total charge** (f_2) detected by each PMT in an event is obtained by integrating the deconvoluted waveform over the entire readout window. It is also a measure of the proximity of the PMT to the interaction vertex. The sum of the total charge for all PMTs scales directly with the quenched deposited energy E_{Qdep} of the events.
- The **slope** (f_3) describes the average rise of the deconvoluted waveform directly after the FHT and quantifies the local steepness of the signal onset. The slope carries important information about whether an event is point-like or rather track-like and helps to determine the weighted vertex $\vec{r}_{\mathrm{Qdep}}$.
- The **charge ratio** (f_4) is defined as the fraction of charge collected within the first 4 ns after the FHT relative to the total charge. While also emphasizing the early part of the waveform, this feature measures the promptness of the detected light with respect to the full time distribution and is sensitive to both scintillation time constants and event geometry. Since PMTs, located close to the effective light front of a propagating charged particle, observe a more temporally clustered signal, the charge ratio carries directional information about the particle [79].

Similar waveform feature sets have been successfully employed in several ML-based reconstruction approaches in JUNO, particularly for directional reconstruction and particle identification (PID) studies of atmospheric neutrino events [79, 126, 147]. In principle, additional features can be extracted from the deconvoluted waveform, such as the peak charge and peak time, as well as the first four statistical moments (mean, standard deviation, skewness, and kurtosis) [79]. However, these quantities do not carry significant information about the interaction vertex and are therefore not considered as an input for the reconstruction in this work.
For the training, 240,000 IBD events were generated with GENIE and processed through all four stages (`DetSim` to `Reco`) of the JUNO simulation framework presented in Sec. 4.4 (cf. dataset *D*6 in Tab. C.1). Accordingly, all relevant electronic effects, such as pre- and

after-pulses, as well as PMT-specific characteristics including the transit time spread (TTS), gain, and detection efficiency, were accounted for in the simulation to obtain the final deconvoluted waveforms within the first 1.25 μs for each individual PMT. Before the waveform features are used as input parameters for the NN, the original features are transformed into a Gaussian-like distribution by means of a suitable transformation $f_i \rightarrow f_i^{\mathrm{t}}$. The original distributions shown in red in the left column of Fig. 8.2 undergoes a specific transformation. While the FHT already exhibits a Gaussian-like distribution (cf. upper left panel) and therefore does not need to be transformed $f_1^{\mathrm{t}} = f_1$, the other three features show an asymmetric distribution. Thus, the total charge is logarithmically transformed according to $f_2^{\mathrm{t}} = \ln(1 + f_2)$ to compress the broad distribution and the long tail. The slope is scaled by a factor of 100 and also logarithmically transformed according to $f_3^{\mathrm{t}} = \ln(1 + 100 \cdot f_3)$. For the charge ratio, which is intrinsically defined on the interval $[0, 1]$, a logit transformation according to $f_4^{\mathrm{t}} = \ln(f_4/(1 - f_4))$ is applied. The transformed features are subsequently normalized according to

$$x_i = \frac{f_i^{\mathrm{t}} - \bar{f}_i^{\mathrm{t}}}{\sigma_i^{\mathrm{t}}} \tag{8.1}$$

where $\bar{f}_i^{\mathrm{t}}$ is the mean and σ_i^{t} is the standard deviation of the transformed distributions. Due to this definition, the mean of the final input parameters x_i for the NN is at $\bar{x}_i = 0$ and the standard deviation is at $\sigma_x = 1$ (cf. blue distributions in Fig. 8.2). This preprocessing ensures that all features contribute equally to the learning process and that different scales do not cause unstable gradients. In Fig. 8.3, the final normalized features x_i per PMT are shown exemplarily for an IBD event with a visible energy of $E_{\mathrm{vis}} = 252.5\,\mathrm{MeV}$ and a distance of $R = 9.24\,\mathrm{m}$ from the detector center. The axes represent the zenith θ_{PMT} and azimuth angle ϕ_{PMT} of the individual PMTs, while the colors encode the normalized feature values[2]. The PMT nearest to the true interaction vertex $\vec{r}_{\mathrm{IBD}}$ is marked with a black cross, while the PMT closest to the energy-weighted vertex $\vec{r}_{\mathrm{Qdep}}$ is marked by a red cross. The displacement between these marked positions indicates the track-like nature of the event. The energy-weighted vertex $\vec{r}_{\mathrm{Qdep}}$, which is to be reconstructed by the NN, is shifted along the positron propagation direction relative to the true interaction vertex $\vec{r}_{\mathrm{IBD}}$. As expected, both the shortest FHT (upper left panel) and the largest total charge (upper right panel) are found at the PMTs located near the vertex $\vec{r}_{\mathrm{Qdep}}$. The charge ratio (lower right panel) exhibits a slight ring structure, whose center indicates the positron propagation direction [79]. The slope pattern (lower left panel) also shows a directional bias, with the center being shifted along the positron propagation direction.

For a given PMT, the features can only be extracted if the signals are not too weak or distorted by electronic effects, causing the waveform deconvolution to fail. Even with successful deconvolution, the length of the hit must exceed a minimum value for reliable waveform extraction, so that at least one peak above a sufficiently well-defined baseline can be detected [148]. If one of the criteria is not met, invalid values are assigned to this PMT in the reconstruction algorithm. In the feature input of the NN developed in this work, these invalid values are set to zero, which corresponds to the mean of the final normalized distributions (cf. Fig. 8.2). Since this can affect a substantial fraction of PMTs, particularly at lower visible energies (up to 90 %), a mask is provided as a fifth feature in addition to the four waveform features, encoding invalid values with 0 and

[2]Note that the colorbar for the FHT (upper left) and the charge ratio (lower right) is inverted compared to the total charge (upper right) and the slope (lower left) for better visualization.

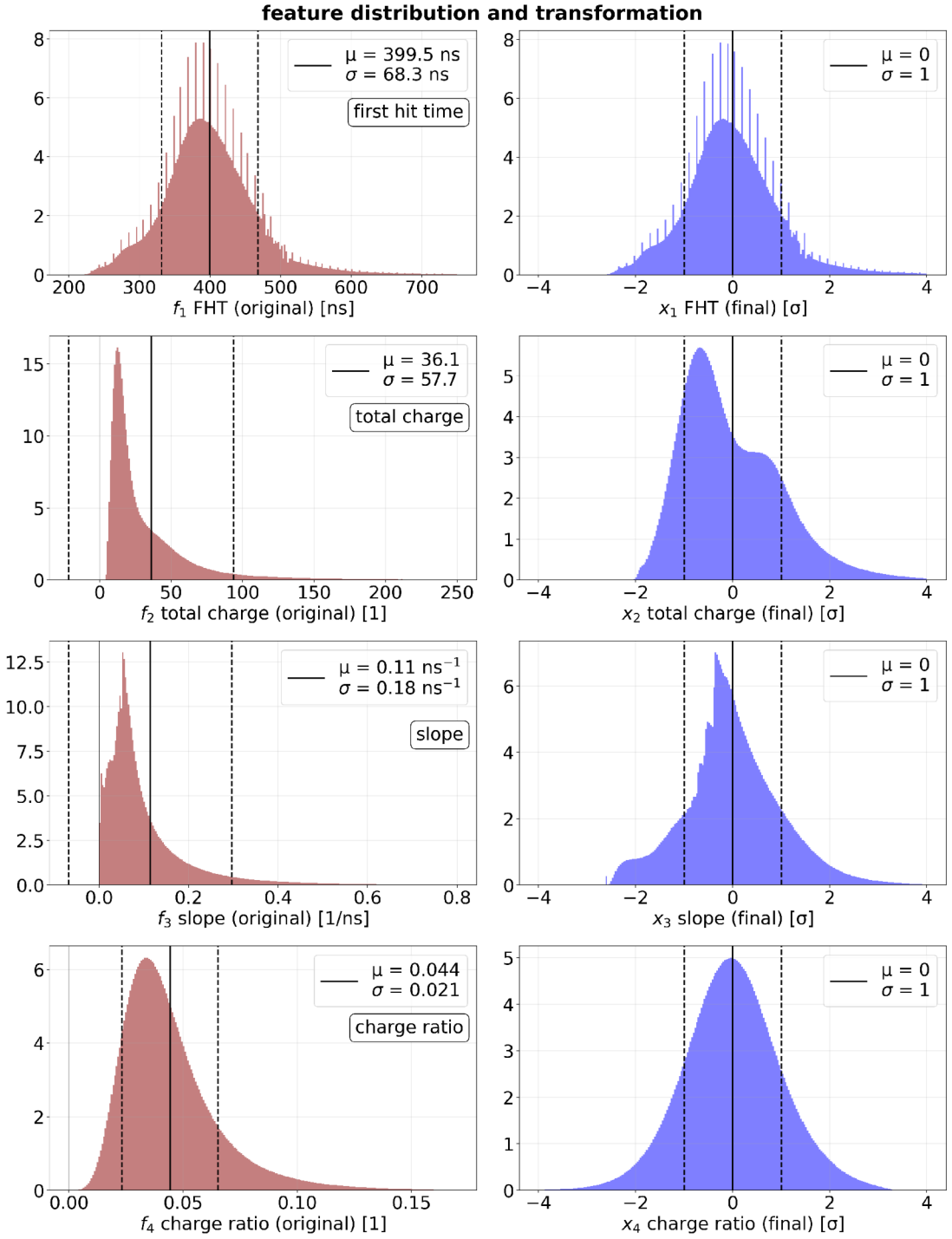

Figure 8.2: Feature distributions before (left) and after transformation and normalization (right). The original feature distributions show different absolute scales ranges and large asymmetries. Suitable transformations followed by a normalization map the features to nearly gaussian shaped distributions centered at zero with a variance one. The solid black line marks the mean of the distributions, while the dashed lines indicate the $\pm 1\,\sigma$ standard deviations.

valid values with 1. Therefore, the input dimension of the NN is $5 \times 17{,}612 = 88{,}060$ features per event, while the output dimension consists of the three spatial vertex

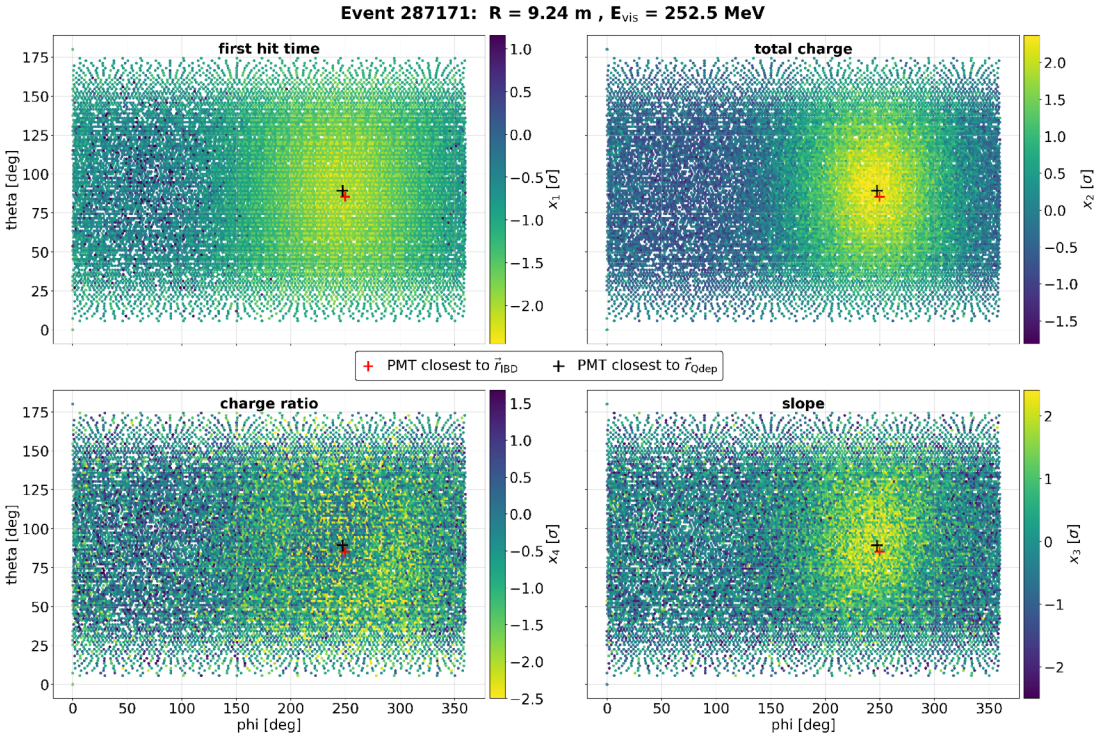

Figure 8.3: Final waveform features x_i after transformation and subsequent normalization for a representative IBD event ($R = 9.24\,\mathrm{m}$ and $E_{\mathrm{vis}} = 252.5\,\mathrm{MeV}$). The normalized features were projected onto the θ_{PMT}–ϕ_{PMT} plane and color-coded for each of the 17,612 PMTs. The black cross marks the PMT closest to the true interaction vertex $\vec{r}_{\mathrm{IBD}}$, while the red cross indicates the closest PMT to the vertex $\vec{r}_{\mathrm{Qdep}}$ weighted by the quenched deposited energy.

coordinates of $\vec{r}_{\mathrm{Qdep}}$. Since the IBD events were generated isotropically in the fiducial volume with $r_{\mathrm{IBD}} = 16\,\mathrm{m}$, the mean of the three coordinates is already at zero. All three output features are normalized with a fixed value of $r_{\mathrm{norm}} = 8\,\mathrm{m}$, which corresponds to a standard deviation of approximately 1σ, considering the full detector radius of $17.7\,\mathrm{m}$[3]. The training data were distributed evenly in the visible energy window to prevent an energy dependent performance bias of the NN. For training, 180,000 events are used, while 20,000 events are reserved as a validation set for hyperparameter selection. An independent test set of 40,000 additional events is used to evaluate the final model performance and is not used during training or hyperparameter optimization.

8.1.2 Network Architecture and Training Procedure

To reconstruct the vertex coordinates $\vec{r}_{\mathrm{Qdep}} = (x_{\mathrm{q,edep}}, y_{\mathrm{q,edep}}, z_{\mathrm{q,edep}})$ from 88,060 input features, a Multi-Layer Perceptron (MLP) architecture is employed, including an encoder for dimensionality reduction, a stack of residual blocks that refine the extracted features, and an output head that provides the final prediction of the vertex coordinates. The encoder contains several fully connected hidden layers, mapping the high-dimensional input data to a more compact feature space. Each layer is followed by batch normal-

[3]The selection criterion $r_{\mathrm{IBD}} \leq 16\,\mathrm{m}$ constrains only the initial interaction vertex. Due to the finite positron track length, the true energy-weighted vertex $\vec{r}_{\mathrm{Qdep}}$ can extend beyond this boundary, reaching up to the full detector radius of $17.7\,\mathrm{m}$.

ization to stabilize the training [149], a nonlinear activation function, and includes dropout. The residual blocks connected sequentially after the encoder prevent vanishing gradients by allowing the NN to model only the deviation from the identity through skip connections. As a result, each residual block refines the features rather than recomputing them entirely, which accelerates convergence and enables more stable trainings [150]. Each block consists of two linear fully connected layers with identical feature dimension as the last hidden layer, including batch normalization, activation function, and dropout. The final output head reduces the feature dimensionality to 64 neurons and projects them to the three output coordinates. The optimal hyperparameters for this MLP architecture were determined using the Optuna framework [151] by evaluating more than 200 configurations in the following hyperparameter space:

- Number (1–5) and sizes (128, 256, 1024, 2048, 4096) of the hidden layers
- Number of residual blocks (0–5)
- Dropout rate (0.1–0.5) and batch size (64, 128, 512)
- Activation function (`ReLU`, `GELU`, `SiLU`)
- Learning rate (10^{-5}–10^{-3}) and weight regularization (10^{-6}–10^{-3}), sampled log-uniformly

The best performance was achieved by wide networks with few hidden layers in combination with multiple residual blocks and a small learning rate (LR). The `GeLU` activation function [152] outperformed `ReLU` and `SiLU`. With each configuration trained for a maximum of 150 epochs, the final configuration is summarized in Tab. 8.1. The result-

Table 8.1: Optimal hyperparameter configuration for the MLP architecture used in IBD vertex reconstruction. The values were determined by evaluating over 200 configurations using the Optuna framework [151].

Hyperparameter	**Value**
Encoder layers	2: $4096 \to 4096$
Residual blocks	3×4096
Activation function	`GELU`
Dropout rate	0.1
Batch size	256
Learning rate (LR)	7.7×10^{-4}
Weight decay	1.5×10^{-5}
Total parameters	~ 478 M

ing model contains approximately 478 million trainable parameters, with the majority ($\sim 75\,\%$) located in the first encoder layer due to the high-dimensional input. The Mean Squared Error (MSE) is used as the loss function to minimize the difference between predicted and true vertex coordinates, while `AdamW` serves as the optimizer [153]. The LR is dynamically adapted by a `ReduceLROnPlateau` scheduler, reducing the LR by a factor of 0.3 once the validation loss has not decreased for 15 epochs. The training was performed on a NVIDIA A100 GPU and typically converged after 50–70 epochs.

8.1.3 Results of the ML-based Vertex Reconstruction

In Fig. 8.4, the test set distributions of the differences between the vertex coordinates reconstructed by the MLP and the true values are shown separately for each spatial direction. Each distribution shows an approximately Gaussian shape with mean values

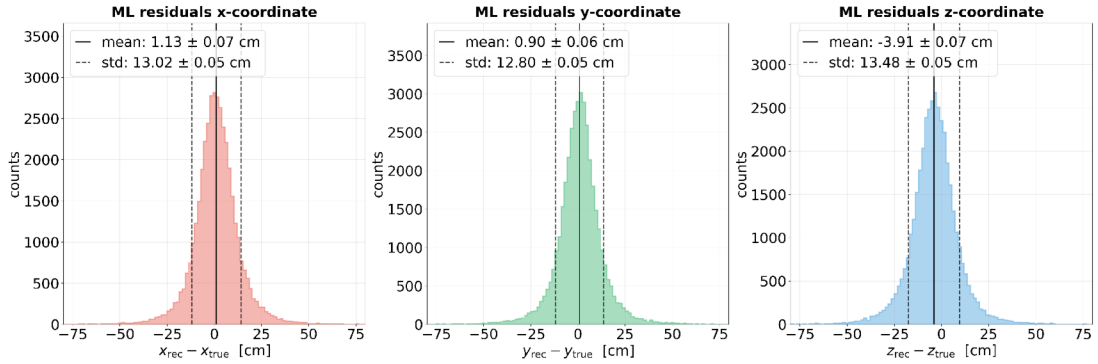

Figure 8.4: Residuals of the MLP vertex reconstruction for all spatial coordinates, including the mean values and the standard deviation of the distributions.

close to zero ($< 4\,\text{cm}$). This demonstrates, that the NN exhibits no significant spatial bias in any of the spatial directions. The standard deviation for each coordinate with approximately 16 cm is a measure of the vertex resolution of this ML-based reconstruction method and is used in the following background reduction methods in Sec. 8.2 and 8.3. To quantify the feature relevance for the ML performance, a permutation importance analysis is performed on the test dataset. In this procedure, each of the four final PMT features x_i defined in Eq. 8.1 is randomly permuted across all PMTs, while the remaining features are kept unchanged. The resulting increase in the mean vertex reconstruction error serves as a measure of the importance of the permuted feature. According to this analysis, the most dominant feature is the FHT (x_1), with a relative contribution of 52.6 %, since it is directly correlated with the distance between the PMTs and the vertex $\vec{r}_{\text{Qdep}}$. The total charge (x_2) exhibits the second-highest relevance with 25.5 %, as it encodes not only vertex information but also sensitivity to the total event energy. The slope (x_3) contributes 13.0 %, while the charge ratio (x_4) accounts for the remaining 8.8 %. Since the fifth feature acts as a PMT mask and excludes invalid values, it cannot be permuted independently of the other features and was therefore excluded from this analysis. In addition, the sensitivity of the MLP to the hyperparameters is analyzed within the Optuna optimization using the fANOVA method [154]. The dropout rate is identified as the most influential hyperparameter, with a contribution of 41.3 %, highlighting the importance of model regularization to prevent overfitting. The dimensionality of the second hidden layer in the encoder exhibits a comparable importance of 41.2 %, while the dimensionality reduction in the first hidden layer has only a minor impact, contributing 2.5 %. The initial LR and the activation function each contribute 4.2 % to the MLP performance, whereas the relevance of the remaining hyperparameters is below 3 %.

Fig. 8.5 shows the distribution of the total deviation $d_{\text{rec}} = |\vec{r}_{\text{rec}} - \vec{r}_{\text{true}}|$ between the reconstructed and true energy-weighted vertex $\vec{r}_{\text{Qdep}}$ for the test dataset. The distribution exhibits a median of 15.0 cm and a mean of $\bar{d}_{\text{rec}} = 18.3\,\text{cm}$, with the majority of events being reconstructed within 30 cm. The overall vertex resolution is thus well below 1 m, which was assumed in a previous sensitivity study for low-energy atmospheric neutrinos

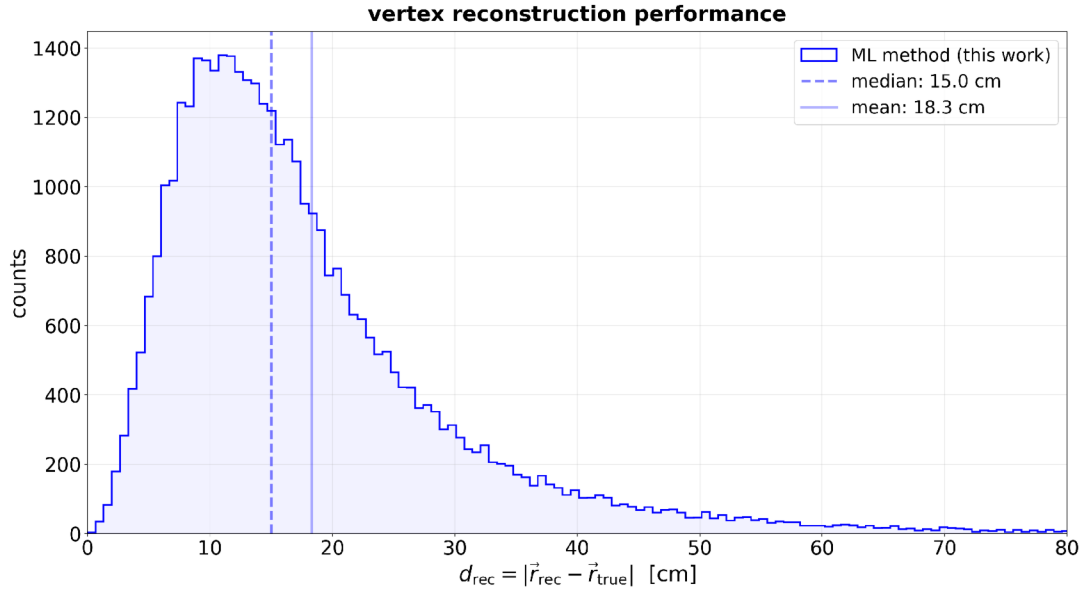

Figure 8.5: Distribution of the distances $d_{\text{rec}} = |\vec{r}_{\text{rec}} - \vec{r}_{\text{true}}|$ between reconstructed and true energy weighted vertex $\vec{r}_{\text{Qdep}}$ for the ML-based approach developed in this work. The median (dashed vertical line) and the mean (solid vertical line) values of the residuals are added.

in JUNO [99]. In the following, the distribution of the reconstruction residuals d_{rec} with respect to the visible energy E_{vis} and the true radial position of the energy-weighted vertex $\vec{r}_{\text{Qdep}}$ is examined in more detail.

Energy Dependence

The mean vertex resolution per bin is shown in the upper panel of Fig. 8.6 as a function of the visible energy E_{vis}. While the resolution above $\sim 150\,\text{MeV}$ reaches a plateau of $\sim 15\,\text{cm}$, the mean deviation increases significantly towards lower energies and reaches values of about 35 cm at $E_{\text{vis}} \approx 12\,\text{MeV}$. This behavior can be attributed to the decreasing photoelectron statistics at lower energies, which is also indicated by the fraction of PMTs for which no waveform features could be extracted due to insufficient signal quality. The resulting fraction of invalid features is shown in the lower panel of Fig. 8.6 and exhibits a drastic trend. While only $\sim 7\,\%$ of the features carry invalid entries at $E_{\text{vis}} = 300\,\text{MeV}$, this fraction rises to nearly 90 % at 12 MeV, leaving the NN with only about 1,761 valid PMTs for the vertex reconstruction.

A further consequence of the reduced photon statistics concerns the relative statistical fluctuations of the input features. In particular, the temporal resolution of the FHT is increasingly limited by the smearing of the TTS. The energy-dependent vertex resolution is therefore proportional to $d_{\text{rec}} \propto 1/\sqrt{E_{\text{vis}}}$ for low energies [145], which is also observed in the ML-based approach of this work. Despite these limiting factors, the results of the ML-based vertex resolution developed in this work are consistent with those of the classical OMILREC method, as well as other ML-based approaches in the transition region to the reactor neutrino regime, which also yield a resolution of $\sim 30\,\text{cm}$ at 12 MeV [147, 155]. The total mean resolution of $\bar{d}_{\text{rec}} = 18.3\,\text{cm}$ remains valid within the standard deviation across nearly the entire energy range, as indicated by the shaded band in the upper panel of Fig. 8.6.

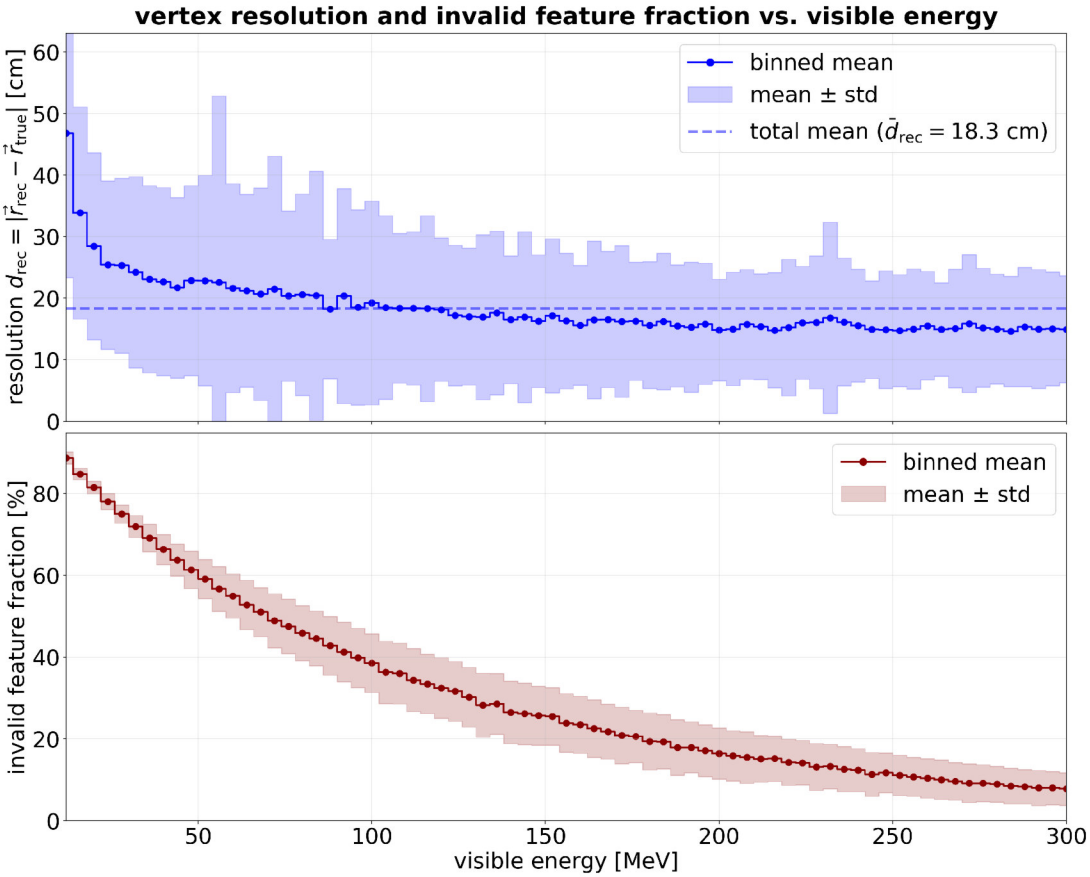

Figure 8.6: Upper panel: Mean vertex reconstruction resolution $d_{\text{rec}} = |\vec{r}_{\text{rec}} - \vec{r}_{\text{true}}|$ as a function of the visible energy E_{vis}. The blue histogram shows the binned mean with the shaded band indicating $\pm 1\sigma$. The dashed horizontal line marks the overall mean resolution $\bar{d}_{\text{rec}} = 18.3\,\text{cm}$. Lower panel: Mean fraction of invalid input features per event as a function of the visible energy.

Radial Dependence

Fig. 8.7 shows the residual distribution for each vertex coordinate separately as a function of the respective true coordinate values, to analyze the ML reconstruction

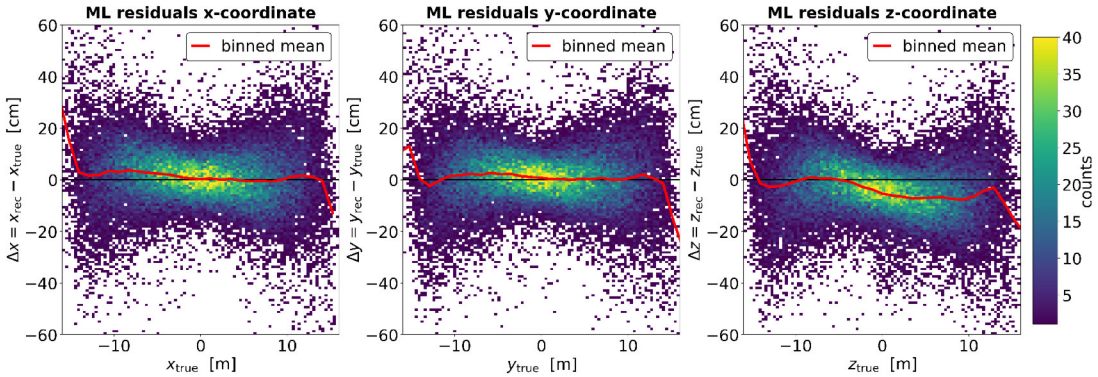

Figure 8.7: Residuals of the reconstructed ML vertex coordinates as a function of the true position. The red curves indicate the binned mean values.

performance in the fiducial detector volume. Within the fiducial volume $R_{\text{fid}} \leq 16\,\text{m}$, the ML vertex reconstruction is robust and exhibits only small mean deviations, with the largest discrepancies appearing at the detector edge (cf. red curve).
A more detailed comparison of the radial dependence is shown in Fig. 8.8, where the vertex resolution obtained with the ML approach is displayed as a function of the true energy-weighted radial position $r = |\vec{r}_{\text{true}}|$. The upper panel displays the mean and

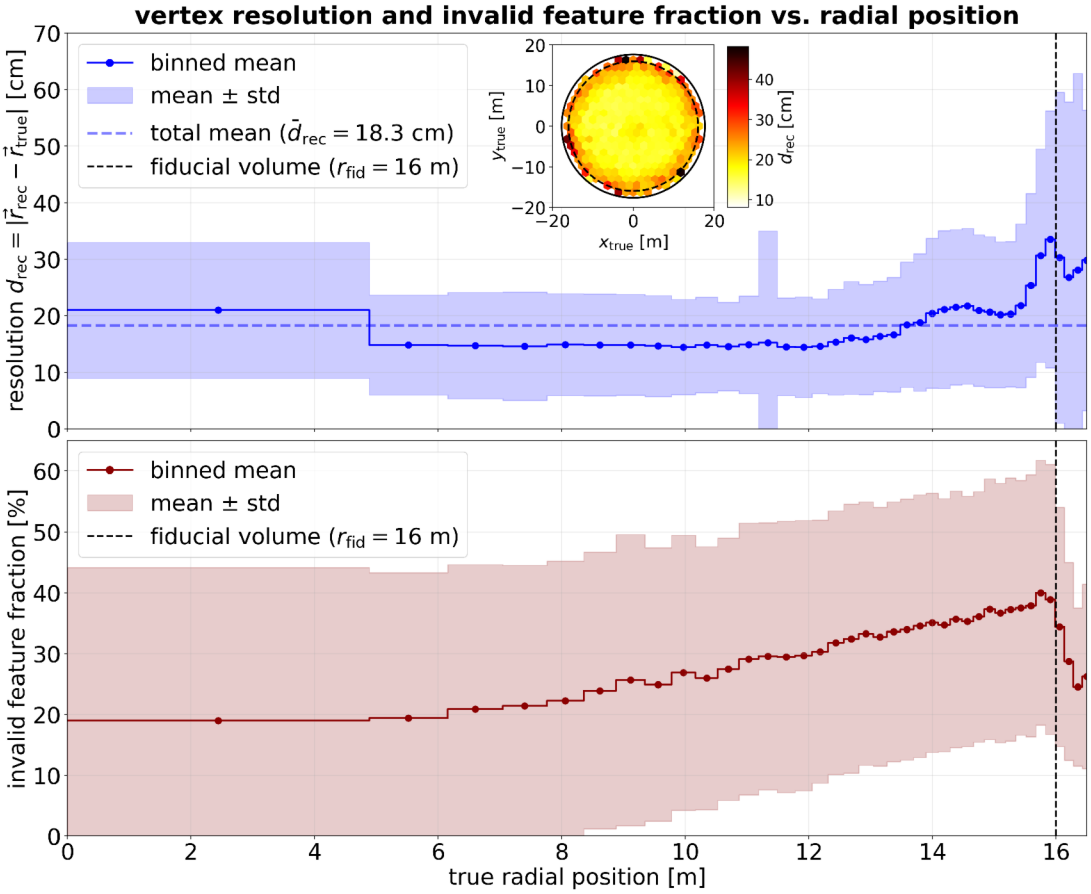

Figure 8.8: Upper panel: Mean vertex reconstruction resolution $d_{\text{rec}} = |\vec{r}_{\text{rec}} - \vec{r}_{\text{true}}|$ as a function of the true energy-weighted radial position $r = |\vec{r}_{\text{true}}|$. The blue histogram shows the volume-equidistant binned mean resolution with the shaded band indicating $\pm 1\sigma$. The dashed horizontal line marks the overall mean resolution of $\bar{d}_{\text{rec}} = 18.3\,\text{cm}$. The inset plot in the upper panel shows the residual distribution in the x-y plane, while the dashed circle marks the fiducial volume with $r_{\text{fid}} = 16\,\text{m}$ and the solid line corresponds to the full detector volume $r = 17.7\,\text{m}$. Lower panel: Mean fraction of invalid input features per event as a function of the radial position. The vertical dashed black lines indicate the fiducial volume radius of $r_{\text{fid}} = 16\,\text{m}$, which was applied as a selection criterion on the MC truth interaction vertex $\vec{r}_{\text{IBD}}$ of the training data (cf. Sec. 8.1.1).

standard deviation of the resolution per radial bin, which were chosen in a volume-equidistant manner ($\propto r^3$) to ensure comparable statistics across all bins. The mean vertex resolution within the fiducial volume shows a largely constant performance and remains within the 1σ uncertainty of the overall mean of $\bar{d}_{\text{rec}} = 18.3\,\text{cm}$ (dashed blue line) across the entire radial range. For $r > 14\,\text{m}$, a slight increase in the mean deviation

is observed, which becomes more pronounced above $\sim 15.5\,\mathrm{m}$ and reaches $\sim 33\,\mathrm{cm}$ at $r = 16\,\mathrm{m}$. One factor contributing to the degradation of reconstruction at the detector edge is total reflection at the interface between LS and water, which becomes relevant at a radius of $r \gtrsim 15.9\,\mathrm{m}$ [145]. This particularly affects the accuracy of the FHT time information, while at the same time, the asymmetric distribution of detected scintillation photons across the PMTs for events near the detector boundary leads to a distorted charge pattern.
Another factor contributing to poorer reconstruction performance at the detector edge is the increasing fraction of invalid input features, which is shown in the lower panel of Fig. 8.8. At the edge of the fiducial volume, the average fraction of failed waveform feature extraction is approximately 40 %, which is almost twice as large as in the center of the detector ($\sim 20\,\%$). However, the fraction of invalid features is much more strongly influenced by the visible energy (lower panel of Fig. 8.6) than by the radial position of the event, as reflected by the large standard deviations in the radial bins, which are averaged over all energies. The geometry thus plays a subordinate role compared to the energy dependence in determining the feature validity.
Since the initial interaction vertex $r_{\mathrm{IBD}} \leq r_{\mathrm{fid}} = 16\,\mathrm{m}$ was restricted to the fiducial volume when generating the training data (cf. Sec. 8.1.1), there are individual events whose energy-weighted vertex $\vec{r}_{\mathrm{Qdep}}$ exceeds this limit. The two dimensional projection of the residuals in the x-y plane shown in the inset plot indicates that the largest outliers are found in this region, which is also confirmed by the sharp increase in standard deviation for $r > 16\,\mathrm{m}$.

Summary and Discussion

In this section, a ML–based approach for the vertex reconstruction of IBD events in the visible energy window $E_{\mathrm{vis}} \in [12, 300]\,\mathrm{MeV}$ was developed, which is not covered by any other reconstruction method in JUNO. The MLP reconstructs the energy-weighted event vertex $\vec{r}_{\mathrm{Qdep}}$ from four waveform features per PMT together with an additional mask identifying invalid features. The optimized model yields a mean three-dimensional deviation of $\bar{d}_{\mathrm{rec}} = 18.3\,\mathrm{cm}$ with a median of 15.0 cm, which is well below the uncertainty of 1 m assumed in a previous sensitivity study [99]. The coordinate specific reconstruction uncertainties

$$\begin{aligned} \Delta x &= (13.02 \pm 0.05)\,\mathrm{cm} \\ \Delta y &= (12.80 \pm 0.05)\,\mathrm{cm} \\ \Delta z &= (13.48 \pm 0.05)\,\mathrm{cm} \end{aligned} \tag{8.2}$$

are displayed in Fig. 8.4 and used as an estimate of the vertex resolution for the prompt event in the subsequent sections[4]. The radial dependence shows largely constant performance within the fiducial volume, with moderate deterioration above $r \gtrsim 14\,\mathrm{m}$, reconstruction, among other things, by total reflection at the LS-water interface. In addition to the vertex resolution, the same waveform features could also be used as input for an ML-based energy reconstruction, which should be investigated in future work.

[4]The quoted uncertainties of $\pm 0.05\,\mathrm{cm}$ on the coordinate resolutions correspond to the standard error of the standard deviation, given by $\Delta\sigma = \sigma/\sqrt{2(N-1)}$ for Gaussian-distributed residuals, where $N = 40{,}000$ is the test sample size.

8.2 IBD Event Topology Selection

IBD events provide a characteristic prompt-delayed signature that enables powerful background suppression. The prompt signal, defined within the first 1000 ns after the neutrino event, is primarily generated by the positron depositing its kinetic energy in the LS. The delayed event is produced by the capture of a single neutron after its thermalization, occurring with a typical time constant of 219.7 μs [115]. This spatial and temporal coincidence leads to a characteristic event topology with a well-defined delayed signal energy, which corresponds to the characteristic γ-ray released during the n-capture. For capture on ^{1}H, which accounts for $\sim 99\,\%$ of all captures, this energy is $E_{\gamma,\mathrm{nCap}} = 2.2\,\mathrm{MeV}$. In contrast, CC events (excluding IBD) and NC events exhibit diverse topologies with either no or multiple delayed signals from n-captures. Especially at higher energies, usually multiple neutrons are produced through final state interactions, leading to multiple delayed signals. Additionally, CC events from ν_μ and $\bar{\nu}_\mu$ also frequently produce delayed signals from muon decays or captures (cf. Sec. 5.2.2), which can be distinguished from n-captures with high probability. To identify genuine IBD event topologies, several reactor neutrino studies have previously discussed effective IBD selection cuts for JUNO and optimized them concerning the dominant backgrounds in the low energy region $E_\mathrm{vis} < 10\,\mathrm{MeV}$ (cf. Sec. 7.1) [67, 156]. Since this work extends the IBD channel up to a visible energy of $E_\mathrm{vis} = 300\,\mathrm{MeV}$, a separate analysis of the optimal IBD cuts was performed. For this purpose, more than 500,000 IBD events and approximately 2 million CC events (excluding IBD) and NC events were analyzed, which were generated isotropically within the fiducial volume of 14.77 kton ($R_\mathrm{fid} \leq 16\,\mathrm{m}$) using the JUNO detector simulation[5] (cf. dataset $D7$ in Tab. C.1). All relevant detector effects, including nonlinearity and quenching, are accounted for in the JUNO detector simulation. The MC truth for energy and vertex of both prompt and delayed events is smeared with the corresponding resolution in JUNO, reflecting the effects from readout electronics and reconstruction algorithm methods. As discussed in detail in Sec. 5.3, the energy resolution in JUNO depends on the energy regime and is considered for the prompt and the delayed events by applying the parameterized energy resolution given in Eq. 5.12 to the quenched deposited energy E_Qdep. The vertex resolution of the prompt events was discussed in detail in Sec. 8.1, where a ML-based approach for vertex reconstruction was introduced. The coordinate-specific mean uncertainties in Eq. 8.2 were used as an effective vertex resolution over the entire visible energy spectrum and were applied in the form of a Gaussian smearing to the true, energy-weighted vertices $\vec{r}_\mathrm{Qdep}$. In the region $E_\mathrm{vis} < 6\,\mathrm{MeV}$, which is relevant for the n-captures of hydrogen ^{1}H and carbon ^{12}C, the OMILREC vertex resolution can be estimated as

$$\Delta r_\mathrm{vert} = \frac{90\,\mathrm{mm}}{\sqrt{E_\mathrm{vis}/[\mathrm{MeV}]}} \,,$$

which corresponds to a vertex resolution of $\sim 60\,\mathrm{mm}$ for an n-capture on ^{1}H ($E_\mathrm{vis} = 2.2\,\mathrm{MeV}$) and $\sim 40\,\mathrm{mm}$ for an n-capture on ^{12}C ($E_\mathrm{vis} = 4.9\,\mathrm{MeV}$) [145].

[5] The IBD and NC events are uniformly distributed in the visible energy range $E_\mathrm{vis} \in [12, 300]\,\mathrm{MeV}$. The CC events (excluding IBD) are uniformly distributed for energies above 100 MeV but have lower statistics for smaller visible energies due to the dominance of the IBD channel. For CC and NC events, neutrino energies up to 20 GeV were considered, since these produce visible energies in the relevant window, as shown in Fig. 5.6.

8.2.1 IBD Selection Cuts and Detection Efficiency

In the following, the five selection criteria for IBD events are presented, and the total IBD detection efficiency $\varepsilon_{\text{top,IBD}}(E_{\text{vis}})$ after restricting the event topology is discussed as a function of the prompt visible energy E_{vis}. The five IBD selection criteria include the

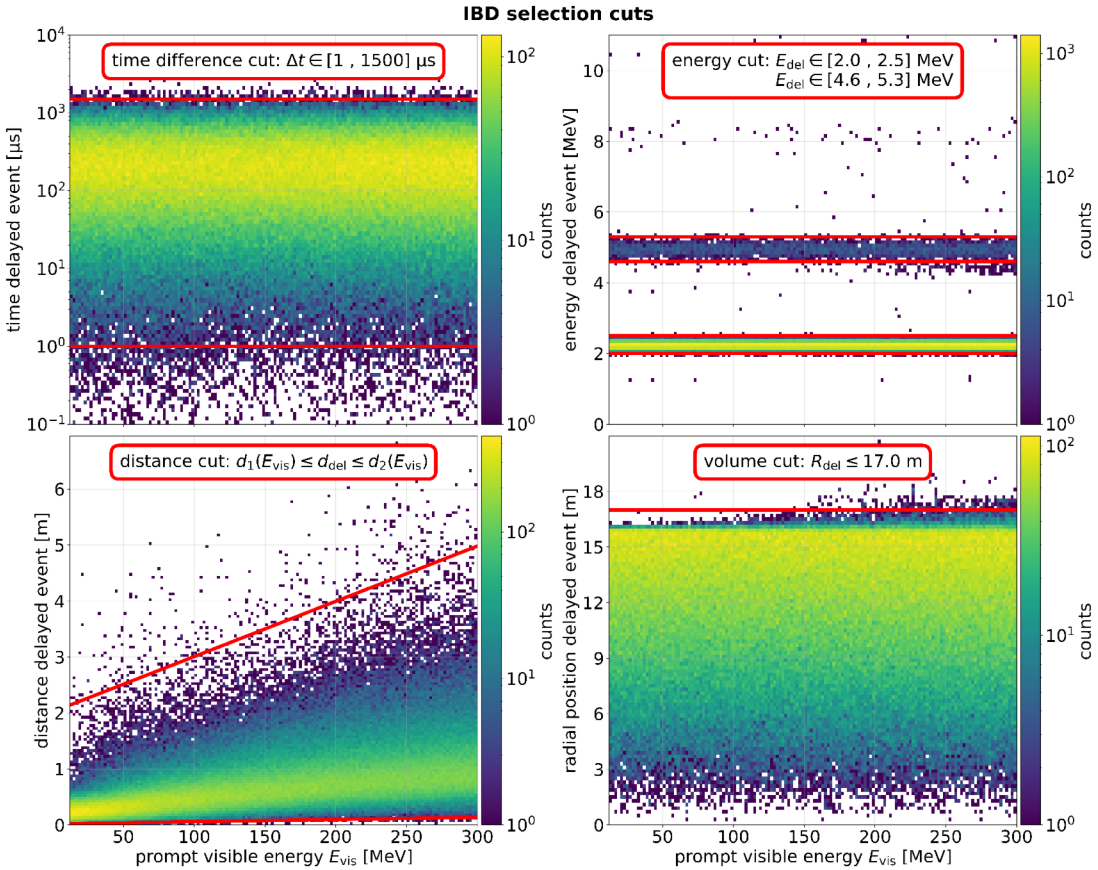

Figure 8.9: Distribution of all delayed events from 500,000 MC simulated IBD events in a visible energy range $E_{\text{vis}} \in [12, 300]$ MeV (cf. IBD dataset $D7$ in Tab. C.1). The red lines indicate the independent selection cuts for the time coincidence Δt_{del} (upper left), the delayed energy E_{del} (upper right), the distance d_{del} between IBD vertex an n-capture (lower left) and the volume cut with R_{del} (lower right).

time difference Δt_{del} and the spatial separation d_{del} between the prompt and delayed events, exploiting their characteristic temporal and spatial coincidence. In addition, the energy E_{del} and the radial position R_{del} of the delayed event are considered. The distributions of these parameters for all simulated IBD events are shown in Fig. 8.9. Additionally, the multiplicity N_{del} of delayed events is included in the IBD selection to account for the CC0p1n topology of genuine IBD interactions. In the following, each selection cut is discussed separately.

Temporal Coincidence Cut

As a first step, all delayed events that exhibit the correct temporal correlation are filtered. Since the prompt window is defined within $t_{\text{prompt}} \leq 1\,\mu$s, the condition for the time

difference between prompt and delayed signal was chosen to be

$$1.0\,\mu\text{s} \leq \Delta t_{\text{del}} \leq 1.5\,\text{ms}\ . \tag{8.3}$$

In Fig. 8.10, the cumulative distribution of n-capture times is shown, together with the characteristic time constant of $\tau = 215\,\mu$s implemented in the JUNO simulation, after which approximately 63 % of all neutrons are captured (obtained from IBD dataset $D7$ in Tab. C.1). Within the prompt time window of $t < 1.0\,\mu$s (gray hatched), only 0.46 % of n-captures occur, therefore the lower time cut causes a negligible loss of events, and the upper limit of $1.5\,\text{ms} \sim 7\,\tau$ contains more than 99.67 % of all captures. Thus, within the time interval defined in Eq. 8.3, a total of 99.21 % all n-capture events are covered.

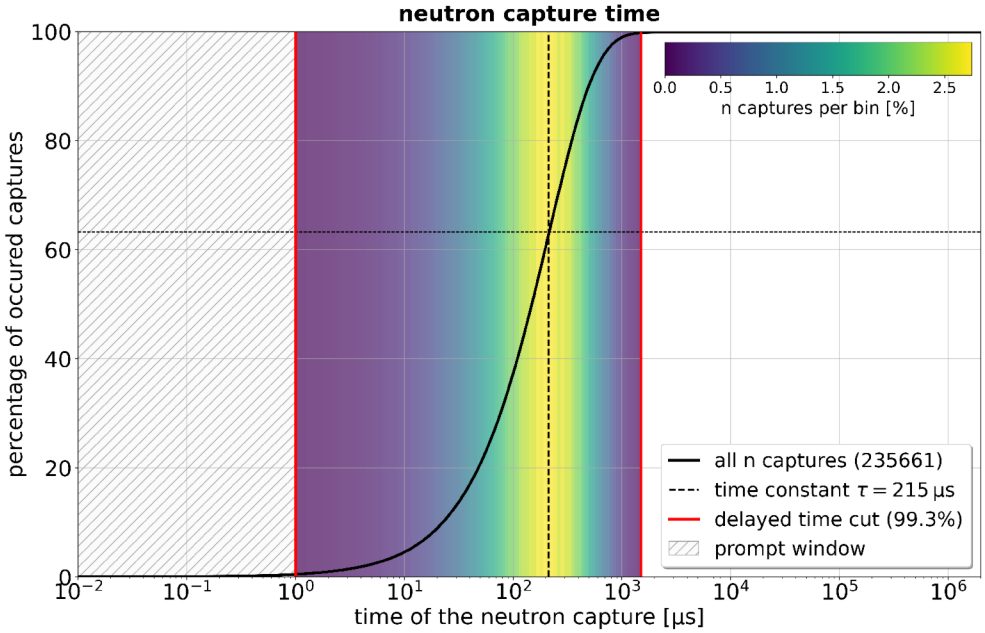

Figure 8.10: Cumulative distribution of capture times for all simulated delayed IBD n-capture events. The black curve shows the percentiles of the capture times, while the dashed line marks the n-capture time $\tau = 215\,\mu$s obtained in the data. The red lines mark the chosen delayed time window covering 99.3 % of all events. The colored bins in the delayed time window (100 bins in total) indicate the relative n-captures in that time interval, which reflects the n-capture probability. The gray shaded region below 1 μs corresponds to the prompt time window.

Multiplicity Cut

Since exactly one event from the n-capture is expected in the delayed time window for genuine IBD events, the multiplicity for the number of delayed events is set to

$$N_{\text{del}} = 1 \tag{8.4}$$

This cut is particularly effective for suppressing NC and other CC events (apart from IBD), as multiple neutrons or other delayed events, such as μ decays or de-excitations of unstable isotopes, are frequently produced during these interactions.

Delayed Energy Cut

The visible energy of the delayed event E_{del} can be constrained very precisely since it corresponds to the n-capture γ energies. Although most neutrons are captured by protons, two energy intervals are defined for the energy cut [67]

$$2.0\,\text{MeV} \leq E_{\text{del}} \leq 2.5\,\text{MeV} \quad \text{or} \quad 4.6\,\text{MeV} \leq E_{\text{del}} \leq 5.3\,\text{MeV} \; . \tag{8.5}$$

The first window covers the 2.2 MeV γ-ray from n-capture on ^{1}H and contains 98.77 % of all events, while the second window corresponds to the 4.9 MeV γ-ray from n-capture on ^{12}C, containing an additional 1.12 %.

Distance Cut

In addition to the temporal correlation, the IBD topology also provides a spatial coincidence since the neutron does not travel a large distance in the LS during its thermalization. Accordingly, a cut on the distance d_{del} between the prompt and the n-capture vertex can be applied. However, the reconstructed prompt vertex does not correspond to the original interaction vertex $\vec{r}_{\text{IBD}}$, but describes the vertex $\vec{r}_{\text{Qdep}}$ weighted by the quenched deposited energy (cf. Sec. 8.1). As illustrated in Fig. 8.1, the track along which the positron deposits its kinetic energy becomes larger with increasing visible energy, and the prompt event becomes less point-like. As illustrated in Fig. 8.3, the reconstructed weighted vertex $\vec{r}_{\text{Qdep}}$ moves further away from the original interaction vertex $\vec{r}_{\text{IBD}}$ for higher visible energies, while the n-capture of the simulated IBD events occurs within a constant median distance of $\sim$ 20 cm from the original interaction location. For this reason, a linear correlation can be observed in the lower left panel of Fig. 8.9. For the distance $d_{\text{del}} = |\vec{r}_{\text{Qdep}} - \vec{r}_{\text{nCap}}|$ between the prompt and delayed vertex, an energy-dependent linear cut is therefore defined according to

$$d_1(E_{\text{vis}}) \leq d_{\text{del}} \leq d_2(E_{\text{vis}}) \tag{8.6}$$

with $d_i(E_{\text{vis}}) = m_i \cdot E_{\text{vis}} + c_i$. The parameters m_i and c_i are determined such that for each of 50 energy bins in the range $E_{\text{vis}} \in [12, 300]\,\text{MeV}$, at most 0.1 % of the events are excluded at the upper and lower bounds, respectively. The best-fit results are $m_1 = (0.391 \pm 0.026)\,\text{mm/MeV}$ and $c_1 = (18.3 \pm 1.7)\,\text{mm}$ for the lower cut and $m_2 = (10.32 \pm 0.41)\,\text{mm/MeV}$ and $c_2 = (2001 \pm 74)\,\text{mm}$ for the upper bound.

Fiducial Volume Cut

In addition to the fiducial volume cut of $R_{\text{fid}} \leq 16\,\text{m}$ applied to the prompt event (cf. Sec. 7.5), a separate volume criterion is introduced for the delayed signal. This requires the delayed event to be reconstructed within a radius of R_{del} which suppresses edge effects, such as reflections from the acrylic sphere and the fast neutron (FN) background (cf. Sec. 7.2).

Fig. 8.11 shows the average cut efficiencies as a function of visible energy E_{vis} in 2 MeV bins. The delayed coincidence cut (red curve) removes all events that fail to produce a delayed signal. While such events remain rare for $E_{\text{vis}} < 50\,\text{MeV}$, their fraction increases substantially at higher energies, mainly due to the inelastic secondary process $^{12}\text{C}(n,\alpha)^{9}\text{Be}$ (cf. Eq. 5.4), in which the neutron is absorbed. For $E_{\text{vis}} > 100\,\text{MeV}$, the temporal coincidence cut maintains a constant efficiency of approximately 95 %. In this energy regime, the multiplicity cut (green curve) becomes the dominant cut, as multiple delayed events are increasingly produced. This is primarily due to the

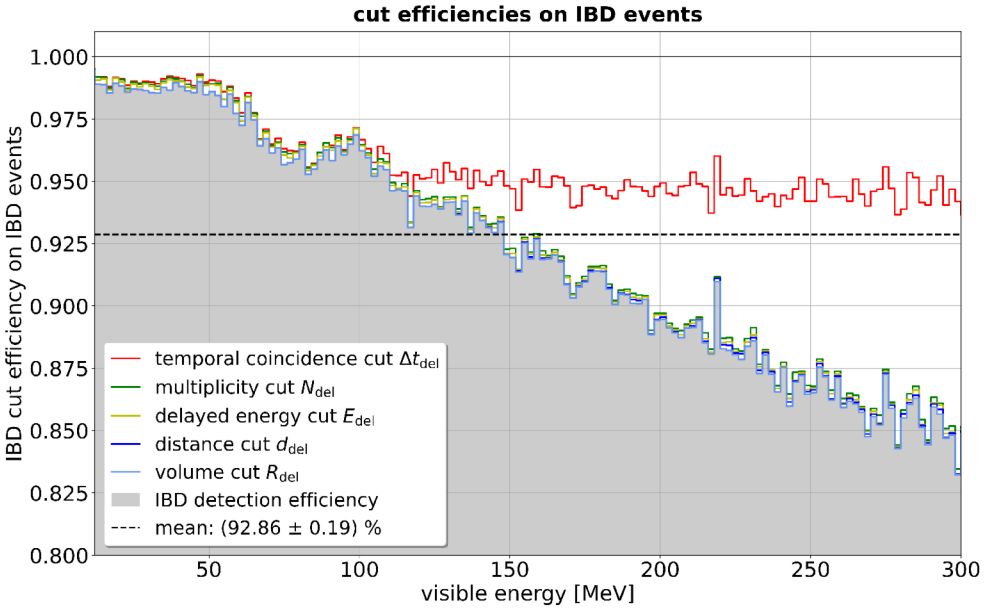

Figure 8.11: IBD detection efficiency $\varepsilon_{\text{top,IBD}}(E_{\text{vis}})$ (gray hatched) as a function of the visible energy of the event. The individual contributions of different selection cuts are shown as colored lines and summarized in Tab. 8.2.

inelastic secondary process $^{12}\text{C}(n, n + 3\alpha)$ (cf. Eq. 5.5), where ionizing alpha particles frequently generate additional neutrons through collisions. The delayed energy cut (yellow curve), distance cut (dark blue curve), and volume cut (light blue curve) retain most events, resulting in a final IBD detection efficiency (gray shaded region) that is primarily controlled by the temporal coincidence cut for $E_{\text{vis}} < 100\,\text{MeV}$ and by the multiplicity cut for $E_{\text{vis}} > 100\,\text{MeV}$. The individual average cut efficiencies and the mean total IBD detection efficiency of $\varepsilon_{\text{top,IBD}} = 92.86\,\%$ are summarized in Tab. 8.2.

Table 8.2: Selection criteria and cut parameters for the delayed signal of IBD events. N_{before} denotes the number of simulated IBD events before the cut was applied and N_{after} is the number of event, which passed the cut. With these number the efficiency of each selection cut, including its statistical uncertainty as well as the average IBD detection efficiency $\varepsilon_{\text{top,IBD}}$ from the topological selection is derived.

selection criteria	IBD signal cut	N_{before}	N_{after}	$\varepsilon_{\text{top,IBD}}[\%]$
Delayed Time	$1\,\mu\text{s} \leq \Delta t_{\text{del}} \leq 1.5\,\text{ms}$	505,349	484,925	95.96 ± 0.19
Multiplicity	$N_{\text{del}} = 1$	484,925	470,637	97.05 ± 0.20
Delayed Energy	$2.0\,\text{MeV} \leq E_{\text{del}} \leq 2.5\,\text{MeV}$ $4.6\,\text{MeV} \leq E_{\text{del}} \leq 5.3\,\text{MeV}$	470,637	470,132	99.89 ± 0.21
Distance	$d_1(E_{\text{vis}}) \leq d_{\text{del}} \leq d_2(E_{\text{vis}})$	470,132	469,420	99.85 ± 0.21
Fiducial Volume	$R_{\text{del}} \leq 17.0\,\text{m}$	469,420	469,267	99.97 ± 0.21
IBD Detection Efficiency		**505,349**	**469,267**	$\mathbf{92.86 \pm 0.19}$

8.2.2 Cut Efficiency of CC and NC Events

In the visible spectrum shown in Fig. 7.9, all CC and NC events are initially considered without any restrictions on the event topology. However, only those events that survive the IBD cuts represent a background for the IBD channel. To determine the fraction of such events, approximately 2 million CC events (excluding IBD) and 7 million NC events in the energy window $E_{\text{vis}} \in [12, 300]\,\text{MeV}$ were analyzed. The MC events were simulated isotropically in the detector using the JUNO detector simulation and, analogous to the IBD events in Sec. 8.2.1, were smeared according to the corresponding vertex and energy resolution. All events that produce a signal in the LS after the prompt window of $1\,\mu\text{s}$ were examined in the analysis. In addition to n-captures, these can be triggered by the de-excitation of excited isotopes or by muon decays.
In Fig. 8.12, the IBD cut efficiencies $\varepsilon_{\text{top,CC}}(E_{\text{vis}})$ for CC events without IBD (upper panel) and $\varepsilon_{\text{top,NC}}(E_{\text{vis}})$ for NC events (lower panel) are shown as a function of the visible energy E_{vis}. The colored lines show, analogously to Fig. 8.11, the fraction of events that satisfy the individual IBD selection cuts and thus exhibit an IBD-like topology. The gray shaded area is the final cut efficiency after all IBD selection criteria have been applied and thus reflects the probability with which a CC or NC event mimics an IBD signal. Approximately 80 % of the CC events (excluding IBD) produce at least one delayed event in the relevant time window defined in Eq. 8.3. However, since only about 32 % of the events produce a single delayed event, while in the other events, either multiple n-captures or muon decays cause more than one event in the relevant time window, many of these events are excluded by the multiplicity cut in Eq. 8.4. The selection cuts for the delayed energy in Eq. 8.5 suppress an additional 24 % of the events remaining after the multiplicity cut, while the distance and volume cuts reject only a further 6 % of the CC events. In total, $(78.08 \pm 0.04)\,\%$ of all considered IBD-like CC events are rejected, such that on average only $(21.93 \pm 0.04)\,\%$ of CC events exhibit an IBD-like topology and remain relevant as background. The final cut efficiency $\varepsilon_{\text{top,CC}}(E_{\text{vis}})$ after applying all selection cuts (gray hatched area in the upper panel of Fig. 8.12) is relatively constant over the entire visible energy window and only slightly decreases towards larger energies. However, the statistics for energies $E_{\text{vis}} < 100\,\text{MeV}$ are relatively low, since the IBD channel clearly dominates in this region. CC events that are not IBD events at these energies are mainly ν_e interactions on ^{1}H that do not produce any neutrons.
For NC events (lower panel of Fig. 8.12), the overall suppression is even more efficient. The two most effective selection criteria are the time difference cut (red curve) and the multiplicity cut (green curve), suppressing 78 % of all NC events. Especially at higher visible energies of $E_{\text{vis}} > 150\,\text{MeV}$, only about 19 % of the events exhibit a single delayed event and can therefore mimic a real IBD event. The energy cut (yellow curve) excludes hardly any additional NC events, since the delayed events are almost always n-captures. However, especially at small visible energies, up to half of the NC events can be suppressed by the distance cut (dark blue curve), since the neutrons are often captured further away from the reconstructed prompt vertices $\vec{r}_{\text{Qdep}}$ than for IBD events. This is mainly because NC events involve spallation neutrons that have a higher kinetic energy than the IBD neutrons, which leads to a larger diffusion distance before they are captured. Overall, the distance cut excludes a further 30 % of the events that survive the energy cuts. The volume cut (light blue curve) contributes only marginally to the final cut efficiency (gray shaded area in Fig. 8.12), which remains constant over a wide energy range. Overall, $(86.65 \pm 0.03)\,\%$ of all NC events are removed by the IBD selection, such that on average only $\varepsilon_{\text{top,NC}} = (13.36 \pm 0.03)\,\%$ of NC events pass the topological constraints and remain as IBD-like background.

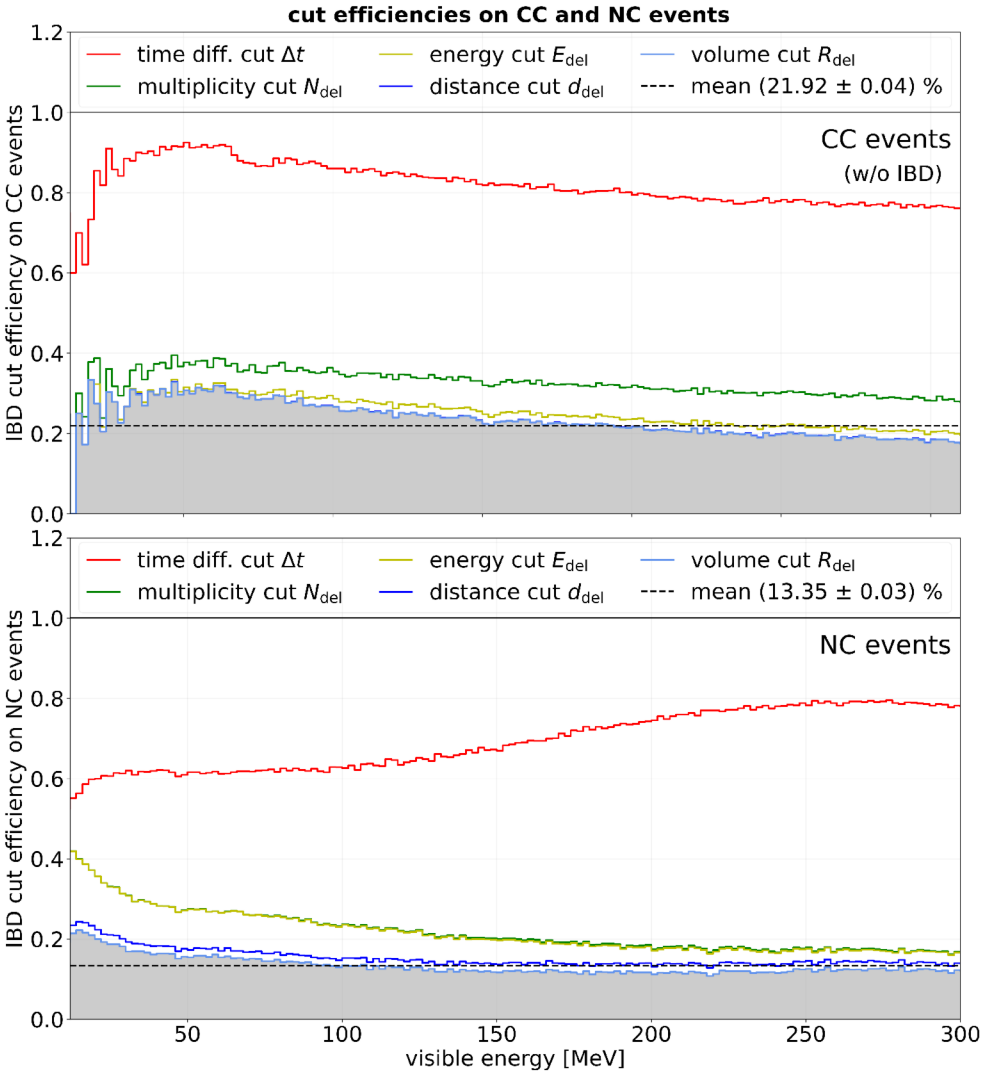

Figure 8.12: IBD cut efficiencies on CC (excluding IBD) and NC events as a function of the visible energy E_{vis}. The final cut efficiencies $\varepsilon_{\text{top,CC}}(E_{\text{vis}})$ and $\varepsilon_{\text{top,NC}}(E_{\text{vis}})$ (gray) indicate the fraction of events that pass the IBD cuts and can thus mimic an IBD event. The average cut efficiency are indicated by the dashed lines.

In summary, the results of the topological event classification show that the selection cuts retain $\varepsilon_{\text{top,IBD}} \approx 92.8\,\%$ of genuine IBD events, while at the same time only $\varepsilon_{\text{top,CC}} \approx 21.9\,\%$ of all other CC events and only $\varepsilon_{\text{top,NC}} \approx 13.4\,\%$ of the NC events survive. The temporal coincidence cut and the multiplicity cut are predominantly responsible for the cut efficiency across all channels. The remaining background represents the actual relevant background for the sensitivity study in the MeV energy range.

8.2.3 Visible Energy Spectrum after Applying IBD Cuts

To obtain the expected visible spectrum for the IBD channel in the energy window of $E_{\text{vis}} \in [12, 300]\,\text{MeV}$, both the DM signal and the background contributions illustrated in Fig. 7.9 must be multiplied by the corresponding cut efficiencies $\varepsilon_{\text{top,IBD}}$, $\varepsilon_{\text{top,CC}}$ and $\varepsilon_{\text{top,NC}}$, which depend on the visible energy E_{vis}. Fig. 8.13 shows the expected visible energy spectrum after 10 yr of data taking in a fiducial volume of 14.77 kton before

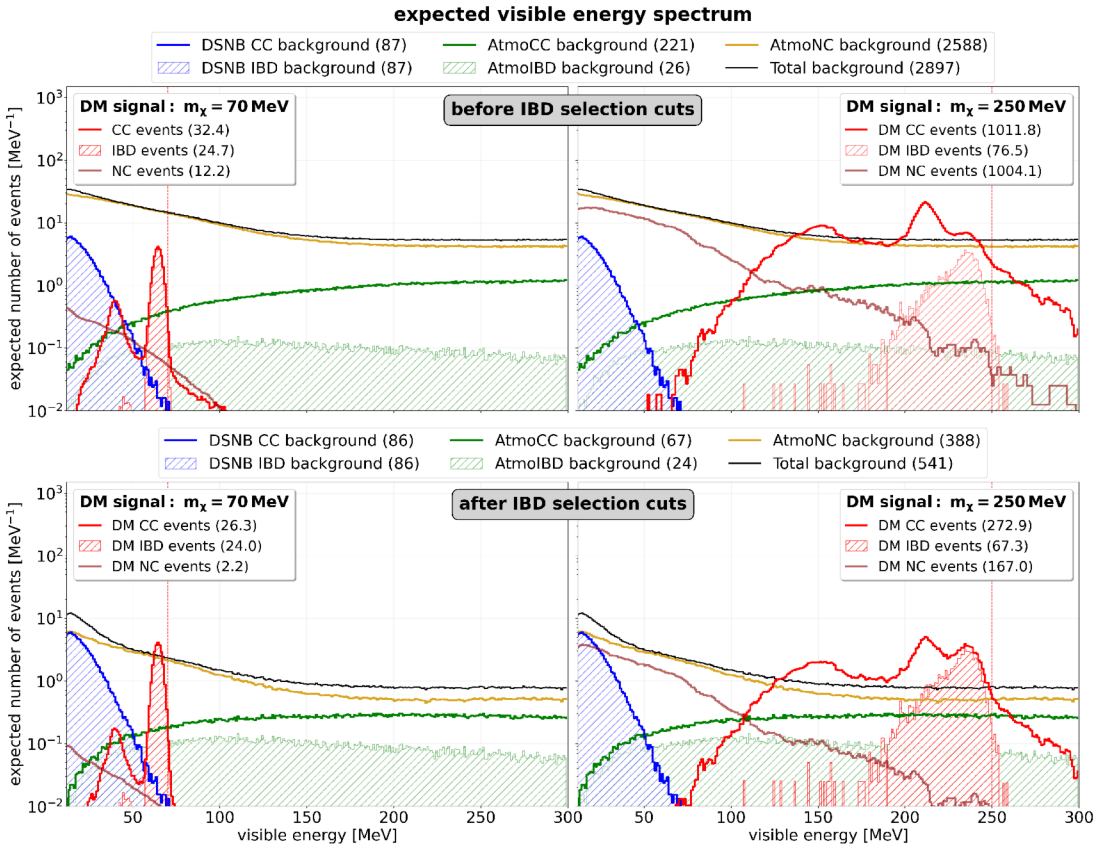

Figure 8.13: Expected visible energy spectrum in JUNO for a fiducial mass of 14.77 kton after 10 yr data taking before (top row) and after (bottom row) applying the IBD selection cuts. The left panel corresponds to the DM mass $m_\chi = 70\,\text{MeV}$ and the right panel to $m_\chi = 250\,\text{MeV}$. The atmospheric CC (green) and NC (yellow) background, as well as the DSNB background (blue) is shown together with the total background (black). The IBD component of CC contributions are indicated by hatched areas. For the DM signals the CC and NC contributions are shown in red, and the vertical dashed line indicates the DM mass. The numbers correspond to the expected event number in the visible energy range.

and after applying the IBD selection cuts (top and bottom rows, respectively). The spectra are shown for two representative DM signal masses $m_\chi = 70\,\text{MeV}$ (left) and $m_\chi = 250\,\text{MeV}$ (right). Since the background contributions before and after applying the IBD cuts are identical for both DM scenarios, they are summarized in common legends above each row, including the expected event numbers for the individual background components. The background consists of atmospheric CC (green) and NC events (yellow), as well as contributions from the DSNB (blue). The hatched areas indicate the IBD fraction of the CC-induced background. Applying the IBD selection cuts reduces the total expected background from 2897 events (black curve top row) to 540 events (black curve bottom row) for the examined exposure time, which corresponds to approximately 15 % of the original events.

The DM scenario for a mass of $m_\chi = 70\,\text{MeV}$ (left column) shows a characteristic sharp IBD peak as discussed in Sec. 6.2.1, which is barely reduced by applying the selection cuts due to the high IBD detection efficiency of $\sim 99\,\%$ in this region (cf. Fig. 8.11). The DSNB background, as well as the IBD fraction of the atmospheric CC

background, represents an irreducible contribution in this region, which is, however, subdominant at 70 MeV. The dominant background from atmospheric NC events can be reduced to $\sim 20\,\%$ by the selection cuts, so that the DM signal represents the most dominant contribution in a narrow energy range under the assumption of the Super-K limits for the thermally averaged self-annihilation cross section (cf. Sec. 6.1). The signal-to-background (S2B) ratio

$$\text{S2B ratio:} \quad \frac{n_S}{\sqrt{n_S + n_B}} \,, \tag{8.7}$$

which takes into account the event numbers for signal n_S and all backgrounds n_B, is increased by 91 % to $1.19\,\sigma$ after applying the IBD selection cuts. This confirms that constraining the event topology is a powerful tool for background suppression in the MeV energy range.
In contrast, the DM scenario with $m_\chi = 250\,\text{MeV}$ (upper right panel) exhibits a broad CC-induced energy spectrum, which produces an IBD event in only about 13 % of cases. In particular, the characteristic ν_e CC1p0n peak, discussed in detail in Sec. 6.2.2, is strongly suppressed by the IBD selection cuts, since no neutron is produced at the primary interaction vertex. The fact that the S2B ratio is reduced by approximately a factor of two, from 28.8 to 14.0, already indicates that this background suppression strategy loses effectiveness in the sub-GeV energy regime. Instead, the sensitivity increases when the full CC channel is taken into account. Determining the transition between the IBD and CC dominated regions is part of this work. After applying the IBD selection cuts, a residual background from other CC (excluding IBD) and NC events remains. These IBD-like events can be further suppressed using pulse shape discrimination (PSD), as discussed in the following section.

8.3 Pulse Shape Discrimination

In addition to constraining the event topology, which exploits the characteristic temporal and spatial coincidence as well as the well-defined delayed n-capture energy of genuine IBD events, there is another powerful tool for background suppression in the MeV energy range. The pulse shape discrimination (PSD) exploits the temporal shape of the prompt scintillation signal, which differs for various ionizing particles. The underlying principle is rooted in the detection principle of a LS detector and was already discussed in Sec. 4.3. During energy transfer, different ionizing particles produce different excited molecular states in the scintillator, whose decay times can vary considerably. While highly ionizing

Table 8.3: Decay time components τ_i and corresponding weights ω_i of the JUNO LS as implemented in the JUNO simulation version J24.1.2

	τ_1 / ω_1	τ_2 / ω_2	τ_3 / ω_3	τ_4 / ω_4
γ, e^-, e^+	4.6 ns / 70.7 %	15.1 ns / 20.5 %	76.1 ns / 6.0 %	397.0 ns / 2.8 %
p, n	4.5 ns / 61.4 %	15.7 ns / 23.2 %	76.2 ns / 9.0 %	367.0 ns / 6.4 %
α	4.4 ns / 49.8 %	17.6 ns / 27.4 %	89.1 ns / 14.7 %	544.5 ns / 8.1 %

heavy particles, such as α particles or hadrons, preferentially populate triplet states with relatively long decay times, lighter particles such as electrons, positrons, and due to compton scattering also γ rays predominantly excite singlet states that decay more rapidly [68]. The emission time profile of the JUNO LS in Eq. 4.1 is best described

by four distinct components for different particle species. Tab. 8.3 summarizes the corresponding decay time constants τ_i and their relative weights ω_i as implemented in the JUNO detector simulation, which forms the basis of this analysis. The goal of this study is to identify suitable methods to quantify the ratio of fast to slow scintillation components, with the aim of further suppressing the residual CC and NC background contributions after applying the IBD selection cuts (cf. Fig. 8.13), while simultaneously retaining IBD events with high efficiency.

8.3.1 Pulse Shapes and Dataset Preparation

The pulse shape of an event describes the temporal emission profile of the LS of the energy deposition of the ionizing particle. In this analysis, pulse shape discrimination is performed on IBD-like background events—specifically, those CC (excluding IBD) and NC events that survived the IBD topology selection cuts. The pulse shapes are reconstructed from the arrival times of the scintillation photons at the photocathode of the PMTs, which must be corrected, for each PMT, by the time of flight (TOF) required for the scintillation light to travel from the emission point to the photocathode [7]. The emission point is approximated by the weighted vertex $\vec{r}_{\mathrm{Qdep}}$, which is smeared with the uncertainty obtained in Sec. 8.1. At the photocathode, the photons are converted into photoelectrons with a specific photon detection efficiency (PDE) that depends on the PMT type. For the PSD in this work, the measured signals of the 17,612 20-inch PMTs were used. About 72 % of these large PMTs are micro-channel plate PMTs (Northern Night Vision Technology Co. (NNVT), China) with a mean PDE of 28.5 %, while the remaining ones are dynode-PMTs with a PDE of 30.3 % (Hamamatsu Photonics K.K., Japan) [6, 74]. The PDE of the respective PMT type is already taken into account in the `DetSim` stage of the JUNO simulation through the conversion of scintillation photons into photoelectrons at the photocathode (cf. Sec. 4.4). The temporal resolution of the PMTs is characterized by their transit time spread (TTS), which specifies the FWHM of the transit time distribution of the photoelectrons and, for a Gaussian distribution, is related to the standard deviation by $\mathrm{TTS} = 2\,\sigma_{\mathrm{t}}\sqrt{2\ln 2}$. For the micro-channel plate PMTs (NNVT) the mean TTS is 12 ns, while dynode-PMTs have a much lower TTS of 2.7 ns [74].

In this analysis, the time information of individual PMT hits from approximately 20,000 simulated MC events for each interaction channel (IBD, CC excluding IBD, and NC) is processed by first correcting the true photon arrival times for the TOF between the vertex $\vec{r}_{\mathrm{Qdep}}$ and each large PMT (cf. dataset $D8$ in Tab. C.1). The TOF correction is performed using an effective group velocity v_g, which was determined from reconstruction tuning studies and accounts for the average photon propagation in the JUNO LS [7]. After the TOF subtraction, each individual hit time is smeared by σ_t, to model the intrinsic time resolution due to TTS of the PMTs. This procedure transforms the simulated photon hit times into a detector-level time representation of the photon emission time t_{pe}. The MC events are generated isotropically within the fiducial volume with $R_{\mathrm{fid}} \leq 16\,\mathrm{m}$ and are uniformly distributed in the visible energy window $E_{\mathrm{vis}} \in [12, 300]\,\mathrm{MeV}$ to avoid an energy-dependent bias in the PSD analysis. The average pulse shapes for IBD (green) and NC events (blue) in JUNO within a prompt window of 1 μs are shown in Fig. 8.14. Since the energy deposition in NC events is predominantly hadronic, while the prompt energy in IBD events is mainly deposited by the positron, the ratio of fast to slow scintillation components for NC events is smaller than for IBD events, as summarized in Tab. 8.3. Consequently, their pulse shapes exhibit a slower decay on average. Although the energy deposition in CC (excluding IBD) is also primarily caused

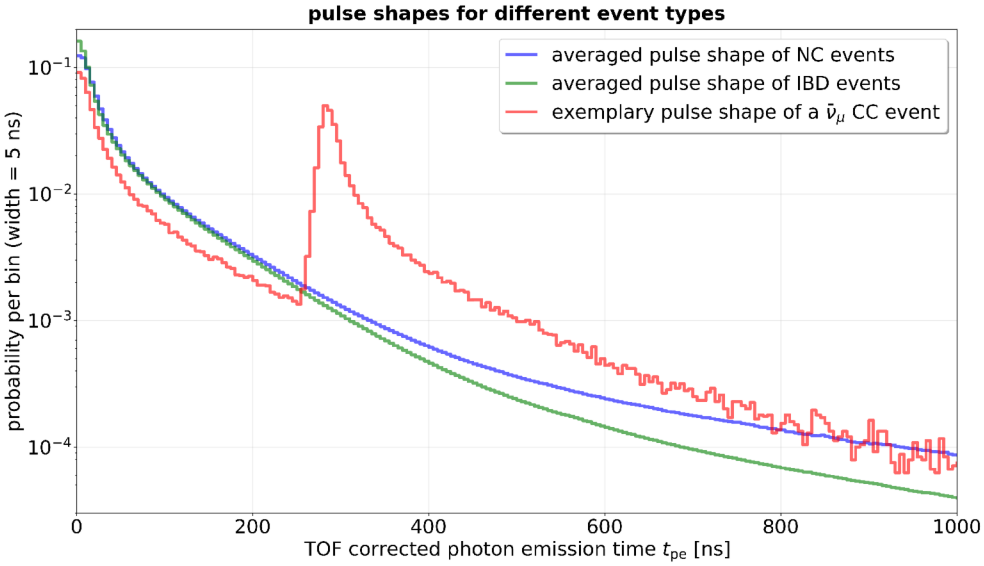

Figure 8.14: Averaged normalized pulse shapes of more than 10,000 IBD events (green) and NC events (blue) in the prompt time window, derived from TOF corrected hit times simulated with the JUNO detector simulation and smeared with the TTS. Additionally an exemplary pulse shape of a CC $\bar{\nu}_\mu$ event is added, where the muon decay happens in the prompt time window.

by leptons, especially at higher visible energies, multiple nucleons can be knocked out of the nuclei either in the primary interaction or through subsequent FSIs (cf. Sec. 5.2.2). These nucleons contribute to the prompt energy deposition and lead to pulse shapes with a slightly slower decay. In addition, many CC events induced by ν_μ and $\bar{\nu}_\mu$ can also be suppressed by PSD, since 36.6 % of the muon decays occur within the prompt window of 1 μs, considering a typical time constant of 2.197 μs (cf. Eq. 5.6). With an appropriate PSD criterion, such events can therefore also be suppressed, since their pulse shapes differ significantly from IBD events, as exemplarily illustrated in Fig. 8.14 (red curve).

8.3.2 Classical Approach: Tail-to-Total Ratio

A well known criterion to effectively reduce NC-induced backgrounds is the tail-to-total ratio (TTR) which is conventionally defined as

$$\mathrm{TTR} = \frac{\int_{\mathrm{t_s}}^{\mathrm{t_e}} \mathrm{P(t_{pe})}\,\mathrm{dt_{pe}}}{\int_{0\,\mathrm{ns}}^{\mathrm{t_{max}}} \mathrm{P(t_{pe})}\,\mathrm{dt_{pe}}}\,, \tag{8.8}$$

and quantifies the fraction of charge contained in a specific time window between t_s and t_e relative to the total charge integrated up to t_{max} [8, 68, 98]. In order to exclude after-pulses, which are not taken into account in the JUNO `DetSim` and occur at around 850 ns [74], the maximum integration time was set to $t_{\mathrm{max}} = 700\,\mathrm{ns}$[6]. Based on the mean pulse shapes shown in Fig. 8.14, lower TTR values are expected for genuine IBD events than for NC and CC events (excluding IBD). By introducing a TTR cut that allows only events below a certain threshold value to pass, NC- and CC-induced

[6]The probability of a muon decays to occur within this window is 27.3 %.

background events can therefore be reduced. To obtain the optimal TTR cut for different start times t_s and end times t_e, the S2B ratio defined in Eq. 8.7 for the IBD-induced DM spectra was optimized with respect to the background contributions shown in Fig. 8.13. For each tail configuration, the mean value for different DM signals with masses ranging from $m_\chi = 20\,\text{MeV}$ to $m_\chi = 200\,\text{MeV}$ in steps of 10 MeV, and $m_\chi = 250\,\text{MeV}$ was obtained. The results of the TTR analysis for all tail configurations with start times $t_s \in [200, 250, 300, 350, 400, 450]$ ns and end times $t_e \in [550, 600, 650, 700]$ ns are illustrated in Fig. 8.15. The S2B ratio (left panel) defines the optimal tail configuration,

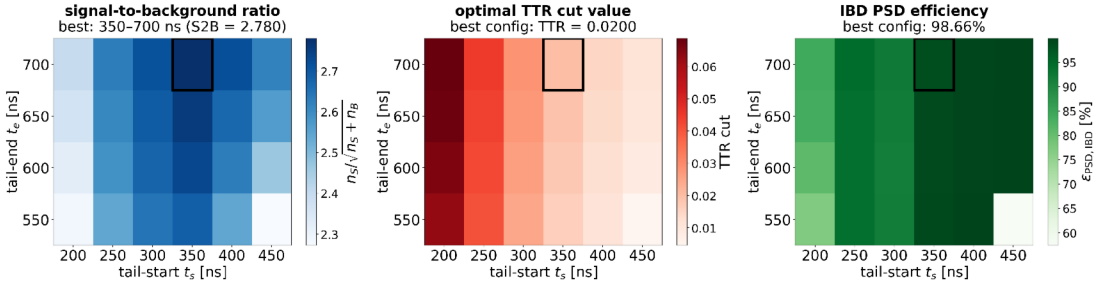

Figure 8.15: PSD results for different tail configurations with $t_{\text{max}} = 700\,\text{ns}$. The left panel displays the S2B ratio, which identifies the optimal configuration at $t_s = 350\,\text{ns}$ and $t_e = 700\,\text{ns}$ (black frame). The middle panel shows the corresponding TTR cut value for each configuration, while the right panel illustrates the averaged IBD PSD efficiency, indicating the fraction of signal events that survive the TTR cut.

which is determined to be $t_s = 350\,\text{ns}$ and $t_e = 700\,\text{ns}$ for all DM masses. The optimal tail window found in [7], 200–600 ns, is located at slightly earlier times. However, since later start times $t_s > 200\,\text{ns}$ were not considered in the analysis presented in [7], a direct comparison of the results is difficult. The S2B values in Fig. 8.15 were obtained under the assumption of the Super-K limit for the strength of the DM signal[7] (cf. Sec. 6.1). The middle panel in Fig. 8.15 shows the optimal TTR cut for each tail configuration, with the best tail definition yielding a cut value of TTR = 0.0200. The TTR values of all simulated events for this configuration are shown in Fig. 8.17 as a function of the visible energy E_{vis}. The upper panel shows all CC events, with IBD events highlighted in green, and the lower panel compares the TTR distributions of NC and IBD events. In both subplots, IBD events (green) exhibit the lowest TTR values. While the NC TTR distribution is clearly separated from IBD events and shows only a slight overlap in the low-energy region ($E_{\text{vis}} < 50\,\text{MeV}$), the TTR distribution of CC events (excluding IBD) overlaps with the IBD values[8]. The red line marks the optimal TTR cut determined for this tail window (cf. the middle panel of Fig. 8.15).

The right panel of Fig. 8.15 shows the averaged IBD PSD efficiency for different tail configurations, indicating the fraction of IBD events that survive the TTR cut. For the optimal tail window, an average efficiency of $\varepsilon_{\text{PSD,IBD}} = (98.66 \pm 0.07)\,\%$ is obtained[9] and found to be relatively constant over the visible energy range, as shown by the green curve in Fig. 8.17. The survival efficiencies for CC events (excluding IBD) and NC events that survive the IBD selection cuts described in Sec. 8.2.1 exhibit a weak

[7]When assuming the natural self-annihilation cross section $\langle \sigma_A v \rangle$, only the absolute S2B value changes, while the optimal configuration depends only on the shape of the IBD-induced DM signal.

[8]Those CC events that exhibit a muon capture within $t_{\text{max}} = 700\,\text{ns}$ exceed the IBD TTR values by several orders of magnitude and are therefore not shown in Fig. 8.17.

[9]This result is comparable to the IBD PSD efficiency reported in [7] for the energy range $E_{\text{vis}} \in [10, 100]\text{MeV}$. The uncertainties of the PSD efficiencies were calculated assuming binomial statistics.

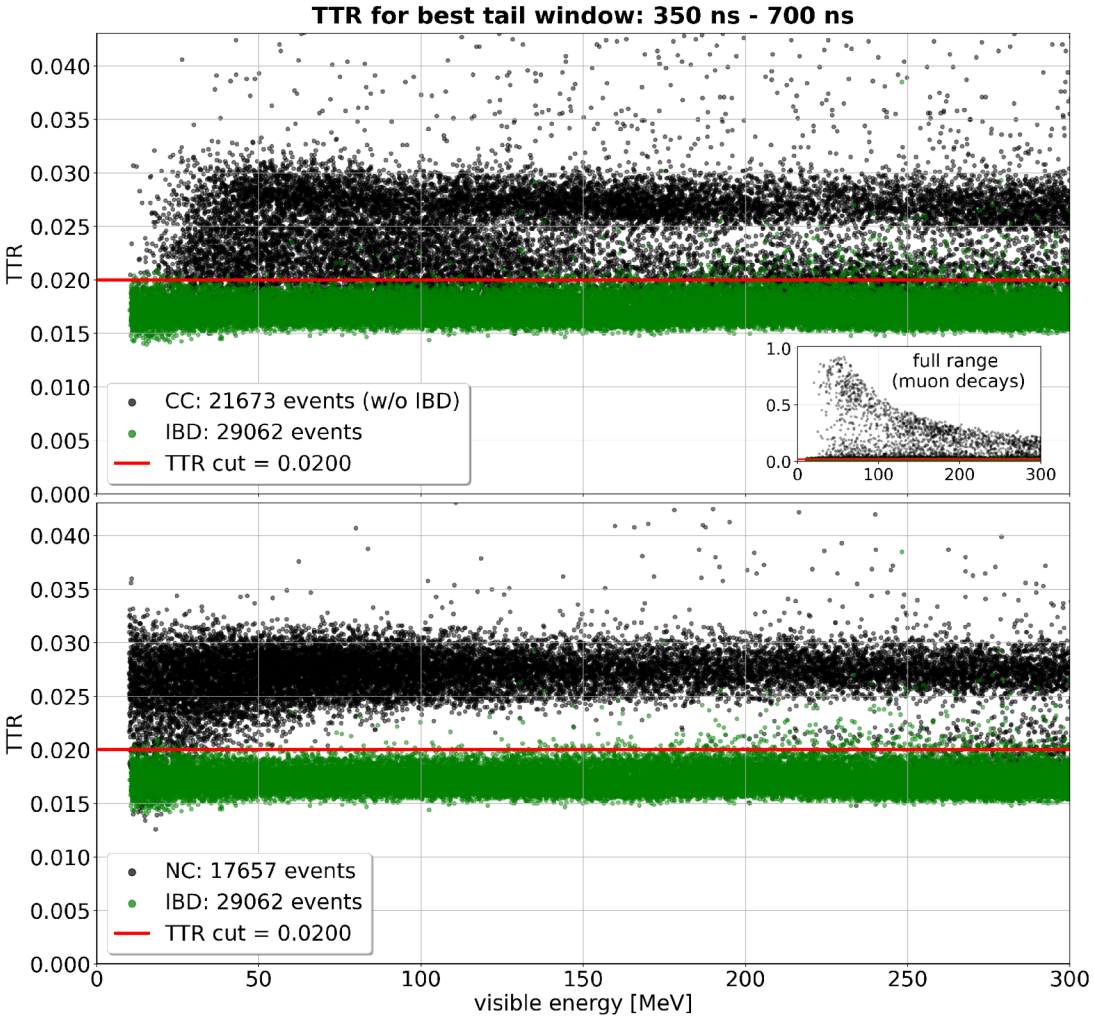

Figure 8.16: Distribution of the TTR values as a function of E_{vis} for the best tail configuration 350-700 ns. In the upper panel the distribution of CC (excluding IBD) vs. IBD events is shown. The inset plot shows the full range including the CC events with muon decay or capture. In the lower panel the TTR values of NC vs. IBD events are illustrated. In both plots IBD events are marked in green and the best TTR cut value is indicated by the red line (cf. Fig. 8.15).

energy dependence. While IBD-like NC events (blue) are almost perfectly suppressed in the energy range 50–160MeV, the survival efficiency increases toward lower visible energies, consistent with other PSD analyses in JUNO [7, 8, 98]. This behavior is mainly driven by NC interactions that produce a ^{11}C isotope in the final state, which decays via electromagnetic de-excitation γ cascades, generating an IBD-like prompt signal [8, 98]. At the same time, a neutron is emitted in this interaction (cf. Eq. 5.9), allowing these events to also pass the IBD selection cuts. With an averaged survival efficiency of $\varepsilon_{\text{PSD,NC}} = (5.00 \pm 0.16)\,\%$ for IBD-like NC events, the PSD method is highly effective in suppressing NC-induced background contributions. The average PSD efficiency for IBD-like CC events (cf. the red curve in Fig. 8.16) amounts to $\varepsilon_{\text{PSD,CC}} = (23.79 \pm 0.29)\,\%$. Therefore, the TTR criterion provides a method to reduce CC events (excluding IBD) that cannot be suppressed by the topological constraints by approximately one quarter. Using these PSD survival efficiencies, the number of background events in the visible

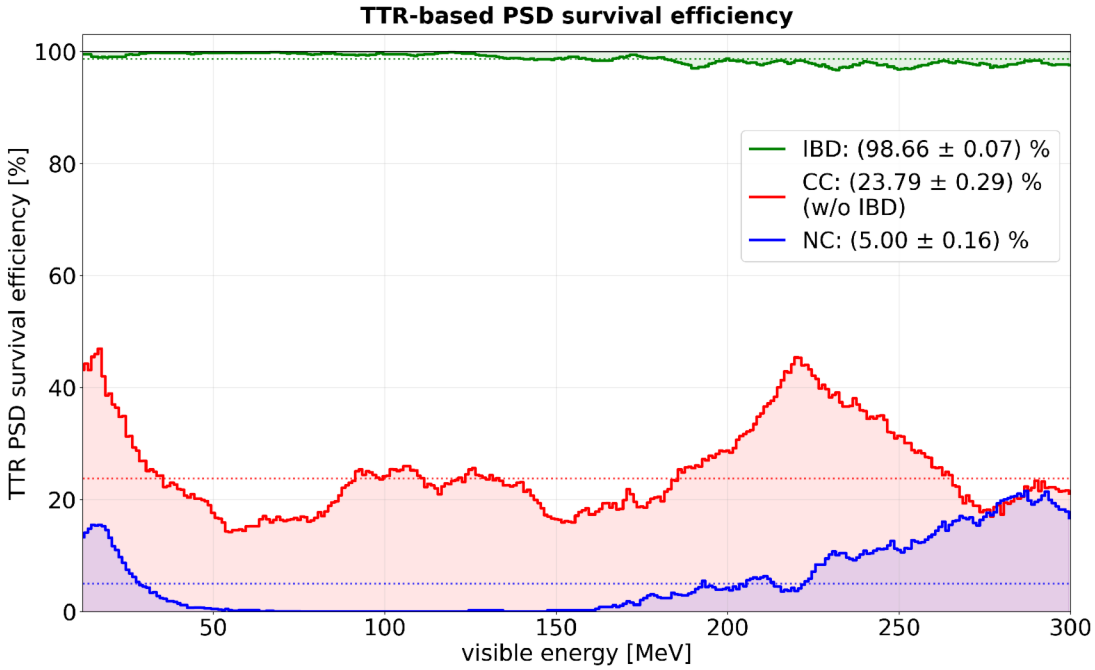

Figure 8.17: PSD survival efficiency of IBD (green), CC (red) and NC events (blue) that passed the IBD selections cuts, defined in Sec. 8.2.1, as a function of the visible energy E_{vis}.

energy range $E_{\text{vis}} \in [12, 300]$MeV can be reduced from $n_B = 576 \pm 24$ after applying the IBD selection cuts (cf. Fig. 8.13) to only 175 ± 13, while the number of IBD-induced DM signal events remains nearly unaffected.

8.3.3 Machine Learning Approach: Event Classification

So far, only classical methods such as the TTR have been used for pulse shape discrimination (PSD), which are limited to extracting a single parameter from the pulse shape. An ML approach, in contrast, which takes the entire pulse shape up to $t_{\text{max}} = 700\,\text{ns}$ as input and predicts an event classification as signal (IBD = 1) or background (IBD-like CC and NC = 0), is able to learn much more subtle features of the pulse shape. In this work, a ML-based approach for PSD in the energy range $E_{\text{vis}} \in [12, 300]$MeV is presented for the first time as an alternative to the TTR criterion discussed in Sec. 8.3.2. For this purpose, the same pulse shapes as used for the TTR analysis (cf. Fig. 8.14), are employed and split into training and validation sets in an 80:20 ratio. For the classifier, an MLP was chosen as the NN architecture, similar to Sec. 8.1.2. However, instead of minimizing the Mean Squared Error (MSE) loss, the Binary Cross Entropy (BCE) loss was used. The hyperparameter space is optimized using the Optuna framework [151] with five-fold cross-validation, where each hyperparameter configuration is evaluated across all folds, and the mean validation loss is used for optimization. The parameter search space includes the number (1–4) and dimensionality (16–256) of the hidden layers, dropout regularization (0–0.3), as well as training parameters such as the LR (10^{-5}–10^{-2}), weight decay (10^{-6}–10^{-3}), and batch size (64–512). The optimal configuration is identified from 50 optimized configurations and consists of four hidden layers with 156, 205, 129 and 68 neurons, respectively, and a minimal dropout rate of 1.15 %. The MLP is trained using the `AdamW` optimizer with an initial LR of 2.25×10^{-4}

and a weight decay of 1.57×10^{-3} [153]. The LR is adjusted during training by a `ReduceLROnPlateau` scheduler, which reduces the LR by a factor of 0.37 after 11 epochs without a reduction in the validation loss.

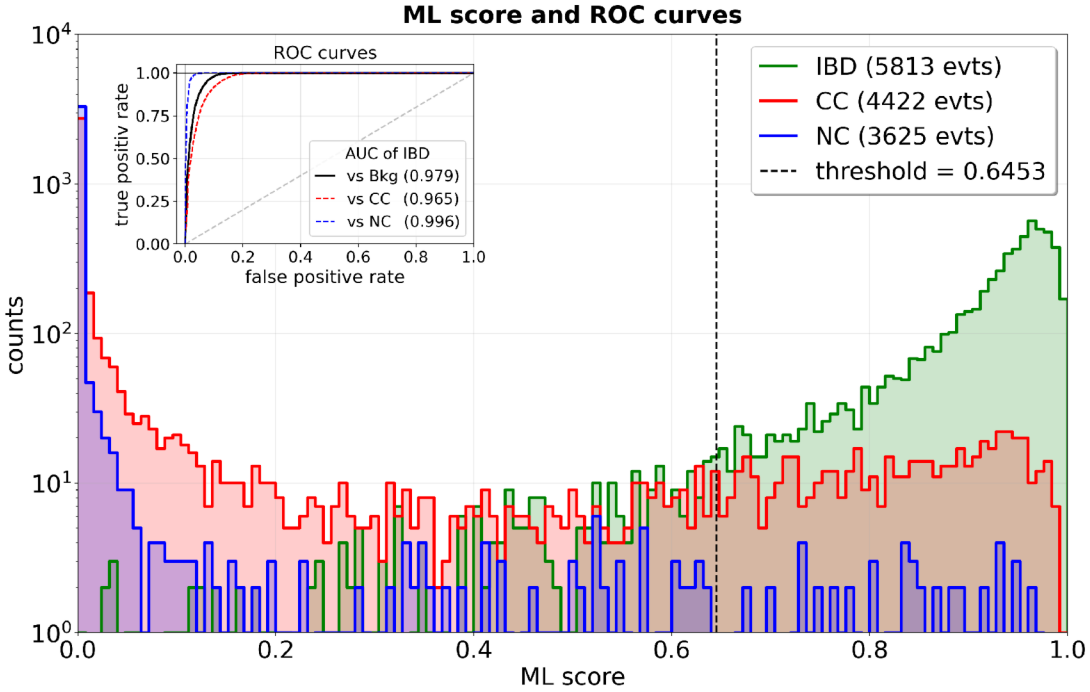

Figure 8.18: ML score distribution for IBD (green), IBD-like CC (red) and IBD-like NC events (blue). The optimal threshold at 0.6453 (dashed black line) was derived by maximizing the S2B ratio for all DM signals considered for the PSD optimization. The inset plot demonstrates the Receiver Operating Characteristic (ROC) for IBD events against all backgrounds (black curve) and the ROC separated for CC (red) and NC events (blue). The corresponding AUC is added in brackets.

Fig. 8.18 shows the distribution of the ML scores separated by the three event classes. The trained NN assigns events with scores around 1 to IBD events, while events with scores around 0 are classified as background (Bkg). A clear separation is visible, with genuine IBD events (green) accumulating at high scores, whereas NC events (blue) are concentrated at very low scores. IBD-like CC events (red) show a broader distribution, which reflects the similarity between the pulse shapes of CC events (excluding IBD) and IBD events due to electromagnetic showers from the positron. As already observed in the TTR analysis in Sec. 8.3.2, the separation between IBD and NC events (hadronic pulse shapes) is more reliable, as also demonstrated by the Receiver Operating Characteristic (ROC) curves shown in the inset of Fig. 8.18. The Area Under the Curve (AUC) for the separation of IBD and NC events (blue) shows that NC events get a lower ML score than IBD events in 99.6 % of all cases. The separation of IBD events from other CC events is slightly weaker, with an AUC of 96.5 %. Consequently, the overall discrimination power of the classifier for IBD events against all background events (Bkg) amounts to an AUC of 97.9 % (black curve). The threshold value of 0.6453 (black vertical line) was derived analogously to the TTR cut by maximizing the S2B ratio, averaged over all DM scenarios considered in the analysis. These scenarios cover masses ranging from $m_\chi = 20\,\text{MeV}$ to $m_\chi = 200\,\text{MeV}$ in steps of 10 MeV, as well as $m_\chi = 250\,\text{MeV}$. Fig. 8.19 shows the confusion matrix between IBD events and all background events (Bkg) in the

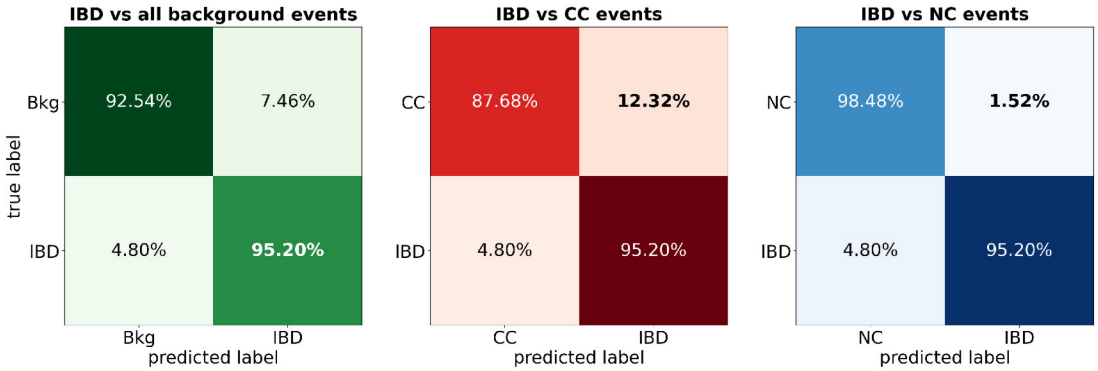

Figure 8.19: Confusion matrices of the classifier for IBD events versus all background events (Bkg) are shown in the left panel. The middle and right panels show the corresponding matrices for the two background classes separately, IBD vs. CC (excluding IBD) and IBD vs. NC events, respectively.

left panel. Fig. 8.19 shows the confusion matrix between IBD events and all background events (Bkg) in the left panel. Overall, 95.20 % of all IBD events are correctly classified, while 7.46 % of background events are misclassified as IBD events. The middle and right panels show the confusion matrices separated by the different background classes. In total, 12.32 % of all CC events (excluding IBD) survive the ML cut with a threshold of 0.6453, whereas only 1.52 % of all NC events are misclassified as IBD events. The classifier trained in this work is designed to categorize events that survive the IBD selection cuts described in Sec. 8.2.1 into IBD and background events (Bkg) based on their pulse shape, thereby providing an alternative to the TTR criterion discussed in Sec. 8.3.2. Fig. 8.20 shows the PSD performance of the classifier as a function of the visible energy E_{vis}, separated by the two background classes. The performance is robust

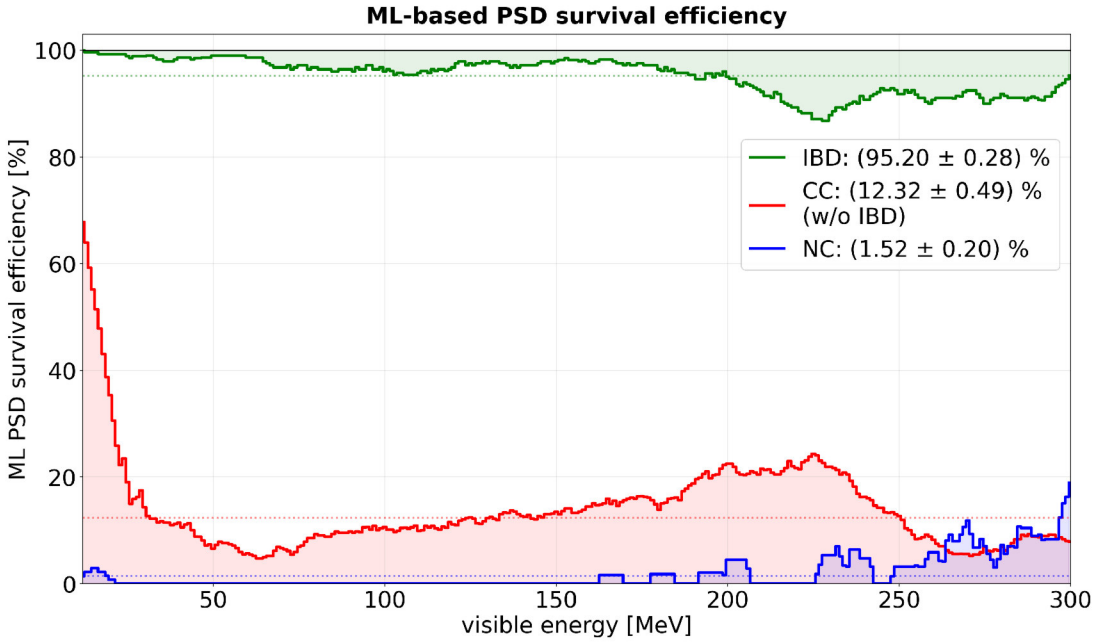

Figure 8.20: ML-based PSD survival efficiency of IBD (green), IBD-like CC (red) and IBD-like NC events (blue), as a function of the visible energy E_{vis}.

over the entire visible energy range and exhibits a higher rejection efficiency for IBD-like CC and NC background events compared to the classical TTR approach (cf. Fig. 8.17). However, the survival efficiency for IBD events $\varepsilon_{\mathrm{PSD,IBD}} = (95.20 \pm 0.28)\,\%$ is slightly lower for the ML-based approach, compared to the classical TTR approach.

8.4 Summary and Visible Energy Spectrum

In this chapter, methods for background suppression for the indirect DM search in JUNO were discussed for the energy range $E_{\mathrm{vis}} \in [12, 300]\,\mathrm{MeV}$. First, a data-driven ML-based vertex reconstruction approach for IBD-like events was developed in Sec. 8.1, providing stable performance across the entire visible energy window with an average accuracy of $\sigma_{\vec{r}_{\mathrm{Qdep}}} = 18.3\,\mathrm{cm}$. The reconstruction of the energy weighted vertex $\vec{r}_{\mathrm{Qdep}}$ constitutes a technical prerequisite for the subsequent background reduction methods.
To determine the final visible IBD-driven spectrum in JUNO, the event topology of the MC simulated events is first constrained. In Sec. 8.2, selection criteria are introduced that exploit the spatial and temporal coincidence of genuine IBD events, as well as the characteristic energy signature of the delayed signal. The survival efficiencies of these cuts, $\varepsilon_{\mathrm{top,(ch)}}(E_{\mathrm{vis}})$, are determined as a function of the visible energy for all three channels ch $\in$ {IBD, CC (excluding IBD), NC}. On average, the cuts retain $\varepsilon_{\mathrm{top,IBD}} = (92.84 \pm 0.19)\,\%$ of all genuine IBD events, while only $\varepsilon_{\mathrm{top,CC}} = (21.92 \pm 0.04)\,\%$ of CC events (excluding IBD) and $\varepsilon_{\mathrm{top,NC}} = (13.35 \pm 0.03)\,\%$ of NC events survive. Events passing these cuts are referred to as IBD-like, as they exhibit the same topology as genuine IBD events. To further suppress such background events, a PSD method is subsequently applied, which classifies events as genuine IBD or IBD-like background based on the pulse shape of the prompt signal. First, a classical TTR optimization was performed, considering not only NC backgrounds but also IBD-like CC backgrounds, which become increasingly relevant at higher visible energies. As an alternative to the TTR method, an ML-based classifier was presented for the first time, which processes the full pulse shape and is therefore capable of evaluating more subtle features. The PSD survival efficiency, $\varepsilon_{\mathrm{PSD,(ch)}}(E_{\mathrm{vis}})$, is determined independently for both methods as a function of the visible energy for each channel ch. The final number of expected events per energy bin i can then be obtained for each channel ch from the original number $N^{\mathrm{orig}}_{\mathrm{(ch)}}({E_{\mathrm{vis}}}^i)$ by

$$N^{\mathrm{final}}_{\mathrm{(ch)}}({E_{\mathrm{vis}}}^i) = N^{\mathrm{orig}}_{\mathrm{(ch)}}({E_{\mathrm{vis}}}^i) \cdot \varepsilon_{\mathrm{top,(ch)}}({E_{\mathrm{vis}}}^i) \cdot \varepsilon_{\mathrm{PSD,(ch)}}({E_{\mathrm{vis}}}^i)\ . \tag{8.9}$$

The total number of background events in the visible energy window after 10 yr data-taking and a fiducial volume of 14.77 kton before and after the cuts is listed in Tab. 8.4. Overall, the ML-based PSD method suppresses about 10 % more background events in JUNO and provides particularly improved performance for NC-induced backgrounds.
Fig. 8.21 shows the expected energy spectrum in JUNO before any cuts (upper row), after applying the IBD selection cuts (middle row), and after the additional application of PSD (lower row). For the illustration of the PSD application, the ML-based approach was chosen due to better performance. Two different DM scenarios with $m_\chi = 70\,\mathrm{MeV}$ (left column) and $m_\chi = 250\,\mathrm{MeV}$ (right column) are shown for the same background composition. The IBD-induced background contributions (hatched area), such as the DSNB (blue) and the atmospheric IBD component (green), constitute the irreducible background in the IBD-driven spectrum in JUNO. The PSD method is particularly powerful for suppressing the dominant NC background, which is already reduced from

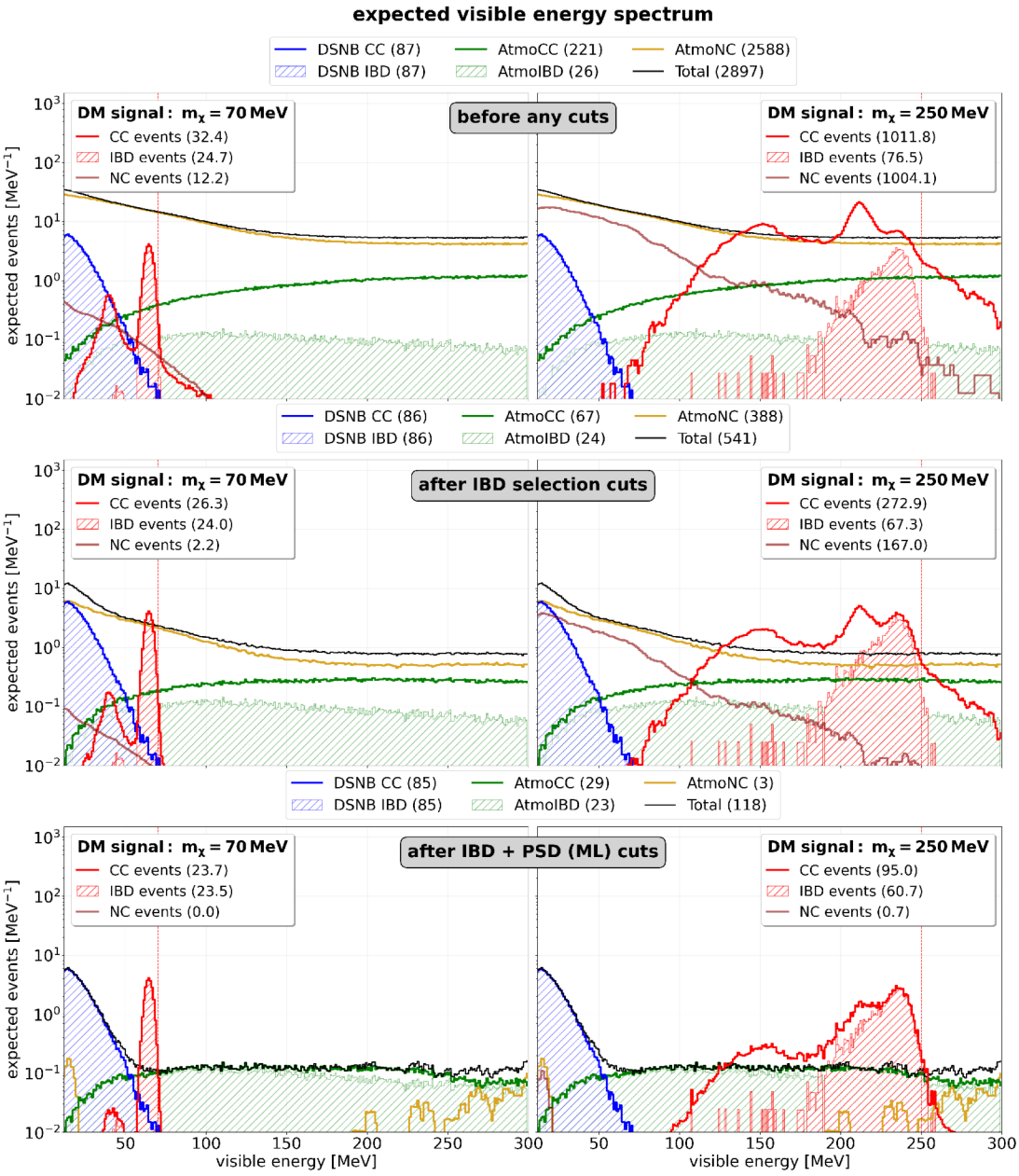

Figure 8.21: Expected visible energy spectrum in JUNO for a fiducial mass of 14.77 kton after 10 yr of data taking. The top row shows the spectrum before any cuts, the middle row after applying the IBD selection cuts, and the bottom row after further applying the ML-based PSD. The left and right columns correspond to DM masses of $m_\chi = 70\,\text{MeV}$ and $m_\chi = 250\,\text{MeV}$. The atmospheric CC (green) and NC (yellow) backgrounds, as well as the DSNB background (blue), are shown together with the total background (black). The IBD component of the CC background is indicated by hatched areas. For the DM signal, the CC and NC contributions are shown in red and the vertical dashed line marks the corresponding DM mass. Numbers in the legends denote the event counts in the visible energy range.

2588 to 388 events by applying the IBD selection cuts (cf. yellow curve in the middle panel), and is further suppressed to 18 events using the classical TTR method and to only

Table 8.4: Expected number of background events n_B for different background contributions before and after applying the only the IBD selection cuts described in Sec. 8.2 and additionally the PSD cuts using both methods introduced in Sec. 8.3. The numbers correspond to 10 yr of data-taking and a fiducial volume of 14.77 kton in the visible energy range $E_{\text{vis}} \in [12, 300]$ MeV. in JUNO.

Background	no cuts	IBD selection cut	PSD TTR cut	PSD ML cut
DSNB	87 ± 9	86 ± 9	85 ± 9	85 ± 9
Atmo. CC	221 ± 15	67 ± 8	35 ± 6	29 ± 5
Atmo. NC	2588 ± 51	388 ± 20	18 ± 4	3 ± 2
Total	2897 ± 54	542 ± 23	139 ± 12	118 ± 11

3 remaining events with the ML-based approach. The sensitivity study in Sec. 10.2 for the IBD-dominated energy region was performed independently for both PSD methods and subsequently compared.

9 | Signal-to-Background Optimization for (sub-)GeV DM

After all, Ginger Rogers did everything that Fred Astaire did. She just did it backwards and in high heels.

– Ann Richards

In Chap. 8, background reduction methods for indirect DM search in the MeV range $m_\chi \in [15, 300]\,\text{MeV}$ are discussed, where the inverse beta decay (IBD) was selected as the signal channel. In the sub-GeV range $m_\chi \in [0.1, 1]\,\text{GeV}$ and the GeV range $m_\chi \in [1, 10]\,\text{GeV}$, however, CC and NC interactions on ^{12}C dominate instead (cf. Sec. 5.2.2). The expected visible spectrum from DM annihilations in the sub-GeV energy range exhibits characteristic spectral features, which are discussed in detail in Sec. 6.2.2. In Sec. 9.1, two approaches are investigated with the goal to enhance these spectral features of the DM-induced signal. In the GeV energy range, where RES and DIS interactions become increasingly dominant (cf. Sec. 6.2.3), the characteristic spectral features of a monoenergetic neutrino signal disappear. However, at these energies, the neutrino direction can be reconstructed with an uncertainty of less than 30° [79], making it possible to enhance the S2B ratio through a directional analysis by considering only DM signals originating from a region of interest (ROI) around the Galactic Center (GC), which is discussed in Sec. 9.2 for different DM halo profiles.

9.1 Signal-to-Background Optimization for sub-GeV DM

To exploit the spectral features of DM-induced neutrino spectra in the sub-GeV energy range (cf. Sec. 6.3), two approaches are pursued in this section. In the transition region between an IBD- and a CC-dominated signal ($\simeq 0.1 - 0.2\,\text{GeV}$) the two characteristic peaks are primarily defined by CC interactions of $\bar{\nu}_e$ on hydrogen (IBD) and ν_e-induced CC1p0n interactions on carbon which is illustrated in Fig. 6.6. Therefore, the first approach, discussed in Sec. 9.1.1, involves a flavor selection aimed at enhancing CC $\nu_e/\bar{\nu}_e$-like events. For DM masses $\gtrsim 0.2\,\text{GeV}$, however, the double-peak structure is largely determined by CC1p0n interactions of ν_e and ν_μ on ^{12}C, while the IBD peak becomes less pronounced (cf. Fig. 6.4). Since CC1p0n interactions are characterized by a zero-neutron topology at the interaction vertex, the second selection approach employs a topology-based zero-neutron selection, which is presented in Sec. 9.1.2.
It should be noted that the specific shape of the spectral structures strongly depends on the assumption of a democratic flavor composition for the DM self-annihilation channel in Eq. 3.1, leading to an identical neutrino flux for all neutrino flavors ν_ℓ (cf. Eq. 3.13 with $\kappa_1 = 3$).

9.1.1 Flavor Selection

The $\bar{\nu}_e$-induced IBD peak, which is characteristic in the MeV regime, remains clearly visible as a spectral feature in the sub-GeV range up to $m_\chi \lesssim 0.2\,\text{GeV}$ (cf. Fig. 6.6). At the same time, in particular for sub-GeV DM with masses $m_\chi \lesssim 0.5\,\text{GeV}$, the characteristic CC1p0n peak induced by CC ν_e interactions with carbon is clearly pronounced (cf. Sec. 6.2.2). The maximum of the CC1p0n peak is shifted with respect to the neutrino energy by the Q-value of approximately 17.9 MeV (cf. Eq. 5.7), while the IBD peak remains close to the neutrino energy in the visible spectrum with a threshold energy of $E_{\text{IBD,th}} = 1.806\,\text{MeV}$ (cf. Eq. 5.3). The resulting characteristic peak structure in the transition region from IBD- to CC-dominated DM spectra is therefore defined by CC contributions from ν_e and $\bar{\nu}_e$ and can be enhanced relative to a flat background spectrum by means of a flavor-based event selection[1].

The potential of JUNO for particle identification (PID) in the GeV range up to $E_{\text{vis}} = 15\,\text{GeV}$ is reported in [126], where the neutrino flavor is classified based on primary and secondary trigger information with two different neural network (NN). The `PointNet++` model treats the individual PMT hits as a three-dimensional point cloud and learns characteristic patterns from their spatial distribution, while the `DeepSphere` model interprets the signals as an image on the spherical detector surface and identifies structures directly on the sphere [126]. Two different classification strategies are applied for both NN models: the 3+2-label strategy first classifies events into $\nu_e/\bar{\nu}_e$-like, $\nu_\mu/\bar{\nu}_\mu$-like, and NC-like (3 labels), using characteristic primary trigger PMT-wise waveform features that were already introduced for vertex reconstruction in Sec. 8.1. In a second step, CC events are further separated into neutrino and antineutrino interactions (2 labels) by additionally incorporating delayed n-capture information and neutron multiplicity. In the 5-label strategy, however, prompt and delayed trigger information are considered simultaneously, to directly identify the interaction category as one of five classes (ν_e, $\bar{\nu}_e$, ν_μ, $\bar{\nu}_\mu$ and NC).

To estimate the separation performance of ν_e and $\bar{\nu}_e$ events, as well as the background leakage from $\nu_\mu/\bar{\nu}_\mu$ and NC events in the sub-GeV range, the energy-dependent Area Under the Curve (AUC) results for $E_{\text{vis}} \leq 1\,\text{GeV}$ in [126] are used. Since the 3-label classification yields AUC$\simeq 0.94$ for both the `PointNet++` and the `DeepSphere` model in this energy range, an average background leakage of $\sim 6\,\%$ is assumed. A further separation of the combined $\nu_e/\bar{\nu}_e$-like sample into neutrino ν_e and antineutrino $\bar{\nu}_e$ is slightly weaker, with AUC$\simeq 0.82$ for the 3+2-label strategy and AUC$\simeq 0.84$ for the 5-label strategy [126]. Based on these results, the fraction of correctly classified $\nu_e/\bar{\nu}_e$ events in the sub-GeV range is estimated to be $\sim 80\,\%$[2].

The PID-method presented in [126] was developed and optimized for atmospheric neutrino events with visible energies up to 15 GeV and therefore provides only limited statistics for the sub-GeV range below 1 GeV. To verify whether the assumption of a constant PID efficiency in the sub-GeV energy range is reasonable, an independent cross-check was performed in the energy range $E_{\text{vis}} \leq 0.5\,\text{GeV}$ by using a simple MLP classifier based on PSD, which was developed in this work. This classifier is trained to distinguish between $\nu_e/\bar{\nu}_e$ events on the one hand and $\nu_\mu/\bar{\nu}_\mu$ and NC interactions on the other hand, analogous to the approach presented in Sec. 8.3.3. The use of pulse shape information for PID in this energy range has been employed previously in JUNO [99] and is motivated by the fact that $\nu_e/\bar{\nu}_e$ events produce short electromagnetic

[1] In the following, $\nu_e/\bar{\nu}_e$ and $\nu_\mu/\bar{\nu}_\mu$ denote CC events only.

[2] An examination of the selection efficiency and background leakage as a function of visible energy reveals an approximately constant behavior in the sub-GeV range.

showers, while $\nu_\mu/\bar{\nu}_\mu$ interactions leave longer muon tracks, and NC events exhibit more temporally extended signatures due to hadronic processes (cf. Sec. 8.3). However, the method presented in [99] exploits the standard deviation of the pulse shapes to discriminate between $\nu_e/\bar{\nu}_e$-like and other events, and therefore relies solely on a single classical criterion[3]. Instead of performing the classification based on a single pulse shape parameter, the MLP developed for this purpose takes the full pulse shape within the first 700 ns as input (cf. dataset *D*8 in Tab. C.1) and classifies events into $\nu_e/\bar{\nu}_e$-like and non-$\nu_e/\bar{\nu}_e$-like events by minimizing the Binary Cross Entropy (BCE) loss. The architecture of the classifier was chosen analogously to the architecture presented in Sec. 8.3.3. A limited variation of the hyperparameters showed only a negligible impact on the model performance. The results of this classification in the energy range from

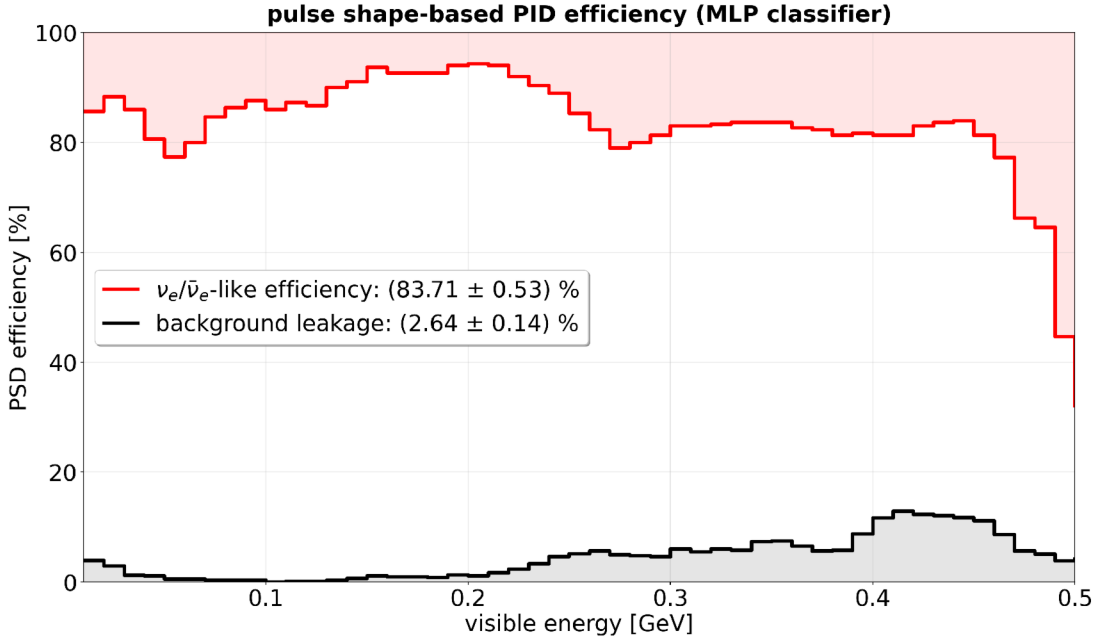

Figure 9.1: PID efficiency of the MLP classifier developed in this work for $\nu_e/\bar{\nu}_e$-like events as a function of the visible energy E_{vis}. The red curve shows the fraction of correctly classified $\nu_e/\bar{\nu}_e$ events and the black curve shows the misclassified fraction of $\nu_\mu/\bar{\nu}_\mu$ and NC events.

$E_{\text{vis}} = 12\,\text{MeV}$ to $E_{\text{vis}} = 0.5\,\text{GeV}$ are shown in Fig. 9.1. The red curve indicates the fraction of correctly classified $\nu_e/\bar{\nu}_e$ events, while the black curve represents the averaged fraction of misclassified $\nu_\mu/\bar{\nu}_\mu$ and NC events. This MLP-based cross-check yields a mean $\nu_e/\bar{\nu}_e$-like efficiency of $(83.71 \pm 0.53)\,\%$ with a background leakage of $(2.64 \pm 0.14)\,\%$, which is comparable to the PID results obtained in [126] for $E_{\text{vis}} \leq 1\,\text{GeV}$. Despite being based on different input representations - primary trigger and secondary trigger information for the `PointNet++` and `DeepSphere` model and full pulse shapes for the MLP classifier - both methods yield consistent discrimination performances in the overlapping energy range below 0.5 GeV. This agreement supports the assumption of an approximately energy-independent PID efficiency in the sub-GeV range as a first-order

[3]This criterion was also applied in the previous sensitivity study for indirect MeV DM search to suppress $\nu_\mu/\bar{\nu}_\mu$-induced background events [7].

estimate. Based on these results, constant PID efficiencies of

$$\varepsilon_{\text{PID},\,\nu_e/\bar{\nu}_e\text{-like}} = 80\,\% \quad \text{and} \quad \varepsilon_{\text{PID},\,\text{other}} = 6\,\% \tag{9.1}$$

are adopted for the flavor-based $\nu_e/\bar{\nu}_e$-like event selection in the sensitivity analysis presented in Sec. 10.3. It should be emphasized that neither the `PointNet++`/`DeepSphere` model nor the MLP-based classifier developed in this work has been specifically optimized for the sub-GeV regime, and the efficiencies in Eq. 9.1 are therefore intended as a rough estimate of the potential of a flavor-based event selection for indirect DM searches in this energy range. A more reliable assessment would require a dedicated study with a model retrained on a dataset specifically generated for sub-GeV energies with sufficient statistics, which is beyond the scope of this work.

9.1.2 No Neutron Topology Selection

As the DM mass increases, the IBD-induced peak becomes less pronounced. At the same time, the fraction of CC ν_μ events increases, leading to the double-peak structure arising from ν_e and ν_μ-induced CC1p0n interactions (cf. interaction (1) in Tab. 5.2). The peak produced by ν_μ CC1p0n events is shifted relative to the ν_e peak, due to the larger Q-value in Eq. 5.8 and because of the delayed decay of the muon (cf. Sec. 5.2.2). For $m_\chi \gtrsim 0.3\,\text{GeV}$ the CC1p0n induced double-peak structure is the most characteristic spectral feature for sub-GeV DM-induced signals, as illustrated in Fig. 6.6. Consequently, restricting the analysis to $\nu_e/\bar{\nu}_e$-like events in the upper sub-GeV range is no longer promising. Since CC1p0n events are characterized by the absence of free neutrons at the interaction vertex, a topology-based event selection is introduced in this section. Analogous to the IBD selection cuts presented in Sec. 8.2, which exploit a single-neutron topology, a zero-neutron topology is required to extract CC1p0n events. Since NC events in the sub-GeV energy range can be efficiently identified using pulse shape– and waveform feature–based methods (cf. Sec. 9.1.1), this section focuses solely on studying the efficiency of the zero-neutron topology for extracting CC1p0n events relative to other CC interactions. The MC dataset used for this analysis was generated in the same manner as described in Sec. 8.2 (cf. dataset *D7* in Tab. C.1). For this purpose, the presence of n-capture signatures within the delayed time window defined in Eq. 8.3 is examined. If one or more events are observed within this window with energies consistent with the intervals defined in Eq. 8.5, the zero-neutron topology is rejected. Fig. 9.2 shows the efficiency of the topological zero-neutron constraint for extracting CC1p0n events from ν_e and ν_μ (upper panel) and the fraction of other CC events that pass the time-energy veto (lower panel) as a function of the visible energy E_{vis}. Even in the absence of neutrons at the interaction vertex, secondary neutrons can be produced by subsequent FSIs, therefore, not all CC1p0n events survive the topological restriction, particularly at higher visible energies. The inset plot in the upper panel shows the number of n-captures in CC1p0n events. In 15 % of the events, one or more neutrons are produced in subsequent FSIs, which is the main limit for the efficiency $\varepsilon_{\text{CC1p0n,0n-top}} = (83.88 \pm 0.20)\,\%$ of the topological constraint. Considering the remaining CC events (excluding CC1p0n), only about 11.5 % of all interactions produce no neutrons in the final state (cf. inset plot in the lower panel) and therefore pass the time–energy cut. These events are predominantly ν_e/ν_μ interactions on ^{12}C, in which two protons are ejected instead of one while a ^{10}B isotope remains in the final state (cf. interaction (5) in Tab. 5.2). On average, $\varepsilon_{\text{other,0n-top}} = (12.51 \pm 0.03)\,\%$ of all CC events (excluding CC1p0n) survive the time–energy cut defining the zero-neutron topology.

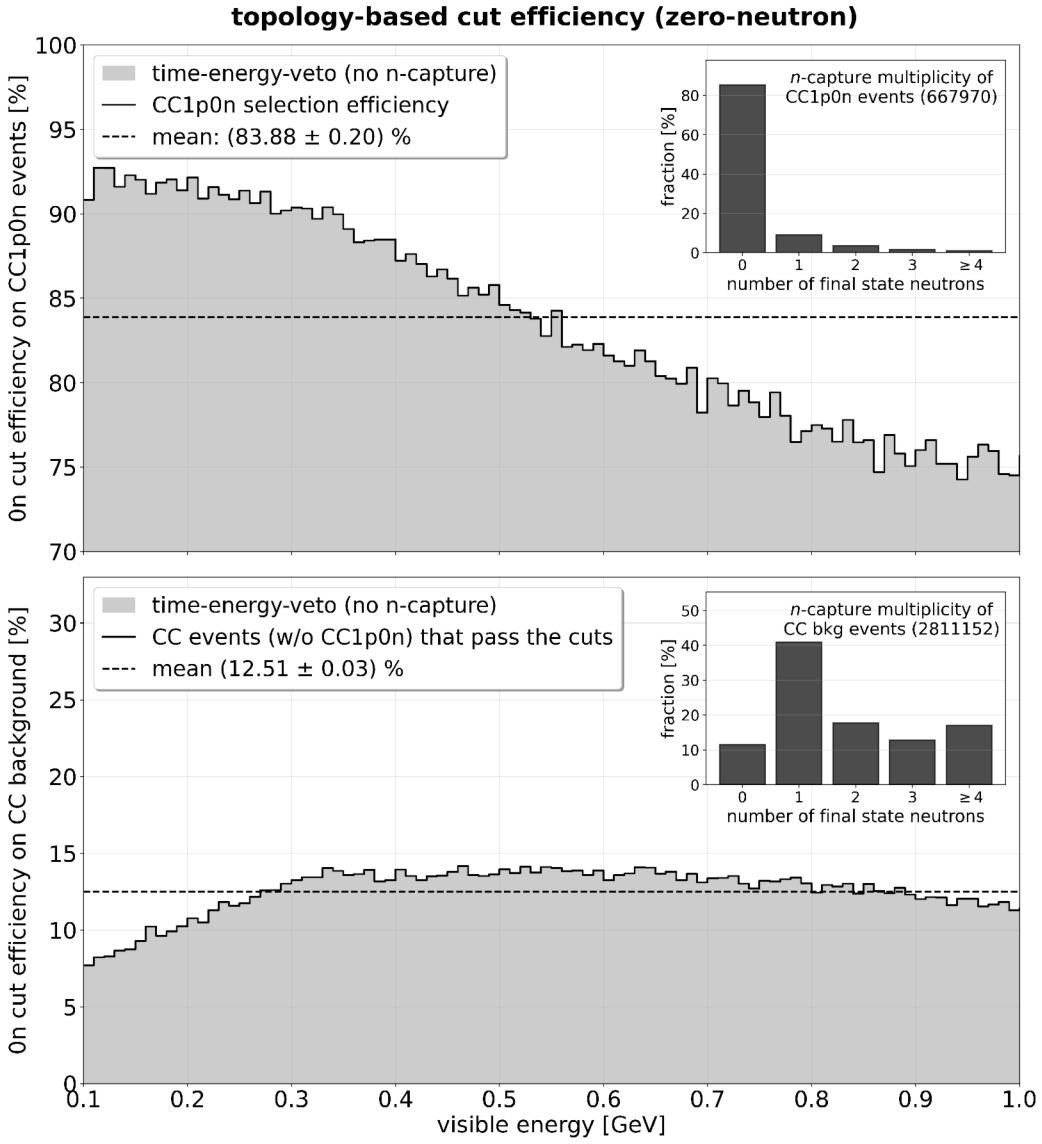

Figure 9.2: Efficiency of the zero-neutron topology for CC1p0n events (upper panel) and other CC events (lower panel) as a function of the visible energy E_{vis}, derived from approximately 660,000 CC1p0n and 2.8 million CC (excluding CC1p0n) events. The inset plots show the relative number of n-captures.

9.1.3 Summary and Visible Energy Spectrum

Fig. 9.3 shows the visible energy spectrum before (upper panel) and after the application of the PID-based flavor cut (lower panel) for two DM scenarios with $m_\chi = 0.15\,\text{GeV}$ (left column), representing the transition region between IBD- and CC-dominated DM signals and $m_\chi = 0.5\,\text{GeV}$ (right column) representing the region with the characteristic peaks induced by ν_e and ν_μ CC1p0n interactions. The expected numbers of background events are summarized in a combined legend above the subplots, while the numbers of DM-induced events are given within the plots. The numbers correspond to a fiducial mass of 14.77 kton after 10 yr of data taking in the visible energy range $E_{\text{vis}} \in [12\,\text{MeV}, 1\,\text{GeV}]$ and the CC contributions of ν_e and $\bar{\nu}_e$ events are indicated by the hatched areas. As intended, for a DM mass of $m_\chi = 0.15\,\text{GeV}$ (left column) in the transition region, the

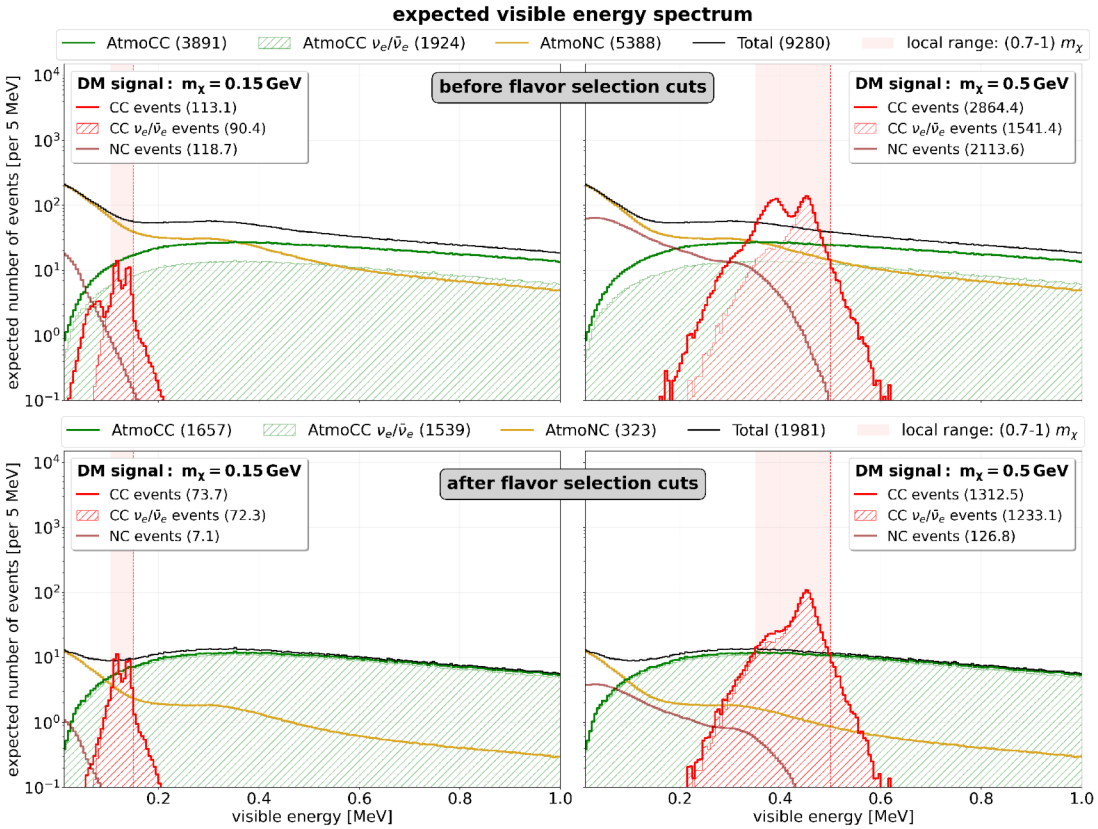

Figure 9.3: Expected visible energy spectrum in JUNO for a fiducial mass of 14.77 kton after 10 yr of data taking. The top row shows the spectrum before any cuts, and the bottom row after applying the PID-based flavor cut. The left and right columns correspond to DM masses of $m_\chi = 0.15\,\text{GeV}$ and $m_\chi = 0.5\,\text{GeV}$. The atmospheric CC (green) and NC (yellow) backgrounds are shown together with the total background (black). The $\nu_e/\bar{\nu}_e$ component of all CC contributions is indicated by hatched areas. For the DM signal, the CC and NC contributions are shown in red and the vertical dashed line marks the corresponding DM mass. Numbers in the legends denote the event counts in the visible energy range $E_{\text{vis}} \in [12\,\text{MeV}, 1\,\text{GeV}]$ and the red shaded region indicates the local feature range defined in the range $E_{\text{vis}} \in [0.7, 1.0]\, m_\chi$.

$\nu_e/\bar{\nu}_e$-like flavor selection discussed in Sec. 9.1.1 enhances the $\bar{\nu}_e$-induced IBD peak and the ν_e-induced CC1p0n contribution, thereby preserving the characteristic two peaks of the transition region. For the larger DM mass $m_\chi = 0.5\,\text{GeV}$ (right column), however, the CC1p0n driven double-peak structure by ν_e and ν_μ is lost for a flavor-based event selection and instead a dominant single-peak structure driven by ν_e-induced CC1p0n events remains.

Instead of a flavour-based selection, Fig. 9.4 shows the expected spectrum before and after the application of the zero-neutron topology cut introduced in Sec. 9.1.2. The hatched areas indicate the contributions from CC1p0n events that are targeted by the topological constraint. In the transition region, the zero-neutron cut suppresses the IBD peak, which is determined by a CC0p1n topology and shows a neutron in the final state for most events (cf. Sec. 8.2). For this reason, a topology-based selection strategy destroys the characteristic spectral structure for $m_\chi = 0.15\,\text{GeV}$ (left column).

In contrast, the CC1p0n driven double-peak structure by ν_e and ν_μ for $m_\chi = 0.5\,\text{GeV}$ is sharpened as desired by the zero-neutron cut (right column).

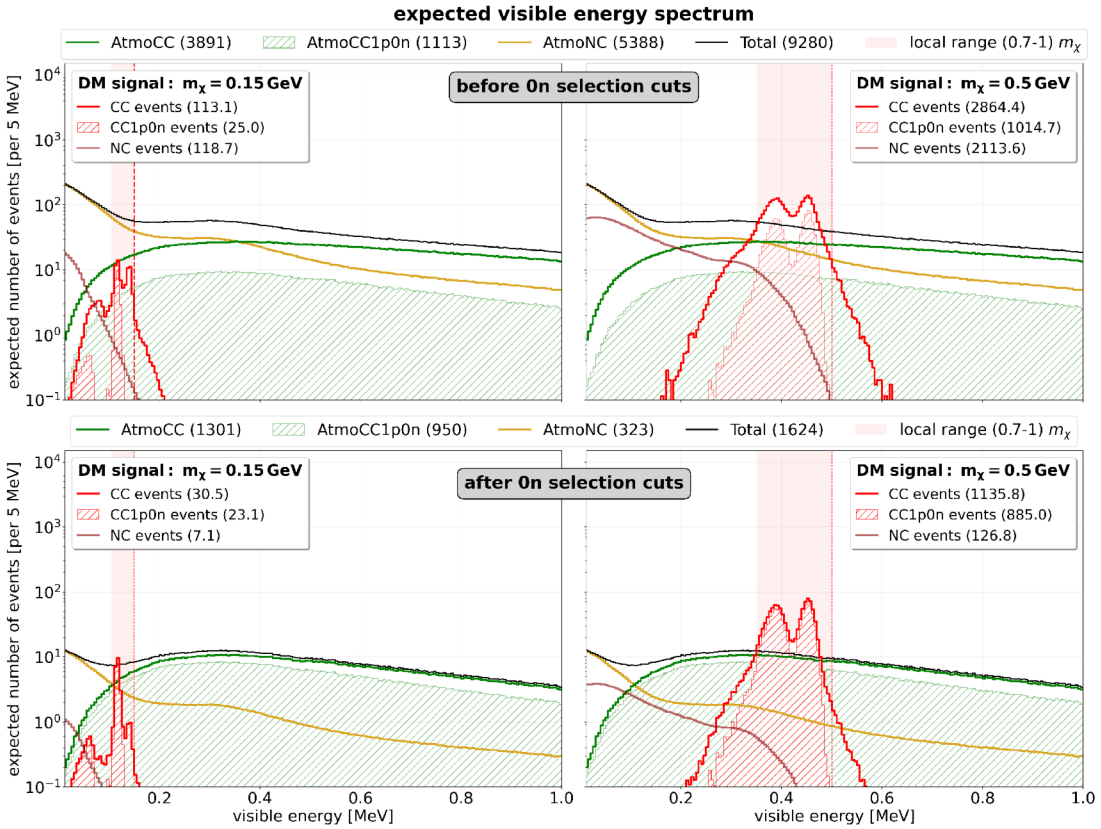

Figure 9.4: Expected visible energy spectrum in JUNO for 14.77 kton LS and 10 yr of data taking. The top row shows the spectrum before any cuts, and the bottom row after applying the zero-neutron topology cut. The contribution of CC1p0n events is indicated by hatched areas. The DM-induced CC and NC contributions are shown in red, with the vertical dashed line marking the DM mass. Numbers in the legends denote the event counts in the visible energy range $E_{\text{vis}} \in [12\,\text{MeV}, 1\,\text{GeV}]$ and the red shaded region indicates the local feature range defined in the range $E_{\text{vis}} \in [0.7, 1.0]\,m_\chi$.

Considering the expected event numbers for the DM-induced signals and the backgrounds in the full visible energy range $E_{\text{vis}} \in [12\,\text{MeV}, 1\,\text{GeV}]$, summarized in Figs. 9.3 and 9.4, the global S2B ratio is reduced for both selection strategies compared to the total uncut spectra. This is caused by the significant loss in event statistics for both selection strategies. Although neither selection strategy is suitable for a pure counting based analysis, they can still locally enhance the S2B ratio in the energy range of the characteristic DM-induced features. In order to analyze the local improvement of the S2B ratio, the feature dominated range is defined as $E_{\text{vis}} \in [0.7, 1.0]\,m_\chi$, which is indicated by the red shaded regions in Figs. 9.3 and 9.4 and contains the dominant spectral peaks. In Tab. 9.1 the expected numbers of signal and background events n_S and n_B in this local range is summarized, along with the corresponding signal-to-background (S2B) ratios as defined in Eq. 8.7.

In the transition region at $m_\chi = 0.15\,\text{GeV}$, the flavor-based $\nu_e/\bar{\nu}_e$ selection improves the local S2B ratio from 3.0 ± 0.3 to 4.9 ± 0.5, which corresponds to a relative increase of

Table 9.1: Expected numbers of DM-induced signal events n_S and background events n_B in the local energy range $E_{\text{vis}} \in [0.7, 1.0]\, m_\chi$, as well as the corresponding local S2B ratios. For both DM scenarios, $m_\chi = 0.15\,\text{GeV}$ and $m_\chi = 0.5\,\text{GeV}$, the three selection approaches are listed separately. The uncertainties are calculated assuming Poisson statistics and are propagated using Gaussian error propagation.

DM mass	selection	signal events n_S	background events n_B	S2B ratio
0.15 GeV	none	80 ± 9	630 ± 25	3.0 ± 0.3
	$\nu_e/\bar{\nu}_e$-like	61 ± 8	92 ± 10	4.9 ± 0.5
	0n topology	25 ± 5	79 ± 9	2.4 ± 0.4
0.5 GeV	none	2576 ± 51	1436 ± 38	40.7 ± 0.6
	$\nu_e/\bar{\nu}_e$-like	1200 ± 35	392 ± 20	30.1 ± 0.6
	0n topology	1065 ± 33	339 ± 18	28.4 ± 0.6

about 63 %, with a moderate signal loss. This improvement in local spectral significance suggests that Bayesian analysis can increase JUNO's sensitivity for sub-GeV DM masses, by exploiting the characteristic peak structure in the transition region (cf. Chap. 10). For larger DM masses in the upper sub-GeV range ($m_\chi = 0.5\,\text{GeV}$), flavor selection, even with a local approach, leads to a reduction in the S2B ratio from 40.7 ± 0.6 to 30.1 ± 0.6, since the ν_μ-induced CC1p0n peak structure is lost due to the restriction to $\nu_e/\bar{\nu}_e$ events. In this energy range, flavor-based selection therefore no longer appears to be beneficial. Topology-based zero-neutron selection does not improve the local S2B ratio for either of the DM masses compared to the uncut spectrum with no selection. For $m_\chi = 0.15\,\text{GeV}$, the zero-neutron section destroys the IBD peak and reduces the S2B ratio to 2.4 ± 0.4, while for $m_\chi = 0.5\,\text{GeV}$ the absolute signal loss leads to a reduced S2B ratio of 28.4 ± 0.6. A combined analysis that simultaneously utilizes both flavor and topology information could potentially provide additional sensitivity, but this is beyond the scope of this work.

9.2 Signal-to-Background Optimization for GeV DM

In contrast to the sub-GeV region, the characteristic spectral structures mainly arising from QES interactions disappear in the GeV range, where RES and DIS interactions become more dominant (cf. Sec. 6.2.3). Instead, the GeV region allows for directional event reconstruction, which can be used to improve the S2B ratio. The underlying idea of a direction-dependent event selection is based on the fact that a DM-induced neutrino signal preferentially originates from the Galactic Center (GC), while background events are isotropically distributed in the detector. The sensitivity improvement achievable through a cone-shaped directional cut around the GC depends on both the underlying DM density profile and the directional resolution in JUNO. Unlike in water Cherenkov detectors, the direction of ionizing particles in LS detectors, such as JUNO, cannot be reconstructed as easily, since the Cherenkov light constitutes only a few percent of the scintillation light. However, for high-energy CC events, the direction of the charged lepton $\hat{p}_{\ell^\pm}$ preferentially follows the original neutrino direction $\hat{p}_\nu$. Fig. 9.5 shows the scatter plot of the angle $\alpha(\hat{p}_\nu, \hat{p}_{\ell^\pm})$ between the initial neutrino direction $\hat{p}_\nu$ and the direction of the charged lepton $\hat{p}_{\ell^\pm}$ after the CC interaction in JUNO as a function of

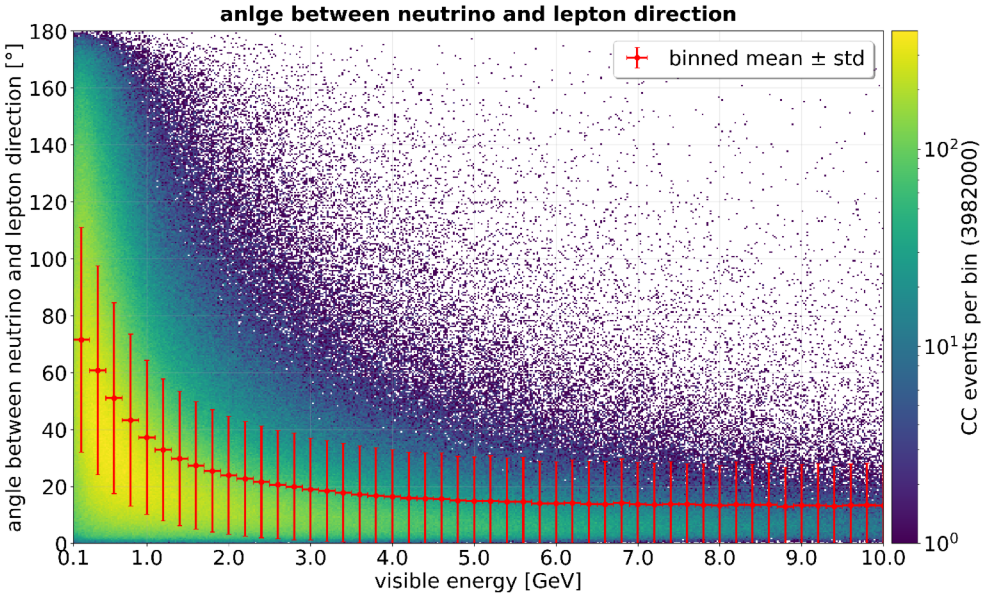

Figure 9.5: Angular distribution between the initial neutrino direction and the lepton direction in CC interactions as a function of the visible energy E_{vis}. The red markers indicate the mean values and standard deviations in the respective bins. The data was provided by the JUNO Collaboration.

the visible energy E_{vis}[4]. The angular distribution for nine representative neutrino energy bins is shown in Fig. B.4. While in the sub-GeV region for $E_{\text{vis}} < 1\,\text{GeV}$, the correlation between neutrino and lepton direction is still very weak, the mean angle between $\hat{p}_\nu$ and $\hat{p}_{\ell^\pm}$ becomes smaller than 40° for $E_{\text{vis}} > 1\,\text{GeV}$. For events with $E_{\text{vis}} = 10\,\text{GeV}$, the mean lepton direction deviates from the original neutrino direction by only about $\sim 13°$. This correlation forms the physical basis for JUNO's directional reconstruction in the GeV range, which is based on a ML-based analysis of the waveform features for each PMT and is presented in the following section.

9.2.1 Directional Reconstruction Method

In LS detectors, information about the particle direction is extracted from the topological structure of waveform features, which encode the superposition of scintillation light emitted along the particle track [79]. These features are obtained for each PMT from the deconvoluted waveforms within the first 1.25 μs [79]. Four of these features (first hit time (FHT), total charge, slope, and charge ratio) were already introduced in Sec. 8.1 in the context of the ML-based vertex reconstruction, where the directional information contributed to the energy weighting of the reconstructed vertex $\vec{r}_{\text{Qdep}}$ (cf. Sec. 8.1.1). For directional reconstruction, two additional features are included: the peak charge and peak time of the waveforms [79]. The performance of three NN architectures (`EfficientNet-V2`, `DeepSphere` and `PointNet++`) was evaluated separately for $\nu_e/\bar{\nu}_e$ and $\nu_\mu/\bar{\nu}_\mu$, and is displayed in Fig. 9.6 for neutrino energies between 1 GeV and 9 GeV [79]. The y-axis shows the 68 % quantile $q_{68\%} = \sigma_\alpha$ of the angular distribution α between the true and reconstructed neutrino direction as a function of the neutrino energy E_ν. The angular resolution improves with increasing energy for both flavors, since at higher energies longer particle tracks and a larger number of scintillation photons lead to a more

[4]The results were obtained from the CC events in dataset $D2$ of Tab. C.1.

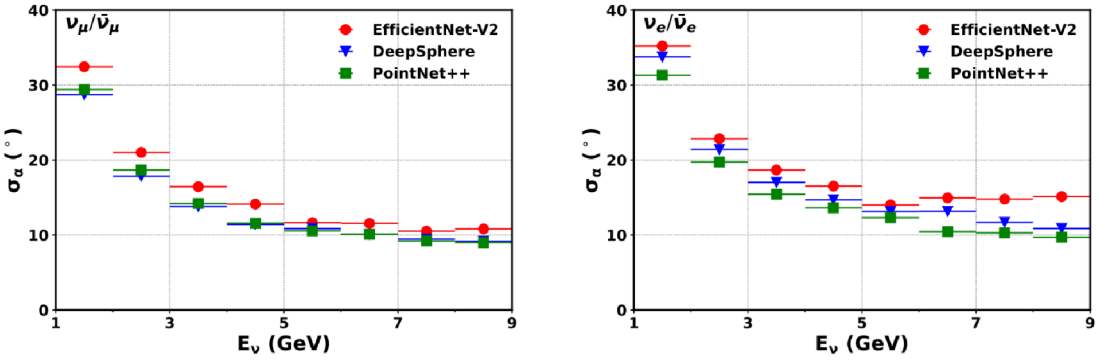

Figure 9.6: Directional reconstruction performance of three different NN models [79]. The values σ_α mark the 68 % quantile $q_{68\%}$ of the angular distribution α between true $\hat{p}_{\text{true}}$ and reconstructed $\hat{p}_{\text{rec}}$ neutrino direction. In the left panel the directional reconstruction performance of CC $\nu_\mu/\bar{\nu}_\mu$ events is shown as a function of the neutrino energy E_ν, while the right panel displays the results for $\nu_e/\bar{\nu}_e$. Plot taken from [79].

pronounced topological structure of the waveform features, from which the ML models extract the directional information. For CC $\nu_\mu/\bar{\nu}_\mu$ events (left panel), the resolution is systematically better at the same energy than for CC $\nu_e/\bar{\nu}_e$ (right panel), since the muon track in the final state exhibits a stronger directional signature than the electron shower[5] [79]. The `PointNet++` model provides the best reconstruction performance over a wide range of energies and is therefore used as the basis for the parameterization of the angular resolution and the directional event selection in this work.
Remarkably, the reconstructed angular resolution $q_{68\%} = \sigma_\alpha$ between true and reconstructed neutrino direction in Fig. 9.6 is smaller than the 68 % quantile of the kinematic angular distribution $\alpha(\hat{p}_\nu, \hat{p}_{\ell^\pm})$ between the neutrino and the final-state lepton direction in Fig. B.4. This is possible because in an LS detector, both the charged lepton and the hadronic components deposit their energy and produce scintillation light. The waveform features thus encode the topological structure of all final-state particles, and the ML models learn to extract the original neutrino direction from the momentum conservation implicitly contained in the combination of both contributions [79]. Although water Cherenkov detectors such as Super-K intrinsically provide clearer directional information of the ionizing particle through the Cherenkov light cone, many hadronic components lie below the Cherenkov threshold and thus remain invisible [79]. The complete deposition of all final-state particles thus constitutes a specific advantage of LS detectors.
In order to analytically parameterize the angular resolution of the directional reconstruction, the Probability Density Function (P.D.F.) of the angular distribution α between the true and reconstructed neutrino directions, averaged over all neutrino energies from 1–20 GeV [79], is approximated by a King Point Spread Function (PSF) [157], which is often used as a model for parameterizing the angular resolution [158]. The King function offers the advantage of being able to represent the tail caused by reconstruction outliers at large angles, which is systematically underestimated in a Gaussian or Rayleigh approximation. In the solid angle representation, the King PSF is defined as [158]

$$\frac{\mathrm{d}P}{\mathrm{d}\Omega}(\alpha \,|\, \omega, \gamma) = \frac{1}{2\pi\omega^2}\left(1 - \frac{1}{\gamma}\right)\left(1 + \frac{\alpha^2}{2\gamma\omega^2}\right)^{-\gamma} ,$$

[5] In the following, $\nu_e/\bar{\nu}_e$ and $\nu_\mu/\bar{\nu}_\mu$ denote CC events only.

which, using $\mathrm{d}\Omega = 2\pi \sin\alpha \, \mathrm{d}\alpha \approx 2\pi\alpha \, \mathrm{d}\alpha$, can be expressed as a one-dimensional angular distribution

$$p(\alpha \,|\, \omega, \gamma) = \frac{\alpha}{\omega^2} \left(1 - \frac{1}{\gamma}\right) \left(1 + \frac{\alpha^2}{2\gamma\omega^2}\right)^{-\gamma} . \tag{9.2}$$

This parameterization is used as an empirical model for the angular resolution in this work. Here, ω denotes the scale parameter and $\gamma > 1$ the shape parameter, which controls the strength of the tail. The factor $(1 - 1/\gamma)/\omega^2$ ensures the normalization $\int_0^\infty p(\alpha) \, \mathrm{d}\alpha = 1$. In Fig. 9.7, the `PointNet++` model P.D.F. of the angular distribution

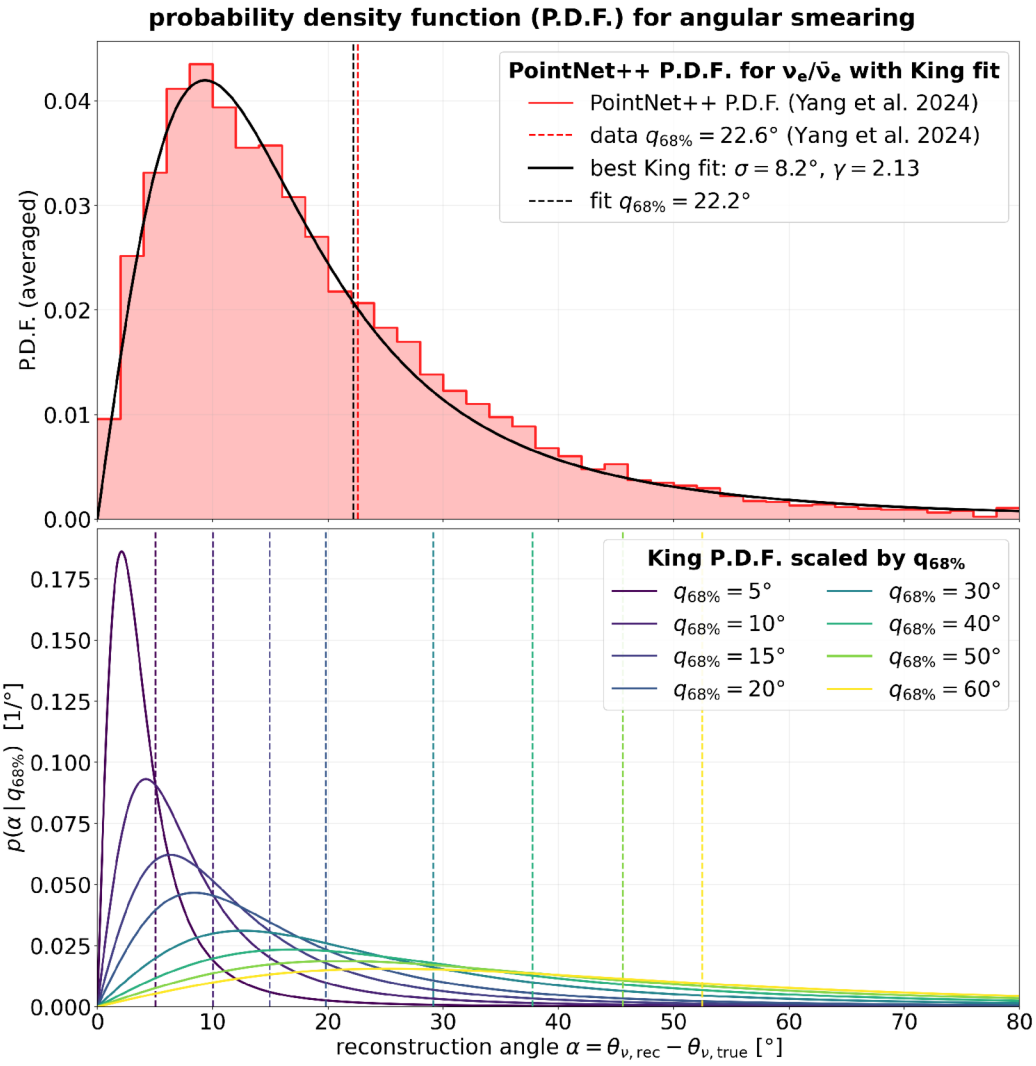

Figure 9.7: Parameterization of the angular resolution using a King PSF according to Eq. 9.2. Upper panel: P.D.F. of the angular distribution α between true and reconstructed neutrino direction, averaged over all neutrino energies from 1–20 GeV, for $\nu_e/\bar{\nu}_e$ events from the `PointNet++` model [79] (red histogram) together with the best King fit (black curve). The dashed vertical lines mark the respective 68 % quantiles $q_{68\%}$ of the data and the fit. Lower panel: Scaling of the King P.D.F. at fixed shape parameter $\gamma = 2.13$ for different values of $q_{68\%}$, corresponding to the energy- and flavor-dependent angular resolutions in Fig. 9.6. The dashed vertical lines indicate the respective $q_{68\%}$ values.

between true and reconstructed neutrino direction for $\nu_e/\bar{\nu}_e$ events is shown, averaged over all neutrino energies from 1–20 GeV (red histogram adapted from [79]). A χ^2 fit (black curve) of the King function according to Eq. 9.2 yields the parameters $\omega = 8.2°$ and $\gamma = 2.13$, resulting in a 68 % quantile of $q_{68\%} = 22.2°$. The same procedure was applied to the averaged `PointNet++` distribution for $\nu_\mu/\bar{\nu}_\mu$ events reported in [79], yielding the best fit results $\omega = 6.5°$ and $\gamma = 1.91$ (cf. Fig. B.5). The fitted $q_{68\%}$ values are in good agreement with those determined directly from the data and reported in [79] ($q_{68\%}^{\text{data}} = 22.6°$ for $\nu_e/\bar{\nu}_e$ and $q_{68\%}^{\text{data}} = 19.9°$ for $\nu_\mu/\bar{\nu}_\mu$), with deviations below $\sim 0.4°$ arising from a slight shape mismatch. A more accurate description could be achieved by a sum of two King functions, which, however, was not pursued in this work given the limited available data. As an alternative model, a double-Rayleigh distribution (three parameters) was fitted, which, despite the additional degree of freedom, yields a $\sim 20\,\%$ higher χ^2 sum, since the exponentially decaying Rayleigh components describe the tail in the data less accurately than the King function.
The parameterization of the averaged angular distribution by Eq. 9.2 with the respective fixed shape parameter γ for each flavor ($\gamma = 2.13$ for $\nu_e/\bar{\nu}_e$ and $\gamma = 1.91$ for $\nu_\mu/\bar{\nu}_\mu$) makes it possible to insert the flavor- and energy-dependent angular resolution $\sigma_\alpha(E_\nu)$ from Fig. 9.6 directly as $q_{68\%}(E_\nu)$ into the King-P.D.F., thus scaling the width of the distribution without changing its shape. The resulting distributions $p(\alpha \,|\, q_{68\%}(E_\nu))$ are shown in the lower panel of Fig. 9.7 for selected values of $q_{68\%}$. The approach is based on the assumption that the shape parameter γ is energy-independent for both flavors and that only the width $q_{68\%}$ changes with the neutrino energy. This is physically motivated by the fact that the shape of the P.D.F. is primarily determined by the reconstruction method, but cannot be verified due to the lack of energy-resolved distributions in [79]. Especially at low energies, it is to be expected that the tails are more pronounced, since the reconstruction is significantly less accurate there.

9.2.2 Directional Event Selection

The directional reconstruction presented in the previous section enables a targeted event selection strategy by accepting only those events whose reconstructed direction lies within a cone of half-opening angle ψ_{cone} around the GC. The choice of the optimal opening angle is determined by the best S2B ratio

$$\text{S2B}(\psi_{\text{cone}}) = \frac{n_S(\psi_{\text{cone}})}{\sqrt{n_S(\psi_{\text{cone}}) + n_B(\psi_{\text{cone}})}} \,, \tag{9.3}$$

where the selected number of signal events $n_S(\psi_{\text{cone}})$ depends on both the WIMP mass and the DM density profiles, which are introduced in Sec. 3.2. The generalised Navarro-Frenk-White (gNFW) profile, parameterized in Eq. 3.7, describes a cuspy profile that increases steeply near the GC [36]. The Einasto profile in Eq. 3.8, in contrast, describes a cored profile with a flat radial density distribution [51]. A directional event selection is more effective for cuspy profiles such as gNFW, since according to Fig. 3.3, a larger fraction of the expected neutrinos from DM annihilation originates from the vicinity of the GC. The Einasto profile, in contrast, represents the conservative scenario for the sensitivity achievable with directional selection. In the following, the expected signal $n_S(\psi_{\text{cone}})$ and background events $n_B(\psi_{\text{cone}})$ within a cone of half-opening angle ψ_{cone} around the GC are determined. First, the S2B ratio according to Eq. 9.3 is evaluated for the case of perfect directional reconstruction, before incorporating the realistic reconstruction performance parameterized according to Eq. 9.2.

Ideal Signal Selection

Since the atmospheric neutrino background is nearly isotropically distributed[6], the probability that an event lies within a cone with half-opening angle ψ_{cone} around the GC is given by

$$\varepsilon_B(\psi_{\text{cone}}) = \frac{\Omega(\psi_{\text{cone}})}{4\pi} = \frac{1-\cos\psi_{\text{cone}}}{2} \ , \tag{9.4}$$

where $\Omega(\psi_{\text{cone}})$ denotes the solid angle defined in Eq. 3.12. In contrast, the signal efficiency $\varepsilon_S(\psi_{\text{cone}})$ follows the integrated spatial DM density distribution, which is encoded by the $\mathcal{J}$-factor. In Sec. 3.2.1, the quantity $\mathcal{J}_{\psi_m}$ is introduced for a cone-shaped region of interest (ROI) with a half-opening angle ψ_m around the GC. The ratio

$$\varepsilon_S(\psi_{\text{cone}}) = \frac{\mathcal{J}_{\psi_{\text{cone}}}}{\mathcal{J}_{\text{FS}}} \tag{9.5}$$

provides a direct measure of the signal efficiency for $\psi_m = \psi_{\text{cone}}$, where $\mathcal{J}_{\text{FS}}$ denotes the full-sky (FS) $\mathcal{J}$-factor corresponding to $\psi_m = 180°$. The signal efficiency is illustrated in Fig. 3.3. The number of signal events after directional selection within ψ_{cone} is obtained as $n_S(\psi_{\text{cone}}) = n_{S,\text{FS}} \cdot \varepsilon_S(\psi_{\text{cone}})$, where $n_{S,\text{FS}}$ denotes the event yield derived in Chap. 6, corresponding to a FS observation. Analogously, the number of background events is given by $n_B(\psi_{\text{cone}}) = n_{B,\text{FS}} \cdot \varepsilon_B(\psi_{\text{cone}})$, with $n_{B,\text{FS}}$ derived in Chap. 7.
Fig. 9.8 shows the results of directional selection assuming ideal directional reconstruction ($\hat{p}_{\text{rec}} = \hat{p}_{\text{true}}$) for the gNFW profile (left) and the Einasto profile (right). The upper row displays the S2B ratio as a function of the half-opening angle ψ_{cone} for masses $m_\chi = 1$–$10\,\text{GeV}$ in steps of $1\,\text{GeV}$. The expected number of DM-induced signal events $n_{S,\text{FS}}$ was calculated from the Super-K upper limits (cf. Sec. 6.1), which are shown in Fig. 3.6 for the GeV mass range [63]. While the cuspy gNFW profile shows that small cone angles of $\psi_{\text{cone}} \approx 1.6°$–$4.8°$ (hatched blue area, upper left panel) yield a significant improvement of the S2B ratio, the optimal half-opening angles for the cored Einasto profile reveal considerably larger values of $\psi_{\text{cone}} \approx 37°$ (hatched red area, upper right panel). The S2B ratio at $\psi_{\text{cone}} = 180°$ corresponds to the FS observation (dashed vertical lines), which are independent of the underlying DM density profile.
The lower row in Fig. 9.8 compares the optimal S2B ratio (solid line, colored markers) with the S2B ratio for a FS observation at $\psi_{\text{cone}} = 180°$ (dashed line, black markers). While the cuspy gNFW profile (lower left panel) can achieve a 4–7 fold increase in the S2B ratio with directional selection, the Einasto profile yields only a moderate improvement of $\sim 58\,\%$ compared to a FS observation, even assuming ideal directional reconstruction. The ideal case serves as an upper limit for the achievable sensitivity and demonstrates the potential of directional selection in the GeV range. The realistic scenario, taking into account the finite angular resolution in JUNO according to Eq. 9.2 is discussed in the next section.

[6]The atmospheric neutrino flux exhibits a zenith angle dependence that is not fully averaged out by the Earth's rotation, since the GC has a fixed declination of approximately $-29°$ and thus never passes near the zenith at JUNO's latitude ($\sim 22°$N). However, over the 10 yr observation period, the azimuthal averaging is complete, and the zenith-dependent effect is small compared to the dominant flux uncertainties and is therefore neglected in this analysis.

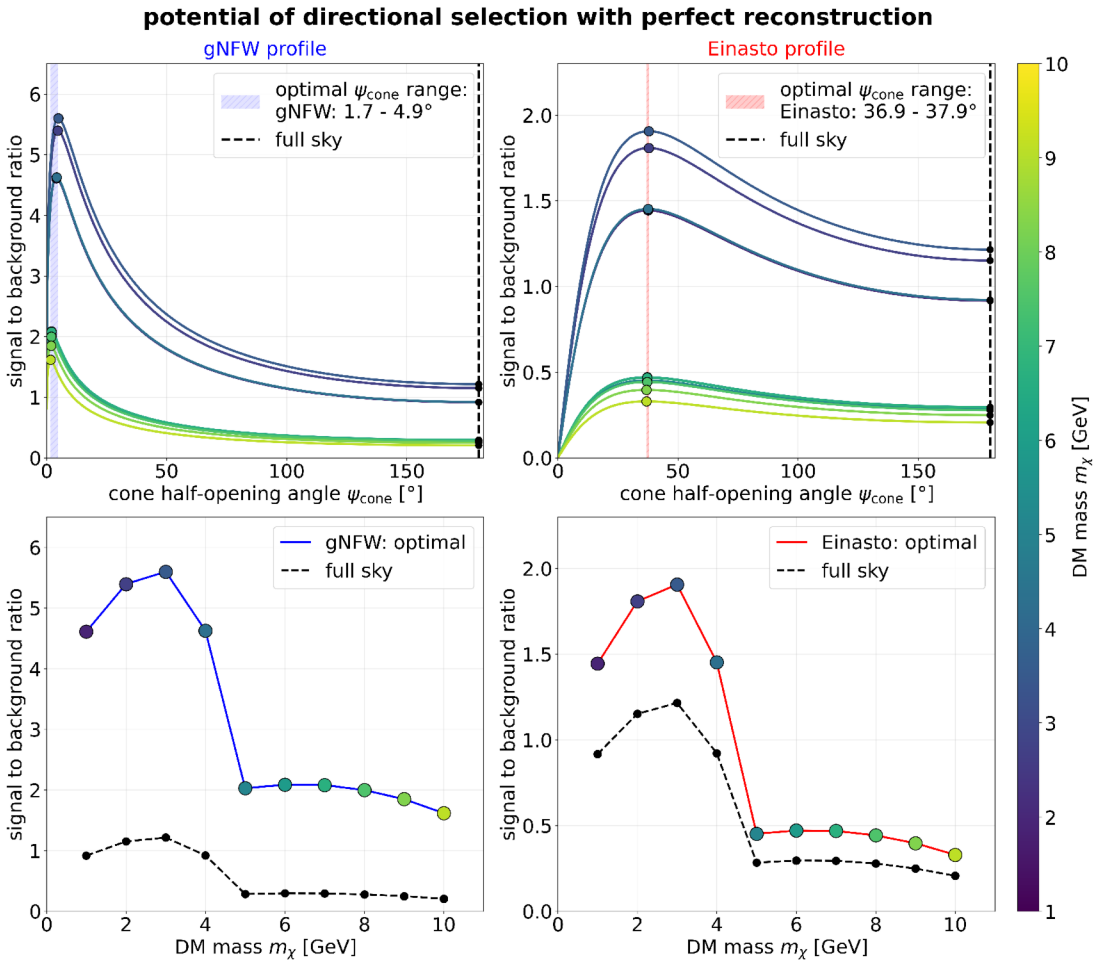

Figure 9.8: S2B ratio for a directional event selection assuming ideal reconstruction ($\hat{p}_{\text{rec}} = \hat{p}_{\text{true}}$) for the gNFW profile (left) and the Einasto profile (right). The upper panels show the S2B ratio as a function of the cone angle ψ_{cone} for DM masses $m_\chi = 1$–$10\,\text{GeV}$, while the colored markers indicate the mass-specific optimal cone angle. The shaded colored bands indicate the range of optimal opening angles, and the dashed black line marks the FS case ($\psi_{\text{cone}} = 180°$). The lower panels compare the mass-specific maximal S2B ratio for the optimal cone angle (colored markers with solid curves) with the S2B ratio for a FS observation (black dashed curves).

Realistic Signal Selection

In the ideal case, the reconstructed neutrino direction $\hat{p}_{\text{rec}}$ corresponds exactly to the true neutrino direction $\hat{p}_{\text{true}}$, and therefore, the directional-dependent S2B ratio can be derived analytically. In the real scenario, however, the reconstructed neutrino direction deviates from the true direction by an angle α, as illustrated in Fig. 9.9. Since the probability $P(\psi_{\text{rec}} \leq \psi_{\text{cone}} \,|\, \psi_{\text{true}}, \alpha)$ of reconstructing an event within the selection cone ψ_{cone} depends on both the true direction ψ_{true} and the stochastic angular deviation α from the reconstruction method presented in Sec. 9.2.1, an analytical treatment is no longer feasible. Instead, a MC-based approach is employed to evaluate the signal efficiency numerically. To this end, two coordinate systems are illustrated in Fig. 9.9. The blue coordinate system K with (x, y, z) represents the galactic reference frame, whose z-axis is aligned toward the GC. The gray cone with half-opening angle ψ_{cone}

defines the ROI for the directional event selection. For an incoming neutrino ν arriving at the detector at an angle ψ_{true} in the galactic reference frame, the local coordinate system K' with (x', y', z') (red) is chosen such that the z'-axis is aligned along $\hat{p}_{\text{true}}$. Without loss of generality, the rotation of K' with respect to K is chosen to be in the x-z plane (indicated by the blue plane), such that the y and y'-axes coincide. Due to the finite angular resolution, the reconstructed direction $\hat{p}_{\text{rec}}$ deviates from $\hat{p}_{\text{true}}$ by an angle α (indicated by the red blurred cone), which is distributed according to the King function (cf. Eq. 9.2) and is characterized by the 68 % quantiles shown in Fig. 9.6, while the azimuthal angle ϕ_α around $\hat{p}_{\text{true}}$ is uniformly distributed. Due to the assumption of an isotropically distributed atmospheric neutrino flux, the background efficiency $\varepsilon_B(\psi_{\text{cone}})$ in Eq. 9.4 remains unchanged even for finite angular resolution, as statistically the same number of background events are scattered out of the ROI as into it. In contrast, the signal efficiency in Eq. 9.5 must be modified, since a neutrino whose true direction $\psi_{\text{true}} \leq \psi_{\text{cone}}$ lies within the cone may be reconstructed outside the cone with a certain probability ($\psi_{\text{rec}} > \psi_{\text{cone}}$). Conversely, neutrinos with $\psi_{\text{true}} > \psi_{\text{cone}}$ can also be scattered into the cone $\psi_{\text{rec}} \leq \psi_{\text{cone}}$. However, since the signal is concentrated toward the GC, the first effect dominates, leading to an effective reduction of the signal efficiency. The probability $P(\psi_{\text{rec}} \leq \psi_{\text{cone}} \,|\, \psi_{\text{true}}, \alpha)$ that the reconstructed direction ψ_{rec} of a neutrino with true direction ψ_{true} lies within the cone ψ_{cone} can be geometrically visualized as the overlap region between the gray selection cone and the red reconstruction cone in Fig. 9.9. This probability is computed numerically using a MC approach, where for a given true angle ψ_{true}, the reconstruction angle α is sampled 50,000 times according to Eq. 9.2, and the azimuthal angle ϕ is drawn uniformly from $[0, 2\pi)$. For each sampled event, the reconstructed neutrino direction in the local coordinate system is given in spherical coordinates by $\hat{p}'_{\text{rec}} = (\sin\alpha\cos\phi,\, \sin\alpha\sin\phi,\, \cos\alpha)$. By applying a rotation $R_y(\beta)$ with $\beta = \psi_{\text{true}}$ around the y-axis, the reconstructed direction can be transformed into the galactic frame according to

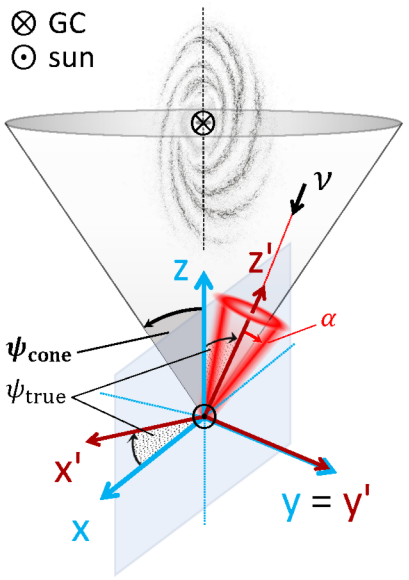

Figure 9.9: Schematic illustration of the geometry for directional event selection with finite angular resolution. The blue coordinate system represents the galactic frame, with the z-axis pointing toward the GC. The local red coordinate system is defined by the arriving neutrino ν and tilted in the x-z plane by an angle ψ_{true}.

$$\hat{p}_{\text{rec}} = R_y(\psi_{\text{true}})\,\hat{p}'_{\text{rec}} = \begin{pmatrix} \cos\psi_{\text{true}} & 0 & \sin\psi_{\text{true}} \\ 0 & 1 & 0 \\ -\sin\psi_{\text{true}} & 0 & \cos\psi_{\text{true}} \end{pmatrix} \begin{pmatrix} \sin\alpha\cos\phi \\ \sin\alpha\sin\phi \\ \cos\alpha \end{pmatrix} .$$

The reconstructed polar angle in the galactic reference frame is obtained from the z-component as $\psi_{\text{rec}} = \arccos(\hat{p}_{\text{rec}})_z$, where $|\hat{p}_{\text{rec}}| = 1$. The probability $P(\psi_{\text{rec}} \leq \psi_{\text{cone}} \,|\, \psi_{\text{true}}, \alpha)$ is then estimated as the fraction of MC samples satisfying $\psi_{\text{rec}} \leq \psi_{\text{cone}}$. With these considerations, the signal efficiency with finite angular resolution can be obtained by convolving the differential $\mathcal{J}$-factor distribution of a cone-like ROI in Eq. 3.9

with the probability for reconstruction within the cone according to

$$\varepsilon_S^{(ch)}(\psi_{\text{cone}}, m_\chi) = \frac{1}{\mathcal{J}_{\text{FS}}} \int_0^{180^\circ} \frac{\mathrm{d}\mathcal{J}_{\psi_{\text{true}}}}{\mathrm{d}\psi_{\text{true}}} P\left(\psi_{\text{rec}} \leq \psi_{\text{cone}} \,|\, \psi_{\text{true}}, \alpha^{(ch)}(m_\chi)\right) \mathrm{d}\psi_{\text{true}} \,. \quad (9.6)$$

Since the angular resolution differs for $\nu_e/\bar{\nu}_e$, $\nu_\mu/\bar{\nu}_\mu$ and NC events, the signal efficiency is computed separately for these event classes (ch). While the $\nu_e/\bar{\nu}_e$ and $\nu_\mu/\bar{\nu}_\mu$ performances are discussed in detail in Sec. 9.2.1 and illustrated in Fig. 9.6, the NC treatment is based on a preliminary energy-dependent directional-reconstruction results within the JUNO collaboration and is incorporated through the same procedure using the corresponding NC angular resolution given as 68 % quantiles.The total number of signal events within the cone with half-opening angle ψ_{cone} is thus given by

$$n_S(\psi_{\text{cone}}) = n_{S,\text{FS}}^{\nu_e/\bar{\nu}_e} \cdot \varepsilon_S^{\nu_e/\bar{\nu}_e}(\psi_{\text{cone}}) + n_{S,\text{FS}}^{\nu_\mu/\bar{\nu}_\mu} \cdot \varepsilon_S^{\nu_\mu/\bar{\nu}_\mu}(\psi_{\text{cone}}) + n_{S,\text{FS}}^{\text{NC}} \cdot \varepsilon_S^{\text{NC}}(\psi_{\text{cone}}) \,, \quad (9.7)$$

where the efficiency $\varepsilon_S^{(ch)}(\psi_{\text{cone}}, m_\chi)$ is evaluated with the MC approach depending on the WIMP mass m_χ by using the corresponding resolution parameter $q_{68\%}^{(ch)}(E_\nu = m_\chi)$. Fig. 9.10 shows the selection efficiency as a function of the cone angle ψ_{cone} for the

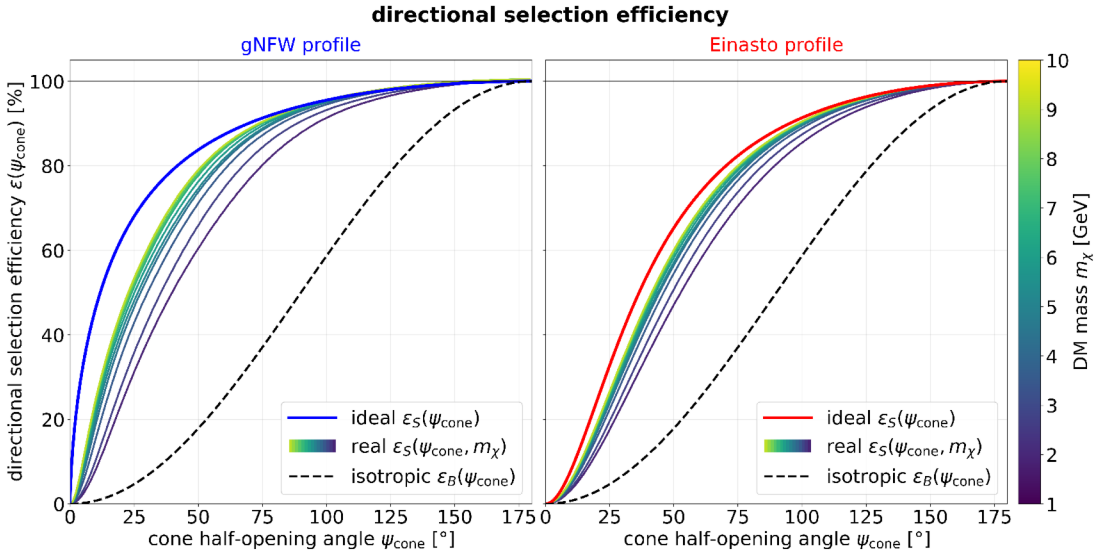

Figure 9.10: Directional selection efficiencies as a function of the cone half-opening angle ψ_{cone} for the gNFW profile (left) and the Einasto profile (right). The solid blue and red lines show the ideal signal efficiency in Eq. 9.5 assuming perfect directional reconstruction. The colored lines represent the realistic signal efficiency $\varepsilon_S(\psi_{\text{cone}}, m_\chi)$ in Eq. 9.6 for DM masses in the range $m_\chi = 1$–$10\,\text{GeV}$, including the finite angular resolution. The black dashed line indicates the background efficiency $\varepsilon_B(\psi_{\text{cone}})$ in Eq. 9.4 for an isotropic distribution.

gNFW profile (left) and the Einasto profile (right), derived with the MC approach. The blue and red curves indicate the signal efficiency ε_S for ideal directional reconstruction according to Eq. 9.5, and correspond exactly to the curves in Fig. 3.3. The black dashed curve shows the background efficiency $\varepsilon_B(\psi_{\text{cone}})$ defined in Eq. 9.4, which is identical to the ideal efficiency due to the isotropic event distribution. The colored curves (cf. colorbar on the right) display the mass-dependent averaged signal efficiencies for all

three channels $\varepsilon_S^{(ch)}(\psi_{\text{cone}}, m_\chi)$ and can be calculated according to

$$\varepsilon_S(\psi_{\text{cone}}, m_\chi) = \frac{n_S(\psi_{\text{cone}})}{n_{S,\text{FS}}(m_\chi)} \quad \text{with } n_{S,\text{FS}}(m_\chi) = n_{S,\text{FS}}^{\nu_e/\bar{\nu}_e} + n_{S,\text{FS}}^{\nu_\mu/\bar{\nu}_\mu} + n_{S,\text{FS}}^{\text{NC}} \tag{9.8}$$

for both DM density profiles. The selected number of signal events $n_S(\psi_{\text{cone}})$ is given in Eq. 9.7, and $n_{S,\text{FS}}(m_\chi)$ denotes the expected total number of events for a FS observation. The signal efficiency of a directional event selection decreases significantly for both DM profiles, when finite angular resolution is taken into account. This effect becomes more pronounced for decreasing DM masses, as the directional resolution is considerably worse in this regime (cf. Fig. 9.6). With these results, the S2B ratio in Eq. 9.3 can now be determined for the case of finite energy-dependent angular resolution $\alpha(E_\nu = m_\chi)$.
Fig. 9.11 shows the results of directional selection for the gNFW profile (left) and the Einasto profile (right), considering the achievable angular resolution in JUNO (cf. Sec. 9.2.1). Compared to the ideal case in Fig. 9.8, the finite angular resolution leads to a significant increase and broadening of the optimal cone angles. For the gNFW profile, the optimal opening angles increase from $\psi_{\text{cone}} \approx 1.6°$–$4.8°$ in the ideal case to $\psi_{\text{cone}} \approx 11°$ for $m_\chi = 10\,\text{GeV}$ and $\psi_{\text{cone}} \approx 34°$ for $m_\chi = 1\,\text{GeV}$ with realistic resolution. This reflects the smearing of the signal distribution due to reconstruction uncertainties, particularly in the range $E_\nu \lesssim 4\,\text{GeV}$ as illustrated in Fig. 9.6. Analogously, the optimal angles for the Einasto profile shift from $\psi_{\text{cone}} \approx 37°$ to $\psi_{\text{cone}} \approx 47°$ for $m_\chi = 10\,\text{GeV}$ and $\psi_{\text{cone}} \approx 72°$ for $m_\chi = 1\,\text{GeV}$. The lower panels in Fig. 9.11 compare the achievable S2B ratio with realistic resolution (colored markers) to the FS observation (black markers) and the ideal case (dotted curves), which are summarized in Tab. 9.2 together with the optimal cone angle ψ_{cone}. While the finite angular resolution reduces the potential improvement compared to the ideal scenario for both models, a significant enhancement ΔS2B of the signal-to-background ratio relative to the FS observation can still be achieved for the cuspy gNFW profile for $m_\chi \geq 4\,\text{GeV}$. For the cored Einasto profile, the reduction of

Table 9.2: Summary of the mass-dependent S2B ratio for a FS observation (which is independent of the directional resolution) compared to a directional event selection assuming two different DM profiles (gNFW and Einasto). The optimal cone angles ψ_{cone} as well as the S2B ratio is compared for an ideal directional reconstruction with $\alpha = 0$ (cf. Fig 9.8) and a realistic reconstruction (cf. Fig 9.11).

scenario	FS	gNFW profile				Einasto profile			
resolution	both	ideal		realistic		ideal		realistic	
m_χ [GeV]	S2B	ψ_{cone}	S2B	ψ_{cone}	S2B	ψ_{cone}	S2B	ψ_{cone}	S2B
1	0.92	4.1 °	4.61	34.1 °	1.34	37.6 °	1.44	72.1 °	1.06
2	1.15	4.7 °	5.39	32.1 °	1.87	37.9 °	1.81	63.1 °	1.40
3	1.22	4.9 °	5.60	20.1 °	2.34	37.9 °	1.91	57.1 °	1.56
4	0.92	4.2 °	4.63	17.1 °	1.99	37.6 °	1.45	53.1 °	1.22
5	0.28	2.0 °	2.03	14.1 °	0.68	37.2 °	0.45	50.1 °	0.38
6	0.30	2.1 °	2.09	13.1 °	0.74	37.2 °	0.47	50.1 °	0.41
7	0.29	2.1 °	2.08	12.1 °	0.77	37.2 °	0.47	48.1 °	0.41
8	0.28	2.0 °	2.00	12.1 °	0.75	37.2 °	0.44	48.1 °	0.39
9	0.25	1.9 °	1.85	11.1 °	0.69	36.9 °	0.40	47.1 °	0.35
10	0.21	1.7 °	1.62	11.1 °	0.58	36.9 °	0.33	47.1 °	0.29

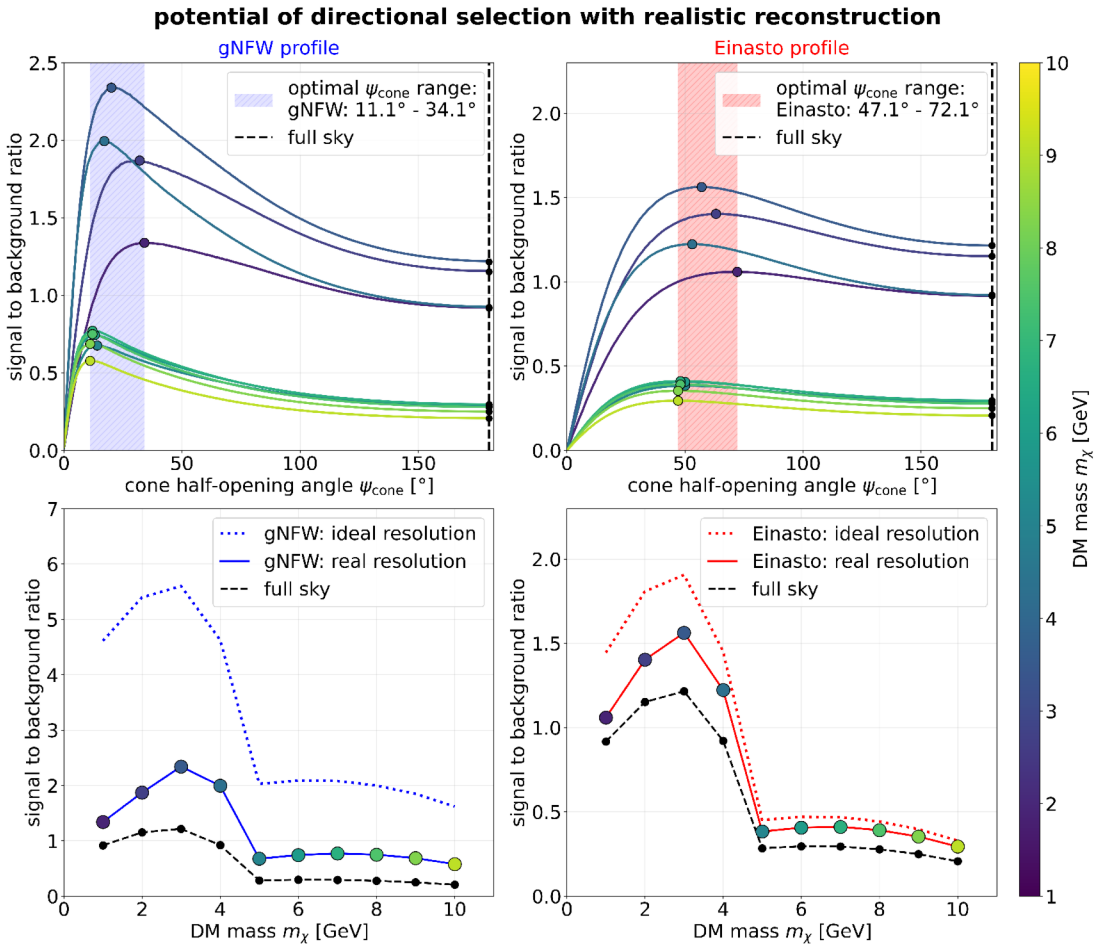

Figure 9.11: S2B ratio for directional event selection considering the angular resolution in Eq. 9.2 for the gNFW profile (left) and the Einasto profile (right). The upper panels show the S2B ratio as a function of the cone angle ψ_{cone} for different DM masses. The colored shaded bands indicate the range of optimal half-opening angles, and the dashed vertical black lines mark the FS case. The lower panels compare the optimal S2B ratio (colored markers) with the FS observation $\psi_{\text{cone}} = 180°$ (black markers) and the case of ideal angular resolution from Fig. 9.8 (dotted curves).

the S2B ratio considering finite directional resolution compared to the ideal case is less pronounced (lower right panel of Fig. 9.11), since the broader signal distribution is less affected by angular smearing. For the same reason, a direction-dependent event selection is overall less effective for the cored Einasto profile with a mean S2B improvement of $\sim 33\,\%$ compared to a FS observation assuming realistic directional resolution (cf. Tab. 9.2). The maximum improvement of $42\,\%$ is achieved for $m_\chi = 10\,\text{GeV}$ since the angular resolution is increasing for larger neutrino energies (cf. Fig. 9.6).
For the cuspy gNFW profile, on the other hand, the impact of finite directional resolution is considerably stronger (lower left panel of Fig. 9.11), since the signal is much more strongly concentrated toward the GC and is therefore more sensitive to angular smearing. As a consequence, the achievable S2B ratio is reduced by a factor ~ 2.7 compared to the ideal case, and the optimal cone angles are shifted to significantly larger values. Nevertheless, a directional event selection remains beneficial for the gNFW profile even in the realistic scenario, yielding a mean improvement of the S2B ratio of $\sim 129\,\%$ relative to the FS observation over the considered mass range (cf. Tab. 9.2). The improvement

becomes more pronounced with increasing WIMP mass, as the angular resolution improves at higher neutrino energies, and reaches its maximum at $m_\chi = 10\,\text{GeV}$ with an enhancement of approximately 180 %.
The results in Tab. 9.2 show that a directional event selection can significantly improve the S2B ratio even when the finite angular resolution in JUNO is taken into account, in particular for the cuspy gNFW profile at larger WIMP masses, where the directional reconstruction achieves sufficient accuracy. The precise sensitivity achievable with the directional event selection is presented in Sec. 10.4.

9.2.3 Summary and Visible Energy Spectrum

The concept of a directional event selection exploits the non-isotropic spatial distribution of the DM-induced signal in the Milky Way by accepting only those events whose reconstructed direction falls within a cone of half-opening angle ψ_{cone} around the GC. The optimal opening angle, obtained by maximizing the S2B ratio in Eq. 9.3, depends on both the WIMP mass m_χ and the assumed DM density profile. When the realistic angular resolution achievable in JUNO is taken into account, the cuspy gNFW profile favors narrow cones in the range $\psi_{\text{cone}} = 11°$–$34°$, whereas a cored profile such as Einasto requires considerably larger opening angles of $\psi_{\text{cone}} = 47°$–$72°$ to achieve the best S2B ratio (cf. Fig. 9.11). To assess the potential of a directional sensitivity study for both DM density distributions, two representative cone angles $\psi_{\text{cone}} = 20°$ and $\psi_{\text{cone}} = 50°$ are chosen. While $\psi_{\text{cone}} = 20°$ maximizes the sensitivity for a strongly concentrated DM-induced signal and simultaneously reduces the background contributions to $\varepsilon_B(20°) = 3.02\,\%$, the larger angle $\psi_{\text{cone}} = 50°$ ensures that an improved sensitivity compared to a FS observation is achieved even in the conservative case of a cored density distribution with $\varepsilon_B(50°) = 17.9\,\%$. Together, the two scenarios cover the physically motivated parameter space and allow for an estimation of the achievable sensitivity in JUNO for the GeV mass range.
The atmospheric background, consisting of CC events (green curve) and NC events (yellow curve), is reduced by the directional selection according to the background efficiency ε_B from 5342.4 events in the FS case to 954.2 events at $\psi_{\text{cone}} = 50°$ ($\varepsilon_B = 17.9\,\%$) and 161.1 events at $\psi_{\text{cone}} = 20°$ ($\varepsilon_B = 3.0\,\%$). This background is identical in both figures, since it is independent of the DM density profile, the number of signal events remaining within the cone, however, differs for cuspy and cored profiles. For the cuspy gNFW profile (Fig. 9.12), 47.3 signal events ($\sim 43\,\%$ of the FS signal) are retained at $\psi_{\text{cone}} = 20°$ and $m_\chi = 3\,\text{GeV}$, while for the flatter Einasto profile only 19.9 events ($\sim 18\,\%$) remain. For the larger cone with $\psi_{\text{cone}} = 50°$, the Einasto profile retains 64.6 events ($\sim 58\,\%$), a significantly higher fraction of the signal, which reflects the broader optimal cone angle for this profile (cf. Fig. 9.11).
Overall, the directional event selection significantly improves the S2B ratio, especially for the gNFW profile with $\psi_{\text{cone}} = 20°$. However, since Super-K has already set strong upper limits on the DM annihilation cross section in the GeV range [63], the resulting S2B ratio in Fig. 9.11 remains around one for most WIMP masses, even after optimized directional selection, indicating that JUNO can confirm but not substantially improve the existing limits after 10 yr of data taking. The precise sensitivity achievable with the directional event selection is presented in Sec. 10.4.

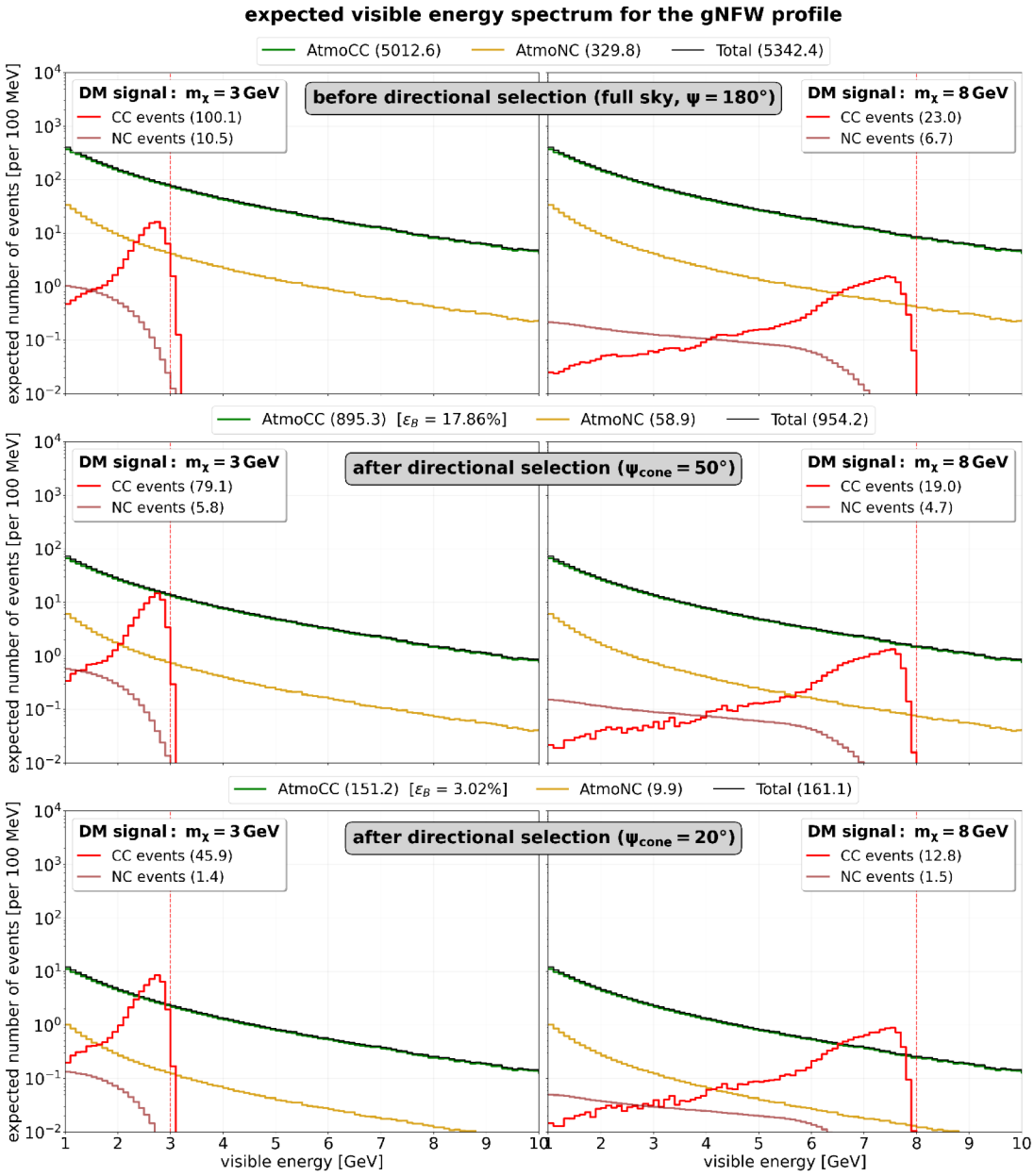

Figure 9.12: Expected visible energy spectrum in JUNO for a fiducial mass of 14.77 kton after 10 yr of data taking, assuming the gNFW DM density profile. The top row shows the spectrum for a FS observation ($\psi_{\text{cone}} = 180°$), the middle row after directional selection with $\psi_{\text{cone}} = 50°$, and the bottom row with $\psi_{\text{cone}} = 20°$. The left and right columns correspond to DM masses of $m_\chi = 3\,\text{GeV}$ and $m_\chi = 8\,\text{GeV}$. The atmospheric CC (green) and NC (yellow) backgrounds are shown together with the total background (black). The DM-induced CC and NC signal contributions are shown in red, and the vertical dashed line marks the corresponding DM mass. Numbers in the legends denote the event counts in the visible energy range.

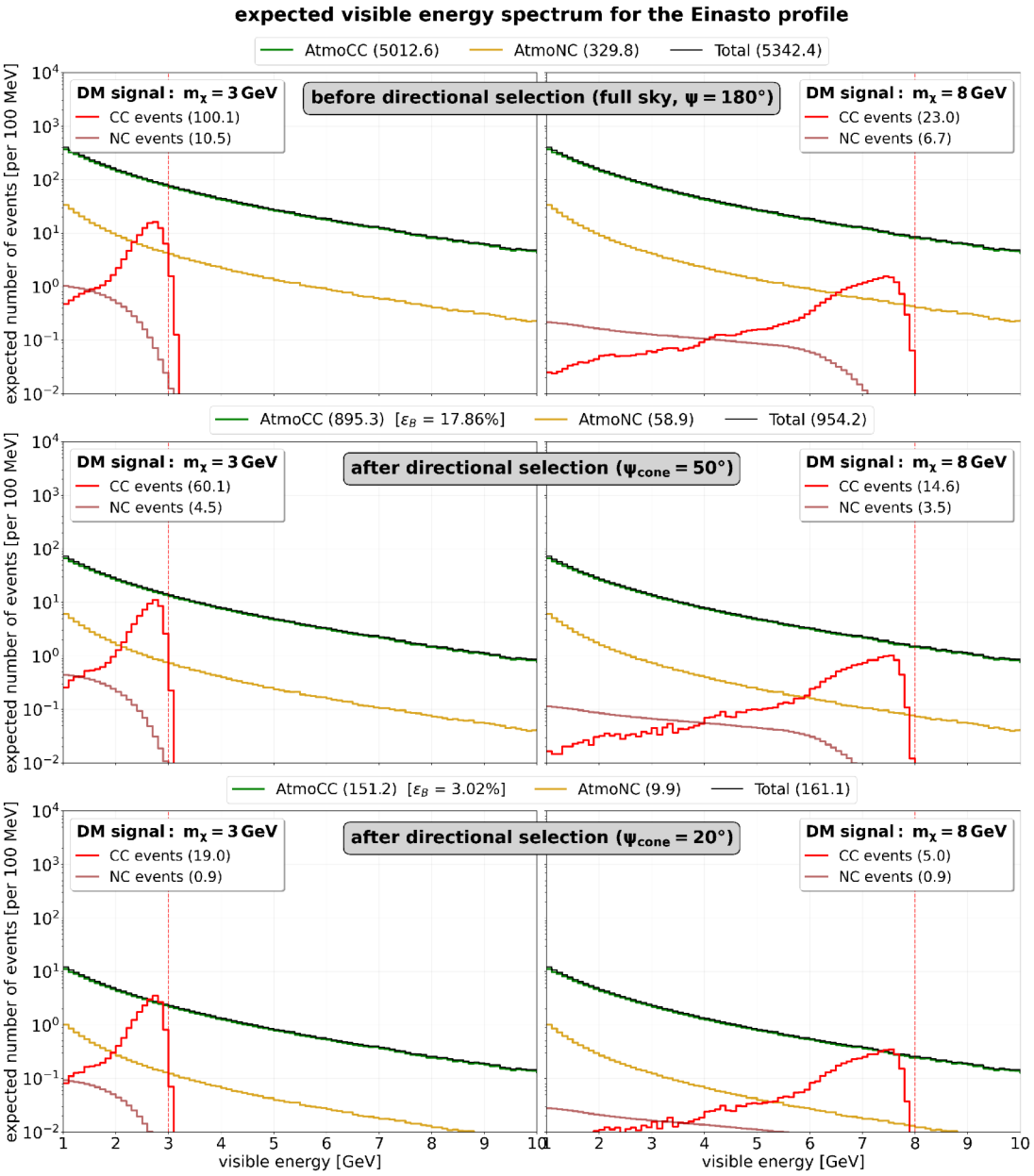

Figure 9.13: Expected visible energy spectrum in JUNO for a fiducial mass of 14.77 kton after 10 yr of data taking, assuming the Einasto DM density profile. The top row shows the spectrum for a FS observation ($\psi_{\text{cone}} = 180°$), the middle row after directional selection with $\psi_{\text{cone}} = 50°$, and the bottom row with $\psi_{\text{cone}} = 20°$. The left and right columns correspond to DM masses of $m_\chi = 3\,\text{GeV}$ and $m_\chi = 8\,\text{GeV}$. The atmospheric CC (green) and NC (yellow) backgrounds are shown together with the total background (black). The DM-induced CC and NC signal contributions are shown in red, and the vertical dashed line marks the corresponding DM mass. Numbers in the legends denote the event counts in the visible energy range.

10 | Sensitivity for Indirect Dark Matter Search in JUNO

We're fools whether we dance or not, so we might as well dance.
– Japanese proverb

The characteristic spectral features of a monoenergetic DM-induced neutrino signal motivate an analysis method that does not rely solely on the total number of expected events, but instead exploits the spectral shape of the individual signal and background contributions. The goal of this analysis is to translate the achievable S2B separation into new exclusion limits on the thermally averaged self-annihilation cross section $\langle \sigma_A v \rangle$ of DM. Since the expected signal rates are small and the considered energy range is strongly background dominated, this work employs a Bayesian analysis approach presented in Sec. 10.1, following previous studies [7, 8, 159]. Since the dominant signal channels and background reduction strategies differ across the three energy regimes, the sensitivity analyses are performed separately for each regime and range from IBD-based topological selections and PSD in the MeV regime (cf. Sec. 10.2) to flavor- and topology-based selections in the sub-GeV regime (cf. Sec. 10.3), and directional event selection in the GeV regime (cf. Sec. 10.4). In Sec. 10.5, the achievable sensitivity of JUNO across all energy regimes is discussed by combining the results derived previously.

10.1 Bayesian Analysis for Exclusion Sensitivity

Bayesian analyses are used to infer physical parameters from measured or expected data by combining them with prior knowledge. They are particularly well suited for low signal rates, which can be properly treated using Poisson statistics, while systematic and statistical uncertainties are explicitly incorporated into the analysis through explicit prior distributions [159]. In this work, JUNO's potential for indirect DM search is evaluated in three energy regimes summarized in Sec. 6.3. The signal and background spectra presented in the previous chapters are based on MC simulations and serve as the basis for Asimov-like data sets. In contrast to an idealized Asimov dataset, which by design contains no statistical fluctuations, MC-generated spectra exhibit statistical fluctuations due to finite event statistics and limited computing resources. While simulating large event samples reduces these fluctuations and approximates the expected distributions, a completely fluctuation-free realization is not achievable. In this chapter, the MC spectra are therefore treated as an approximation to an Asimov data set and will be referred to as Asimov-like in the following. Asimov-like datasets correspond to the expected number of events per energy bin, enabling an expectation-based determination of the median exclusion limits. The analysis is based on binned visible energy spectra with $E_{\text{vis}} \geq 12\,\text{MeV}$, such that reactor neutrino contributions are negligible (cf. Sec. 7.1).

The expected number of events in each bin i can be modeled as a linear combination of signal and background contributions [7]. In the simplest case, it corresponds to

$$\lambda_i = S \cdot f_i^{\text{signal}} + B_{\text{AtmoCC}} \cdot f_i^{\text{AtmoCC}} + B_{\text{AtmoNC}} \cdot f_i^{\text{AtmoNC}} + B_{\text{DSNB}} \cdot f_i^{\text{DSNB}} \ , \quad (10.1)$$

where S and B_{bkg} denote the total numbers of signal and background events, respectively, while f_i represents the corresponding normalized spectral shapes, derived from MC simulations (cf. Chap. 6 and 7). The expected event yields S and B_{bkg}, as well as the spectral shapes f_i of the signal and background components, depend on the applied selection strategy and are explicitly shown in Figs. 8.21, 9.3, 9.12 and 9.13 for exemplary DM masses in the respective regime.
Within the Bayesian analysis framework, it is assumed that the observed number of events n_i in each energy bin i fluctuates according to a Poisson distribution around the expectation value λ_i defined in Eq. 10.1. The likelihood function is therefore given by

$$\mathcal{L}(\boldsymbol{n}|\boldsymbol{\theta}) = \prod_i \frac{\lambda_i(\boldsymbol{\theta})^{\,n_i}\, e^{-\lambda_i(\boldsymbol{\theta})}}{n_i!} \ , \text{ with } \boldsymbol{n} = \{n_i\} \ , \quad (10.2)$$

where $\boldsymbol{\theta}$ denotes the parameter space of the model, which in the simplest case comprises the numbers of signal and background events $\boldsymbol{\theta} = (S, B_{\text{AtmoCC}}, B_{\text{AtmoNC}}, B_{\text{DSNB}})$, as used in Eq. 10.1. The posterior probability density of the model parameters follows from Bayes' theorem [23]

$$p(\boldsymbol{\theta}|\boldsymbol{n}) = \frac{\mathcal{L}(\boldsymbol{n}|\boldsymbol{\theta}) \cdot \pi(\boldsymbol{\theta})}{\int \mathcal{L}(\boldsymbol{n}|\boldsymbol{\theta'}) \cdot \pi(\boldsymbol{\theta'}) \cdot \mathrm{d}\boldsymbol{\theta'}} \ , \quad (10.3)$$

where $\pi(\boldsymbol{\theta})$ represents the joint prior distribution of the parameters $\boldsymbol{\theta}$, which encodes physical and experimental prior knowledge that does not originate directly from the observed spectra [159]. In this work, the main uncertainties arise from the assumed DSNB and atmospheric flux models, the interaction cross sections provided by GENIE (cf. Sec. 5.2), and the detector simulations in JUNO. To account for the uncertainties of the prior knowledge, the parameterization of the prior distributions and the resulting full parameter space are discussed in detail in the following section.

10.1.1 Parameter Space and Prior Distributions

In this work, the prior distributions of the backgrounds are parameterized such that the nominally expected event yields $B_{\text{bkg}}^{(0)}$ are modified by dimensionless scaling parameters θ_{bkg} according to $B_{\text{bkg}} = \theta_{\text{bkg}} \cdot B_{\text{bkg}}^{(0)}$. The prior distributions of the scaling parameters are chosen as log-normal distributions according to

$$\pi(\theta_{\text{bkg}}) = \frac{1}{\theta_{\text{bkg}} \cdot \sigma_{\ln}\sqrt{2\pi}} \exp\left(-\frac{(\ln\theta_{\text{bkg}} - \mu_{\ln})^2}{2\sigma_{\ln}^2}\right)$$

where $\mu_{\ln} = -\frac{1}{2}\sigma_{\ln}^2$ is chosen such that the prior mean of θ_{bkg} equals one, while the shape parameter

$$\sigma_{\ln} = \sqrt{\ln\left(1 + \sigma_{\text{bkg}}^2\right)}$$

is related to the relative uncertainty σ_{bkg} of the individual background contributions. The choice of log-normally distributed priors reflects the multiplicative nature of the underlying uncertainties and ensures strictly positive background rates [23]. They are therefore preferable to truncated Gaussian priors as used in previous DM sensitivity studies [7, 8]. In addition to the normalization uncertainties of the background components, uncertainties in their spectral shapes can also affect the sensitivity. Such effects are incorporated by introducing additional energy-dependent nuisance parameters to modify the spectral shapes f_i^{bkg} without changing the normalization B_{bkg} [160]. To account for these effects, in the simplest approximation a linear spectral tilt is introduced for the normalized atmospheric background spectra f_i^{AtmoCC} and f_i^{AtmoNC} in Eq. 10.1, according to

$$\tilde{f}_i^{\text{bkg}}(\alpha) = N(\alpha) \cdot f_i^{\text{bkg}} \cdot \left(1 + \alpha \cdot \frac{E_i - E_{\text{pivot}}}{E_{\text{scale}}}\right) , \tag{10.4}$$

where α denotes a dimensionless tilt parameter with a normally distributed Gaussian prior (mean $\bar{\alpha} = 0$ and standard deviation $\sigma_\alpha = 0.05$), E_i is the energy of bin i, and E_{pivot} is a pivot energy, where the tilt has no effect. The scale parameter E_{scale} is chosen to be in the order of the considered energy range. The normalization factor $N(\alpha)$ ensures that the tilted spectrum fulfills the normalization condition $\sum_i \tilde{f}_i^{\text{bkg}} = 1$. For the DSNB no such tilt is included, since the spectral uncertainties are already covered by investigating thee different flux models (cf. Sec. 4.5.6).
With the introduction of nuisance parameters for background normalization and spectral shape, the expected number of events in Eq. 10.1 generalizes to

$$\lambda_i(\boldsymbol{\theta}) = S \cdot f_i^{\text{signal}} + \sum_{\text{bkg}} B_{\text{bkg}}^{(0)} \cdot \theta_{\text{bkg}} \cdot \tilde{f}_i^{\text{bkg}}(\alpha_{\text{bkg}}) , \tag{10.5}$$

where the full parameter space is given by $\boldsymbol{\theta} = (S, \boldsymbol{\theta}_{\text{bkg}})$ with the background nuisance parameters $\boldsymbol{\theta}_{\text{bkg}} = (\theta_{\text{AtmoCC}}, \theta_{\text{AtmoNC}}, \theta_{\text{DSNB}}, \alpha_{\text{AtmoCC}}, \alpha_{\text{AtmoNC}})$.
The prior distribution of the signal is chosen to be flat since no experimental information on the true strength of a potential DM signal is available. The signal parameter S is restricted to non-negative values, while the upper bound exceeds the Super-K upper limits shown in Fig. 3.6 by a factor of 10. This choice constitutes a weakly informative signal prior that avoids nonphysically large signal rates. The joint prior distribution can thus be written as

$$\pi(\boldsymbol{\theta}) = \pi(S) \cdot \pi(\theta_{\text{AtmoCC}}) \cdot \pi(\theta_{\text{AtmoNC}}) \cdot \pi(\theta_{\text{DSNB}}) \cdot \pi(\alpha_{\text{AtmoCC}}) \cdot \pi(\alpha_{\text{AtmoNC}}) . \tag{10.6}$$

To assess the robustness of the resulting sensitivity limits with respect to the magnitude of the systematic uncertainties, three scenarios are investigated for the width σ_{bkg} of the prior distributions $\boldsymbol{\theta}_{\text{bkg}}$.
The *baseline* scenario assumes realistic estimates for the dominant uncertainties, including the modeled neutrino flux of the background contributions, uncertainties associated with the event generator GENIE, and an estimate of the detector response uncertainty. The uncertainty of the atmospheric HAKKM14 neutrino flux (cf. Sec. 7.4.2) is estimated with approximately 20 % and is primarily dominated by seasonal and geomagnetic effects [134]. Additional uncertainties arise from the normalization of the FLUKA flux in the MeV energy range discussed in Sec. 7.4.1, as well as from the Preliminary Reference Earth Model (PREM)–dependent calculations of the oscillated flux in Sec. 7.4.2. Taking these contributions into account, a total uncertainty of $\sigma_{\text{atmo-flux}} = 30\,\%$ is assumed for

the atmospheric neutrino flux. Since the DSNB is not measured yet, the flux exhibits strong model-dependent uncertainties, which are discussed in detail in Sec. 7.3. For the sensitivity determination in the MeV energy range (cf. Sec. 10.2), all three models are studied separately in order to comprehensively account for the impact of the DSNB background on the sensitivity of an indirect DM search in JUNO. For each DSNB scenario, an uncertainty of $\sigma_{\text{DSNB-flux}} = 40\,\%$ is assumed, which is primarily dominated by the contribution of failed BHs [133].
Neutrino–nucleon interaction cross sections are subject to energy-dependent uncertainties arising from their modeling with MC generators such as GENIE. In the low-energy regime $E_\nu \lesssim 300\,\text{MeV}$, QES and 2p2h processes dominate (cf. Chap. 5), which show significant discrepancies of 40-60 % for different generator models [161]. Above 300 MeV, the generators exhibit consistent cross-section predictions, therefore, an average uncertainty of $\sigma_{\text{NC}} = 40\,\%$ is assumed for the modeling of NC interactions, which is dominated by nuclear effects and FSI models [161]. The modeling of CC interactions is assigned an effective uncertainty of $\sigma_{\text{CC}} = 25\,\%$ in this work, based on the standard uncertainty estimates provided by GENIE [162]. For the simulated detector response in JUNO, which includes reconstruction uncertainties and quenching effects, an additional uncertainty of $\sigma_{\text{det}} = 10\,\%$ is assumed. Under the assumption of multiplicative uncertainties, this results in a combined prior width for the *baseline* scenario of

$$\begin{aligned}
\sigma_{\text{DSNB}} &= \sqrt{\sigma^2_{\text{DSNB-flux}} + \sigma^2_{\text{CC}} + \sigma^2_{\text{det}}} \approx 50\,\% \\
\sigma_{\text{AtmoCC}} &= \sqrt{\sigma^2_{\text{atmo-flux}} + \sigma^2_{\text{CC}} + \sigma^2_{\text{det}}} \approx 40\,\% \\
\sigma_{\text{AtmoNC}} &= \sqrt{\sigma^2_{\text{atmo-flux}} + \sigma^2_{\text{NC}} + \sigma^2_{\text{det}}} \approx 50\,\%
\end{aligned} \tag{10.7}$$

In contrast to the *baseline* scenario, the *loose* scenario represents a highly conservative approach in which substantially larger relative uncertainties of up to 100 % are allowed for the atmospheric backgrounds and up to 200 % for the DSNB contribution. This scenario is intended to cover potential underestimations of systematic effects and enables an assessment of the sensitivity under minimal prior knowledge. By contrast, the *tight* scenario reflects an optimistic assumption, in which the relative uncertainties are reduced to $\sigma_{\text{AtmoCC}} = 20\,\%$ and $\sigma_{\text{AtmoNC}} = \sigma_{\text{DSNB}} = 30\,\%$.

10.1.2 Marginalization and MCMC-Sampling

To determine the exclusion sensitivity of JUNO to a DM-induced neutrino signal in the presence of the estimated background, a background-only scenario is assumed in the Asimov-like spectra. In this scenario, an observed spectrum is considered, whose bin contents $\boldsymbol{n} = \{n_i\}$ correspond only to the expected background contributions and contain no actual signal component ($\lambda_i(S = 0)$ in Eq. 10.5). In the Bayesian analysis, however, the possibility of a signal contribution is explicitly allowed. Consequently, in the posterior distribution given in Eq. 10.3, the signal strength S is treated as a free parameter, together with all background nuisance parameters $\boldsymbol{\theta}_{\text{bkg}}$, and is marginalized over the full parameter space defined in Sec. 10.1.1.

From the marginalized posterior distribution of the signal strength,

$$p(S|\boldsymbol{n}) = \int p(S, \boldsymbol{\theta}_{\text{bkg}}|\boldsymbol{n}) \cdot \mathrm{d}\boldsymbol{\theta}_{\text{bkg}} \ , \tag{10.8}$$

the one-sided 90 % quantile S_{90} defining the upper credibility limit is determined via

$$\int_0^{S_{90}} p(S|\boldsymbol{n}) \cdot \mathrm{d}S = 0.90 \ . \tag{10.9}$$

This corresponds to the signal strength that can be excluded with 90 % Confidence Level (C.L.) under the assumption of the background-only scenario. A signal strength exceeding S_{90} would therefore most likely no longer be explained by fluctuations due to uncertainties in the background models and would thus contradict the background-only scenario.
Thus, S_{90} marks the minimal signal strength required to distinguish a genuinely present DM-induced neutrino signal from the background contributions with 90 % credibility interval. This sensitivity measure is subsequently associated with the corresponding required monoenergetic neutrino flux, following the method presented in Sec. 6.1, which can in turn be related to the thermally averaged DM self-annihilation cross section $\langle \sigma_{\mathrm{A}} v \rangle$ according to Eq. 3.13. Since the computation of the marginalized posterior distributions $p(S, \boldsymbol{\theta}_{\mathrm{bkg}}|\boldsymbol{n})$ in Eq. 10.3 requires solving the high-dimensional integral, which is generally not analytically possible, the numerical Markov Chain Monte Carlo (MCMC) sampling method is employed using the Python-based affine-invariant ensemble sampler `emcee` [163].
In this procedure, $N_{\mathrm{walkers}} = 100$ parallel Markov chains explore the full parameter space $\boldsymbol{\theta}$. After a burn-in phase of 500 steps, $N_{\mathrm{steps}} = 40,000$ samples are generated for each walker. A Metropolis–Hastings–based algorithm decides whether a proposed point in parameter space is accepted based on the log-posterior probability [163]. This log-posterior is composed of the log-likelihood $\ln \mathcal{L}(\boldsymbol{n}|\boldsymbol{\theta})$ defined in Eq. 10.2 and the log-priors $\ln \pi(\boldsymbol{\theta})$ defined in Eq. 10.6, according to

$$\ln p(\boldsymbol{\theta}|\boldsymbol{n}) = \underbrace{\sum_i \left(n_i \ln \lambda_i(\boldsymbol{\theta}) - \lambda_i(\boldsymbol{\theta}) - \ln(n_i!)\right)}_{\ln \mathcal{L}(\boldsymbol{n}|\boldsymbol{\theta})} + \ln \pi(\boldsymbol{\theta}) \ . \tag{10.10}$$

The density of the accepted samples thus provides a measure of the posterior probability. The results of the Bayesian analysis are discussed separately for different energy regimes in the following sections, considering the different selection strategies presented in Chaps. 8 and 9. Through a consistent comparison of these strategies within the same Bayesian analysis framework, the impact of the respective selection methods on the achievable sensitivity can be systematically quantified.

10.1.3 Toy Monte Carlo Studies and Expected Sensitivity Intervals

To compare the expected exclusion sensitivity for different prior scenarios and selection strategies across all three mass regimes, Asimov-like data sets are used in this work, which provide a robust and numerically stable estimate of the median expectation. However, a purely Asimov-based study does not provide an estimate of the spread of the achievable exclusion limit due to statistical fluctuations in real, background-dominated measurements. For this purpose, selected toy Monte Carlo (MC) studies are performed in this work, where pseudo datasets are generated in a background-only scenario by fluctuating the Asimov-like spectrum in each bin $\boldsymbol{n} = \{n_i\}$ around its expected values λ_i (cf. Eq. 10.5) according to Poisson statistics. For each pseudo-experiment, the full Bayesian analysis presented in Sec. 10.1.2 is performed to determine the upper credibility

limit S_{90} from the marginalized signal posterior distribution according to Eq. 10.9. Due to the high computational effort required for an MCMC marginalization per pseudo-experiment, toy-MC studies are performed in this work only for the best selection strategy in each mass regime and exclusively in the *baseline* prior scenario (cf. Sec. 10.1.1). In this process, $N_{\text{toy}} = 500$ pseudo-experiments are generated for selected DM masses, which are chosen to sufficiently cover the sensitivity curve. The spread of the exclusion limits is specified as a 68 % (1σ) interval (P16-P84 percentile) and a 95 % (2σ) interval (P2.5-97.5 percentile) around the P50 percentile median expectation.
The combination of Asimov-based analyses, which are used to study systematic uncertainties (e.g. prior assumptions, DSNB scenarios, binning strategies) for different selection methods with manageable computational effort, and Toy-MC uncertainty intervals (68 % and 95 %), which quantify the effect of statistical fluctuations in real measurements, enables a reliable statement about the expected exclusion sensitivity in JUNO.

10.2 Exclusion Sensitivity for MeV DM in JUNO

For the Bayesian analysis in the MeV energy range, binned energy spectra in the interval $E_{\text{vis}} \in [12, 300]\,\text{MeV}$ with a bin width of 1 MeV are used (cf. Fig. 8.21). In addition to the atmospheric CC and NC background contributions, all three DSNB scenarios (min, mid and max) shown in Fig. 7.2 are considered separately. The impact of a spectral tilt of the atmospheric CC and NC background contributions on the sensitivity is estimated according to Eq. 10.4, using $E_{\text{pivot}} = 150\,\text{MeV}$ and $E_{\text{scale}} = 200\,\text{MeV}$. The sensitivity is estimated for different DM masses $m_\chi \in \{15, 20, 30, 40, \ldots, 190, 200, 250, 300\,\text{MeV}\}$ by determining the 90 % upper credibility limit $S_{90}(m_\chi)$ on the signal strength from the marginalized posterior distribution (cf. Eq. 10.9). The 90 % credibility upper limit on the DM self-annihilation cross section in JUNO is obtained by comparing the signal strength $S_{90}(m_\chi)$ to the nominal value $S_{\text{SK}}(m_\chi)$ expected under the assumption of a flux equal to the Super-K upper limit (cf. Fig. 3.6) according to

$$\langle \sigma_{\text{A}} v \rangle_{90\%}(m_\chi) = \frac{S_{90}(m_\chi)}{S_{\text{SK}}(m_\chi)} \cdot \langle \sigma_{\text{A}} v \rangle_{\text{SK}}(m_\chi) \; . \tag{10.11}$$

Here, $S_{\text{SK}}(m_\chi)$ denotes the number of signal events for a fiducial volume of 14.77 kton and 10 yr of data taking (cf. Chap. 6), after applying the chosen selection strategy and considering the visible energy window. This linear scaling allows for a direct comparison of JUNO's sensitivity relative to Super-K. The *baseline*, *loose*, and *tight* prior distribution scenarios introduced in Sec. 10.1.1 were analyzed separately for four different selection strategies, considering topological-based and pulse shape-based discrimination methods, which were discussed in detail in Chap. 8. Thus, in total 3 (DSNB models) × 3 (prior distributions) × 4 (selection methods) = 36 analysis configurations were performed. The four selection method dependent scenarios are denoted with roman numbers:

(i) no selection (all CC and NC events),
(ii) topology-based IBD selection cut (cf. Sec. 8.2),
(iii) IBD cut + classical TTR-based PSD selection (cf. Sec. 8.3.2),
(iv) IBD cut + ML-based PSD selection (cf. Sec. 8.3.3).

In Sec. 10.2.1, the results of the different selection methods in the *baseline* scenario are first presented under the assumption of the maximal DSNB flux model. The impact of

different DSNB signals on the sensitivity to DM-induced signals is discussed in Sec. 10.2.2, while the influence of the prior distributions is analyzed in Sec. 10.2.3.

10.2.1 Results for the Baseline Scenario

For the analysis of the *baseline* scenario presented in Sec. 10.1.1, the maximal DSNB flux model shown in Fig. 7.2 is assumed to represent the conservative scenario for the sensitivity estimation of a DM-induced signal in JUNO. Fig. 10.1 shows the marginalized posterior distributions of the model parameters $\boldsymbol{\theta}$ for a DM mass of $m_\chi = 70\,\text{MeV}$ under the background-only assumption[1]. Panel (a) presents the results when no selection method is applied (i), while Panel (b) describes the selection method (iv), considering the topology-based IBD cuts, as well as the additional ML-based PSD method presented

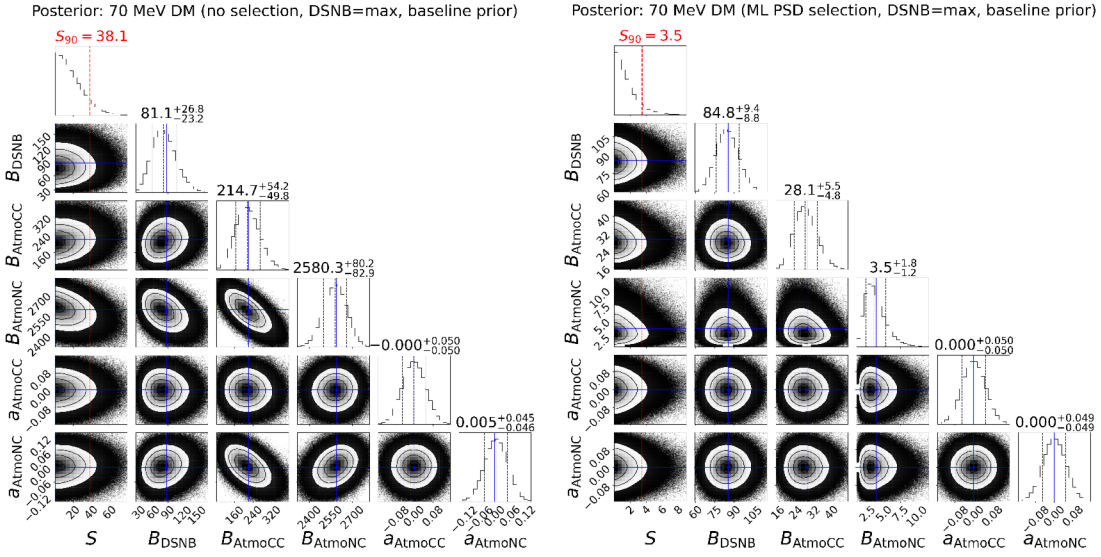

(a) no selection (i)

(b) ML-based PSD selection (iv)

Figure 10.1: Posterior distributions for $m_\chi = 70\,\text{MeV}$ comparing two different selection strategies (i) and (iv). The diagonal plots show the one-dimensional marginalized posteriors for each parameter $\boldsymbol{\theta}$, while the off-diagonal contour plots show the two-dimensional marginalized posteriors as a function of two free parameters revealing possible correlations. The blue lines indicate the nominal values of each contribution in the background-only scenario (with $S = 0$). For the background posteriors, the median with the 1σ credibility interval is shown (black dashed lines), while for the signal posterior (upper left) the 90 % quantile S_{90} is indicated in red. The parameters $a_{\text{AtmoCC/NC}}$ correspond to the tilt parameters α in Eq. 10.4.

in Sec. 8.3.3. The subplots on the diagonal show the posterior distributions for all model parameters $\boldsymbol{\theta}$. The blue lines indicate the nominal values $B^{(0)}_{\text{bkg}}$ of the background contributions, which were determined from the MC-generated spectra (cf. Tab. 8.4), while the black dashed lines mark the median and its 1σ credibility interval. The posterior distribution of the signal (upper left subplots) has its maximum at $S = 0$ due to the background-only scenario. The 90 % quantile S_{90} is indicated by the red line.

[1]The posterior distributions of the background normalizations in Fig. 10.1 show the absolute event numbers $B_{\text{bkg}} = \theta_{\text{bkg}} \cdot B^{(0)}_{\text{bkg}}$ instead of the marginalized dimensionless scaling parameters θ_{bkg} in order to allow a direct comparison with the expected background rates listed in Tab. 8.4.

The nominal expectation values (blue lines) are in agreement with the median values (dashed black lines) of the background components, which confirms the consistency of the fit with the underlying Asimov-like datasets. The tilt parameters α_{AtmoCC} and α_{AtmoNC} are close to zero for both selection methods, which corresponds to the expectation for Asimov-like spectra. In the case of no selection (i), the atmospheric NC background dominates, while it is almost completely suppressed by the IBD cuts and the additional ML-based PSD with selection method (iv). This is the main reason for the significant reduction of the 90 % quantile of the signal strength from $S_{90}^{(\mathrm{i})} = 38.1$ to $S_{90}^{(\mathrm{iv})} = 3.4$. Since DSNB neutrinos primarily produce IBD events, the DSNB represents an irreducible background that is largely unaffected by the selection methods. The off-diagonal contour plots show the two-dimensional marginalized posteriors and thus provide information about correlations between the parameters. While only minimal correlations occur for selection method (iv) in Subfig. 10.1b, the most pronounced correlation between B_{AtmoCC} and B_{AtmoNC} appears in Subfig. 10.1a when no selection method is applied. The negative correlation indicates that an overestimation of B_{AtmoCC} is compensated by a reduction of B_{AtmoNC}, which is caused by the overlap of the two spectral shapes. The fact that the signal strength S shows hardly any correlations with the background parameters suggests that the spectral features of a monoenergetic DM-induced signal can be well distinguished from the flat background distributions within the Bayesian analysis.

Fig. 10.2 shows the 90 % quantile S_{90} of the signal posterior distribution under the background-only hypothesis as a function of the DM mass m_χ for all four selection methods. The topology-based IBD-like selection (ii) already significantly reduces S_{90}

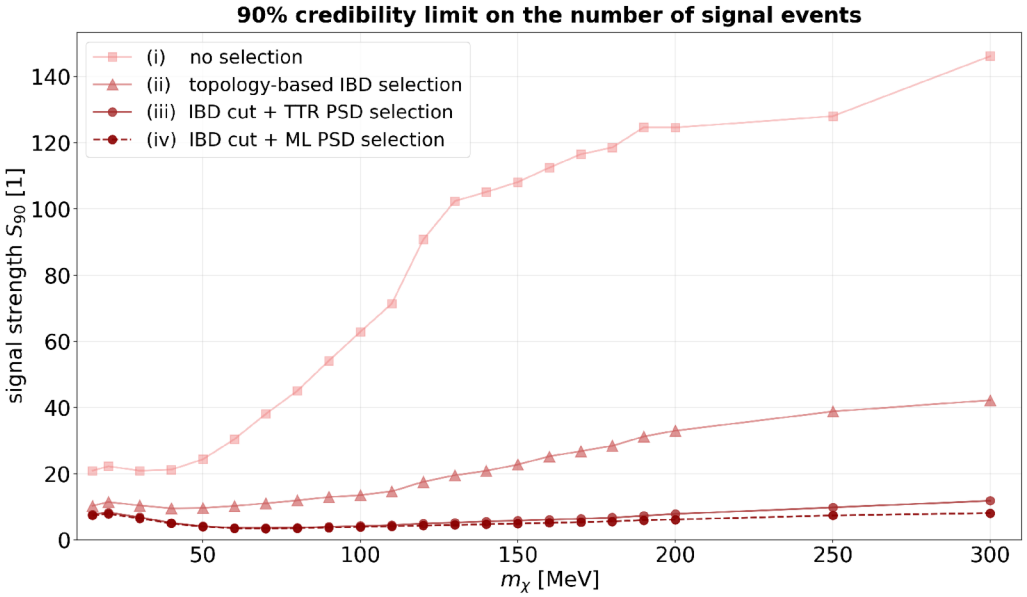

Figure 10.2: Upper 90 % credibility limit S_{90} on the signal strength as a function of the DM mass m_χ for the four selection methods (i)–(iv). The *baseline* prior scenario was used assuming the maximum DSNB flux model.

compared to the scenario without any selection (i). The additional application of the PSD methods (iii) and (iv) further reduces the 90 % credibility limit S_{90}, exhibiting only minimal differences between the TTR-based and the ML-based PSD methods.

According to Eq. 10.11, the signal posterior probability S_{90} can be translated into the

90 % probability upper limit on the DM self-annihilation cross section $\langle\sigma_A v\rangle_{90\%}$ shown in Fig. 10.3. The assumed galactic parameters, such as the distance $R_0 = 8.277\,\text{kpc}$ to the GC, the local DM density of $\rho_0 = 0.4\,\text{GeV/cm}^3$, and the dimensionless averaged $\mathcal{J}$-factor of $J_{\text{avg}} = 3$, are extensively discussed in Chap. 3.

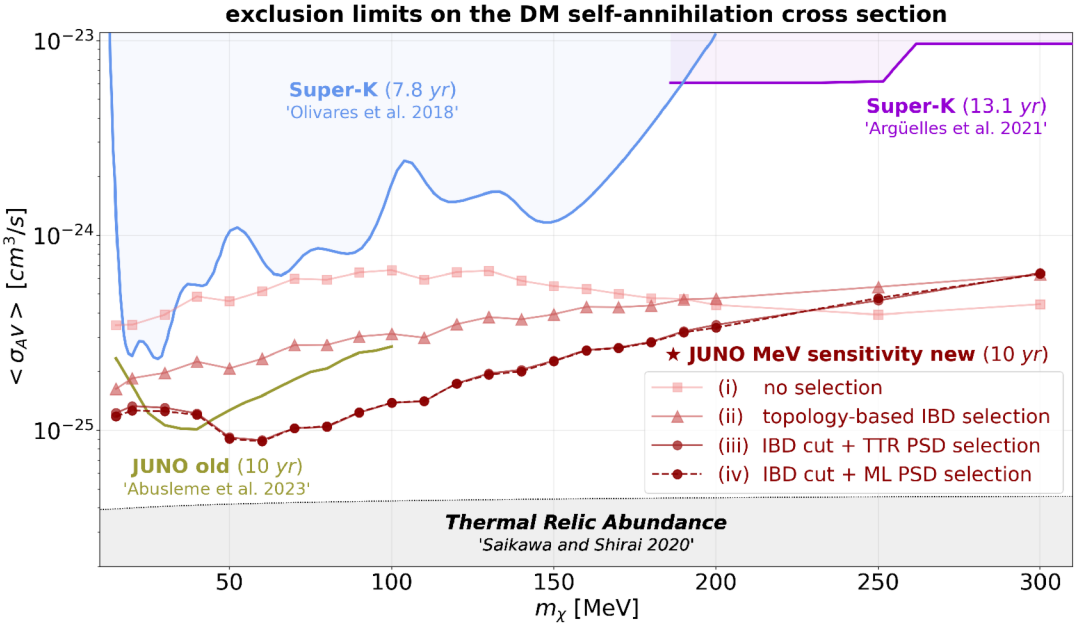

Figure 10.3: Expected 90 % credibility limits on the self-annihilation cross section $\langle\sigma_A v\rangle$ of MeV DM as a function of m_χ for 10 yr of data taking and a fiducial mass of 14.77 kton in JUNO. The results are obtained for Asimov-like dataset in the *baseline* prior scenario, assuming the maximum DSNB flux model. Existing limits from Super-K [62, 36] and the results of a previous JUNO study [8] are shown for comparison, together with the thermal relic abundance [39].

The red curves show the results for all four selection methods after 10 yr of data taking and a fiducial volume of 14.77 kton in JUNO. For comparison, the upper limits of Super-K [62, 36] already presented in Sec. 3.4, as well as a previous sensitivity study of JUNO [8], are included. The natural annihilation cross-section derived from the relic abundance is added in gray [39]. The results show that JUNO can improve the existing upper limits by approximately one order of magnitude over the entire mass range. The direct comparison with the existing upper limits in the region $m_\chi \lesssim 70\,\text{MeV}$ strongly depends on the considered DSNB scenario and will be discussed in more detail in the following section. For DM masses up to approximately 200 MeV, the PSD-based selection methods (iii) and (iv) provide the best sensitivity, which is due to the dominant IBD contribution to the DM-induced signal. Above $\sim 200\,\text{MeV}$, however, a selection of IBD-like events appears to be no longer effective, marking the transition to a CC-based analysis. The comparison of the results for a purely topology-based selection (ii) with those including an additional PSD (iii) and (iv) demonstrates that the pulse-shape-based discrimination between IBD and IBD-like CC and NC events provides a significant contribution to the sensitivity. For the DSNB max flux model, the sensitivity obtained with the TTR-based PSD method (iii) differs only marginally from that of the ML-based PSD method (iv), since the most pronounced improvement of the ML method compared to TTR lies in the suppression of NC events in the region $E_{\text{vis}} < 50\,\text{MeV}$ (cf. Sec. 8.3).

However, for the max DSNB scenario, the sensitivity in this region is limited by the irreducible DSNB background, therefore an improved suppression of the atmospheric NC background does not provide any further advantage. The comparison between selection methods (iii) and (iv) changes, however, for other DSNB scenarios (cf. Sec. 10.2.2).
The significant improvement compared to the previous sensitivity study for JUNO [8] (yellow curve) is primarily due to differences in the treatment of neutrino interactions and background modeling. While the previous analysis focused on the IBD channel and only partially accounted for other CC and NC interactions [7], in this work, all CC and NC interactions have been fully simulated for both the DM signal and all background contributions. In particular, FSIs are taken into account, which significantly affect the event topology and the visible energy of the interaction. The efficiency of the topology-based IBD-like selection (ii) presented in Sec. 8.2 was determined in this work not only for genuine IBD events, but also explicitly for all simulated CC and NC events, which increase significantly for DM masses $> 50\,\mathrm{MeV}$. Similarly, a full MC simulation of all background components was performed in this work, allowing the fraction surviving the topological selection to be determined rather than treating certain contributions as irreducible. The subsequent PSD analysis presented in Sec. 8.3 was then applied only to the remaining IBD-like sample, such that the energy-dependent selection efficiencies $\varepsilon_{\mathrm{top,(ch)}}$ and $\varepsilon_{\mathrm{PSD,(ch)}}$ can be treated multiplicatively for each channel (ch) according to Eq. 8.9. This consistent treatment of all simulated events leads to a more realistic description of the actual remaining composition after applying the chosen selection strategy. Although the expected sensitivity of JUNO shows a significant improvement compared to Super-K, it still remains well above the natural self-annihilation cross section inferred from the thermal relic abundance [39]. Therefore, thermal relic WIMPs in the MeV mass range cannot be excluded with JUNO.

10.2.2 Influence of the DSNB Signal

In particular, in the range $m_\chi < 50\,\mathrm{MeV}$, the exclusion limits depend strongly on the DSNB background. To estimate the uncertainties of the still hypothetical DSNB background, three DSNB scenarios were introduced in Sec. 7.3, covering the plausible physical parameter space. In Fig. 10.4, the expected 90 % credibility limit of $\langle \sigma_{\mathrm{A}} v \rangle_{90\,\%}$ is shown, taking into account the different DSNB scenarios. The solid curves display the results for selection strategy (iii), which employs the classical TTR-based PSD method, while the dashed curve illustrates the results obtained with the ML-based method (iv). The exclusion limits are obtained using the *baseline* prior distribution and a fiducial volume of 14.77 kton after 10 yr of data taking. The results show that JUNO's sensitivity to a monoenergetic DM-induced signal in the region $m_\chi < 70\,\mathrm{MeV}$ strongly depends on the DSNB signal realized in nature. While in the hypothetical max flux scenario (blue curve), about ~ 85 DSNB events are expected in the visible window $E_{\mathrm{vis}} \in [12, 300]\,\mathrm{MeV}$ with selection strategy (iv), only ~ 30 are expected in the mid flux scenario (red curve), and only ~ 5 events in the min flux scenario (gray curve). For comparison, in the previous sensitivity study for JUNO (yellow curve), 11 DSNB events are expected after applying the PSD method [8]. The smaller the expected DSNB contribution, the more pronounced the advantage of the ML-based PSD method (iv) over the classical TTR-based method (iii), since it provides better suppression of the remaining atmospheric NC background. For the min flux scenario (dashed gray curve), the achievable sensitivity at $m_\chi = 30\,\mathrm{MeV}$ lies very close to the thermal relic density (gray hatched area). For DM masses above 70 MeV, neither the DSNB background scenario nor the chosen PSD method plays a significant role.

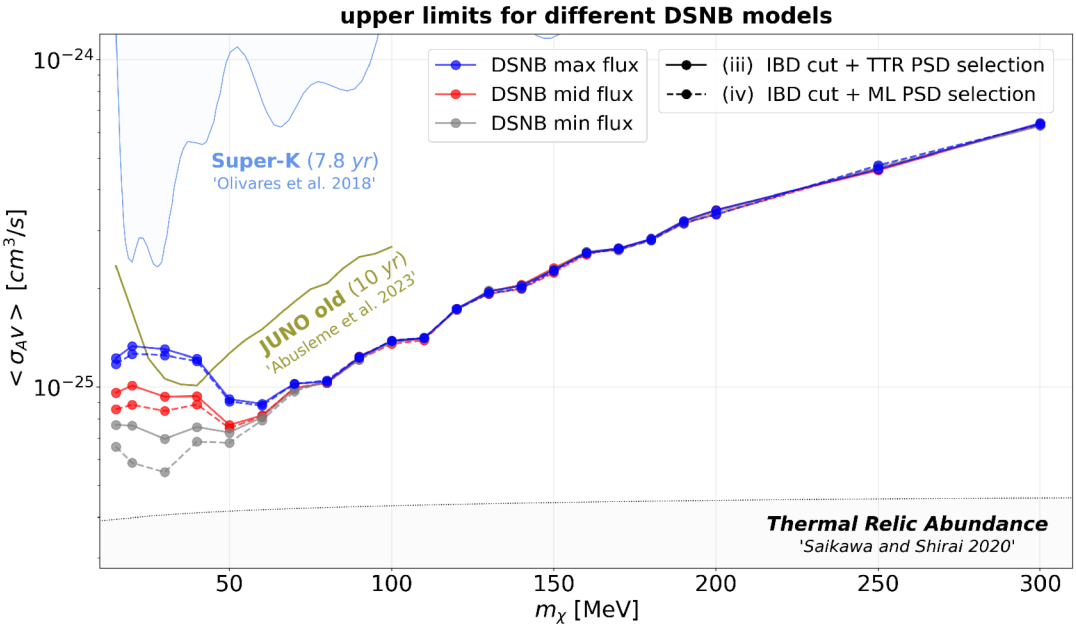

Figure 10.4: Expected 90 % credibility limits on the DM self-annihilation cross section $\langle \sigma_A v \rangle$ as a function of m_χ for the three different DSNB scenarios introduced in Sec. 7.3. Both PSD-based selection methods, using the classic TTR approach (iii) and the ML-based classifier (iv) are compared for each DSNB scenario. Existing limits from Super-K [62] and the previous JUNO study [8] are included for comparison, as well as the natural cross section, derived from the thermal relic abundance [39].

10.2.3 Robustness With Respect to Prior Distributions

To investigate the robustness of the sensitivity limits with respect to different systematic assumptions of the background contributions, three scenarios for the prior distributions were introduced in Sec. 10.1.1. The *baseline* priors represent a conservatively realistic estimate of the dominant systematic uncertainties, while the *loose* scenario assumes minimal prior knowledge and the *tight* scenario assumes reduced uncertainties of the background models. Fig. 10.5 shows the relative deviation of the sensitivity limits $\langle \sigma_A v \rangle_{90\%}$ from the *baseline* scenario (cf. Fig. 10.3) when using the *loose* and *tight* prior distributions. Negative values indicate an improvement of the upper limit compared to the baseline scenario (black horizontal line), while positive values correspond to weaker limits. The hatched regions are defined by the results of the *loose* prior (solid gray curves) and the *tight* prior scenario (dashed gray curves). Only two selection methods (i) and (iv) are shown for comparison. For both selection methods, the variation remains within $\pm 5\,\%$ for DM masses $m_\chi \lesssim 200\,\mathrm{MeV}$, slightly increasing for larger DM masses. A similar result can be obtained for all four selection strategies, demonstrating the robustness of the derived sensitivity in the Bayesian analysis concerning different prior scenarios.

10.2.4 Toy-MC Results for the Baseline Sensitivity

The exclusion limits presented so far are based on Asimov-like datasets and describe the median expected sensitivity curves in the MeV regime. In order to quantify the expected variance due to statistical fluctuations in real measurement data, a selected

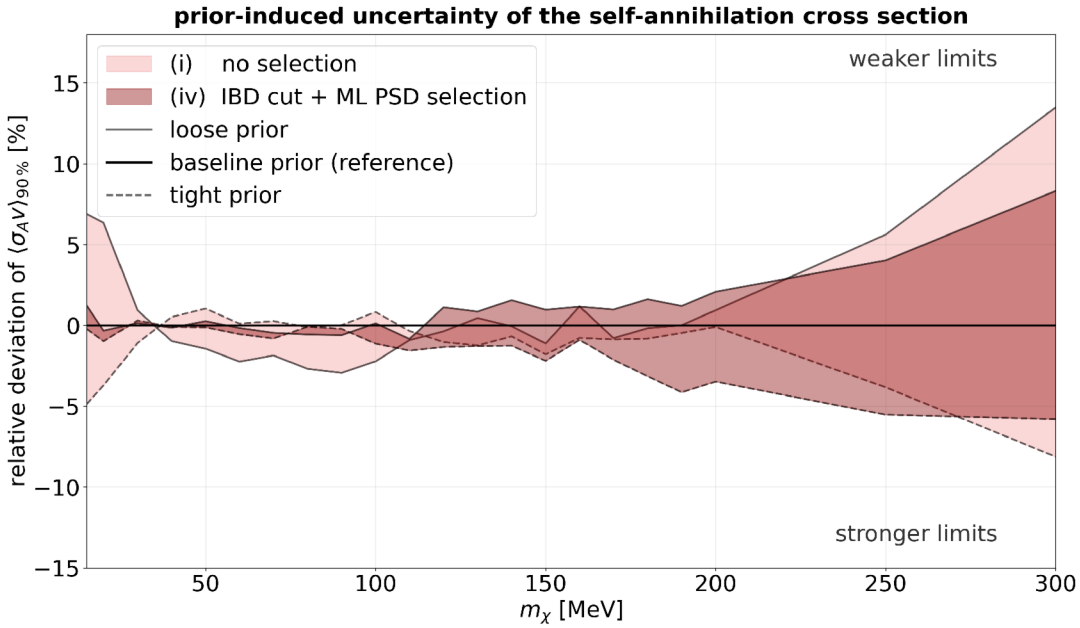

Figure 10.5: Relative deviation of the 90 % credibility limits on $\langle \sigma_A v \rangle$ from the *baseline* scenario for the *loose* (solid line edge) and *tight* (dashed line edge) prior scenarios. The results are shown exemplarily for selection methods (i) and (iv), similar results were obtained for all selection strategies.

toy MC study was performed for the best selection strategy according to the method described in Sec. 10.1.3. In the MeV regime, the best median sensitivity is expected for an ML-based PSD of IBD-like events (cf. Fig. 10.3). Therefore, the toy MC study is performed for selection strategy (iv) in the *baseline* prior scenario, assuming the DSNB max model. Due to the high computational effort, toy-MC studies were performed for 11 selected DM masses $m_\chi \in \{15, 20, 30, 40, 50, 60, 80, 100, 150, 200, 250, 300\,\text{MeV}\}$, which cover in particular the DSNB-influenced mass range with sufficient precision (cf. Fig. 10.4).

The resulting exclusion limits with their uncertainty intervals are shown in Fig. 10.6. The dashed curve shows the sensitivity derived from Asimov-like datasets, which has already been shown for all masses in Fig. 10.3. The shaded bands indicate the expected spread of the 90 % credibility exclusion limits due to statistical fluctuations centered around the median expected Asimov sensitivity. The darker band shows the 68 % probability interval (1σ), while the lighter band quantifies the 95 % level. Due to the low event statistics, the toy-MC results show a mean uncertainty of $+39\,\%/-31\,\%$ around the Asimov exclusion sensitivity for the 68 %-level. For the 95 % interval, the relative deviation is $+91\,\%/-44\,\%$.

These results quantify the expected variation for individual measurement realizations, which is significantly larger than the influence of different prior widths (cf. Sec. 10.2.3). The uncertainty of JUNO's expected exclusion sensitivity is therefore primarily dominated by statistical fluctuations and not by the chosen background prior assumptions. Despite this statistical uncertainty, it is expected that after 10 yr of data taking, JUNO will provide significantly stricter exclusion limits on the thermally averaged self-annihilation cross section $\langle \sigma_A v \rangle$ than the current best limits from Super-K across the entire mass range.

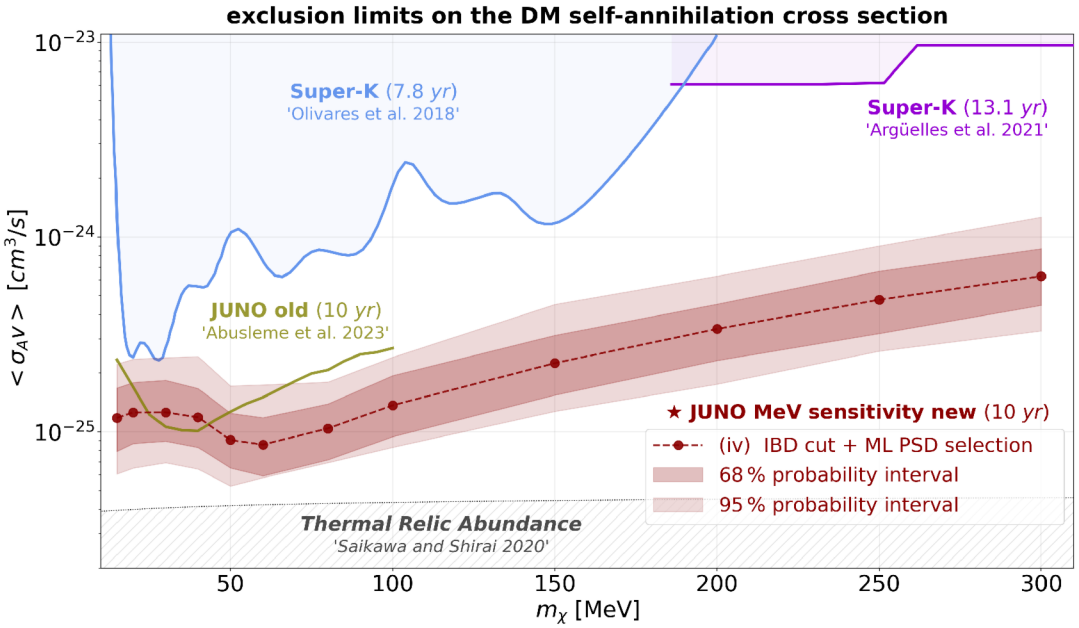

Figure 10.6: Toy-MC results of the expected 90 % credibility exclusion limits on $\langle\sigma_{\mathrm{A}}v\rangle$ for the *baseline* prior scenario and selection method (iv). The dashed curve shows the Asimov sensitivity for the selected DM masses, while the dark shaded band shows the 68 % interval (1σ) and the light shaded band the 95 % interval (2σ) of the $\langle\sigma_{\mathrm{A}}v\rangle_{90\,\%}$ distribution centered around the median.

10.3 Exclusion Sensitivity for sub-GeV DM in JUNO

For the Bayesian analysis in the sub-GeV region, binned energy spectra in the interval $E_{\mathrm{vis}} \in [12\,\mathrm{MeV}, 1\,\mathrm{GeV}]$ are used[2]. To investigate the impact of the chosen binning strategy on the sensitivity results, different bin widths of 1 MeV, 5 MeV, and 10 MeV are considered. In the log-likelihood fit, a possible spectral tilt of the atmospheric CC and NC backgrounds is allowed according to Eq. 10.4, with $E_{\mathrm{pivot}} = 0.55\,\mathrm{GeV}$ and $E_{\mathrm{scale}} = 0.9\,\mathrm{GeV}$. The Bayesian analysis is performed for various DM masses $m_\chi = (0.10, 0.15, 0.20, 0.25, 0.3, 0.4, \ldots, 0.9, 1.0)$GeV, and the expected 90 % credibility limit on the self-annihilation cross section $\langle\sigma_{\mathrm{A}}v\rangle$ is determined analogously to the method described in Sec. 10.2. Three different selection strategies are investigated for each of the prior distribution scenarios presented in Sec. 10.1.1[3]:

(i) no selection (all CC and NC events),
(ii) flavor-based $\nu_e/\bar{\nu}_e$-like selection (cf. Sec. 9.1.1),
(iii) topology-based CC1p0n selection (cf. Sec. 9.1.2).

In Sec. 10.3.1, the results for the *baseline* prior scenario are presented for all three selection methods. Sec. 10.3.2 discusses the impact of the chosen binning on the expected sensitivity and the robustness of the model with respect to different prior distributions.

[2]This choice ensures that the lower-energy NC component of the DM-induced signals is not lost in the analysis.

[3]For all analyses in this section, the maximal DSNB flux scenario was assumed. The impact of different DSNB backgrounds on the sensitivity of sub-GeV DM, however, is negligible (cf. Fig. 10.4).

10.3.1 Results for the Baseline Scenario

In Fig. 10.7, the expected 90 % credibility exclusion limits on the self-annihilation cross section $\langle \sigma_A v \rangle$ are shown in red for DM masses in the sub-GeV region. The results were obtained for the *baseline* prior scenario introduced in Sec. 10.1.1 with a bin width of 5 MeV, taking into account all three selection strategies. The results show that JUNO can

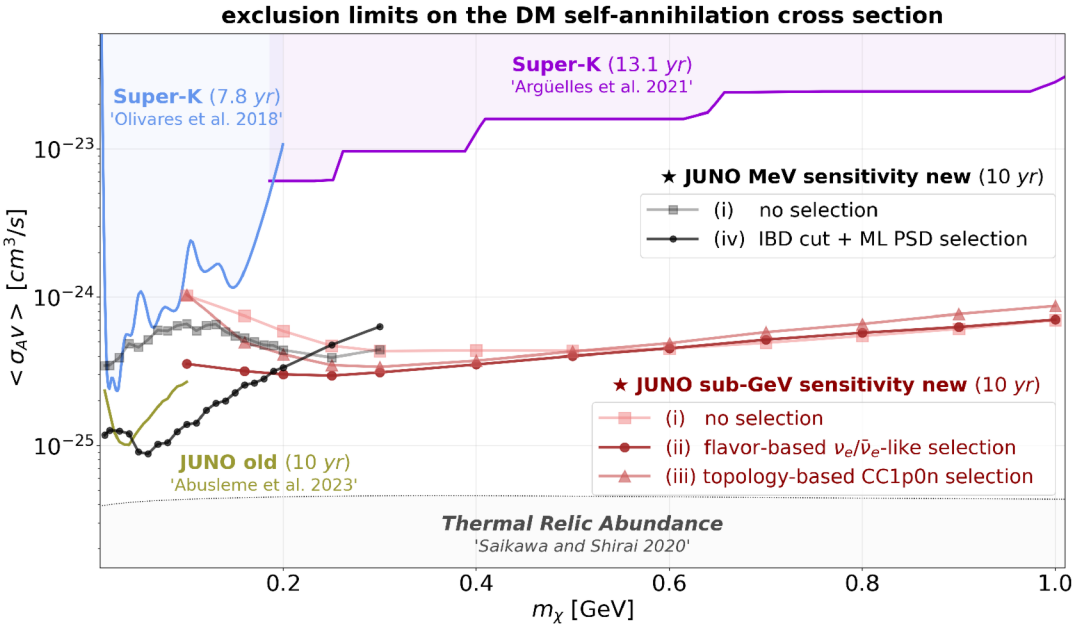

Figure 10.7: Expected 90 % credibility limits on the self-annihilation cross section $\langle \sigma_A v \rangle$ of MeV and sub-GeV DM as a function of the mass m_χ. The sub-GeV results (red curves) are derived for selection strategies (i)–(iii), while the MeV results from Sec. 10.2.1 are shown for no selection (i) and IBD cuts with ML-based PSD (iv). All results are obtained with the *baseline* prior scenario for 10 yr of data taking and a fiducial mass of 14.77 kton in JUNO. Existing limits from Super-K [62, 36] and a previous JUNO study [8] are shown for comparison, together with the thermal relic abundance [39].

improve the currently best upper limits set by Super-K in the sub-GeV region [62, 36] by about one order of magnitude. The flavor-based $\nu_e/\bar{\nu}_e$-like selection strategy (ii) provides the best sensitivity over the entire energy range. Since characteristic spectral features of DM-induced signals become less pronounced for larger DM masses, the spectra without selection (i) yield comparable sensitivities to $\nu_e/\bar{\nu}_e$-like spectra (ii) for $m_\chi \gtrsim 0.6$ GeV. A flavor-based selection is therefore no longer promising in the transition region to the GeV regime. The topological zero-neutron selection (iii) intended to sharpen the characteristic CC1p0n-induced peak structure (cf. Sec. 9.1.2) is inferior to the flavor-based selection (ii) across the entire mass range, as already concluded from the local S2B ratio listed in Tab. 9.1.

One objective of this work is the identification of the optimal transition region between an IBD-based and a CC-based analysis. For this reason, the results presented in Sec. 10.2.1 for the MeV regime, where the optimal transition was identified at approximately $m_\chi \approx 230$ MeV are also shown in Fig. 10.7 (intersection point between the gray (i) and the black (iv) curves with markers). With a flavor-based selection (ii) in the sub-GeV regime, however, this the optimal transition shift to $m_\chi \approx$ 150-200 MeV (intersection

point between dark red and black curve). While the IBD-based analysis with ML-based PSD selection (iv) provides the best sensitivity below DM masses of $\sim 150\,\mathrm{MeV}$ (black curve), the flavor-based sub-GeV analysis (ii) is clearly superior for masses above $\sim 200\,\mathrm{MeV}$ (dark red curve), since this selection strategy retains the ν_e-driven CC1p0n peak as well as the $\bar{\nu}_e$-induced IBD peak (cf. Sec. 9.1.1).
The consistency of the analysis approaches in both energy regimes is confirmed by the good agreement of the results without selection (i) in the overlap region. The deviations arise primarily from the different bin widths of the underlying spectra. It should be noted that the sensitivity limits implicitly exhibit a certain flavor dependence, since the IBD-based analysis (iv) is primarily sensitive to $\bar{\nu}_e$-induced signals, while the flavor-based sub-GeV selection (ii) mainly selects $\nu_e/\bar{\nu}_e$ events. However, since all neutrino flavors contribute equally to the signal modeling in this work (cf. Chap. 6) and the selection methods also contain contributions from other flavors due to their finite efficiency (cf. Chaps. 8 and 9), the limits shown in Fig. 10.7 represent effective, flavor-averaged upper bounds. For a flavor-independent conservative estimate, the results without any selection (i) should be considered, since in this case contributions from all flavors enter equally.
In summary, the combined MeV and sub-GeV analysis demonstrates that JUNO can improve the existing upper limits from Super-K by approximately one order of magnitude over the entire mass range from $\sim 15\,\mathrm{MeV}$ to $1\,\mathrm{GeV}$. The complementary selection methods of a PSD-based IBD selection in the MeV range and a flavor-based $\nu_e/\bar{\nu}_e$-like selection in the sub-GeV range enable optimal exploitation of the characteristic spectral features in DM-induced neutrino signals across the entire energy range. Despite the significant improvement compared to Super-K, thermal relic WIMPs in the sub-GeV mass range cannot be excluded by JUNO, as the achievable limit remains a factor of 6–16 above the natural self-annihilation cross section inferred from the thermal relic density [39].

10.3.2 Influence of the Binning Strategy and the Prior Distribution

To estimate the influence of the chosen bin width on the sensitivity analysis, the Bayesian analysis was performed for binned energy spectra with widths of 1 MeV, 5 MeV, and 10 MeV. Fig. 10.8 shows the relative deviations of the 90 % credibility limits on $\langle \sigma_{\mathrm{A}} v \rangle$ for a bin width of 10 MeV (dashed gray curves) and a bin width of 1 MeV (solid gray curves) with respect to the reference strategy of 5 MeV bin width. The selection strategies (i) without restriction and (ii) with flavor-based selection are illustrated exemplarily. The results show, that the binning strategy has a significant influence, particularly for DM masses below 0.4 GeV. For the analysis without selection (i), a finer binning of 1 MeV leads to an improvement of the upper limit by up to 20 %, while a larger binning of 10 MeV decreases the sensitivity by up to 15 %. This effect can be attributed to the characteristic double-peak structure that is preserved in selection method (i). A finer binning resolves the peaks more effectively, whereas with larger binning the sharpness of the peaks is lost. In contrast, the flavor-based $\nu_e/\bar{\nu}_e$-like selection (ii) shows a significantly weaker dependence on the bin width, with deviations of $< 5\,\%$. This is presumably due to the fact, that the single-peak structure exhibits fewer spectral features and is therefore less sensitive to the bin width. For larger DM masses $m_\chi \gtrsim 0.5\,\mathrm{GeV}$, the results of all binning strategies converge with deviations of less than 2 %, since in this region, the spectral structures are already broadened due to the limited energy resolution. The choice of the bin width, therefore, no longer has a significant influence on the sensitivity.
Analogous to Sec. 10.2.3, the robustness of the results with respect to different prior

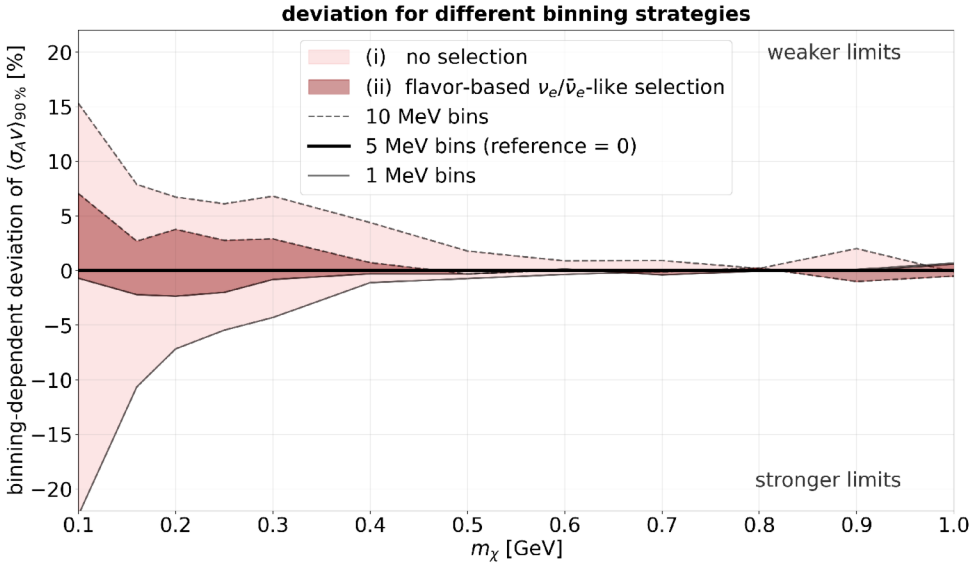

Figure 10.8: Relative deviation of the 90 % credibility limits on $\langle \sigma_A v \rangle$ from 5 MeV binning for the 10 MeV binning (solid line edge) and 1 MeV binning (dashed line edge). The results are shown exemplarily for selection methods (i) and (ii).

distributions is investigated in the sub-GeV region. Fig. 10.9 shows the relative deviation of the 90 % credibility limit on $\langle \sigma_A v \rangle$ for the *loose* (solid black curves) and *tight* (dashed black curves) prior scenarios with respect to the *baseline* reference scenario. The light hatched area shows the deviations in the case of no selection (i), while the darker area demonstrates the flavor-based selection scenario (ii). Compared to the results in the MeV region, the sub-GeV analyses exhibit a weaker dependence on different prior widths, with $\lesssim 2\,\%$ in the entire mass range. This is presumably due to larger event statistics, causing the posteriors to be primarily constrained by the data rather than by the prior assumptions.

10.3.3 Toy-MC Results for the Baseline Sensitivity

Similar to the MeV regime, the expected uncertainty of the exclusion sensitivity due to statistical fluctuations in real measurements is quantified in the sub-GeV regime using selected toy-MC studies (cf. Sec. 10.1.3). These were performed for the most sensitive flavor-based selection strategy (ii) in the *baseline* prior scenario. For reasons of computational effort, the pseudo-experiments were only performed for the masses $m_\chi \in \{0.1, 0.2, 0.3, 0.4, 0.6, 0.8, 1.0\,\text{GeV}\}$, which sufficiently cover the shape of the sensitivity curve (cf. Fig. 10.7). The resulting exclusion limits and the derived 68 % and 95 % uncertainty intervals are shown in red in Fig. 10.10, together with the results in the MeV regime shown in black (cf. Sec. 10.2.4). The red line shows the expected median sensitivity $\langle \sigma_A v \rangle_{90\,\%}$ for the Asimov-like datasets, which is already plotted for all masses in Fig. 10.7. The shaded red bands show the expected 1σ uncertainty (68 %, dark red) and 2σ uncertainty (95 %, light red) of the 90 % exclusion limit around the median sensitivity. Similar to the MeV regime, the relative uncertainty intervals of the toy-MC study in the sub-GeV regime are in the range of $+43\,\%/-30\,\%$ (at the 68 % level) relative to the Asimov sensitivity, and the 2σ C.L. is around $+98\,\%/-48\,\%$ in the whole mass range. Therefore, the influence of statistical fluctuations in the measurements is similar

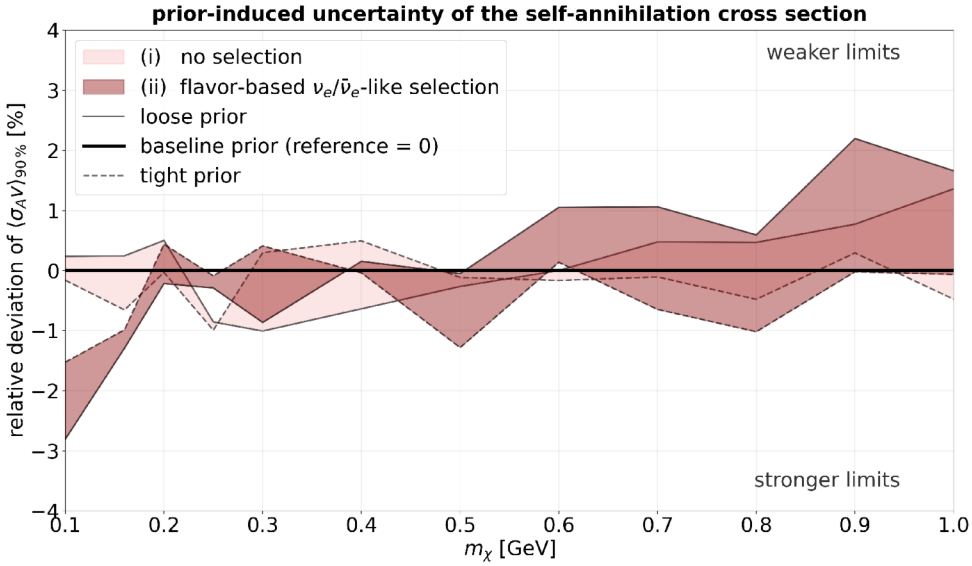

Figure 10.9: Relative deviation of the 90 % credibility limits on $\langle \sigma_A v \rangle$ from the *baseline* scenario for the *loose* (solid black curves) and *tight* (dashed black curves) prior scenarios. The results are shown exemplarily for selection methods (i) and (ii).

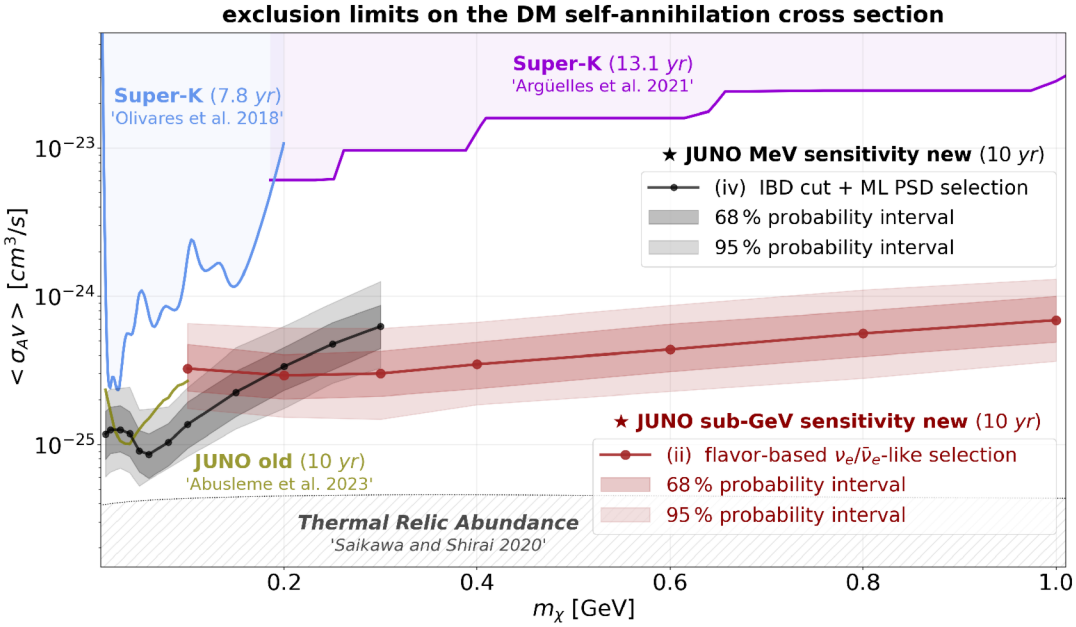

Figure 10.10: Toy-MC results of the expected 90 % credibility exclusion limits on $\langle \sigma_A v \rangle$ in the sub-GeV regime for the *baseline* prior scenario and the flavor-based selection method (ii). The dashed curve indicates the Asimov sensitivity at the selected mass points. The dark shaded band shows the 68 % interval (1σ) and the light shaded band the 95 % interval (2σ) of the $\langle \sigma_A v \rangle_{90\,\%}$ distribution around the median. The Asimov sensitivity and the uncertainty bands for ML-based PSD selection strategy in the MeV regime (iv) are added in black.

in both energy ranges, although it should be noted that the spread may depend on the chosen binning. Although finer binning leads to better preservation of spectral structures

and thus to higher Asimov sensitivity (cf. Sec. 10.3.2), it also reduces the statistics per bin and can therefore increase the vulnerability of individual bins to fluctuations. In order to determine the optimal binning strategy, a systematic investigation of this interaction on the toy-MC fluctuations would be necessary which however, exceeds the scope of this work. Including the uncertainty intervals shown in Fig. 10.10, the optimal transition region between an IBD-based analysis in the MeV regime and a CC-based analysis in the sub-GeV regime remains at $m_\chi \simeq 200\,\mathrm{MeV} \pm 50\,\mathrm{MeV}$. In conclusion, the toy-MC results show that, even taking statistical fluctuations into account, JUNO can significantly exceed the current exclusion limits of Super-K in the MeV and sub-GeV regime after 10 yr of data taking.

10.4 Exclusion Sensitivity for GeV DM in JUNO

For the Bayesian analysis in the GeV regime, binned energy spectra in the interval $E_{\mathrm{vis}} \in [0.1\,\mathrm{GeV}, 10\,\mathrm{GeV}]$ are used with a bin width of 0.1 GeV. A spectral tilt of the atmospheric CC and NC background is allowed according to Eq. 10.4, with $E_{\mathrm{pivot}} = 5\,\mathrm{GeV}$ and $E_{\mathrm{scale}} = 9\,\mathrm{GeV}$. The DSNB background is not considered in the GeV analysis, since DSNB neutrinos are below 100 MeV (cf. Sec. 7.3). The Bayesian analysis is performed for WIMP masses from $m_\chi = 1\,\mathrm{GeV}$ to $m_\chi = 10\,\mathrm{GeV}$ in steps of 1 GeV, and the expected 90 % credibility limit on the self-annihilation cross section $\langle \sigma_{\mathrm{A}} v \rangle$ is determined with the same method described in Sec. 10.2 for the *baseline*, *loose* and *tight* prior distributions. As discussed in Sec. 9.2, in the GeV mass range, a directional event selection strategy can increase the S2B ratio, due to the non-isotropic distribution of DM-induced neutrino signals (cf. Sec. 9.2). This is done, by defining a cone with half-opening angle ψ_{cone} around the GC as the region of interest (ROI) for the signal events. For the sensitivity analysis in this work, two representative cone angles, $\psi_{\mathrm{cone}} = 20\,^\circ$ and $\psi_{\mathrm{cone}} = 50\,^\circ$, are evaluated for both DM density profiles presented in Sec. 3.2. The smaller angle is motivated by cuspy profiles such as gNFW, whose optimum lies between $15\,^\circ$ and $30\,^\circ$ for most masses (cf. Tab. 9.2), whereas the larger angle reflects the optimal range of cored profiles such as Einasto, which peaks around $50\,^\circ$ for $m_\chi \gtrsim 3\,\mathrm{GeV}$. To analyze the directional-dependent sensitivity of JUNO for the indirect DM search in the GeV mass range, five scenarios were therefore considered:

(i) full-sky (FS) observation with $\psi_{\mathrm{cone}} = 180°$ (model independent),
(ii) directional selection with $\psi_{\mathrm{cone}} = 50°$ for gNFW profile,
(iii) directional selection with $\psi_{\mathrm{cone}} = 20°$ for gNFW profile,
(iv) directional selection with $\psi_{\mathrm{cone}} = 50°$ for Einasto profile,
(v) directional selection with $\psi_{\mathrm{cone}} = 20°$ for Einasto profile.

The 90 % quantile S_{90} of the signal posterior distribution is shown in the left panel of Fig. 10.11 for all five scenarios. The FS observation (i) yields the largest S_{90}, as the signal must be distinguished from the full, unreduced background. With a directional cone-like selection, a larger fraction of the background is suppressed relative to the signal, resulting in a decrease of S_{90} with decreasing half-opening angle. For a given cone angle ψ_{cone}, the 90 % credibility limit S_{90} is independent of the assumed DM density profile (gNFW and Einasto), since the spectral shape of the signal is the same, and the background within the cone is identical in both cases. However, according to Eq. 10.11, the same value of S_{90} translates into different upper limits on the self-annihilation cross section $\langle \sigma_{\mathrm{A}} v \rangle_{90\%}$ depending on the assumed profile, since the signal efficiency $\varepsilon_S(\psi_{\mathrm{cone}})$

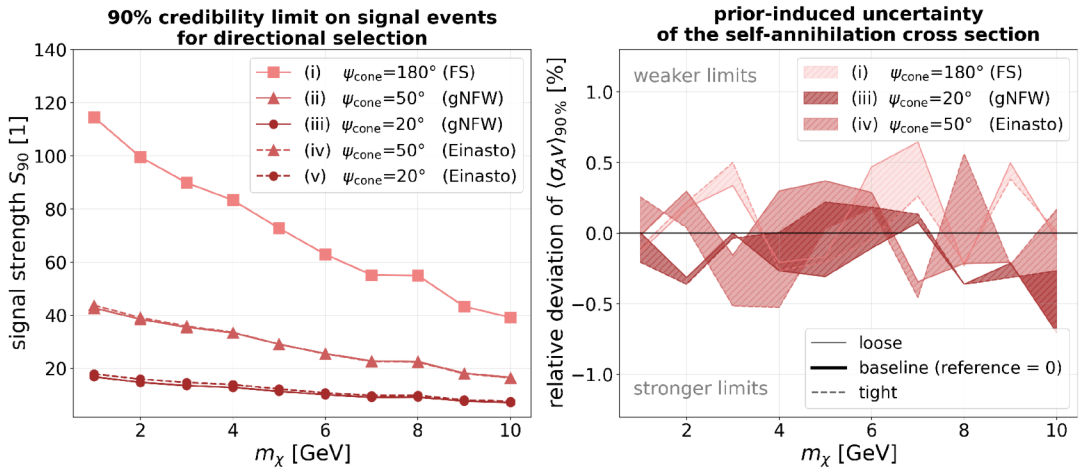

Figure 10.11: Left panel: upper 90 % credibility limit S_{90} on the signal strength as a function of the WIMP mass m_χ for a FS observation ($\psi_{\text{cone}} = 180°$) and the directional selection ($\psi_{\text{cone}} = 20°$ and $50°$) for both DM profiles. Right panel: relative deviation of the 90 % credibility limits on $\langle\sigma_A v\rangle_{90\%}$ for different prior distributions. The reference at 0 corresponds to the *baseline* scenario, and the red hatched bands show the mass-dependent deviations if the *loose* and *tight* prior scenarios are assumed. The results are shown exemplarily for the FS (i), for the gNFW with 20° (iii) and for the Einasto profile with 50° (iv).

differs between the gNFW and Einasto distributions (cf. Fig. 9.10).
Analogous to Figs. 10.5 and 10.9 in the MeV and sub-GeV analysis, the right panel of Fig. 10.11 illustrates the influence of the prior distribution on the sensitivity in the GeV regime, shown exemplarily for the full-sky (FS) observation (i), the gNFW profile with $\psi_{\text{cone}} = 20°$ (iii), and the Einasto profile with $\psi_{\text{cone}} = 50°$ (iv). The relative deviation of $\langle\sigma_A v\rangle_{90\%}$ is given for the *loose* and *tight* prior scenarios concerning the *baseline* scenario, which is used as the reference (black line at zero). The results demonstrate that the prior-induced uncertainty remains below $\lesssim 0.7\,\%$ for all masses in the GeV range, confirming that the posterior distributions are predominantly constrained by the spectral data rather than by the prior assumptions. A variation of the spectral bin width between 50, 100 and 200 MeV revealed a relative deviation of less than 1 %.
The expected 90 % credibility limit on the self-annihilation cross section $\langle\sigma_A v\rangle$ is shown in Fig. 10.12. The upper panel shows the direction-dependent sensitivity for the cuspy gNFW profile, while the lower panel assumes a cored Einasto DM density distribution. For both profiles, the sensitivity obtained with a cone-like ROI of $\psi_{\text{cone}} = 20°$ and $\psi_{\text{cone}} = 50°$ is compared to the FS observation (i). As expected (cf. Tab. 9.2), a directional selection with half-opening angle $\psi_{\text{cone}} = 20°$ (iii) (upper panel, circular markers) enhances the sensitivity for the gNFW profile compared to a cone angle of $\psi_{\text{cone}} = 50°$ (ii) (triangle marker) in the mass range $m_\chi \gtrsim 2\,\text{GeV}$. For $m_\chi = 1\,\text{GeV}$, both half-opening angles yield approximately equal exclusion limits, as the S2B ratios nearly coincide at this mass (cf. Fig. 9.11), with both improving the exclusion limit by approximately 38 % relative to the FS analysis. In summary, a directional-dependent analysis with $\psi_{\text{cone}} = 20°$ (iii) achieves an average improvement of $\sim 60\,\%$ for $m_\chi \gtrsim 3\,\text{GeV}$ compared to the FS observation (i), while a larger cone with $\psi_{\text{cone}} = 50°$ (ii) provides a more moderate improvement of $\sim 46\,\%$.
For the cored Einasto profile (lower panel of Fig. 10.12), a directional-dependent selection

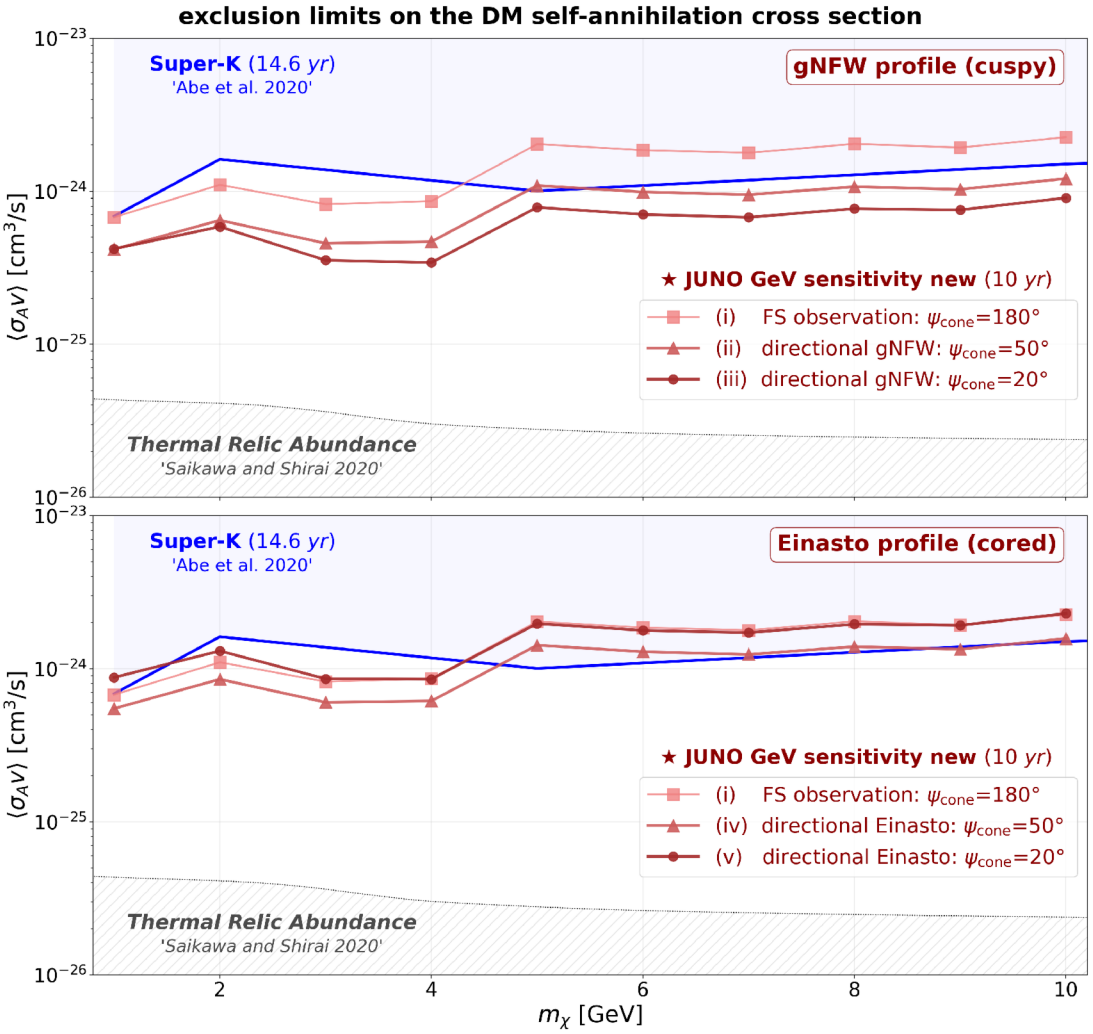

Figure 10.12: Expected 90 % credibility limits on the self-annihilation cross section $\langle \sigma_A v \rangle$ of GeV WIMPs as a function of the mass m_χ. The results are shown for a FS observation, and for a directional selection of events coming from within a cone with half-opening angle $\psi_{\text{cone}} = 20°$ and $\psi_{\text{cone}} = 50°$. The upper panel illustrates the directional-dependent sensitivity in JUNO for the cuspy gNFW profile, while the lower panel demonstrates the conservative scenario of a cored Einasto profile. All results are obtained with the *baseline* prior scenario for 10 yr of data taking and a fiducial mass of 14.77 kton in JUNO. The upper limit set by Super-K [63] is shown for comparison, together with the thermal relic abundance [39].

is less beneficial, since the DM density around the GC is less concentrated than for a cuspy profile. A narrow cone of $\psi_{\text{cone}} = 20°$ (v) offers no improvement over the FS observation (i) and even worsens the sensitivity for $m_\chi \lesssim 3\,\text{GeV}$. A larger cone of $\psi_{\text{cone}} = 50°$ (iv), however, provides a moderate improvement of $\sim 30\,\%$ relative to the FS observation.

For reference, the current best upper limit from Super-K is included in Fig. 10.12 (blue curve) [63], which has already set considerably more stringent limits in the GeV mass range compared to the sub-GeV regime (cf. Fig. 3.6). However, the result is obtained within a likelihood analysis that explicitly exploits the angular distribution of events

relative to the GC. Therefore, in contrast to a FS comparison, the sensitivity depends not only on the averaged J_{avg} factor but also on the differential $\mathcal{J}$-factor of a standard NFW profile and should thus be interpreted as profile-dependent [63]. For a more cored DM density distribution like Einasto, the sensitivity would be reduced and the blue curve would be shifted to larger values. The results in Fig. 10.12 demonstrate that large LS detectors such as JUNO, despite their significantly worse directional resolution compared to water Cherenkov detectors, can achieve a competitive level for indirect DM searches in the GeV range. Due to the smaller fiducial mass and the substantially reduced directional resolution, JUNO is unlikely to significantly surpass the Super-K limits, but is expected to provide an independent cross-check of the results.

10.4.1 Toy-MC Results for the Baseline Sensitivity

Analogous to the preceding energy regimes, the expected uncertainty of the exclusion sensitivity due to statistical fluctuations in real measurement data is also quantified in the GeV range using selected toy-MC studies (cf. Sec. 10.1.3). The pseudo-experiments were performed representatively for the WIMP masses $m_\chi \in \{1, 2, 3, 4, 5, 6, 8, 10\,\text{GeV}\}$ in the *baseline* prior scenario. In contrast to the analyses in the MeV and sub-GeV ranges, the toy-MC study in the GeV regime was performed exclusively for the FS observation without directional selection (i), since the achievable sensitivity of a direction-dependent analysis depends on the DM density distribution realized in the Milky Way. As the FS observation only requires averaged assumptions on the DM

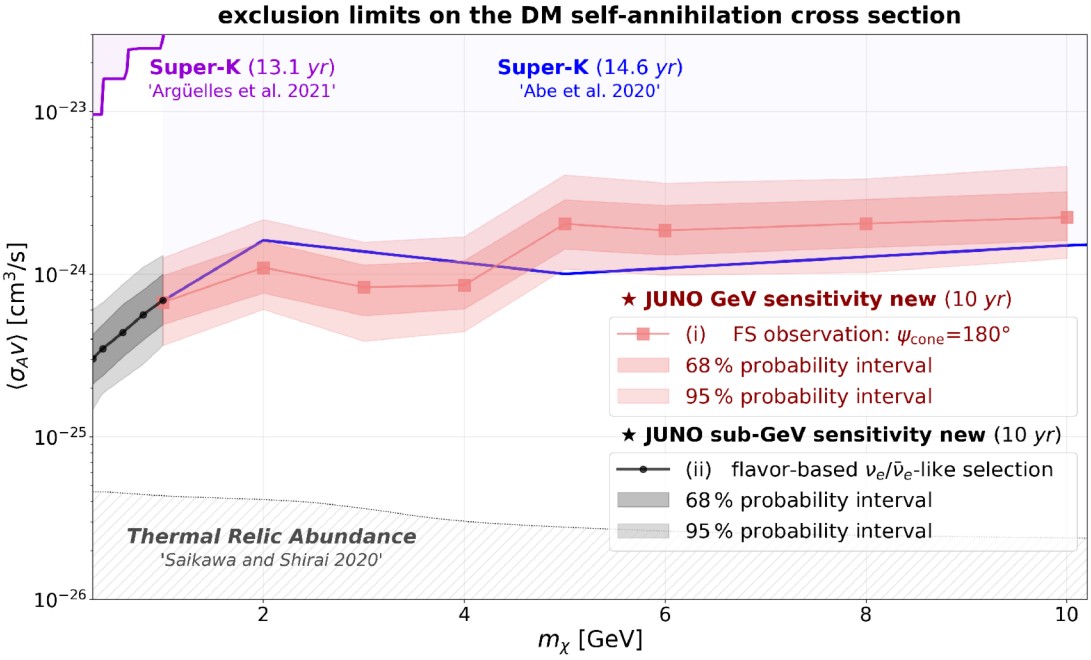

Figure 10.13: Toy-MC results of the expected 90 % credibility exclusion limits on $\langle\sigma_{\text{A}}v\rangle$ in the GeV regime for a FS observation (i) in the *baseline* prior scenario. The solid curve with markers indicates the Asimov sensitivity at the selected mass points. The dark shaded red band shows the 68 % interval (1σ) and the light shaded red band the 95 % interval (2σ) of the $\langle\sigma_{\text{A}}v\rangle_{90\,\%}$ distribution around the median. The Asimov sensitivity and the uncertainty bands for the flavor-based selection strategy in the sub-GeV regime (ii) are added in black.

density profile (cf. Chap. 3), which can be easily scaled to other scenarios, it serves as a model-independent reference scenario for quantifying the purely statistical uncertainty of the exclusion limits. Fig. 10.13 shows the resulting exclusion limits and their uncertainty intervals in the GeV regime (red), together with the results in the sub-GeV regime, derived in Sec. 10.3.3 for the flavor-based selection (ii). The solid red curve with markers indicates the sensitivity derived from Asimov-like datasets of GeV DM, while the dark and light shaded bands represent the 68 % (1σ) and 95 % (2σ) uncertainty intervals of the $\langle\sigma_{\mathrm{A}}v\rangle_{90\,\%}$ distribution around the median. The relative deviation of the toy-MC results from the Asimov sensitivity is approximately $+42\,\%/-29\,\%$ at the 68 % C.L. and $+95\,\%/-47\,\%$ at the 95 % C.L. and remains approximately constant over the entire GeV mass range. The impact of statistical fluctuations of the data on the exclusion sensitivity is therefore comparable in all three mass regimes (cf. Secs. 10.2.4 and 10.3.3). The consistency of the independent sub-GeV and GeV analyses is further confirmed by the good agreement of the Asimov results and the toy-MC uncertainty bands at $m_\chi = 1\,\mathrm{GeV}$, which represents the overlap region of both regimes. In the range $m_\chi = 2-4\,\mathrm{GeV}$ JUNO can exceed the current Super-K limits after 10 yr data taking even with a FS observation with 68 % C.L., which is not feasible for heavier WIMPs with $m_\chi \geq 5\,\mathrm{GeV}$. In this area, a directional analysis must be conducted in order to further increase sensitivity in JUNO.

10.5 JUNO's Potential for Indirect DM Search

In this chapter, the exclusion sensitivity of JUNO for a DM-induced monoenergetic neutrino signal was determined within a consistent Bayesian framework for DM masses ranging from $m_\chi = 15\,\mathrm{MeV}$ to $m_\chi = 10\,\mathrm{GeV}$. Both, systematic effects, through explicit nuisance parameters and prior distributions (cf. Sec. 10.1.1), and statistical uncertainties, through selected toy-MC studies (cf. Sec. 10.1.3), were taken into account. For the different DM mass regimes, dedicated selection methods were investigated that exploit the characteristic properties of a monoenergetic neutrino signature to enhance the signal-to-background (S2B) ratio.

10.5.1 Ten-Year Exclusion Sensitivity of JUNO (s-wave)

The combined expected results for *s*-wave annihilation across all mass regimes (cf. Secs. 10.2, 10.3 and 10.4) are shown in Fig. 10.14 for 10 yr data taking and a fiducial mass of 14.77 kton in JUNO. The black curve indicates the achievable sensitivity for a full-sky (FS) observation without any selection method. In the MeV range (orange curves), the best sensitivity is achieved through an IBD selection combined with ML-based PSD. The uncertainty of the DSNB flux plays a central role in this regime, since it constitutes an irreducible background for IBD-based analyses. The results for the three DSNB models introduced in Sec. 7.3 are indicated by the orange hatched band. In the sub-GeV range (red curve), a $\nu_e/\bar{\nu}_e$-like flavor selection increases the sensitivity, while in the GeV range (dark red), a directional-dependent analysis with a cone-like ROI around the GC provides the strongest background suppression. The directional-dependent analysis, however, depends on the assumed DM density profile, as indicated for both profiles by the dark red hatched band.
The sensitivity limits derived for the different selection strategies are effectively flavor-dependent, since the methods exhibit varying sensitivities to different neutrino flavors (cf. Chaps. 8 and 9). The black curve, in contrast, provides a flavor-independent sensitivity,

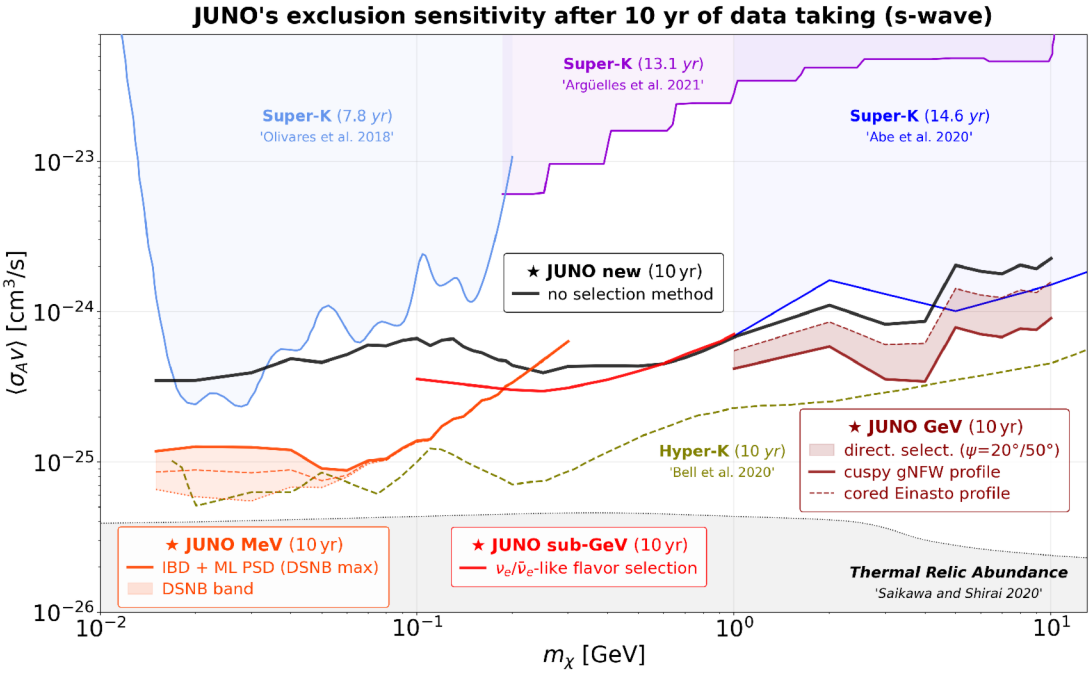

Figure 10.14: Expected 90 % credibility exclusion limit on the self-annihilation cross section $\langle \sigma_A v \rangle$ in the DM mass range from $m_\chi = 15\,\text{MeV}$ to $m_\chi = 10\,\text{GeV}$. The results are obtained with the *baseline* prior scenario for 10 yr of data taking and a fiducial mass of 14.77 kton in JUNO. The black line shows the results for a FS observation without any selection strategy. The red colored curves show the results for each mass regime with the most promising selection strategy, which were discussed before. The upper limits set by Super-K [62, 36, 63] are shown for comparison, together with the thermal relic abundance [39]. The dashed olive line indicates the estimated sensitivity for the next-generation experiments Hyper-K [64].

since all flavors enter equally in the modeling of the signal and background spectra. For comparison, the current best upper limits are shown in Fig. 10.14, which have been set by Super-K across the entire mass range investigated in this work [62, 36, 63]. Compared to Super-K, JUNO benefits at low energies from the excellent energy resolution (cf. Sec. 5.3) and the characteristic spectral signature of the DM-induced signal (cf. Sec. 6.2), enabling an improvement of the existing Super-K limits by approximately one order of magnitude in the range from $m_\chi = 15\,\text{MeV}$ to $m_\chi = 1\,\text{GeV}$. In the GeV range, however, water-based Cherenkov detectors have an inherent advantage due to their superior directional reconstruction. Therefore, JUNO is not expected to significantly improve the existing Super-K limits in this regime, but can nonetheless provide an important independent verification. For future experiments such as Hyper-K, a further improved sensitivity is expected due to the substantially larger fiducial volume.
The sensitivities shown in Fig. 10.14 are based on Asimov-like datasets and therefore represent the expected median performance. To quantify the expected spread due to statistical fluctuations in real measurements, selected toy-MC studies with 500 pseudo-experiments were performed for representative DM masses with the best selection strategy (cf. Secs. 10.2.4, 10.3.3, and 10.4.1). The resulting uncertainty bands confirm that, even at the 95 % C.L., the existing Super-K limits are clearly surpassed in the MeV and sub-GeV range after 10 yr of data taking.

10.5.2 Ten-Year Exclusion Sensitivity for p-Wave Annihilation

All exclusion limits presented so far are derived under the assumption of a velocity-independent s-wave DM annihilation. For a p-wave dominated scenario, however, the thermally averaged cross section $\langle \sigma_{\mathrm{A}} v \rangle$ depends quadratically on the mean relative velocity $\langle v^2 \rangle$ of the DM particles (cf. Eq. 2.4), which is significantly reduced today compared to the early universe. In Sec. 3.3.3, the expected annihilation rate for a p-wave scenario was derived with the modified $\mathcal{J}^{(p)}$-factor according to Eq. 3.14, which allows the s-wave exclusion limits to be converted into upper limits on the p-wave annihilation parameter b_P in Eq. 2.4. In the MeV and sub-GeV mass range, the sensitivity analysis is based on a FS observation ($\psi_{\mathrm{cone}} = 180°$). The expected neutrino flux in Eq. 3.13 therefore depends on the dimensionless J_{avg}, and the transition from s to p-wave limits is obtained by a simple rescaling according to

$$b_{P,90\,\%}(m_\chi) = \langle \sigma_{\mathrm{A}} v \rangle_{90\,\%}(m_\chi) \cdot \frac{J_{\mathrm{avg}}}{J^{(p)}_{\mathrm{avg}}} \,. \tag{10.12}$$

The ratio $J^{(p)}_{\mathrm{avg}}/J_{\mathrm{avg}} = 10^{-6}$ is discussed in Sec. 3.3.3 and illustrated in Fig. A.5. Since the spectral shape of the signal does not change for p-wave annihilation, the 90 % quantile S_{90} of the signal posterior distribution in Eq. 10.9 remains unchanged, and the rescaling shifts the exclusion limits by a constant factor of 10^6 towards higher values of b_P.
In the GeV mass range, however, a directional cone-like event selection with a half-opening angle ψ_{cone} around the GC is applied (cf. Sec. 9.2.2). In this case, the signal efficiency $\varepsilon_S(\psi_{\mathrm{cone}})$ depends on the radial distribution of the annihilation rate in the Milky Way, which differs between the s and p-wave scenarios. In Fig. 3.5, the signal efficiencies for the cuspy gNFW and the cored Einasto density profile are compared for s (dashed curves) and p-wave annihilation (solid curves)[4]. While the signal efficiency for the gNFW profile hardly changes, the annihilation rate for the Einasto profile is more strongly concentrated towards the GC in the p-wave scenario.
To account for the different directional distribution in the rescaling of the p-wave exclusion limits, a mass-dependent correction factor for the chosen cone angle ψ_{cone} is defined according to

$$C(\psi_{\mathrm{cone}}, m_\chi) = \frac{n^{(\mathrm{p})}_S(\psi_{\mathrm{cone}}, m_\chi)}{n^{(s)}_S(\psi_{\mathrm{cone}}, m_\chi)} \,, \tag{10.13}$$

where $n^{(x)}_S$ ($x \in \{s, p\}$) denotes the channel-weighted expected number of signal events within the cone according to Eq. 9.7, with the respective signal efficiencies $\varepsilon^{(ch)}_{S,(x)}(\psi_{\mathrm{cone}}, m_\chi)$. The event classes (ch) (CC $\bar{\nu}_e/\nu_e$, CC $\bar{\nu}_\mu/\nu_\mu$ and NC) are taken into account separately for s and p-wave annihilation. Fig. 10.15 shows the correction factor C for both chosen cone angles $\psi_{\mathrm{cone}} = 20°$ (dashed curves) and $\psi_{\mathrm{cone}} = 50°$ (solid curves) assuming the gNFW profile (blue curves) and the Einasto profile (red curves)[5]. A correction value of $C > 1$ indicates that the p-wave $\mathcal{J}$-factor is more strongly concentrated within the cone than the s-wave $\mathcal{J}$-factor, leading to higher signal efficiency and thus a better limit compared to a FS observation. For the cuspy gNFW profile, $C \approx 1$ is

[4] Fig. 3.5 actually shows the $\mathcal{J}$-factor ratios for a cone-like ROI relative to a FS observation, which, however, correspond to the ideal signal efficiency according to Eq. 9.5.

[5] It should be noted that the optimal cone angles, which were determined in Sec. 9.2.2 by maximizing the S2B ratio, change slightly for p-wave annihilation (cf. Fig. B.8). While this change is negligible for the gNFW profile, the angles decrease by $\sim$ 10–20 % for the Einasto profile.

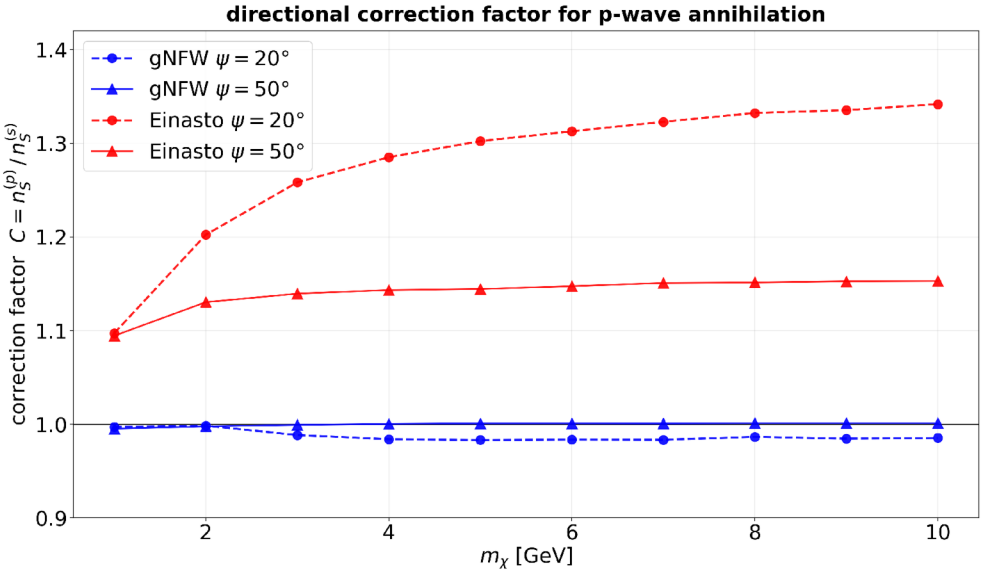

Figure 10.15: Directional correction factor $C = n_S^{(p)}/n_S^{(s)}$ for p-wave annihilation as a function of the DM mass m_χ for the gNFW profile (blue) and the Einasto profile (red). The correction factors are shown for the half-opening cone angles $\psi_{\text{cone}} = 20°$ (dashed) and $\psi_{\text{cone}} = 50°$ (solid). A value of $C > 1$ indicates a higher signal efficiency for p-wave relative to s-wave annihilation within the selected cone, corresponding to an improved exclusion limit from directional selection.

close to one across the entire mass range, indicating that the spatial signal distribution hardly differs between the two scenarios, as expected (cf. Fig. 3.5). For a narrow cone of $\psi_{\text{cone}} = 20°$, the potential for directional selection is even smaller for a p-wave than for an s-wave scenario, which is illustrated by the comparison of the effective signal efficiencies in Fig. B.6. For the cored Einasto profile (red curves), on the other hand, directional selection in the p-wave scenario is more promising than for s-wave annihilation for both cone angles. For $\psi_{\text{cone}} = 50°$, the p-wave exclusion limit improves by a factor of ~ 1.15 compared to the s-wave scenario, while for $\psi_{\text{cone}} = 20°$ it improves by up to ~ 1.35. The upper limit on b_P in the GeV regime is obtained by combining the FS rescaling in Eq. 10.12 with the correction factor C defined in Eq. 10.13 according to

$$b_{P,90\,\%}(m_\chi) = \langle \sigma_{\text{A}} v \rangle_{90\,\%}\,(m_\chi) \cdot \frac{J_{\text{avg}}}{J_{\text{avg}}^{(p)}} \cdot C(\psi_{\text{cone}}, m_\chi)\ . \tag{10.14}$$

The factor $J_{\text{avg}}/J_{\text{avg}}^{(p)}$ describes the global suppression of the present-day p-wave annihilation (cf. Sec. 3.3.3), while $C(\psi_{\text{cone}}, m_\chi)$ corrects for the additional mass-dependent differences of the signal acceptance due to the directional selection for the chosen DM profile (cf. Figs. B.6 and B.7).

In Fig. 10.16 the expected 90 % C.L. exclusion limits on b_P are shown for the entire DM mass range from $m_\chi = 15\,\text{MeV}$ to $m_\chi = 10\,\text{GeV}$. Analogous to the results for s-wave dominated annihilation in Fig. 10.14, the black curve shows the FS sensitivity without selection method, while the colored curves represent the best selection strategy in the respective mass ranges. The reference limits from Super-K [62, 36, 63] were rescaled together with the FS exclusion limits of JUNO (MeV and sub-GeV results) according to Eq. 10.12, such that the relative improvements remain identical to the s-wave scenario.

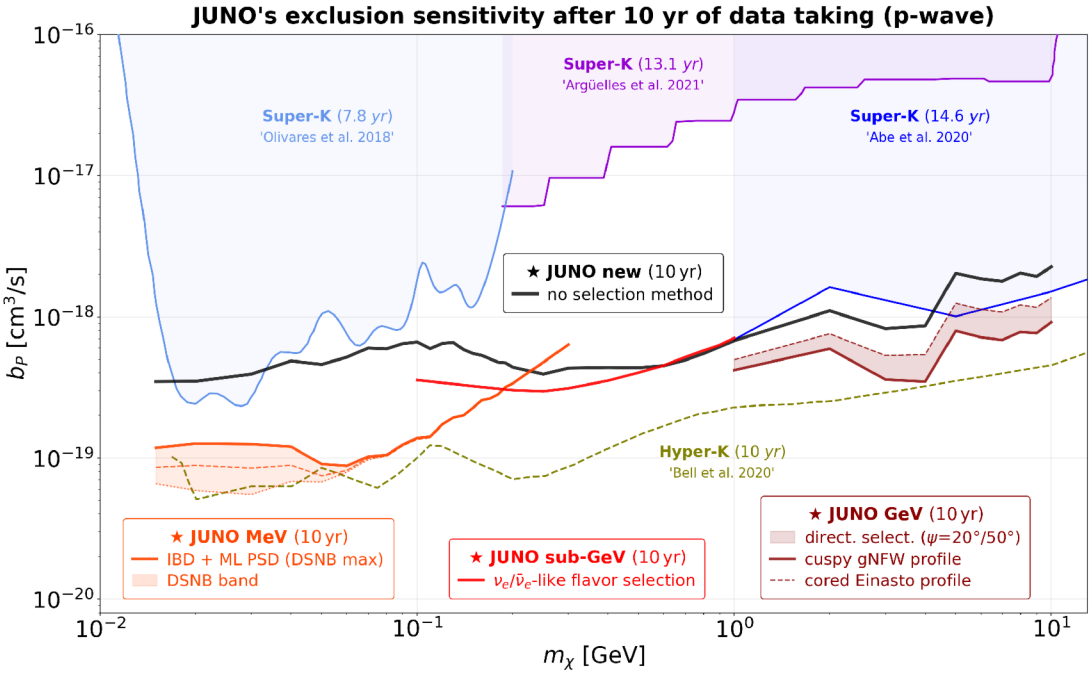

Figure 10.16: Expected 90 % credibility exclusion limit on the p-wave annihilation parameter b_P in Eq. 2.4 for DM masses from $m_\chi = 15\,\text{MeV}$ to $m_\chi = 10\,\text{GeV}$. The results are obtained from rescaling the *baseline* results for s-wave annihilation in Fig. 10.14 according to Eq. 10.12 for a FS observation and Eq. 10.14 for the directional event selection in the GeV mass range (hatched dark red band). The upper limits set by Super-K [62, 36, 63] are rescaled according to Eq. 10.12 and shown for comparison.

In the GeV regime, however, the additional correction factor C in Eq. 10.14 leads to a different behavior of the directional selection compared to the s-wave scenario (cf. dark red hatched band). While the relative improvement for the cuspy gNFW profile (solid dark red curve) remains nearly unchanged with $C \approx 1$, the cored Einasto profile (dashed dark red curve) shows a relative improvement of $\sim 15\,\%$ compared to the s-wave scenario (cf. Fig. 10.15). This can be attributed to the flat DM density profile, which, together with the enhancement from the bulge potential, results in a finite velocity dispersion $v_0(r)$ at the GC (cf. Fig. 3.4). In contrast, the velocity drops steeply at the GC for the gNFW profile, thereby compensating the increasing density (cf. Sec. 3.3). These competing effects cause the directional exclusion limit to be less dependent on the DM density profile in the case of p-wave dominated annihilation, which is illustrated by the narrower hatched dark red band in Fig. 10.16 compared to Fig. 10.14.
Although JUNO can significantly improve the existing exclusion limits on b_P after 10 yr of data taking, the achievable upper limits are in the range $b_{P,90\,\%} \sim 10^{-19}$-$10^{-18}\,\text{cm}^3/\text{s}$, which is approximately seven orders of magnitude above the natural annihilation cross section required to reproduce the observed relic density in the p-wave scenario (cf. right panel of Fig. 2.5). Nevertheless, the exclusion limits can serve as constraints on DM models in which s-wave annihilation is suppressed.

10.5.3 One-Year Exclusion Sensitivity of JUNO (s-wave)

JUNO exhibits particularly high sensitivity in the transition region between the MeV and the sub-GeV regime, enabling the experiment to set new best limits on the self-annihilation cross section $\langle \sigma_A v \rangle$ significantly earlier than after 10 yr. Fig. 10.17 shows

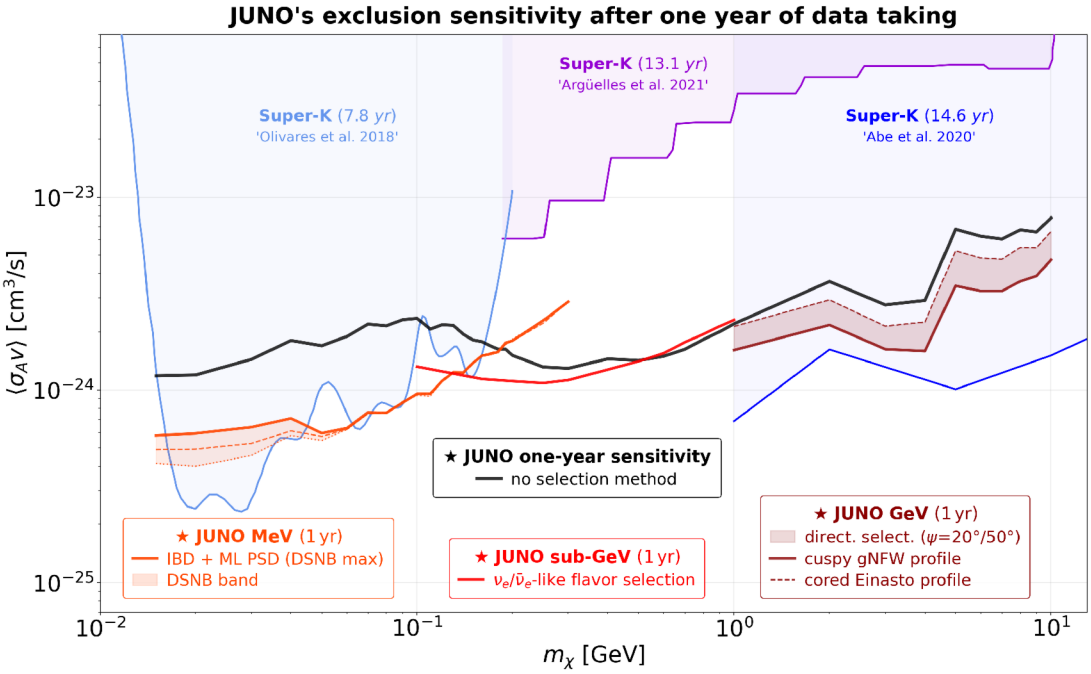

Figure 10.17: Expected 90 % credibility exclusion limit on the self-annihilation cross section $\langle \sigma_A v \rangle$ after 1 yr of data taking and a fiducial mass of 14.77 kton in JUNO. The black line shows the results for a FS observation without any selection strategy. The red colored curves show the results for each mass regime with the most promising selection strategy. The upper limits set by Super-K [62, 36, 63] are shown for comparison.

the expected 90 % credibility limit on $\langle \sigma_A v \rangle$ after only one year of data taking and a fiducial mass of 14.77 kton for s-wave annihilation. The black curve corresponds to the model-independent FS analysis without any selection, while the red curves represent, in each mass regime, the respective most sensitive selection strategy. As expected for a Poisson-dominated sensitivity, the upper limits scale relative to the 10 yr analysis by a factor of $\sim \sqrt{\Delta t} = \sqrt{10} \approx 3.16$. Nevertheless, in the sub-GeV region, JUNO already reaches a sensitivity after one year that clearly surpasses the existing Super-K limits. Also in the MeV range, a ML-based PSD can confirm and partly improve upon the current Super-K limits after one year of data taking. In contrast, in the GeV regime, the 1 yr sensitivities remain clearly above the existing Super-K limits even for directional event selection. In summary, Fig. 10.17 clearly demonstrates that part of JUNO's potential is already accessible during the early operational phase. Since JUNO has been taking data since August 26, 2025 [6], an analysis of the discovery potential after one year of data taking is of particular interest.

10.5.4 One-Year Discovery Potential of JUNO (s-wave)

The Bayesian analysis presented in Sec. 10.1 determines the signal strength S_{90}, which defines the upper 90 % credibility limit for the assumption of a background-only Asimov-like dataset. This exclusion limit thus describes the signal strength that is still compatible with the expected background data. Complementary, the question of discovery can be addressed, which differs conceptually from an exclusion. To determine the discovery sensitivity, the signal strength $S^{5\sigma}_{\text{disc}}$ required to reject the background-only hypothesis with a significance level of 5σ is examined. Particularly in the context of the one-year sensitivity shown in Fig. 10.17, this section aims to determine the statistical significance with which JUNO can detect a DM signal close to the Super-K upper limits after one year of data taking. While the Bayesian exclusion limit S_{90} is based on the posterior probability distribution of S according to Eq. 10.9, a frequentist approach based on a likelihood-ratio test in the Asimov approximation is adopted for the estimation of the discovery sensitivity [164]. For an Asimov-like dataset corresponding to the signal-plus-background hypothesis, the test statistic for rejecting the background-only hypothesis ($S = 0$) is defined via the likelihood-ratio according to [164]

$$q_0 = -2 \ln \left(\frac{\mathcal{L}(\boldsymbol{n}|S = 0, \tilde{\boldsymbol{\theta}}_{\text{bkg}})}{\mathcal{L}(\boldsymbol{n}|\hat{S}, \hat{\boldsymbol{\theta}}_{\text{bkg}})} \right) . \tag{10.15}$$

Here, $\mathcal{L}(\boldsymbol{n}|\boldsymbol{\theta})$ denotes the likelihood function defined in Eq. 10.2, while $\boldsymbol{\theta} = (S, \boldsymbol{\theta}_{\text{bkg}})$ corresponds to the nuisance parameters introduced in Sec. 10.1.1. In the test statistic q_0 in Eq. 10.15, $\hat{S}$ and $\hat{\boldsymbol{\theta}}_{\text{bkg}}$ denote the global maximum-likelihood fitters obtained under the signal-plus-background hypothesis. In contrast, $\tilde{\boldsymbol{\theta}}_{\text{bkg}}$ represents the profiled nuisance parameters that maximize the likelihood under the background-only hypothesis with fixed $S = 0$. In contrast to the Bayesian analysis, the nuisance parameters $\hat{\boldsymbol{\theta}}_{\text{bkg}}$ are not marginalized over their posterior distributions as described in Sec. 10.1.2, but are instead profiled by numerical optimization for each value of S.
While the constraints in [164] enter the extended likelihood as Gaussian penalty terms, this analysis employs log-normal penalty terms with relative uncertainties σ_{bkg} corresponding to the *baseline* scenario (cf. Eq. 10.7). The constraint terms are thus identical to the log-priors $\ln \pi(\boldsymbol{\theta})$ used in the Bayesian analysis, such that the extended log-likelihood is equivalent to the log-posterior in Eq. 10.10. This choice ensures a consistent physical framework for the likelihood-ratio test and the Bayesian analysis, which differs only in the statistical method (profiling + Asimov-like vs. marginalization + MCMC). Using the Asimov-like dataset, q_0 yields the median expected significance $Z = \sqrt{q_0}$ asymptotically according to Wilks' theorem [164]. A significance of $Z \geq 3$ corresponds to evidence (3σ), while $Z \geq 5$ is conventionally referred to as a discovery (5σ).
For the determination of the discovery potential in the MeV and sub-GeV mass range, a DM flux corresponding to the current best upper limits on $\langle \sigma_{\text{A}} v \rangle$ set by Super-K [62, 36, 63] is assumed. The expected number of signal events $S_{\text{SK}}(m_\chi)$ in JUNO is calculated for 1 yr of data taking and a fiducial volume of 14.77 kton, taking into account the respective selection strategy (cf. Eq. 6.1). The expected discovery significance $Z = \sqrt{q_0}$ assuming the Super-K upper limits is shown in Fig. 10.18 as a function of the DM mass m_χ. The black curve shows the results of the analysis with no selection method in the mass range from 15 MeV to 1 GeV. In the overlap region of the two regimes from 0.1 to 0.3 GeV, the higher significance of both regimes is shown for each DM mass. In addition, in the MeV regime, the IBD selection with additional ML-based PSD (light red) and in the sub-GeV regime, the $\nu_e/\bar{\nu}_e$-like flavor selection (dark red) are shown.

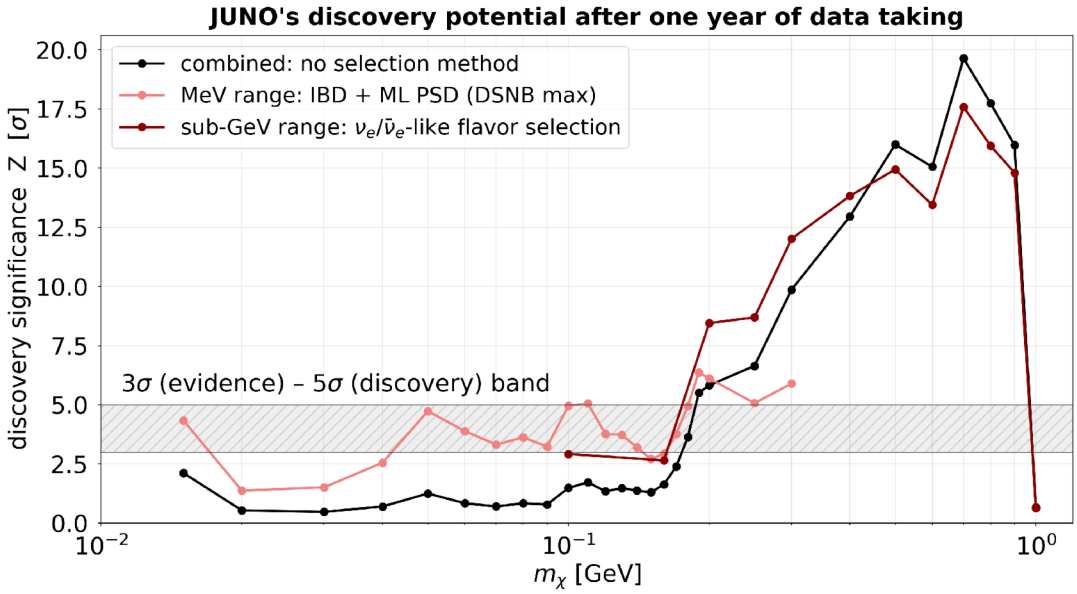

Figure 10.18: Expected discovery significance Z after one year of data taking in JUNO assuming the Super-K upper limits on the DM self-annihilation cross section [62, 36]. The gray hatched band marks the region between 3σ evidence and 5σ discovery. The black curve shows the analysis with no selection method, while in the MeV regime the IBD selection with ML-based PSD (light red), and the in the sub-GeV regime the $\nu_e/\bar{\nu}_e$-based flavor selection are illustrated (dark red). All results are obtained for the maximum DSNB flux with the *baseline* prior scenario and a fiducial volume of 14.77 kton.

In the MeV regime for $m_\chi \gtrsim 50\,\text{MeV}$, the ML-based PSD for IBD-like events (light red) can reach an evidence significance of $Z \gtrsim 3\sigma$ after one year of data taking. For individual DM masses, the sensitivity even approaches a discovery significance of $Z \gtrsim 5\sigma$. In the mass range $m_\chi < 50\,\text{MeV}$, however, the significance drops considerably, with the exception of $m_\chi = 15\,\text{MeV}$, which is located at the lower mass boundary of the Super-K limits presented in [62] (cf. Fig. 10.17). In the sub-GeV regime for $m_\chi \gtrsim 0.2\,\text{GeV}$, both the ML-based PSD method (light red) and the $\nu_e/\bar{\nu}_e$-like flavor selection (dark red) yield a discovery significance of $Z \gtrsim 5\sigma$. The combined analysis with no selection method (black curve) yields lower significances than the dedicated selection strategies up to $m_\chi \approx 0.5\,\text{GeV}$ and remains clearly below the evidence threshold for $m_\chi < 180\,\text{MeV}$. In the sub-GeV regime for $m_\chi \gtrsim 0.2\,\text{GeV}$, however, the discovery potential of JUNO exceeds $Z \gtrsim 5\sigma$ even without any selection strategy and remains only slightly below the potential of the flavor-based selection (dark red). For $m_\chi \gtrsim 0.5\,\text{GeV}$, it even yields a higher significance of up to 20σ, which is consistent with the sensitivity results discussed in Sec. 10.3.1. The pronounced drop at $m_\chi = 1\,\text{GeV}$ is due to the stronger Super-K limits in this mass region [63], leading to a lower expected signal strength S_{SK} and consequently to a reduced significance.

In summary, the results demonstrate that JUNO achieves significant discovery sensitivity across a broad mass range already after one year of data taking, assuming a DM signal at the current Super-K limits. In particular, a discovery with $Z \geq 5\sigma$ would be possible in the range $m_\chi \approx 0.2\text{-}0.9\,\text{GeV}$, highlighting the particular potential of JUNO in the sub-GeV regime. The results of the discovery potential are consistent with the one-year exclusion sensitivities shown in Fig. 10.17.

10.5.5 Model-Independent Limit on a Monoenergetic Neutrino Flux

Finally, it should be emphasized that the analysis presented in this work is formally not restricted to DM-induced signals. Methodologically, in the FS analyses an upper limit on a monoenergetic neutrino flux is determined, independent of its physical origin. The interpretation in terms of a bound on the thermally averaged self-annihilation cross section $\langle \sigma_A v \rangle$ is performed within a specific DM model, but the underlying sensitivity of JUNO refers generally to line-like neutrino signals in the investigated energy range. The corresponding model-independent 90 % C.L. upper limits on a monoenergetic neutrino flux $\Phi_\nu^{\text{mono}}(E_\nu)$ are shown in Fig. 10.19 for the entire energy range from $E_\nu = 15\,\text{MeV}$ to $E_\nu = 10\,\text{GeV}$. The results in the MeV range (orange curve) are consistent with the

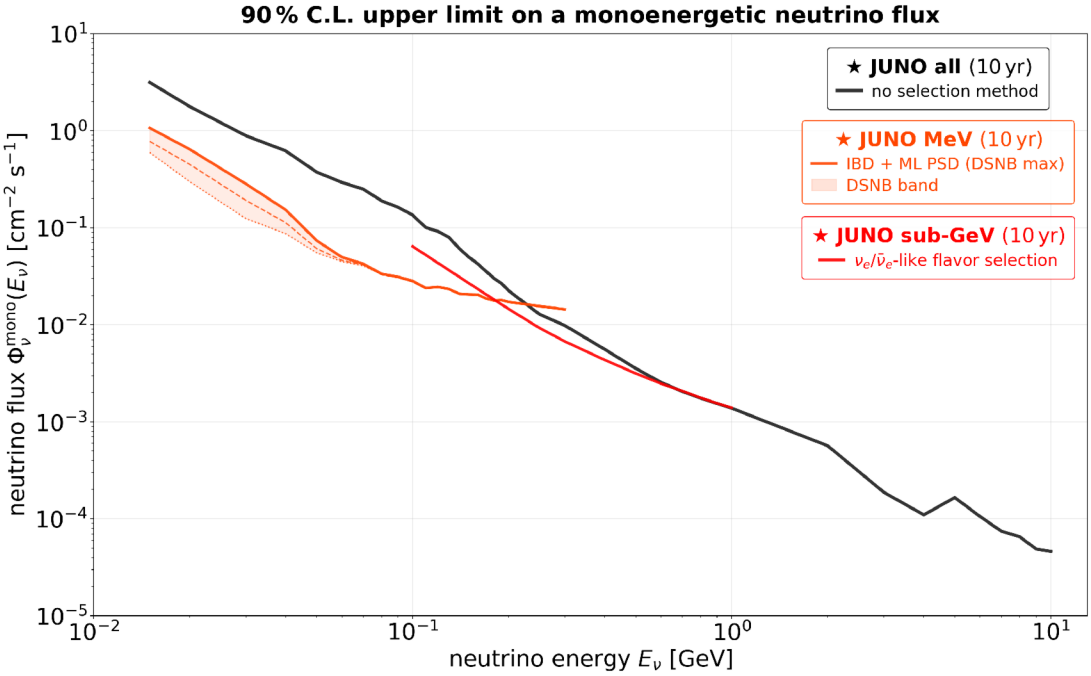

Figure 10.19: Expected 90 % C.L. upper limits on a monoenergetic neutrino flux with energy E_ν after 10 yr of data taking and a fiducial mass of 14.77 kton in JUNO. The black line shows the results without any selection strategy, while the red colored curves show the best FS results in the MeV and sub-GeV regime.

findings reported in [7]. While the upper 90 % credibility flux limit at $E_\nu = 15\,\text{MeV}$ is of the order of $1\,\text{cm}^{-2}\,\text{s}^{-1}$, the sensitivity improves to the order of 10^{-5}-$10^{-4}\,\text{cm}^{-2}\,\text{s}^{-1}$ at $E_\nu = 10\,\text{GeV}$, which can primarily be attributed to the increasing neutrino interaction cross section. The results of the directional event selection in the GeV range are not included in this figure, since they require a DM model-dependent signal distribution and therefore do not represent a universal FS limit on a monoenergetic neutrino flux.

11 | Summary and Outlook

We should consider every day lost on which we have not danced at least once.

– Friedrich Nietzsche

In this work, the potential of the Jiangmen Underground Neutrino Observatory (JUNO) for an indirect search for galactic Dark Matter (DM) in the mass range $m_\chi = 15\,\mathrm{MeV}$ to $m_\chi = 10\,\mathrm{GeV}$ was investigated. A monoenergetic neutrino signal from the direct self-annihilation channel $\chi\chi \to \nu\bar{\nu}$ was considered, assuming both a constant s-wave and a velocity-dependent p-wave dominated annihilation scenario. For simplicity, an approximately democratic flavor ratio of $1:1:1$ at Earth was assumed. This approximation is motivated by vacuum neutrino oscillations over Galactic baselines, which strongly reduce flavor hierarchies present at production, even though the exact flavor composition at Earth depends on the initial annihilation channel [36]. The galactic DM halo was modeled as spherically symmetric, and the astrophysical dependence of the expected neutrino flux was summarized in the dimensionless $\mathcal{J}$-factor $J_{\mathrm{avg}} = 3$ for a full-sky (FS) observation. This canonical value represents the average between a cuspy generalised Navarro-Frenk-White (gNFW) profile and a cored Einasto profile [51], using current values for the distance to the Galactic Center (GC) $R_0 = 8.277\,\mathrm{kpc}$ [52], and the local DM density $\rho_0 = 0.4\,\mathrm{GeV/cm^3}$ [51, 54]. This convention allows the FS exclusion limits to be directly rescaled to other astrophysical parametrizations. Direction-dependent analyses, however, additionally depend on the angular distribution of the assumed DM density model.

In previous DM analyses for JUNO, only the mass range up to $m_\chi = 100\,\mathrm{MeV}$ was studied, considering exclusively the dominant inverse beta decay (IBD) [7, 8]. The prompt visible signal spectra were derived from the IBD kinematics and modeled considering pure positron energy deposition [7]. In this work, however, the visible spectra for DM masses spanning the full range from $m_\chi = 15\,\mathrm{MeV}$ to $m_\chi = 10\,\mathrm{GeV}$ were generated using extensive MC simulations (GENIE combined with the full JUNO detector simulation [76, 75]), which take into account all charged current (CC) and neutral current (NC) interactions, final state interactions, and subsequent de-excitations of residual daughter nuclei [78]. The spectra were subsequently folded with an energy-dependent effective energy resolution in order to account for electronic and reconstruction effects not included in the simulation. In the MeV regime, the MC-based spectra refine the previous parametric IBD models [7], while in the sub-GeV regime, characteristic peak structures in the CC signal were identified, which provides a distinctive spectral signature for monoenergetic neutrino sources in JUNO.

In addition to the signal spectra, all relevant background contributions were modeled within the same simulation framework. The Diffuse Supernova Neutrino Background (DSNB), which constitutes a dominant but still hypothetical background in the MeV regime, was included by treating different astrophysical DSNB models separately to

account for the large theoretical uncertainties. Atmospheric neutrinos, which represent the central background source across the entire energy range, were propagated to the JUNO site assuming three-flavor oscillations including matter effects in the Earth. This work therefore covers the entire mass range from the MeV to the GeV regime in a consistent detector and analysis framework, modeling signals and relevant backgrounds in a unified simulation chain.

A central element of this work is an energy-dependent optimization of the signal-to-background (S2B) ratio through suitable selection strategies, based on the respective dominant interaction mechanisms in the three mass ranges. In the MeV regime $m_\chi \in [15, 300]\,\mathrm{MeV}$, the dominant IBD channel was chosen as the primary signal channel and extended from 100 MeV to 300 MeV compared to previous analyses [7, 8]. A prerequisite for the background suppression methods developed in this regime is a reliable vertex reconstruction. Since classical point-source methods are not optimized for visible energies above $\sim 12\,\mathrm{MeV}$, a new ML-based vertex reconstruction was developed in this work. The optimized Multi-Layer Perceptron (MLP) infers the energy-weighted vertex from waveform features of the 17,612 large PMTs and achieves a stable mean vertex resolution of $\sim 18\,\mathrm{cm}$ across the full energy range and detector volume.

Based on this vertex reconstruction, two complementary background suppression techniques were applied. Topology-based selection cuts exploit the spatial and temporal prompt-delayed coincidence of the IBD interaction, retaining $\sim 93\,\%$ of genuine IBD events while allowing only $\sim 22\,\%$ of other CC events and $\sim 13\,\%$ of NC events to pass. A subsequent pulse shape discrimination (PSD) method exploits differences in the scintillation time profiles between electromagnetic and hadronic energy depositions. While previous analyses used exclusively the classical tail-to-total ratio (TTR) criterion, this work presents for the first time an ML-based classifier that processes the full pulse shape within the first 700 ns, reducing the NC survival rate from $\sim 5\,\%$ (TTR) to $\sim 1.5\,\%$ and the CC survival rate from $\sim 24\,\%$ to $\sim 12\,\%$. The combination of topology selection and ML-based PSD reduces the total background from approximately 2900 to 118 events, corresponding to a suppression by more than one order of magnitude.

In the sub-GeV regime $m_\chi \in [0.1, 1]\,\mathrm{GeV}$, QES CC and NC interactions on carbon dominate. The spectral structure of DM-induced signals is shaped by an $\nu_e/\bar{\nu}_e$-driven peak structure in the transition region up to $\sim 200\,\mathrm{MeV}$ and a characteristic CC1p0n double-peak structure from ν_e and ν_μ for larger masses. To enhance these features, a flavor-based $\nu_e/\bar{\nu}_e$-like event selection and a topology-based zero-neutron selection were investigated. While both methods reduce the global S2B ratio due to the loss of event statistics, a flavor-based selection locally sharpen the characteristic spectral features, which can be exploited in a spectral Bayesian analysis.

In the GeV range $m_\chi \in [1, 10]\,\mathrm{GeV}$, the spectral features from QES interactions disappear as RES and DIS processes become dominant, but a direction-based selection strategy becomes feasible. A mass-dependent optimization of the S2B ratio motivates an optimal half-opening angle of $\psi_{\mathrm{cone}} \approx 20^\circ$ for the cuspy gNFW profile, reducing the background to $\sim 3\,\%$ while retaining $40 - 50\,\%$ of the signal, and $\psi_{\mathrm{cone}} \approx 50^\circ$ for the cored Einasto profile with a more moderate background reduction of $\sim 18\,\%$.

The exclusion sensitivity of JUNO was determined within a unified Bayesian framework based on a Poisson likelihood of binned energy spectra. Systematic uncertainties on the background normalizations are accounted for through log-normally distributed nuisance parameters and a spectral tilt of the atmospheric contributions, where the prior widths are varied across three scenarios (*baseline*, *loose*, *tight*). The prior distribution of the signal is chosen to be flat, since no experimental information on the actual signal strength is

available. The upper 90 % credibility limit S_{90} is derived from the marginalized posterior distribution of the signal strength, obtained via a Markov Chain Monte Carlo (MCMC) method (`emcee`), and is subsequently translated into an upper bound on the thermally averaged self-annihilation cross section $\langle\sigma_{\mathrm{A}}v\rangle_{90\,\%}$. The robustness of the results with respect to systematic variations between different prior scenarios, binning strategies and selection methods was analyzed with Asimov-like datasets, while the impact of statistical fluctuations in real data was quantified by selected toy-MC studies with 500 pseudo-experiments for each representative DM mass.

11.1 Summary of JUNO's Potential for Indirect DM Search

The results for s-wave annihilation show that JUNO can improve the existing upper limits from Super-K by approximately one order of magnitude in the mass range $m_\chi = 15\,\mathrm{MeV}$ to $m_\chi \approx 1\,\mathrm{GeV}$ after 10 yr of data taking and a fiducial volume of 14.77 kton. In the MeV range, the combination of topological IBD selection and ML-based PSD provides the best sensitivity, with the hypothetical DSNB background representing the dominant irreducible contribution for $m_\chi \lesssim 70\,\mathrm{MeV}$. In the sub-GeV range, the flavor-based $\nu_e/\bar{\nu}_e$ selection achieves the highest sensitivity for $m_\chi \lesssim 0.6\,\mathrm{GeV}$, while for larger masses the total CC and NC spectrum with no selection yields comparable results. The exclusion limits without selection are independent of the particle identification (PID) method, which in this work serves only as a rough estimate of the potential and was not optimized for the sub-GeV range. The optimal transition region between the IBD- and the CC-based analysis was identified at $m_\chi \approx 150$–$200\,\mathrm{MeV}$ if a flavor-based selection is applied and at $m_\chi \approx 200$–$250\,\mathrm{MeV}$ if all CC events are considered. In the GeV range, JUNO can complement the existing Super-K limits through a directional analysis, but cannot significantly surpass them due to the limited angular resolution.

The robustness of the exclusion limits for different prior widths yields deviations of less than 5 % for Asimov-like datasets in the whole energy regime, confirming that the posterior distributions are primarily constrained by spectral information rather than by prior assumptions. The toy-MC studies quantify the expected statistical spread of the exclusion limits with a mean relative uncertainty of $+41\,\%/-30\,\%$ at the 68 % Confidence Level (C.L.) and $+95\,\%/-47\,\%$ at the 95 % Confidence Level (C.L.), which is significantly larger than the impact of systematic prior variations due to the low event statistics. Even within the 95 % C.L. interval, however, the existing Super-K exclusion limits are clearly surpassed in the MeV and sub-GeV range after 10 yr of data taking, indicating that JUNO can set new best exclusion limits well before this reference period.

For 1 yr of data taking, the upper bounds scale by a factor of $\sqrt{10} \approx 3.16$ relative to the 10 yr analysis. Already after one year, JUNO clearly surpasses the existing Super-K limits in the sub-GeV range, while in the MeV range the current Super-K bounds can be confirmed and partially improved. Complementary to the Bayesian exclusion analysis, the discovery potential after 1 yr was determined using a frequentist likelihood-ratio test in the Asimov approximation, assuming a true DM signal at the current Super-K upper limits [62, 36]. In the sub-GeV range for $m_\chi \gtrsim 0.2\,\mathrm{GeV}$, JUNO reaches a discovery significance of $Z \geq 5\sigma$, while in the MeV range for $m_\chi \gtrsim 50\,\mathrm{MeV}$ evidence at the $Z \geq 3\sigma$ level can be achieved. Since JUNO has been taking data since August 26, 2025 [6], a first DM search in the sub-GeV range is realistic within the next year.

In addition to the s-wave scenario, the exclusion limits were also determined for a p-wave dominated annihilation scenario. Since the p-wave $\mathcal{J}^{(p)}$-factor is suppressed by a factor of $\sim 10^{-6}$ relative to the s-wave factor, the upper bounds on the annihilation parameter b_P

shift accordingly. Despite the significant improvement compared to current upper limits from Super-K, the achievable limits of $b_P \sim 10^{-19}$–$10^{-18}\,\mathrm{cm}^3/\mathrm{s}$ remain approximately seven orders of magnitude above the value expected from the thermal relic abundance.

11.2 Possible Improvements and Outlook

The sensitivity study presented in this work can be further developed in several areas. In the following, the most promising approaches for improvement are summarized.
In the MeV range, the ML-based PSD could be further developed through an extension of the time window to $2\,\mu$s (after carefully studying the impact of after pulses), the inclusion of PMT-wise waveform features, and more powerful architectures such as graph-based networks or transformers. Preliminary studies of directional reconstruction for IBD events indicate a mean angular resolution of $\sim 50^\circ$ for $E_{\mathrm{vis}} \in [100, 300]\,\mathrm{MeV}$, which is insufficient for an effective cone-based selection but could serve as an additional observable in a multivariate analysis.
In the sub-GeV range, the PID-based flavor selection offers considerable optimization potential, since neither `PointNet++` nor the MLP classifier were optimized for this energy range. A dedicated PID strategy, combined with topological constraints on the remaining $\nu_e/\bar{\nu}_e$-selected events, could further enhance the spectral structures and simultaneously reduce the background. In the GeV range, the directional analysis was performed with two fixed cone angles. A fully angle-dependent analysis exploiting the complete angular distribution of events [63], or a mass-specifically optimized cone angle $\psi_{\mathrm{cone}}(m_\chi)$, could further improve the sensitivity.
Beyond the individual energy regimes, the sequential application of hard selection cuts followed by a spectral Bayesian analysis could be replaced by a joint likelihood fit over multiple observables, such as E_{vis}, PSD score, neutron multiplicity, and reconstructed direction. Such an approach would preserve information that is lost through hard cuts and could exploit correlations between the observables. Furthermore, the results in this work were obtained for a fiducial volume of $R_{\mathrm{fid}} \leq 16\,\mathrm{m}$ (14.77 kton). An extension to the full detector volume of $R_{\mathrm{fid}} \leq 17.7\,\mathrm{m}$ (20 kton) would increase the event statistics and thereby improve the exclusion sensitivity in the background-limited scenario by approximately 14 %, but requires a careful treatment of edge effects.
All results in this work are based entirely on MC simulations. For future simulation-based analyses, a comparison of different neutrino generators would be desirable to quantify the modeling uncertainties, in particular for the NC background production in the MeV range [161]. Since JUNO has been taking data since August 2025 [6], real pulse shapes can be used to validate and refine the PSD methods, and the measured energy spectra can be compared to MC predictions, enabling a data-driven tuning of the generator models and detector response. The selection strategies and the Bayesian analysis framework developed in this work can be directly applied to the first measurement data, making a first indirect DM search in the sub-GeV range realistic within the next year.
Should JUNO detect or significantly constrain the DSNB, the currently dominant irreducible background in the MeV range would be directly measured rather than modeled, substantially reducing the uncertainty of the DM sensitivity for $m_\chi \lesssim 70\,\mathrm{MeV}$.
Beyond the $\chi\chi \to \nu\bar{\nu}$ channel considered in this work, other annihilation channels such as $\chi\chi \to \tau^+\tau^-$ or $\chi\chi \to b\bar{b}$, which produce continuous neutrino spectra, could be investigated within the same analysis framework [165]. Likewise, extragalactic DM contributions could be analyzed as additional signal sources in JUNO [36]. On a longer timescale, Hyper-Kamiokande (Hyper-K) with a fiducial volume of $\sim 187\,\mathrm{kton}$ and

excellent directional reconstruction could significantly improve the existing Super-K limits, particularly in the GeV range [65]. JUNO remains complementary especially in the MeV range due to the excellent energy resolution and strong PSD possibilities. The model-independent flux limits on monoenergetic neutrinos determined in this work represent a general result that is applicable beyond the DM interpretation to any source of monoenergetic neutrino signals.

A | $\mathcal{J}$-Factor Calculations

A.1 Numerical Integration with Gauss–Legendre Quadrature

Since the integrand in Eq. 3.9 exhibits strong gradients close to the GC due to the DM density distribution, a suitable method for numerical integration must be employed. To this end, a logarithmically spaced grid was used for the integration over the viewing angle ψ, and a Gauss–Legendre quadrature was applied on two suitably chosen sub-intervals for the integration along the LOS coordinate s. The Gauss–Legendre quadrature provides an exact approximation of the integral $\int_{-1}^{1} f(x)\,dx$ for polynomial functions $f(x)$ by the weighted sum $\sum_{i=1}^{N} w_i f(x_i)$ up to degree $2N-1$. The nodes x_i are defined as the eigenvalues of the Legendre polynomial on the interval $[-1,1]$, while the corresponding weights w_i can be expressed in terms of the derivatives of the Legendre polynomial at the nodes, which sum to 2 for $f(x)=1$. For the LOS integration of the $\mathcal{J}$-factor in Eq. 3.9, the Gauss–Legendre quadrature was extended to an arbitrary interval $L=[a,b]$ according to

$$\int_a^b f(s)\ \mathrm{d}s \approx \sum_{i=1}^{N} f\left(s_i\right)\ \mathrm{d}s_i$$

by means of a suitable change of variables [166]

$$s_i([a,b]) = \frac{b-a}{2} x_i + \frac{a+b}{2} \quad \text{with the weights} \quad \mathrm{d}s_i([a,b]) = \tfrac{b-a}{2} w_i\ . \tag{A.1}$$

The integration along the LOS coordinate s was split into two suitable sub-intervals. The first sub-interval $L_1=[0, s_0(\psi)]$ accounts for the integration from the observer on Earth ($s=0$) up to the pericenter

$$s_0(\psi) = \begin{cases} R_0 \cos\psi & \text{for} \quad \psi < \pi/2\ , \\ 0 & \text{else}\ , \end{cases}$$

which denotes the smallest distance to the GC for a given angle ψ, and thus yields the steepest gradient in the density profile $\rho\big(r(s_0(\psi),\psi)\big)$ along the angle ψ[1]. The second sub-interval $L_2=[s_0(\psi), s_m(\psi)]$ starts at the pericenter and ends at the edge of the Galactic halo $s_m(\psi)$ (cf. Eq. 3.10). With these sub-intervals, the integrand in Eq. 3.9

[1] For angles $\psi \geq \pi/2$, the observer's position on Earth at $s=0$ is the nearest point to the GC.

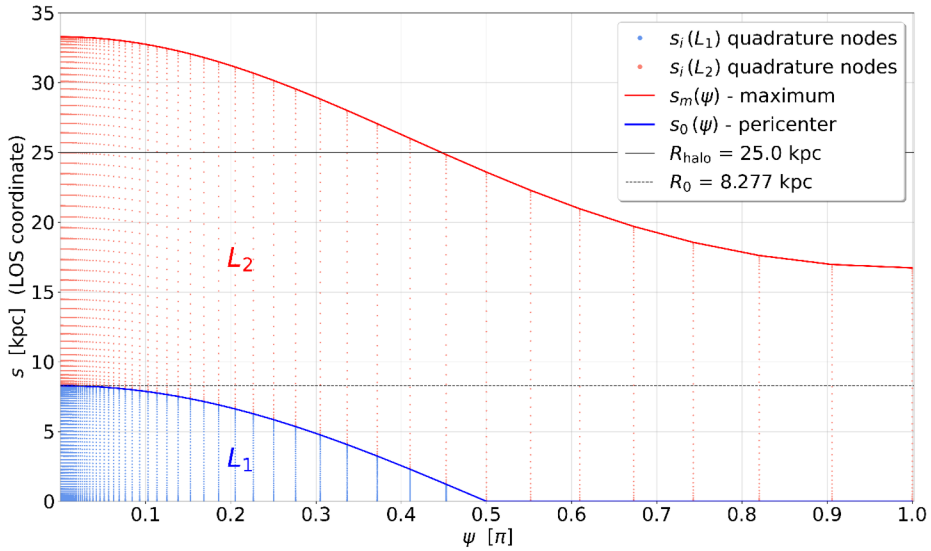

Figure A.1: Quadrature nodes in the s-ψ plane used for the LOS integration for the $\mathcal{J}$-factor calculation in Eq. 3.9. The points mark the Gauss–Legendre nodes of the LOS coordinate s on the sub-intervals $s_i(L_1) \in [0, s_0(\psi)]$ up to the pericenter (blue), as well as $s_i(L_2) \in [s_0(\psi), s_m(\psi)]$ up to the maximal integration limit (red). Logarithmically distributed values were used for the viewing angle ψ to account for the large gradients of the density profile near the GC ($\psi \approx 0$). The parameters used in this figure are listed in Tab. A.1. The dashed black line marks the solar distance $R_0 = 8.277\,\mathrm{kpc}$ to the GC.

along the LOS coordinate s for a chosen angle ψ_j can be calculated according to

$$I_j = \int_0^{s_m(\psi_j)} \rho^2\big(r(s,\psi_j)\big)\,\mathrm{d}s \approx \sum_{i=1}^{N} \rho^2\big(r(s_i(L_1),\psi_j)\big)\,\mathrm{d}s_i(L_1) + \sum_{i=1}^{N} \rho^2\big(r(s_i(L_2),\psi_j)\big)\,\mathrm{d}s_i(L_2) \tag{A.2}$$

where the nodes $s_i(L_{1,2})$ and weights $\mathrm{d}s_i(L_{1,2})$ of the Gauss–Legendre quadrature were calculated for $L_{1,2}$ according to Eq. A.1. The convergence criterion for the number of nodes N was defined such that the relative change of $\mathcal{J}_{\psi_m}$, averaged over ψ_m, remains below 10^{-3} when N is doubled. In Fig. A.1, the Gauss–Legendre quadrature nodes are shown as points in the s-ψ plane for $n_\psi = 100$ logarithmically spaced values of $\psi_j \in [\psi_{\min}, \pi]$. On both sub-intervals L_1 (blue) and L_2 (red), the node density is particularly high near the interval boundaries. This leads, in particular, near the pericenter $s_0(\psi)$ (blue line), to a fine sampling of the integral. In addition, due to the logarithmically spaced values of ψ_j, the node density increases towards the GC ($\psi \to 0$). Together with the Gauss–Legendre quadrature, this ensures that large gradients in the density profile are captured more accurately and that numerical oscillations are reduced.

In Fig. A.2, the nodes $s_i(L)$ and weights $\mathrm{d}s_i(L)$ in Eq. A.2 are shown for the two sub-intervals L_1 and L_2. Since $s_0(\psi) = 0$ for angles $\psi \geq \pi/2$, only angles up to $\pi/2$ are represented for the sub-interval L_1 (left panel), whereas all angles are included for the sub-interval L_2 (right panel). For better visualization, reduced quadrature parameters

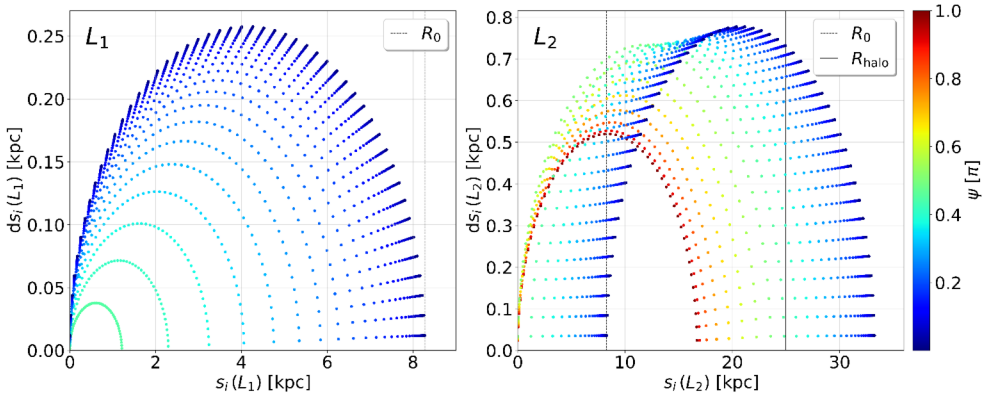

Figure A.2: Distribution of the Gauss–Legendre quadrature nodes $s_i(L)$ and weights $\mathrm{d}s_i(L)$ for both sub-intervals L_1 and L_2. As visualized in Fig. A.1 for L_1 (left panel) only angles $\psi < \pi/2$ are represented, whereas in L_2 (right panel), all angles are considered. For comparison the Halo radius R_{halo} and the distance R_0 between Sun and GC are also included in the plots.

were used in Figures A.1 and A.2 compared to the final computations. The relevant parameters are listed in Tab. A.1.

Table A.1: Summary of the quadrature and integration parameters used for the LOS integration in Eq. 3.9. The third column lists the reduced values chosen for the figures in this section for better visualization. The fourth column lists the parameters actually used for the integration. N denotes the number of Gauss–Legendre quadrature nodes per sub-interval in Eq. A.2, while n_ψ indicates the number of logarithmically spaced values of the viewing angle ψ in the interval $[\psi_{\mathrm{min}}, \pi]$. The $\mathcal{J}$-factor converges for a halo radius $R_{\mathrm{halo}} > 20\,\mathrm{kpc}$ (cf. Fig. A.4) and was chosen smaller for the figures for better visualization.

parameter	symbol	values for figures	values for calculations
number of nodes	N	50	511
number of viewing angles	n_ψ	10^2	10^4
minimum angle [deg]	ψ_{min}	10^{-2}	10^{-6}
halo radius [kpc]	R_{halo}	25	100

A.2 p-Wave Annihilation

In the case of s-wave annihilation, according to Eq. A.2 only the squared DM density profile $\rho^2\big(r(s(L_{1,2}), \psi_j)\big)$ is integrated. When considering the velocity-dependent p-wave annihilation, however, the mean squared relative velocities $\big\langle v^2\big(r(s_i(L_{1,2}), \psi_j)\big)\big\rangle$ of the DM particles must also be taken into account in both sub-intervals $L_{1,2}$ (cf. Eq. 3.14). To do this, the one-dimensional Jeans equation in 3.16 was numerically integrated backward using the trapezoidal rule on a logarithmically spaced radial grid $r \in [1\,\mathrm{pc}, R_{\mathrm{halo}}]$ with 10,000 points, with the boundary condition $v_0^2(R_{\mathrm{halo}}) \to 0$ applied. Since the LOS quadrature requires the values of $\langle v^2(r)\rangle$ at the nodes of both sub-intervals L_1

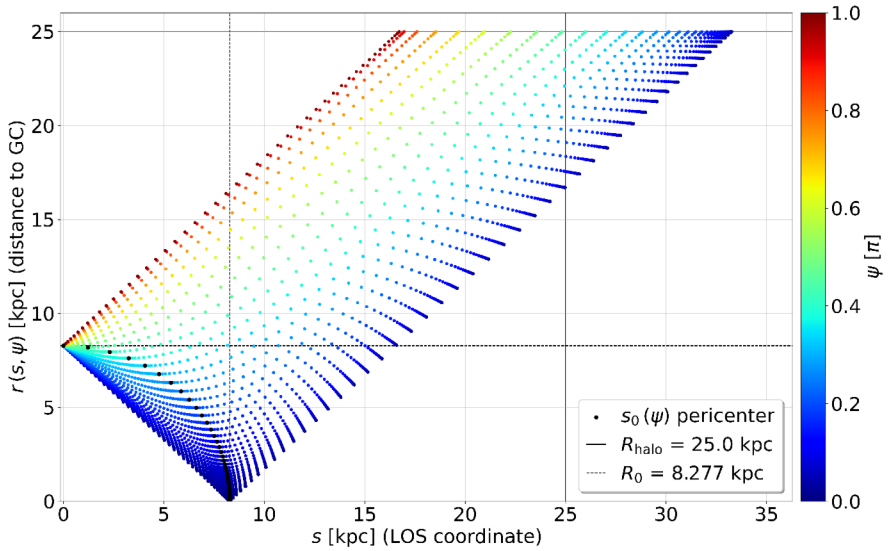

Figure A.3: Two-dimensional nodes of the radial distance $r(s_i(L_{1,2}), \psi_j)$ from the GC. Along each logarithmically spaced sight angle ψ_j the quadrature nodes from the LOS coordinate s are illustrated in both sub-intervals $L_{1,2}$. The first sub-interval L_1 is indicated by the points from $s = 0$ to the black points, denoting the pericenter $s_0(\psi_j)$ for a chosen angle ψ_j. The second interval L_2 contains all nodes for $s \geq s_0(\psi_j)$ up to the end of the Galactic halo $r = R_{\text{halo}}$. As a reference, the distance R_0 between the Sun and the GC was included in the plot.

and L_2, the one-dimensional solution $v_0^2(r)$ was interpolated onto the two-dimensional nodes $r(s_i(L_{1,2}), \psi_j)$, which are illustrated in Fig. A.3. The nodes from $s = 0$ up to the black points at the pericenter $s_0(\psi)$ correspond to sub-interval L_1, and the points for $s \geq s_0(\psi)$ up to the edge of the Galactic halo $r = R_{\text{halo}}$ correspond to sub-interval L_2.

In summary, for the calculation of the $\mathcal{J}$-factor in Eq. 3.9 (for s-waves) and 3.14 (for p-waves), the squared DM density $\rho^2(r)$ and, in the p-wave case, also the mean squared relative DM velocity $\langle v^2(r) \rangle$ are evaluated at all quadrature nodes $r(s_i(L_{1,2}), \psi_j)$ as well as over all angles $\psi_j \leq \psi_m$ (cf. Fig. A.3), and are subsequently summed, taking into account the weights $\mathrm{d}s_i(L_{1,2})$ shown in Fig. A.2.

A.3 J-Factor Analysis

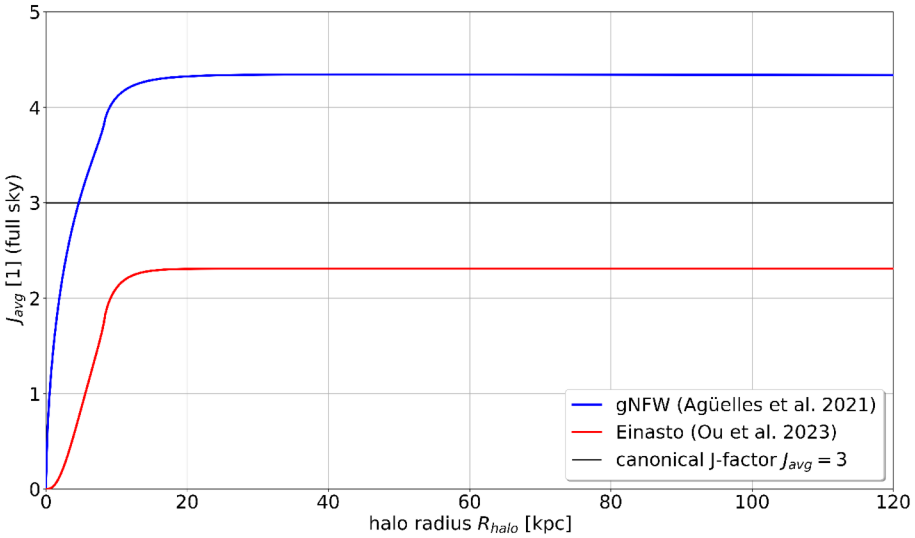

Figure A.4: FS dimensionless J_{avg} as a function of the halo radius R_{halo} for the gNFW profile and the Einasto profile (cf. Fig. 3.2). Both curves converge at $R_{\text{halo}} \approx 20\,\text{kpc}$ to $J_{\text{avg}} \approx 4.3$ for the gNFW profile and to $J_{\text{avg}} \approx 2.4$ for the Einasto profile. The chosen canonical reference value $J_{\text{avg}} = 3$ is indicated by the horizontal black line.

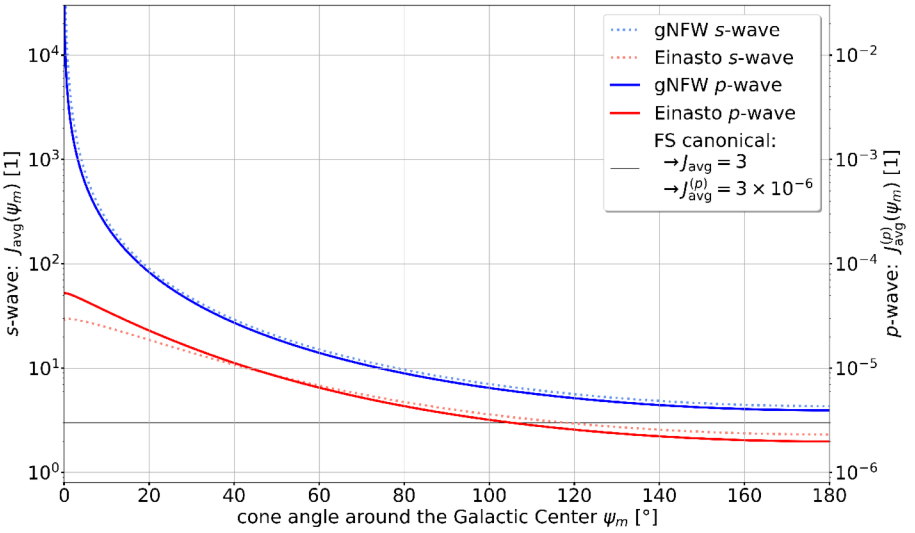

Figure A.5: The dimensionless J_{avg} for s-wave annihilation (left axis) and $J^{(p)}_{\text{avg}}$ for p-wave (right axis) as a function of the half-opening angle ψ_m around the GC (cf. Eq. 3.11). The FS flux in a gNFW scenario is approximately twice as large as in an Einasto scenario. For p-waves the flux is reduced by a factor $\sim 10^{-6}$ due to the small average velocity of the DM particles in the Milky Way of $\sim 10^{-3}\ c$. The chosen canonical reference value $J_{\text{avg}} = 3$ (s-wave) and $J^{(p)}_{\text{avg}} = 3 \times 10^{-6}$ (p-wave) is indicated by the horizontal black line.

B | Additional Figures

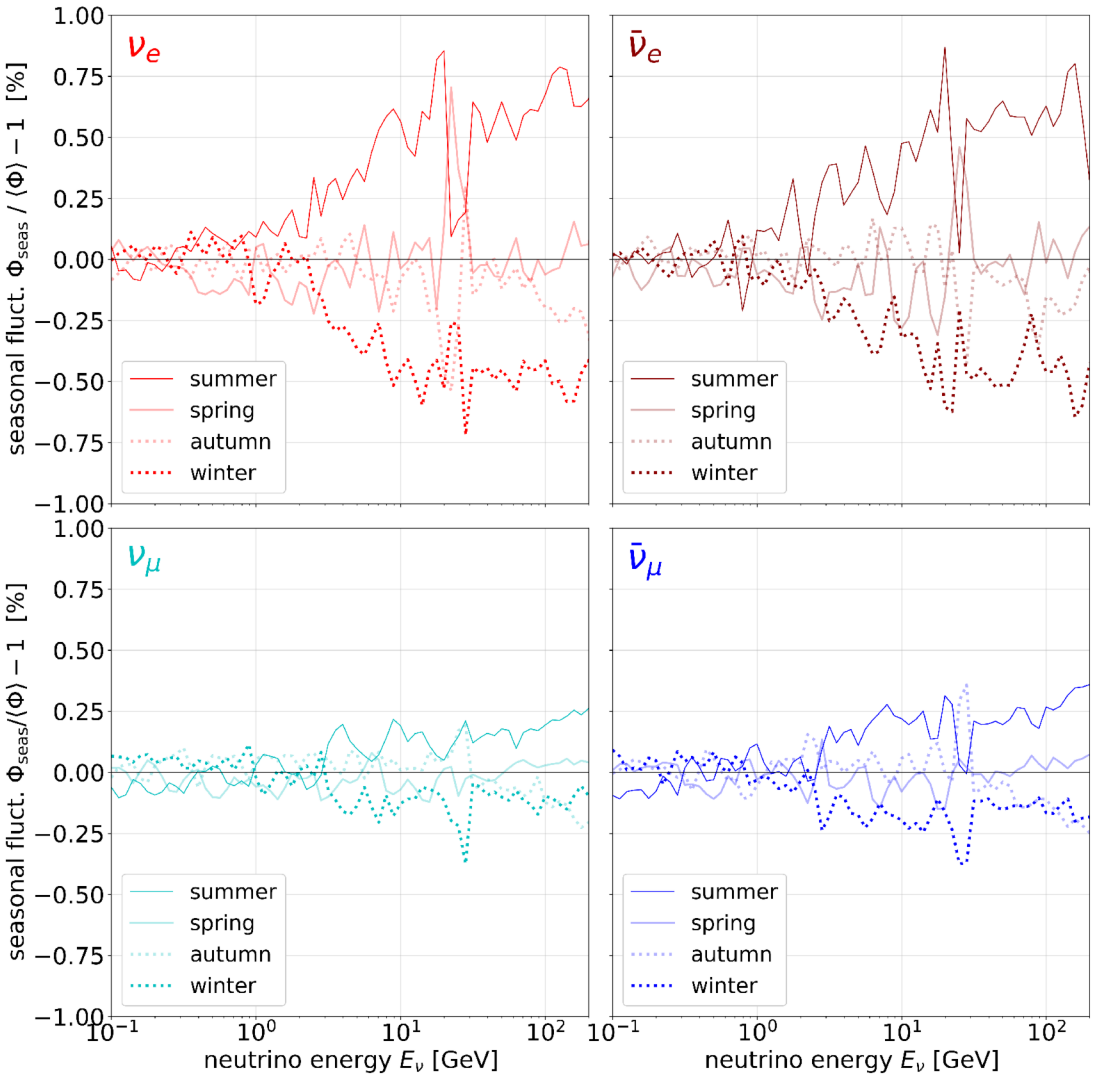

Figure B.1: Seasonal variations of the expected atmospheric neutrino flux in Kamioka [136]. The percentage deviations between the averaged neutrino flux $\langle\Phi\rangle$ and the four seasonal fluxes Φ_{seas} are illustrated for ν_e, $\bar{\nu}_e$, ν_μ and $\bar{\nu}_\mu$.

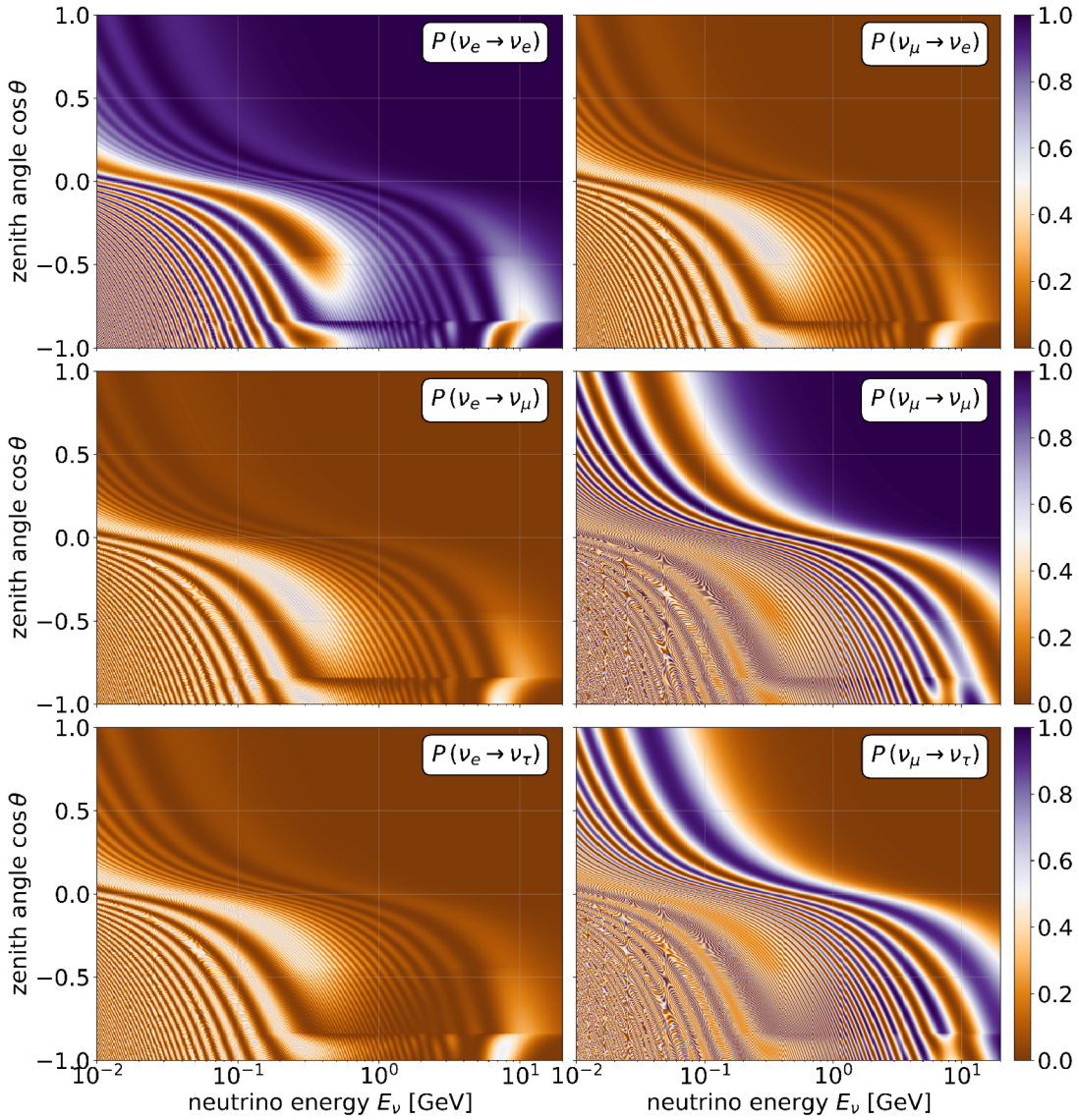

Figure B.2: Oscillation probabilities for atmospheric neutrinos at a mean production height of 18 km (NO scenario), including matter effects in the Earth. The transition probabilities $P(\nu_e \to \nu_\alpha)$ for ν_e (left column) and $P(\nu_\mu \to \nu_\alpha)$ for ν_μ (right column) are shown as a function of the neutrino energy E_ν and the zenith angle $\cos\theta$. The upper region ($\cos\theta > 0$) corresponds to downward-going neutrinos with nearly vacuum oscillations, while the lower region ($\cos\theta < 0$) describes upward-going neutrinos that traverse the three layers of the earth according to Preliminary Reference Earth Model (PREM) and exhibit strong matter resonances (cf. Sec. 7.4.2). The color coding indicates the respective transition probability in the range $0 \leq P \leq 1$.

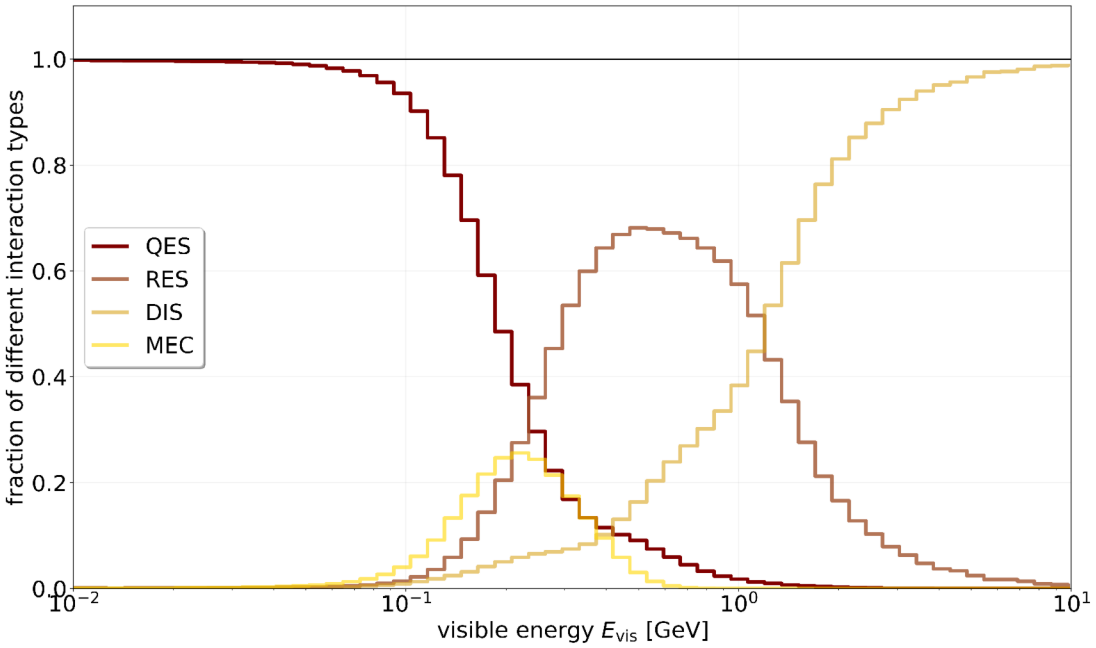

Figure B.3: Fraction of NC interaction types (QES, RES, DIS and MEC) as a function of visible energy E_{vis}. At low energies, QES scattering dominates, while DIS becomes the dominant contribution above $\sim 2\,\text{GeV}$. The peaks of MEC and RES reflect the typical energy transfer of the Valencia model's 2p2h calculation and $\Delta(1232)$ resonance production, respectively [143, 144].

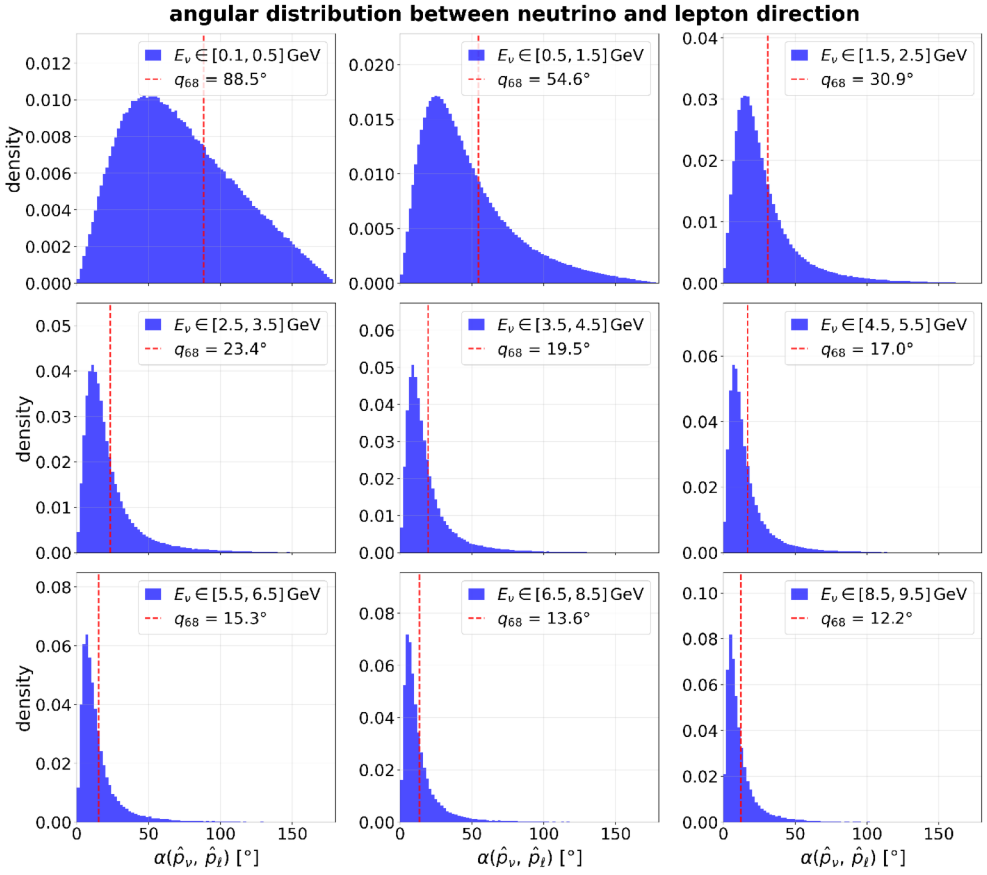

Figure B.4: Distribution of the angle $\alpha(\hat{p}_\nu, \hat{p}_\ell)$ between initial neutrino and lepton direction in CC event for different visible energies E_{vis}. Each panel shows the α distribution (blue histogram) together with the mean $\bar{\alpha}$. The MC results of the CC dataset from $D2$ in Tab. C.1 are used.

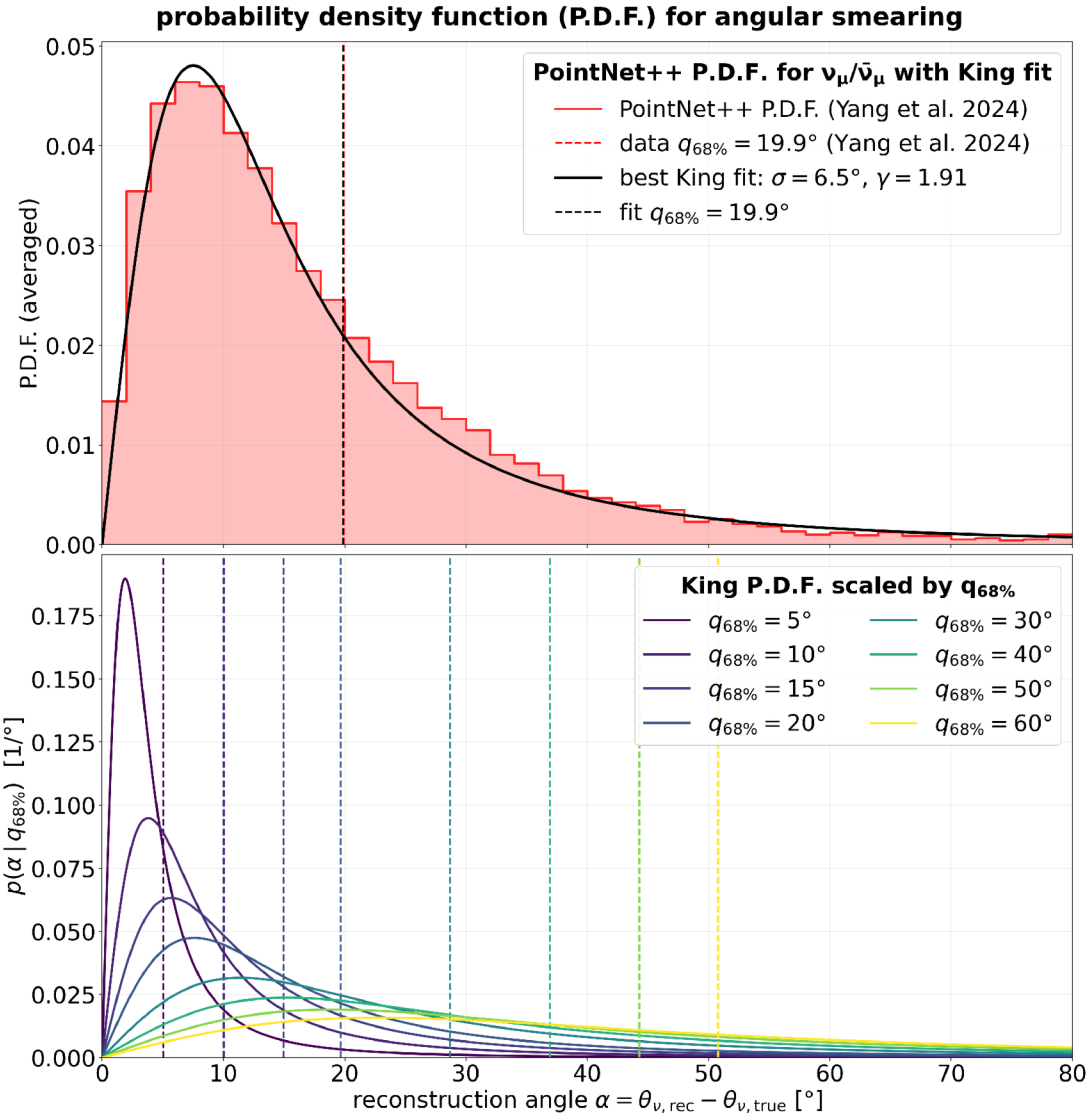

Figure B.5: Parameterization of the angular resolution using a King PSF according to Eq. 9.2. Upper panel: The angular distribution α between true and reconstructed neutrino direction, averaged over all neutrino energies from 1–20 GeV, for $\nu_\mu/\bar{\nu}_\mu$ events from the `PointNet++` model [79] (red histogram) together with the best King fit (black curve). The dashed vertical lines mark the respective 68 % quantiles $q_{68\%}$ of the data and the fit. Lower panel: Scaling of the King P.D.F. at fixed shape parameter $\gamma = 1.91$ for different values of $q_{68\%}$, corresponding to the energy- and flavor-dependent angular resolutions in Fig. 9.6. The dashed vertical lines indicate the respective $q_{68\%}$ values.

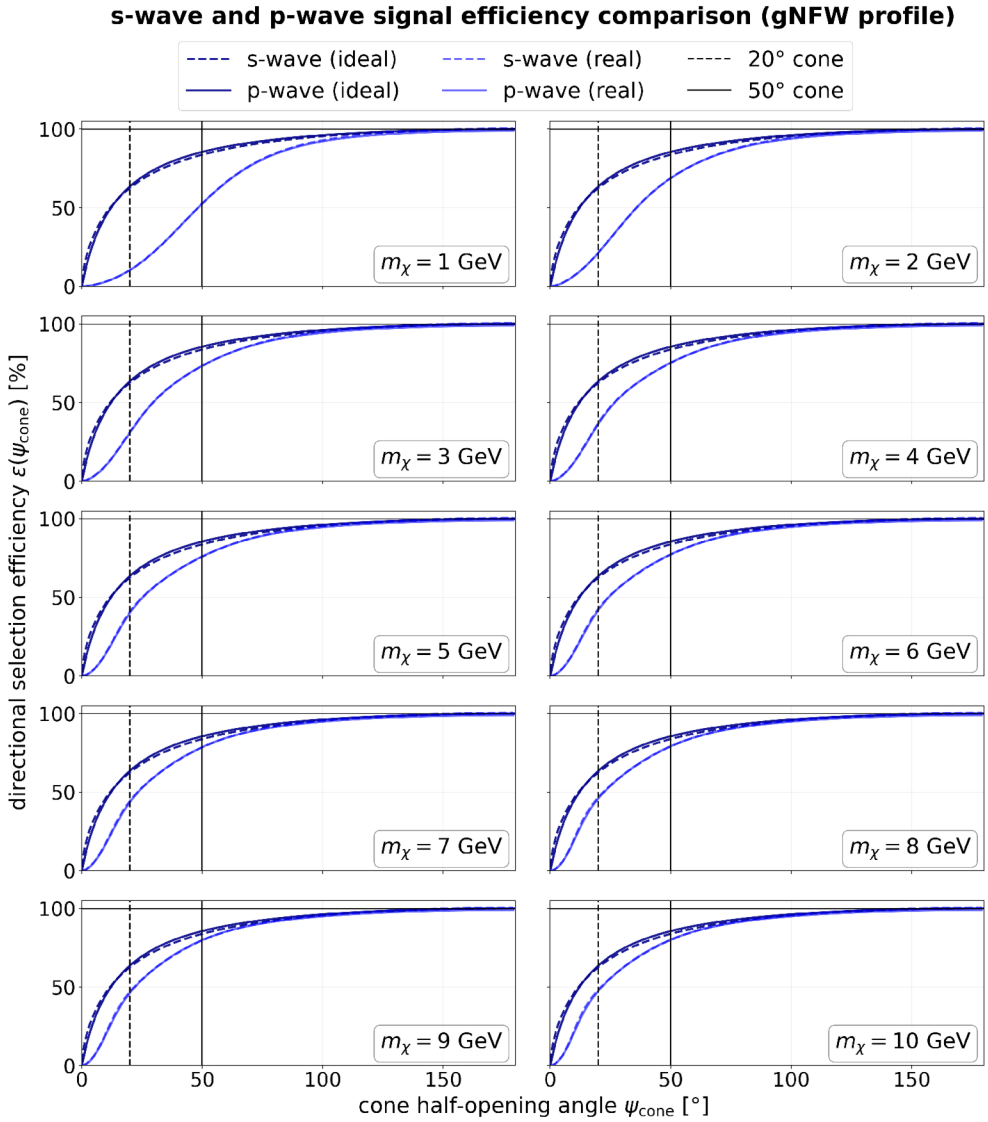

Figure B.6: Ideal (dark blue) and realistic (light blue) directional selection efficiencies assuming the cuspy generalised Navarro-Frenk-White (gNFW) DM density distribution as a function of the cone half-opening angle ψ_{cone}. The signal efficiencies $\varepsilon_{S,(x)}(\psi_{\text{cone}}, m_\chi)$ for a s-wave ($x = s$, dashed curves) and p-wave ($x = p$, solid curves) dominated annihilation scenario according to Eq. 9.8 are shown separately. The black vertical lines indicate the half-opening angles $\psi_{\text{cone}} = 20°$ (dashed) and $\psi_{\text{cone}} = 50°$ (solid), which are chosen for the calculations of the exclusion limit in JUNO (cf. Sec. 10.4).

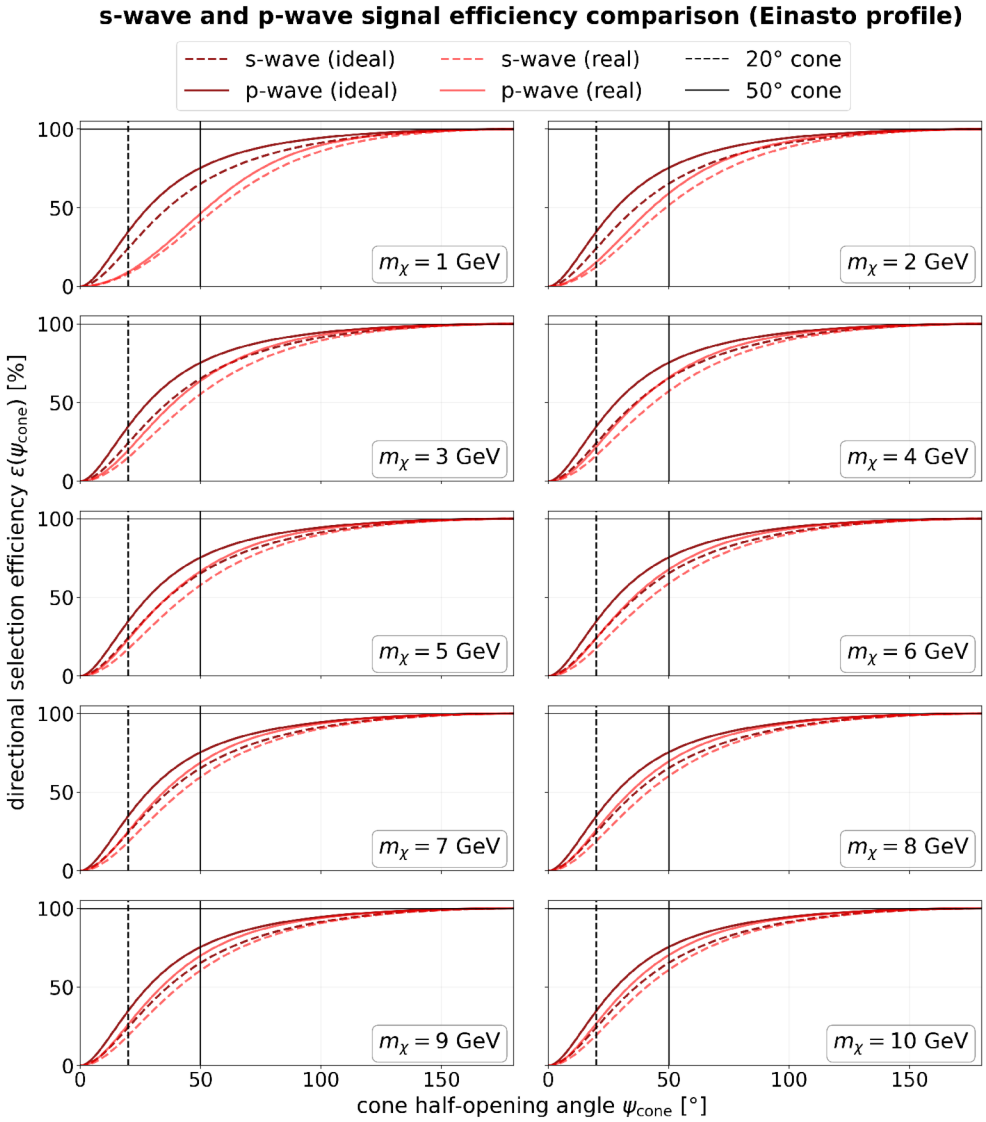

Figure B.7: Ideal (dark red) and realistic (light red) directional selection efficiencies assuming the cored Einasto DM density distribution as a function of the cone half-opening angle ψ_{cone}. The signal efficiencies for a s-wave (dashed curves) and p-wave (solid curves) dominated annihilation scenario are shown. The black vertical lines indicate the half-opening angles $\psi_{\text{cone}} = 20°$ (dashed) and $\psi_{\text{cone}} = 50°$ (solid), which are chosen for the calculations of the exclusion limit in JUNO (cf. Sec. 10.4).

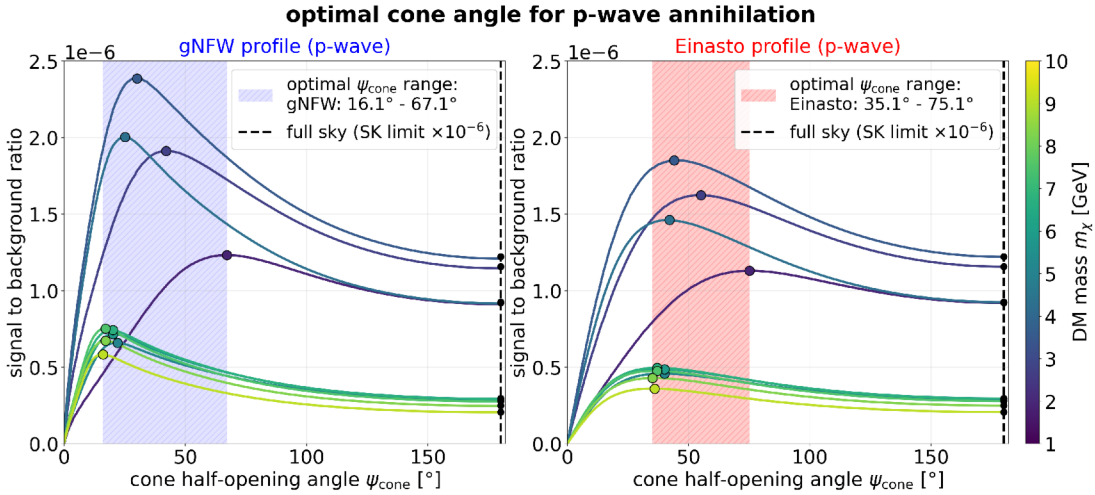

Figure B.8: S2B ratio for directional selection in a p-wave dominated annihilation as a function of the cone angle ψ_{cone} assuming the gNFW DM density distribution (left panel) and the Einasto profile (right panel). The colored shaded bands indicate the range of optimal half-opening angles, and the dashed vertical black lines marks a FS observation.

C | Author's Contribution, Data Production, and Tools

C.1 Author's Contribution

The Monte Carlo (MC) simulation infrastructure and parts of the simulation data were provided by the JUNO collaboration (cf. Sec. C.2). All analytical developments, optimizations, and results built on this foundation were developed independently:

- **Astrophysical modeling:** $\mathcal{J}$-factor calculations for different DM density profiles (gNFW, Einasto), solution of the Jeans equation to determine the velocity dispersion, rescaling for p-wave annihilation (cf. Chap. 3)
- **Atmospheric background model:** Full neutrino oscillation treatment (HAKKM14, FLUKA) including matter effects, combination into a consistent flux model over 10 MeV – 20 GeV (cf. Sec. 7.4)
- **ML methods:** Development, training, and optimization of novel ML approaches. A Multi-Layer Perceptron (MLP) for vertex reconstruction achieving $\sim$ 18 cm resolution (cf. Sec. 8.1). A ML-based PSD reducing NC background from 5 % to 1.5 % (cf. Sec. 8.3.3). Independent cross-check of flavor-based selection in the sub-GeV regime using an MLP classifier (cf. Sec. 9.1.1)
- **Selection strategies:** Energy-dependent optimization for all three energy regimes (MeV/sub-GeV/GeV) and systematic determination of all selection efficiencies (cf. Chaps. 8 and 9)
- **Bayesian analysis framework:** Full implementation of the statistical analysis with Poisson likelihood, MCMC marginalization, log-normal priors for systematic uncertainties, and robustness studies, toy-MC with 500 pseudo-experiments for selected DM masses quantifying statistical uncertainties (cf. Chap. 10)
- **Sensitivity results:** Determination of exclusion sensitivity for s- and p-wave annihilation, model-independent flux limits for monoenergetic neutrinos, discovery potential analyses (cf. Chap. 10)

C.2 Monte Carlo Datasets

Tab. C.1 lists self-created datasets of this work generated with the JUNO simulation framework, as well as simulation data provided by the collaboration. All data were produced with GENIE version 3.2.0 (`G18_10b_02_11b` model tuning) and the JUNO simulation version J24.1.2, which was presented in Sec. 4.4 [75].

Table C.1: Overview of the MC datasets used in this work. All simulations are generated isotropically in the detector volume using GENIE version 3.2.0 (`G18_10b_02_11b` model tuning) and the JUNO simulation framework J24.1.2 (cf. Sec. 4.4). Datasets and reconstruction results officially provided by the JUNO collaboration are indicated accordingly in the source column. All visible energy spectra were obtained by convolving the `DetSim` output of the quenched prompt deposited energy with the parametrized energy resolution from Eq. 5.12.

no.	MC simulated dataset	source	reference
$D1$	**flat IBD dataset:** $\sim$ 800,000 events, $E_\nu \in [10, 350]$ MeV, fiducial volume $r \leq 16$ m, `DetSim` level	**this work**	Sec. 5.2.1, Fig. 5.5
$D2$	**flat CC and NC dataset:** $>$ 7 million events (all flavors), $E_\nu \in [0.1, 20]$ GeV, full detector volume $r \leq 17.7$ m, `DetSim` level including delayed event information (n-capture, de-excitation, radioactive decay, muon decay/capture)	JUNO collaboration	Sec. 5.2.2, Fig. 5.6, Sec. 8.2.2, Sec. 9.1.2
$D3$	**DSNB IBD background spectra:** $\sim$ 50,000 IBD events, $E_\nu \in [10, 100]$ MeV, fiducial volume $r \leq 16$ m, `DetSim` level for all three DSNB flux models (min, mid, max)	**this work**	Sec. 7.3, Fig. 7.2
$D4$	**atmospheric CC/NC background spectra:** reweighting of the datasets from no. 2) with the oscillated flux spectra. Supplemented by self-produced simulation data in the range $E_\nu \in [10, 500]$ MeV (FLUKA flux, not covered by no. 2). Combination of both datasets in the overlap region	JUNO collaboration / **this work**	Sec. 7.4.3, Fig. 7.7, Fig. 7.8
$D5$	**DM-induced signal spectra:** $\geq$ 25,000 CC/NC events for each DM mass (38 masses in the range $m_\chi = 15$ MeV–10 GeV), fiducial volume $r \leq 16$ m, flavor composition 1:1:1	**this work**	Sec. 6.2, Figs. 6.2 - 6.6
$D6$	**flat ML training data (IBD vertex):** 240,000 IBD events, $E_\nu \in [10, 350]$ MeV, fiducial volume $r \leq 16$ m, full simulation (`DetSim` to `Reco`) including waveform features of large PMTs	**this work**	Sec. 8.1
$D7$	**topological cuts (IBD, zero-neutron):** $\sim$ 500,000 uniformly distributed IBD events, $E_\nu \in [10, 350]$ MeV, fiducial volume $r \leq 16$ m, `DetSim` level including delayed event information. CC/NC cut efficiencies evaluated using the datasets from no. 2), supplemented by self-produced data for $E_\nu \leq 100$ MeV	JUNO collaboration / **this work**	Sec. 8.2.1, Fig. 8.11, Sec. 9.1.2
$D8$	**pulse shape-based optimization (PSD/PID):** $\sim$ 20,000 for each channel: IBD in $E_\nu \in [10, 350]$ MeV, CC in $E_\nu \in [10, 600]$ MeV and NC in $E_\nu \in [10, 2000]$ MeV (uniformly distributed), fiducial volume $r \leq 16$ m, `DetSim` level including TOF corrections of all hit times for pulse shape calculations	**this work**	Sec. 8.3.1, Sec. 9.1.2

C.3 Use of Generative AI Tools

In the preparation of this thesis, generative AI tools (ChatGPT 5.4, Claude Opus 4.6, and GitHub Copilot) were used in two limited capacities:

1. As a research aid for background information retrieval, analogous to a search engine, all results were independently verified against primary sources.

2. As a programming assistant for parts of the analysis scripts, in particular for suggestions regarding syntax, debugging, and code structuring, all generated code was reviewed, adapted, and validated by the author.

No part of the scientific argumentation, interpretation, or written text of this thesis was generated by AI tools. The intellectual content and all conclusions are entirely the author's own work.

Acronyms

$0\nu\beta\beta$ neutrinoless double beta decay.

1p1h 1-particle 1-hole.

2p2h 2-particle 2-hole.

AUC Area Under the Curve.

BBN Big Bang Nucleosynthesis.

BCE Binary Cross Entropy.

BH Black Hole.

Bis-MSB 1,4-Bis (2-methylstyryl) benzene.

C.L. Confidence Level.

CC charged current.

CCSN Core Collapse Supernova.

CD central detector.

CDM Cold Dark Matter.

CEνNS Coherent Elastic Neutrino-Nucleus Scattering.

CMB Cosmic Microwave Background.

COH coherent.

CP charge parity.

DCR dark count rate.

DIS deeply inelastic scattering.

DM Dark Matter.

DSNB Diffuse Supernova Neutrino Background.

ES eleastic scattering.

FHT first hit time.

FN fast neutron.

FS full-sky.

FSI final state interaction.

FWHM full width at half maximum.

GC Galactic Center.

GENIE Generates Events for Neutrino Interaction Experiments.

gNFW generalised Navarro-Frenk-White.

GUT Grand Unified Theories.

HAKKM14 Honda–Athar–Kajita–Kasahara–Midorikawa.

HDM Hot Dark Matter.

Hyper-K Hyper-Kamiokande.

IBD inverse beta decay.

IO Inverted Ordering.

JUNO Jiangmen Underground Neutrino Observatory.

LAB linear alkyl benzene.

LHC Large Hadron Collider.

LOS line of sight.

LR learning rate.

LS liquid scintillator.

MACHO Massive Astrophysical Compact Halo Object.

MC Monte Carlo.

MCMC Markov Chain Monte Carlo.

MEC meson exchange currents.

ML machine learning.

MLP Multi-Layer Perceptron.

MOND Modified Newtonian Dynamics.

MSE Mean Squared Error.

MSW Mikheyev–Smirnov–Wolfenstein.

NC neutral current.

NFW Navarro-Frenk-White.

NMO neutrino mass ordering.

NN neural network.

NO Normal Ordering.

OMILREC Optical Maximum-likelihood Reconstruction.

OSIRIS Online Scintillator Internal Radioactivity Investigation System.

P.D.F. Probability Density Function.

PBH Primordial Black Hole.

PDE photon detection efficiency.

PE photoelectron.

PID particle identification.

PMNS Pontecorvo-Maki-Nakagawa-Sakata.

PMT photomultiplier tube.

pp proton-proton.

PPO 2,5-Diphenyloxazole.

PREM Preliminary Reference Earth Model.

PSD pulse shape discrimination.

PSF Point Spread Function.

QCD Quantum Chromodynamics.

QE quasieleastic.

QES quasieleastic scattering.

RES resonant scattering.

ROC Receiver Operating Characteristic.

ROI region of interest.

S2B signal-to-background.

SD spin-dependent.

SI spin-independent.

SM standard model.

SN supernova.

Super-K Super-Kamiokande.

TAO Taishan Antineutrino Observatory.

TOF time of flight.

TTR tail-to-total ratio.

TTS transit time spread.

WDM Warm Dark Matter.

WIMP Weakly Interacting Massive Particle.

Bibliography

[1] F. Zwicky. „Die Rotverschiebung von extragalaktischen Nebeln“. In: *Helvetica Physica Acta* 6 (Jan. 1933), pp. 110–127.

[2] Simon Knapen, Tongyan Lin and Kathryn M. Zurek. „Light dark matter: Models and constraints“. In: *Phys. Rev. D* 96 (11 Dec. 2017), p. 115021. DOI: 10.1103/PhysRevD.96.115021.

[3] Anna M. Suliga and George M. Fuller. „Searching for MeV-mass neutrinophilic dark matter with large scale dark matter detectors“. In: *Phys. Rev. D* 111 (6 Mar. 2025), p. 063052. DOI: 10.1103/PhysRevD.111.063052.

[4] JUNO Collaboration. „Neutrino physics with JUNO“. In: *Journal of Physics G: Nuclear and Particle Physics* 43.3 (Feb. 2016), p. 030401. ISSN: 1361-6471. DOI: 10.1088/0954-3899/43/3/030401.

[5] JUNO Collaboration. *JUNO Conceptual Design Report*. 2015. arXiv: 1508.07166 [physics.ins-det].

[6] JUNO Collaboration. *Initial performance results of the JUNO detector*. 2025. arXiv: 2511.14590 [hep-ex].

[7] David Blum. „Indirect Dark Matter Search with Neutrinos in JUNO and THEIA - A Sensitivity Study“. Dissertation. Tübingen: Eberhard Karls Universität Tübingen, 2022.

[8] JUNO collaboration. „JUNO sensitivity to the annihilation of MeV dark matter in the galactic halo“. In: *Journal of Cosmology and Astroparticle Physics* 2023.09 (Sept. 2023), p. 001. DOI: 10.1088/1475-7516/2023/09/001.

[9] N. Aghanim et al. „Planck 2018 results - VI. Cosmological parameters“. In: *Astronomy and Astrophysics* 641 (2020), A6. DOI: 10.1051/0004-6361/201833910.

[10] Gianfranco Bertone, Dan Hooper and Joseph Silk. „Particle dark matter: evidence, candidates and constraints“. In: *Physics Reports* 405.5 (2005), pp. 279–390. ISSN: 0370-1573. DOI: 10.1016/j.physrep.2004.08.031.

[11] Vera C. Rubin and W. Kent Ford Jr. „Rotation of the Andromeda Nebula from a Spectroscopic Survey of Emission Regions“. In: *Astrophysical Journal* 159 (Feb. 1970), p. 379. DOI: 10.1086/150317.

[12] K. G. Begeman, A. H. Broeils and R. H. Sanders. „Extended rotation curves of spiral galaxies: dark haloes and modified dynamics“. In: *Monthly Notices of the Royal Astronomical Society* 249.3 (Apr. 1991), pp. 523–537. ISSN: 0035-8711. DOI: 10.1093/mnras/249.3.523.

[13] F. Zwicky. „Die Rotverschiebung von extragalaktischen Nebeln“. In: *Helv. Phys. Acta* 6 (1933), pp. 110–127. DOI: 10.1007/s10714-008-0707-4.

[14] Matthias Bartelmann and Peter Schneider. „Weak gravitational lensing“. In: *Physics Reports* 340.4–5 (Jan. 2001), pp. 291–472. ISSN: 0370-1573. DOI: 10.1016/s0370-1573(00)00082-x.

[15] Douglas Clowe et al. „A Direct Empirical Proof of the Existence of Dark Matter“. In: *The Astrophysical Journal* 648.2 (Aug. 2006), pp. L109–L113. ISSN: 1538-4357. DOI: 10.1086/508162.

[16] A. Vikhlinin et al. „ChandraSample of Nearby Relaxed Galaxy Clusters: Mass, Gas Fraction, and Mass-Temperature Relation“. In: *The Astrophysical Journal* 640.2 (Apr. 2006), pp. 691–709. ISSN: 1538-4357. DOI: 10.1086/500288.

[17] Igor Tkachev. „Cosmology and Dark Matter“. In: *CERN Yellow Reports: School Proceedings* (2017), Vol 5 (2017): Proceedings of the 2016 European School of High–Energy Physics. DOI: 10.23730/CYRSP-2017-005.259.

[18] A. A. Penzias and R. W. Wilson. „A Measurement of Excess Antenna Temperature at 4080 Mc/s.“ In: *The Astrophysical Journal* 142 (July 1965), pp. 419–421. DOI: 10.1086/148307.

[19] Benoit Famaey and Amel Durakovic. „Modified Newtonian Dynamics (MOND)“. In: *Encyclopedia of Astrophysics* (Jan. 2025). arXiv: 2501.17006 [astro-ph.GA].

[20] Ben Moore et al. „Dark Matter Substructure within Galactic Halos“. In: *The Astrophysical Journal* 524.1 (Oct. 1999), pp. L19–L22. ISSN: 0004-637X. DOI: 10.1086/312287.

[21] Qishan Liu and Kenny C. Y. Ng. *Sensitivity floor for primordial black holes with neutrino searches*. 2024. arXiv: 2312.06108 [hep-ph].

[22] B. P. Abbott et al. „Observation of Gravitational Waves from a Binary Black Hole Merger“. In: *Physical Review Letters* 116.6 (Feb. 2016). ISSN: 1079-7114. DOI: 10.1103/physrevlett.116.061102.

[23] Particle Data Group et al. „Review of Particle Physics“. In: *Progress of Theoretical and Experimental Physics* 2020.8 (Aug. 2020), p. 083C01. ISSN: 2050-3911. DOI: 10.1093/ptep/ptaa104.

[24] M. Sajjad Athar et al. „Status and perspectives of neutrino physics“. In: *Progress in Particle and Nuclear Physics* 124 (2022), p. 103947. ISSN: 0146-6410. DOI: 10.1016/j.ppnp.2022.103947.

[25] Y. Fukuda et al. „Evidence for Oscillation of Atmospheric Neutrinos“. In: *Physical Review Letters* 81.8 (Aug. 1998), pp. 1562–1567. ISSN: 1079-7114. DOI: 10.1103/physrevlett.81.1562.

[26] Q. R. Ahmad et al. „Measurement of the Rate of $\nu_e + d \rightarrow p + p + e^-$ Interactions Produced by ^8B Solar Neutrinos at the Sudbury Neutrino Observatory“. In: *Phys. Rev. Lett.* 87 (7 July 2001), p. 071301. DOI: 10.1103/PhysRevLett.87.071301.

[27] A. Boyarsky, M. Drewes, T. Lasserre, S. Mertens and O. Ruchayskiy. „Sterile neutrino Dark Matter“. In: *Progress in Particle and Nuclear Physics* 104 (Jan. 2019), pp. 1–45. ISSN: 0146-6410. DOI: 10.1016/j.ppnp.2018.07.004.

[28] Steven Weinberg. „A New Light Boson?“ In: *Phys. Rev. Lett.* 40 (4 Jan. 1978), pp. 223–226. DOI: 10.1103/PhysRevLett.40.223.

[29] Particle Data Group Collaboration. „Review of Particle Physics“. In: *Phys. Rev. D* 110 (3 Aug. 2024), p. 030001. DOI: 10.1103/PhysRevD.110.030001.

[30] Gerard Jungman, Marc Kamionkowski and Kim Griest. „Supersymmetric dark matter“. In: *Physics Reports* 267.5 (1996), pp. 195–373. ISSN: 0370-1573. DOI: 10.1016/0370-1573(95)00058-5.

[31] Edward W. Kolb and Michael S. Turner. *The Early Universe*. Vol. 69. Taylor and Francis, May 2019. ISBN: 978-0-429-49286-0. DOI: 10.1201/9780429492860.

[32] Leszek Roszkowski, Enrico Maria Sessolo and Sebastian Trojanowski. „WIMP dark matter candidates and searches—current status and future prospects“. In: *Reports on Progress in Physics* 81.6 (May 2018), p. 066201. ISSN: 1361-6633. DOI: 10.1088/1361-6633/aab913.

[33] Mark Srednicki, Richard Watkins and Keith A. Olive. „Calculations of relic densities in the early universe“. In: *Nuclear Physics B* 310.3 (1988), pp. 693–713. ISSN: 0550-3213. DOI: 10.1016/0550-3213(88)90099-5.

[34] Paolo Gondolo and Graciela Gelmini. „Cosmic abundances of stable particles: Improved analysis“. In: *Nuclear Physics B* 360.1 (1991), pp. 145–179. DOI: 10.1016/0550-3213(91)90438-4.

[35] Yang Bai and Joshua Berger. „Lepton Portal dark matter“. In: *Journal of High Energy Physics* 2014.8 (Aug. 2014), p. 153. ISSN: 1029-8479. DOI: 10.1007/JHEP08(2014)153.

[36] Carlos A. Argüelles, Alejandro Diaz, Ali Kheirandish, Andrés Olivares-Del-Campo, Ibrahim Safa and Aaron C. Vincent. „Dark matter annihilation to neutrinos“. In: *Rev. Mod. Phys.* 93 (3 Sept. 2021), p. 035007. DOI: 10.1103/RevModPhys.93.035007.

[37] Benjamin W. Lee and Steven Weinberg. „Cosmological Lower Bound on Heavy-Neutrino Masses“. In: *Phys. Rev. Lett.* 39 (4 July 1977), pp. 165–168. DOI: 10.1103/PhysRevLett.39.165.

[38] Gary Steigman, Basudeb Dasgupta and John F. Beacom. „Precise relic WIMP abundance and its impact on searches for dark matter annihilation“. In: *Physical Review D* 86.2 (July 2012). ISSN: 1550-2368. DOI: 10.1103/physrevd.86.023506.

[39] Torsten Bringmann, Paul Frederik Depta, Marco Hufnagel and Kai Schmidt-Hoberg. „Precise dark matter relic abundance in decoupled sectors“. In: *Physics Letters B* 817 (June 2021), p. 136341. ISSN: 0370-2693. DOI: 10.1016/j.physletb.2021.136341.

[40] Ken'ichi Saikawa and Satoshi Shirai. „Precise WIMP dark matter abundance and Standard Model thermodynamics“. In: *Journal of Cosmology and Astroparticle Physics* 2020.08 (Aug. 2020), pp. 011–011. ISSN: 1475-7516. DOI: 10.1088/1475-7516/2020/08/011.

[41] Nashwan Sabti, James Alvey, Miguel Escudero, Malcolm Fairbairn and Diego Blas. „Refined bounds on MeV-scale thermal dark sectors from BBN and the CMB“. In: *Journal of Cosmology and Astroparticle Physics* 2020.01 (Jan. 2020), p. 004. DOI: 10.1088/1475-7516/2020/01/004.

[42] Christopher V. Cappiello, P. S. Bhupal Dev and Amol V. Patwardhan. *New Supernova Constraints on Neutrinophilic Dark Sector*. 2025. arXiv: 2503.09691 [hep-ph].

[43] Nicolò Trevisani. „Collider Searches for Dark Matter (ATLAS + CMS)“. In: *Universe* 4.11 (2018). ISSN: 2218-1997. DOI: 10.3390/universe4110131.

[44] Nicole F. Bell and Thomas D. Jacques. „Gamma-ray constraints on dark matter annihilation into charged particles“. In: *Phys. Rev. D* 79 (4 Feb. 2009), p. 043507. DOI: 10.1103/PhysRevD.79.043507.

[45] Marco Cirelli, Nicolao Fornengo, Bradley J. Kavanagh and Elena Pinetti. „INTEGRAL x-ray constraints on sub-GeV dark matter“. In: *Phys. Rev. D* 103 (6 Mar. 2021), p. 063022. DOI: 10.1103/PhysRevD.103.063022.

[46] Rouven Essig, Eric Kuflik, Samuel D. McDermott, Tomer Volansky and Kathryn M. Zurek. „Constraining light dark matter with diffuse X-ray and gamma-ray observations“. In: *Journal of High Energy Physics* 2013.11 (Nov. 2013), p. 193. ISSN: 1029-8479. DOI: 10.1007/JHEP11(2013)193.

[47] Mathieu Boudaud, Julien Lavalle and Pierre Salati. „Novel Cosmic-Ray Electron and Positron Constraints on MeV Dark Matter Particles“. In: *Phys. Rev. Lett.* 119 (2 July 2017), p. 021103. DOI: 10.1103/PhysRevLett.119.021103.

[48] Sergio Palomares-Ruiz and Silvia Pascoli. „Testing MeV dark matter with neutrino detectors“. In: *Phys. Rev. D* 77 (2 Jan. 2008), p. 025025. DOI: 10.1103/PhysRevD.77.025025.

[49] Lars Bergström, Piero Ullio and James H. Buckley. „Observability of γ rays from dark matter neutralino annihilations in the Milky Way halo“. In: *Astroparticle Physics* 9.2 (1998), pp. 137–162. ISSN: 0927-6505. DOI: 10.1016/S0927-6505(98)00015-2.

[50] Marco Cirelli et al. „PPPC 4 DM ID: a poor particle physicist cookbook for dark matter indirect detection“. In: *Journal of Cosmology and Astroparticle Physics* 2011.03 (Mar. 2011), p. 051. DOI: 10.1088/1475-7516/2011/03/051.

[51] Xiaowei Ou, Anna-Christina Eilers, Lina Necib and Anna Frebel. „The dark matter profile of the Milky Way inferred from its circular velocity curve“. In: *Monthly Notices of the Royal Astronomical Society* 528.1 (Jan. 2024), pp. 693–710. ISSN: 0035-8711. DOI: 10.1093/mnras/stae034.

[52] GRAVITY Collaboration. „Mass distribution in the Galactic Center based on interferometric astrometry of multiple stellar orbits“. In: *Astronomy and Astrophysics* 657 (2022), p. L12. DOI: 10.1051/0004-6361/202142465.

[53] Maria Benito, Alessandro Cuoco and Fabio Iocco. „Handling the uncertainties in the Galactic Dark Matter distribution for particle Dark Matter searches“. In: *Journal of Cosmology and Astroparticle Physics* 2019.03 (Mar. 2019), p. 033. DOI: 10.1088/1475-7516/2019/03/033.

[54] Laurin Söding, Ruben Bartel and Philipp Mertsch. *Local dark matter density from Gaia DR3 K-dwarfs using Gaussian processes*. 2025. arXiv: 2506.02956 [astro-ph.GA].

[55] Kimberly K. Boddy, Jason Kumar and Louis E. Strigari. „Effective J-factor of the Galactic Center for velocity-dependent dark matter annihilation“. In: *Phys. Rev. D* 98 (6 Sept. 2018), p. 063012. DOI: 10.1103/PhysRevD.98.063012.

[56] Konrad Kuijken and Gerard Gilmore. „The mass distribution in the galactic disc – I. A technique to determine the integral surface mass density of the disc near the Sun“. In: *Monthly Notices of the Royal Astronomical Society* 239.2 (July 1989), pp. 571–603. ISSN: 0035-8711. DOI: 10.1093/mnras/239.2.571.

[57] Misiriotis, A., Xilouris, E. M., Papamastorakis, J., Boumis, P. and Goudis, C. D. „The distribution of the ISM in the Milky Way - A three-dimensional large-scale model“. In: *Astronomy and Astrophysics* 459.1 (2006), pp. 113–123. DOI: 10.1051/0004-6361:20054618.

[58] J. A. Sellwood and Stacy S. McGaugh. „The Compression of Dark Matter Halos by Baryonic Infall“. In: *The Astrophysical Journal* 634.1 (Nov. 2005), p. 70. DOI: 10.1086/491731.

[59] P.F. de Salas, K. Malhan, K. Freese, K. Hattori and M. Valluri. „On the estimation of the local dark matter density using the rotation curve of the Milky Way“. In: *Journal of Cosmology and Astroparticle Physics* 2019.10 (Oct. 2019), p. 037. DOI: 10.1088/1475-7516/2019/10/037.

[60] J. Binney and S. Tremaine. *Galactic Dynamics: Second Edition*. Princeton Series in Astrophysics. Princeton University Press, 2008. ISBN: 9780691130279.

[61] Yoichiro Suzuki. „The Super-Kamiokande experiment“. In: *The European Physical Journal C* 79 (2019). ISSN: 1434-6052. DOI: 10.1140/epjc/s10052-019-6796-2.

[62] Andrés Olivares-Del Campo, Céline Bœhm, Sergio Palomares-Ruiz and Silvia Pascoli. „Dark matter-neutrino interactions through the lens of their cosmological implications“. In: *Phys. Rev. D* 97 (7 Apr. 2018), p. 075039. DOI: 10.1103/PhysRevD.97.075039.

[63] Super-Kamiokande Collaboration. „Indirect search for dark matter from the Galactic Center and halo with the Super-Kamiokande detector“. In: *Phys. Rev. D* 102 (7 Oct. 2020), p. 072002. DOI: 10.1103/PhysRevD.102.072002.

[64] Nicole F. Bell, Matthew J. Dolan and Sandra Robles. „Searching for Sub-GeV dark matter in the galactic centre using Hyper-Kamiokande“. In: *Journal of Cosmology and Astroparticle Physics* 2020.09 (Sept. 2020), p. 019. DOI: 10.1088/1475-7516/2020/09/019.

[65] Hyper-Kamiokande Proto-Collaboration. *Hyper-Kamiokande Design Report*. 2018. arXiv: 1805.04163 [physics.ins-det].

[66] JUNO Collaboration. „Potential to identify neutrino mass ordering with reactor antineutrinos at JUNO*“. In: *Chinese Physics C* 49.3 (Mar. 2025), p. 033104. DOI: 10.1088/1674-1137/ad7f3e.

[67] JUNO Collaboration. *First measurement of reactor neutrino oscillations at JUNO*. 2025. arXiv: 2511.14593 [hep-ex].

[68] M. Beretta et al. „Fluorescence emission of the JUNO liquid scintillator“. In: *Journal of Instrumentation* 20.05 (May 2025), P05009. DOI: 10.1088/1748-0221/20/05/P05009.

[69] C. Landini et al. „Distillation and gas stripping purification plants for the JUNO liquid scintillator“. In: *Nuclear Instruments and Methods in Physics Research Section A: Accelerators, Spectrometers, Detectors and Associated Equipment* 1069 (2024), p. 169887. ISSN: 0168-9002. DOI: 10.1016/j.nima.2024.169887.

[70] Jiaxuan Ye et al. „Development of water extraction system for liquid scintillator purification of JUNO“. In: *Nuclear Instruments and Methods in Physics Research Section A: Accelerators, Spectrometers, Detectors and Associated Equipment* 1027 (2022), p. 166251. ISSN: 0168-9002. DOI: 10.1016/j.nima.2021.166251.

[71] Jessica Eck, Dhanushka Bandara, Gina Grünauer, Tobias Heinz and Tobias Lachenmaier. „A novel method for measuring the attenuation length and the group velocity of transparent liquids in a variable length cavity“. In: *Nuclear Instruments and Methods in Physics Research Section A: Accelerators, Spectrometers, Detectors and Associated Equipment* 1077 (2025), p. 170507. ISSN: 0168-9002. DOI: 10.1016/j.nima.2025.170507.

[72] J.B. Birks, D.W. Fry, L. Costrell and K. Kandiah. *The Theory and Practice of Scintillation Counting: International Series of Monographs in Electronics and Instrumentation*. International series of monographs on electronics and instrumentation. Pergamon, 2013. ISBN: 9781483156064.

[73] Paolo Lombardi, Fausto Ortica, Gioacchino Ranucci and Aldo Romani. „Decay time and pulse shape discrimination of liquid scintillators based on novel solvents". In: *Nuclear Instruments and Methods in Physics Research Section A: Accelerators, Spectrometers, Detectors and Associated Equipment* 701 (2013), pp. 133–144. ISSN: 0168-9002. DOI: 10.1016/j.nima.2012.10.061.

[74] JUNO Collaboration. „Mass testing and characterization of 20-inch PMTs for JUNO". In: *The European Physical Journal C* 82 (2022), p. 1168. DOI: 10.1140/epjc/s10052-022-11002-8.

[75] Tao Lin et al. „Simulation software of the JUNO experiment". In: *The European Physical Journal C* 83.5 (2023), p. 382. DOI: 10.1140/epjc/s10052-023-11514-x.

[76] Luis Alvarez-Ruso et al. „Recent highlights from GENIE v3". In: *The European Physical Journal Special Topics* 230.24 (1st Dec. 2021), pp. 4449–4467. ISSN: 1951-6401. DOI: 10.1140/epjs/s11734-021-00295-7.

[77] Júlia Tena-Vidal et al. „Neutrino-nucleus CC0π cross-section tuning in GENIE v3". In: *Phys. Rev. D* 106 (11 Dec. 2022), p. 112001. DOI: 10.1103/PhysRevD.106.112001.

[78] A.J. Koning, D. Rochman, J.-Ch. Sublet, N. Dzysiuk, M. Fleming and S. van der Marck. „TENDL: Complete Nuclear Data Library for Innovative Nuclear Science and Technology". In: *Nuclear Data Sheets* 155 (2019). Special Issue on Nuclear Reaction Data, pp. 1–55. ISSN: 0090-3752. DOI: 10.1016/j.nds.2019.01.002.

[79] Zekun Yang et al. „First attempt of directionality reconstruction for atmospheric neutrinos in a large homogeneous liquid scintillator detector". In: *Phys. Rev. D* 109 (5 Mar. 2024), p. 052005. DOI: 10.1103/PhysRevD.109.052005.

[80] Ivan Esteban, M. C. Gonzalez-Garcia, Michele Maltoni, Ivan Martinez-Soler, João Paulo Pinheiro and Thomas Schwetz. „NuFit-6.0: updated global analysis of three-flavor neutrino oscillations". In: *Journal of High Energy Physics* 2024.12 (30th Dec. 2024), p. 216. ISSN: 1029-8479. DOI: 10.1007/JHEP12(2024)216.

[81] KATRIN Collaboration. „Direct neutrino-mass measurement based on 259 days of KATRIN data". In: *Science* 388.6743 (2025), pp. 180–185. DOI: 10.1126/science.adq9592.

[82] LEGEND Collaboration. „First results on the search for lepton number violating neutrinoless double-β decay with the LEGEND-200 experiment". In: *Phys. Rev. Lett.* (Sept. 2025). DOI: 10.1103/25tk-nctn.

[83] LEGEND Collaboration. *LEGEND-1000 Preconceptual Design Report*. 2021. arXiv: 2107.11462 [physics.ins-det].

[84] Super-Kamiokande Collaboration and T2K Collaboration. „First Joint Oscillation Analysis of Super-Kamiokande Atmospheric and T2K Accelerator Neutrino Data". In: *Phys. Rev. Lett.* 134 (1 Jan. 2025), p. 011801. DOI: 10.1103/PhysRevLett.134.011801.

[85] Daya Bay Collaboration. „Improved measurement of the reactor antineutrino flux and spectrum at Daya Bay*“. In: *Chinese Physics C* 41.1 (Jan. 2017), p. 013002. DOI: 10.1088/1674-1137/41/1/013002.

[86] Double Chooz Collaboration. „Improved measurements of the neutrino mixing angle θ_{13} with the Double Chooz detector“. In: *Journal of High Energy Physics* 2014.10 (14th Oct. 2014), p. 86. ISSN: 1029-8479. DOI: 10.1007/JHEP10(2014)086.

[87] RENO Collaboration. „Observation of Energy and Baseline Dependent Reactor Antineutrino Disappearance in the RENO Experiment“. In: *Phys. Rev. Lett.* 116 (21 May 2016), p. 211801. DOI: 10.1103/PhysRevLett.116.211801.

[88] JUNO Collaboration. *TAO Conceptual Design Report: A Precision Measurement of the Reactor Antineutrino Spectrum with Sub-percent Energy Resolution*. 2020. arXiv: 2005.08745 [physics.ins-det].

[89] Ran Han, Yu-Feng Li, Liang Zhan, William F McDonough, Jun Cao and Livia Ludhova. „Potential of geo-neutrino measurements at JUNO*“. In: *Chinese Physics C* 40.3 (Mar. 2016), p. 033003. DOI: 10.1088/1674-1137/40/3/033003.

[90] JUNO Collaboration. „The design and sensitivity of JUNO's scintillator radiopurity pre-detector OSIRIS“. In: *The European Physical Journal C* 81.11 (Nov. 2021), p. 973. DOI: 10.1140/epjc/s10052-021-09544-4.

[91] JUNO collaboration. „JUNO sensitivity to 7Be, pep, and CNO solar neutrinos“. In: *Journal of Cosmology and Astroparticle Physics* 2023.10 (Oct. 2023), p. 022. DOI: 10.1088/1475-7516/2023/10/022.

[92] JUNO Collaboration. „Feasibility and physics potential of detecting 8B solar neutrinos at JUNO*“. In: *Chinese Physics C* 45.2 (Feb. 2021), p. 023004. DOI: 10.1088/1674-1137/abd92a.

[93] K. Hirata et al. „Observation of a neutrino burst from the supernova SN1987A“. In: *Phys. Rev. Lett.* 58 (14 Apr. 1987), pp. 1490–1493. DOI: 10.1103/PhysRevLett.58.1490.

[94] R. M. Bionta et al. „Observation of a neutrino burst in coincidence with supernova 1987A in the Large Magellanic Cloud“. In: *Phys. Rev. Lett.* 58 (14 Apr. 1987), pp. 1494–1496. DOI: 10.1103/PhysRevLett.58.1494.

[95] E.N. Alexeyev, L.N. Alexeyeva, I.V. Krivosheina and V.I. Volchenko. „Detection of the neutrino signal from SN 1987A in the LMC using the INR Baksan underground scintillation telescope“. In: *Physics Letters B* 205.2 (1988), pp. 209–214. ISSN: 0370-2693. DOI: 10.1016/0370-2693(88)91651-6.

[96] M. Aglietta et al. „On the Event Observed in the Mont Blanc Underground Neutrino Observatory during the Occurrence of Supernova 1987a“. In: *Europhysics Letters* 3.12 (June 1987), p. 1315. DOI: 10.1209/0295-5075/3/12/011.

[97] JUNO collaboration. „Real-time monitoring for the next core-collapse supernova in JUNO“. In: *Journal of Cosmology and Astroparticle Physics* 2024.01 (Jan. 2024), p. 057. DOI: 10.1088/1475-7516/2024/01/057.

[98] JUNO collaboration. „Prospects for detecting the diffuse supernova neutrino background with JUNO“. In: *Journal of Cosmology and Astroparticle Physics* 2022.10 (Oct. 2022), p. 033. DOI: 10.1088/1475-7516/2022/10/033.

[99] JUNO Collaboration. „JUNO sensitivity to low energy atmospheric neutrino spectra“. In: *The European Physical Journal C* 81.10 (8th Oct. 2021), p. 887. ISSN: 1434-6052. DOI: 10.1140/epjc/s10052-021-09565-z.

[100] Peter B. Denton. „Probing CP Violation with Neutrino Disappearance Alone“. In: *Phys. Rev. Lett.* 133 (3 July 2024), p. 031801. DOI: 10.1103/PhysRevLett.133.031801.

[101] M.V. Smirnov, Zh.J. Hu, S.J. Li and J.J. Ling. „The possibility of leptonic CP-violation measurement with JUNO“. In: *Nuclear Physics B* 931 (2018), pp. 437–445. ISSN: 0550-3213. DOI: https://doi.org/10.1016/j.nuclphysb.2018.05.003.

[102] JUNO Collaboration. „JUNO sensitivity on proton decay p → νK+ searches*“. In: *Chinese Physics C* 47.11 (Nov. 2023), p. 113002. DOI: 10.1088/1674-1137/ace9c6.

[103] Ivan Girardi, Davide Meloni, Tommy Ohlsson, He Zhang and Shun Zhou. „Constraining sterile neutrinos using reactor neutrino experiments“. In: *Journal of High Energy Physics* 2014.8 (8th Aug. 2014), p. 57. ISSN: 1029-8479. DOI: 10.1007/JHEP08(2014)057.

[104] J. A. Formaggio and G. P. Zeller. „From eV to EeV: Neutrino cross sections across energy scales“. In: *Rev. Mod. Phys.* 84 (3 Sept. 2012), pp. 1307–1341. DOI: 10.1103/RevModPhys.84.1307.

[105] Tom Van Cuyck. „Short-range correlations and meson-exchange currents in neutrino-nucleus scattering“. PhD thesis. Ghent University, 2017, pp. VIII, 199.

[106] M. Sajjad Athar, A. Fatima and S.K. Singh. „Neutrinos and their interactions with matter“. In: *Progress in Particle and Nuclear Physics* 129 (2023), p. 104019. ISSN: 0146-6410. DOI: 10.1016/j.ppnp.2022.104019.

[107] O. Lalakulich, U. Mosel and K. Gallmeister. „Neutrino energy reconstruction in quasielastic-like scattering in the MiniBooNE and T2K experiments“. In: *Phys. Rev. C* 86 (5 Nov. 2012), p. 054606. DOI: 10.1103/PhysRevC.86.054606.

[108] Weijun Li. *Centre-of-momentum Variables in $\nu_\mu CC1p1\pi$*. 2025. arXiv: 2501.08984 [hep-ex].

[109] MiniBooNE Collaboration. „Measurement of the antineutrino neutral-current elastic differential cross section“. In: *Phys. Rev. D* 91 (1 Jan. 2015), p. 012004. DOI: 10.1103/PhysRevD.91.012004.

[110] JUNO Collaboration. „Calibration strategy of the JUNO experiment“. In: *Journal of High Energy Physics* 2021.3 (2021), p. 4. ISSN: 1029-8479. DOI: 10.1007/s41365-025-01678-4.

[111] Si-Yuan Zhang, Yong-Bo Huang, Miao He, Cheng-Feng Yang and Guo-Ming Chen. „Sub-GeV events energy reconstruction with 3-inch PMTs in JUNO“. In: *Nuclear Science and Techniques* 36.5 (2025), p. 84. DOI: 10.1007/s41365-025-01678-4.

[112] JUNO Collaboration. „JUNO sensitivity to invisible decay modes of neutrons“. In: *The European Physical Journal C* 85 (2025). ISSN: 1434-6052. DOI: 10.1140/epjc/s10052-024-13638-0.

[113] Jie Liu et al. „12C(n,n+3α) and 12C(n,α0)9Be cross sections in the MeV neutron energy region“. In: *Physics Letters B* 842 (2023), p. 137985. ISSN: 0370-2693. DOI: 10.1016/j.physletb.2023.137985.

[114] Meng Wang, W.J. Huang, F.G. Kondev, G. Audi and S. Naimi. „The AME 2020 atomic mass evaluation (II). Tables, graphs and references*“. In: *Chinese Physics C* 45.3 (Mar. 2021), p. 030003. DOI: 10.1088/1674-1137/abddaf.

[115] D.F. Measday. „The nuclear physics of muon capture“. In: *Physics Reports* 354.4 (2001), pp. 243–409. ISSN: 0370-1573. DOI: 10.1016/S0370-1573(01)00012-6.

[116] JUNO Collaboration. „JUNO sensitivity to low energy atmospheric neutrino spectra“. In: *The European Physical Journal C* 81 (2021). ISSN: 1434-6052. DOI: 10.1140/epjc/s10052-021-09565-z.

[117] Francesco Renga. „Experimental searches for muon decays beyond the Standard Model“. In: *Reviews in Physics* 4 (2019), p. 100029. ISSN: 2405-4283. DOI: 10.1016/j.revip.2019.100029.

[118] International Atomic Energy Agency. *IAEA Live Chart of Nuclides*. Accessed: 2025-06-26. 2025. URL: https://www-nds.iaea.org/relnsd/vcharthtml/VChartHTML.html.

[119] J.H. Kelley, E. Kwan, J.E. Purcell, C.G. Sheu and H.R. Weller. „Energy levels of light nuclei A=11“. In: *Nuclear Physics A* 880 (2012), pp. 88–195. ISSN: 0375-9474. DOI: 10.1016/j.nuclphysa.2012.01.010.

[120] M. Fukugita, Y. Kohyama and K. Kubodera. „Neutrino reaction cross sections on 12C target“. In: *Physics Letters B* 212.2 (1988), pp. 139–144. ISSN: 0370-2693. DOI: 10.1016/0370-2693(88)90513-8.

[121] B. Zeitnitz. „Spektroskopie mit Neutrinos — Resultate von KARMEN“. In: *Physikalische Blätter* 52.6 (1996), pp. 545–550. DOI: 10.1002/phbl.19960520607.

[122] W. Ma, S.-Y. Zhang, M. He, Y.-B. Huang and JUNO Collaboration. „Reconstruction of Atmospheric Neutrinos in JUNO Using Machine Learning on PMT Waveforms“. In: *22nd International Workshop on Advanced Computing and Analysis Techniques in Physics Research (ACAT 2024)*. Conference presentation, ACAT 2024, Stony Brook University, Stony Brook, Long Island NY, USA, March 10–15. CERN. 2024. URL: https://indico.cern.ch/event/1330797/contributions/5796849.

[123] Rosmarie Irma Wirth. „Reconstruction of Atmospheric Neutrino Events in JUNO using GCNs and Calibration of the OSIRIS Radiopurity Pre-Detector“. Dissertation. Hamburg: Universität Hamburg, 2025.

[124] JUNO Collaboration. „Prediction of energy resolution in the JUNO experiment*“. In: *Chinese Physics C* 49.1 (Jan. 2025), p. 013003. DOI: 10.1088/1674-1137/ad83aa.

[125] Miao He and JUNO Collaboration. „Double Calorimetry System in JUNO“. In: *Radiation Detection Technology and Methods* 1.2 (2017), p. 21. ISSN: 2509-9949. DOI: 10.1007/s41605-017-0022-2.

[126] Jiaxi Liu et al. „Neutrino type identification for atmospheric neutrinos in a large homogeneous liquid scintillation detector“. In: *Phys. Rev. D* (June 2025). DOI: 10.1103/fznt-z257.

[127] The JUNO Collaboration. „Radioactivity control strategy for the JUNO detector“. In: *Journal of High Energy Physics* 2021.11 (15th Nov. 2021), p. 102. ISSN: 1029-8479. DOI: 10.1007/JHEP11(2021)102.

[128] SNO+ Collaboration. „Measurement of the ^{8}B solar neutrino flux in SNO+ with very low backgrounds“. In: *Phys. Rev. D* 99 (1 Jan. 2019), p. 012012. DOI: 10.1103/PhysRevD.99.012012.

[129] RENO Collaboration. „Measurement of cosmogenic ^{9}Li and ^{8}He production rates at RENO“. In: *Phys. Rev. D* 106 (1 July 2022), p. 012005. DOI: 10.1103/PhysRevD.106.012005.

[130] Cristiano Galbiati and John F. Beacom. „Measuring the cosmic ray muon-induced fast neutron spectrum by (n, p) isotope production reactions in underground detectors“. In: *Phys. Rev. C* 72 (2 Aug. 2005), p. 025807. DOI: 10.1103/PhysRevC.72.025807.

[131] V.A. Kudryavtsev, N.J.C. Spooner and J.E. McMillan. „Simulations of muon-induced neutron flux at large depths underground“. In: *Nuclear Instruments and Methods in Physics Research Section A: Accelerators, Spectrometers, Detectors and Associated Equipment* 505.3 (2003), pp. 688–698. ISSN: 0168-9002. DOI: 10.1016/S0168-9002(03)00983-5.

[132] Super-Kamiokande Collaboration. „Diffuse supernova neutrino background search at Super-Kamiokande“. In: *Phys. Rev. D* 104 (12 Dec. 2021), p. 122002. DOI: 10.1103/PhysRevD.104.122002.

[133] Super-Kamiokande Collaboration. *Search for Diffuse Supernova Neutrino Background with 956.2 days of Super-Kamiokande Gadolinium Dataset*. 2025. arXiv: 2511.02222 [astro-ph.HE].

[134] M. Honda, M. Sajjad Athar, T. Kajita, K. Kasahara and S. Midorikawa. „Atmospheric neutrino flux calculation using the NRLMSISE-00 atmospheric model“. In: *Phys. Rev. D* 92 (2 July 2015), p. 023004. DOI: 10.1103/PhysRevD.92.023004.

[135] G. Battistoni, A. Ferrari, T. Montaruli and P.R. Sala. „The atmospheric neutrino flux below 100MeV: The FLUKA results“. In: *Astroparticle Physics* 23.5 (2005), pp. 526–534. ISSN: 0927-6505. DOI: 10.1016/j.astropartphys.2005.03.006.

[136] M. Honda. *Atmospheric Neutrino Flux Calculations*. http://www-rccn.icrr.u-tokyo.ac.jp/mhonda/public/. Accessed: 2025-12-02. 2025.

[137] Marius S. Potgieter. „Solar Modulation of Cosmic Rays“. In: *Living Reviews in Solar Physics* 10.1 (June 2013), p. 3. ISSN: 1614-4961. DOI: 10.12942/lrsp-2013-3.

[138] Super-Kamiokande Collaboration. „Measurements of the atmospheric neutrino flux by Super-Kamiokande: Energy spectra, geomagnetic effects, and solar modulation“. In: *Phys. Rev. D* 94 (5 Sept. 2016), p. 052001. DOI: 10.1103/PhysRevD.94.052001.

[139] Martin Freund. „Analytic approximations for three neutrino oscillation parameters and probabilities in matter“. In: *Phys. Rev. D* 64 (5 July 2001), p. 053003. DOI: 10.1103/PhysRevD.64.053003.

[140] Adam M. Dziewonski and Don L. Anderson. „Preliminary reference Earth model“. In: *Physics of the Earth and Planetary Interiors* 25.4 (1981), pp. 297–356. ISSN: 0031-9201. DOI: 10.1016/0031-9201(81)90046-7.

[141] W.F. McDonough. „2.15 - Compositional Model for the Earth's Core“. In: *Treatise on Geochemistry*. Ed. by Heinrich D. Holland and Karl K. Turekian. Oxford: Pergamon, 2003, pp. 547–568. ISBN: 978-0-08-043751-4. DOI: https://doi.org/10.1016/B0-08-043751-6/02015-6.

[142] G. L. Fogli, E. Lisi, A. Mirizzi and D. Montanino. „Three-generation flavor transitions and decays of supernova relic neutrinos“. In: *Phys. Rev. D* 70 (1 July 2004), p. 013001. DOI: 10.1103/PhysRevD.70.013001.

[143] J. Nieves, I. Ruiz Simo and M. J. Vicente Vacas. „Inclusive charged-current neutrino-nucleus reactions“. In: *Phys. Rev. C* 83 (4 Apr. 2011), p. 045501. DOI: 10.1103/PhysRevC.83.045501.

[144] S. Dolan, G. D. Megias and S. Bolognesi. „Implementation of the SuSAv2-meson exchange current 1p1h and 2p2h models in GENIE and analysis of nuclear effects in T2K measurements“. In: *Phys. Rev. D* 101 (3 Feb. 2020), p. 033003. DOI: 10.1103/PhysRevD.101.033003.

[145] Zi-Yuan Li et al. „Event vertex and time reconstruction in large-volume liquid scintillator detectors“. In: *Nuclear Science and Techniques* 32.5 (2021), p. 49. DOI: 10.1007/s41365-021-00885-z.

[146] W. Ma et al. „Reconstruction of atmospheric neutrinos and muons using Machine Learning-based methods in JUNO“. In: *22nd International Workshop on Advanced Computing and Analysis Techniques in Physics Research (ACAT 2024)*. Conference presentation, ACAT 2024, Stony Brook University, Stony Brook, Long Island NY, USA, March 10–15. CERN. 2024. URL: https://indico.cern.ch/event/1330797/contributions/5796849.

[147] Zi-Yuan Li et al. „Improvement of machine learning-based vertex reconstruction for large liquid scintillator detectors with multiple types of PMTs“. In: *Nuclear Science and Techniques* 33.7 (2022), p. 93. ISSN: 2210-3147. DOI: 10.1007/s41365-022-01078-y.

[148] Ping Zhang. *Improvement on first hit time reconstruction*. Internal collaboration document JUNO-doc-6399-v2. Internal JUNO collaboration document. JUNO Collaboration, Sept. 2022.

[149] Sergey Ioffe and Christian Szegedy. *Batch Normalization: Accelerating Deep Network Training by Reducing Internal Covariate Shift*. 2015. arXiv: 1502.03167 [cs.LG]. URL: https://arxiv.org/abs/1502.03167.

[150] Kaiming He, Xiangyu Zhang, Shaoqing Ren and Jian Sun. *Deep Residual Learning for Image Recognition*. 2015. arXiv: 1512.03385 [cs.CV]. URL: https://arxiv.org/abs/1512.03385.

[151] Takuya Akiba, Shotaro Sano, Toshihiko Yanase, Takeru Ohta and Masanori Koyama. „Optuna: A Next-generation Hyperparameter Optimization Framework“. In: *Proceedings of the 25th ACM SIGKDD International Conference on Knowledge Discovery and Data Mining*. 2019. URL: https://arxiv.org/abs/1907.10902.

[152] Dan Hendrycks and Kevin Gimpel. *Gaussian Error Linear Units (GELUs)*. 2023. arXiv: 1606.08415 [cs.LG]. URL: https://arxiv.org/abs/1606.08415.

[153] Ilya Loshchilov and Frank Hutter. *Decoupled Weight Decay Regularization*. 2019. arXiv: 1711.05101 [cs.LG]. URL: https://arxiv.org/abs/1711.05101.

[154] Frank Hutter, Holger Hoos and Kevin Leyton-Brown. „An Efficient Approach for Assessing Hyperparameter Importance“. In: *Proceedings of the 31st International Conference on Machine Learning*. Ed. by Eric P. Xing and Tony Jebara. Vol. 32. Proceedings of Machine Learning Research 1. Bejing, China: PMLR, June 2014, pp. 754–762.

[155] Zhen Qian et al. „Vertex and energy reconstruction in JUNO with machine learning methods“. In: *Nuclear Instruments and Methods in Physics Research Section A: Accelerators, Spectrometers, Detectors and Associated Equipment* 1010 (2021), p. 165527. ISSN: 0168-9002. DOI: 10.1016/j.nima.2021.165527.

[156] JUNO Collaboration. „Sub-percent precision measurement of neutrino oscillation parameters with JUNO*“. In: *Chinese Physics C* 46.12 (Dec. 2022), p. 123001. DOI: 10.1088/1674-1137/ac8bc9.

[157] Ivan R. King. „The structure of star clusters. II. Steady-state velocity distributions“. In: *Astronomical Journal* 70 (June 1965), p. 376. DOI: 10.1086/109750.

[158] M. Ackermann et al. „The Fermi Large Area Telescope on Orbit: Event Classification, Instrument Response Functions, and Calibration“. In: *The Astrophysical Journal Supplement Series* 203.1 (Oct. 2012), p. 4. DOI: 10.1088/0067-0049/203/1/4.

[159] A. Caldwell and K. Kröninger. „Signal discovery in sparse spectra: A Bayesian analysis“. In: *Phys. Rev. D* 74 (9 Nov. 2006), p. 092003. DOI: 10.1103/PhysRevD.74.092003.

[160] The NOvA Collaboration and The T2K Collaboration. „Joint neutrino oscillation analysis from the T2K and NOvA experiments“. In: *Nature* 646.8086 (2025), pp. 818–824. ISSN: 1476-4687. DOI: 10.1038/s41586-025-09599-3.

[161] Jie Cheng, Min Li, Yu-Feng Li, Gao-Song Li, Hao-Qi Lu and Liang-Jian Wen. „Neutral-current background induced by atmospheric neutrinos at large liquid-scintillator detectors: III. Comprehensive prediction for low energy neutrinos“. In: *The European Physical Journal C* 85.3 (2025), p. 295. ISSN: 1434-6052. DOI: 10.1140/epjc/s10052-025-14009-z.

[162] NOvA Collaboration. „Adjusting neutrino interaction models and evaluating uncertainties using NOvA near detector data“. In: *The European Physical Journal C* 80.12 (2020), p. 1119. ISSN: 1434-6052. DOI: 10.1140/epjc/s10052-020-08577-5.

[163] Daniel Foreman-Mackey, David W. Hogg, Dustin Lang and Jonathan Goodman. „emcee: The MCMC Hammer“. In: *Publications of the Astronomical Society of the Pacific* 125.925 (Feb. 2013), p. 306. DOI: 10.1086/670067.

[164] Glen Cowan, Kyle Cranmer, Eilam Gross and Ofer Vitells. „Asymptotic formulae for likelihood-based tests of new physics“. In: *The European Physical Journal C* 71.2 (2011), p. 1554. ISSN: 1434-6052. DOI: 10.1140/epjc/s10052-011-1554-0.

[165] Marco Cirelli, Nicolao Fornengo, Teresa Montaruli, Igor Sokalski, Alessandro Strumia and Francesco Vissani. „Spectra of neutrinos from dark matter annihilations“. In: *Nuclear Physics B* 727.1 (2005), pp. 99–138. ISSN: 0550-3213. DOI: 10.1016/j.nuclphysb.2005.08.017.

[166] Gene H. Golub and John H. Welsch. „Calculation of Gauss Quadrature Rules“. In: *Mathematics of Computation* 23.106 (1969), 221–s10. ISSN: 00255718, 10886842. (Visited on 03/09/2025).

List of Figures

List of Tables

Danksagung

Diese Arbeit wäre ohne die Unterstützung zahlreicher Personen nicht möglich gewesen, daher möchte ich mich an dieser Stelle von Herzen für die fachliche, organisatorische und seelische Begleitung bedanken.

Zu allererst gilt mein besonderer Dank **Prof. Dr. Tobias Lachenmaier** für das Vertrauen und die Möglichkeit, meine Dissertation in seiner Gruppe anzufertigen. Durch Bachelor-, Master- und nun auch Doktorarbeit durfte ich über viele Jahre hinweg von seiner enormen fachlichen Expertise profitieren. Vielen Dank für all die lehrreichen Meetings und Diskussionen, die meine fachliche Entwicklung maßgeblich geprägt haben.

Auch bei meinem Zweitbetreuer **Prof. Dr. Josef Jochum** möchte ich mich sowohl für die anregenden fachlichen Diskussionen als auch für die Unterstützung in herausfordernden Phasen dieser Promotion bedanken.

Ein weiterer Dank geht an **Dr. Günter Lang**, **Gaby Behring**, **Gabriele Enßlin-Richter** und **Dr. Florian Jessen**, die mir bei allen organisatorischen und technischen Fragen stets zur Seite standen. Ganz besonders möchte ich an dieser Stelle **Gaby Behring** hervorheben, die darüber hinaus auch für persönliche Herausforderungen im Arbeitsumfeld immer ein offenes Ohr und einen guten Rat hatte.

Bei der **JUNO Kollaboration** möchte ich mich für die bereichernden Meetings und den Rahmen für meine Dissertation bedanken. Es war mir eine Ehre bei einem Projekt dieser Dimension mitwirken zu dürfen. Ein besonderer Dank geht dabei an **Dr. Marta Colomer Molla**, an die ich all meine fachlichen Fragen adressieren konnte.

Meine Kollegen und Kolleginnen **Dr. Gina Grünauer**, **Dr. Tobias Heinz**, **Lukas Bieger** und **Dr. Tobias Sterr** haben bei der Entstehung dieser Arbeit eine ganz besondere Rolle gespielt, daher möchte ich sie im Folgenden direkt adressieren:
Gina, als Bürokolleginnen haben wir fast alle Höhen und Tiefen während unserer Promotion gemeinsam erlebt und haben uns dabei nicht nur fachlich entwickelt, sondern sind vor allem auch menschlich gemeinsam gewachsen. Auch wenn wir auf die ein oder andere Erfahrung sicher gerne verzichtet hätten, bin ich unendlich dankbar, dass du jederzeit an meiner Seite warst.
Tobi H., seit der Betreuung meiner Bachelorarbeit bis zur Fertigstellung der Dissertation warst du an meiner Seite und hast mich zu allen Zeiten sowohl fachlich also auch persönlich unterstützt. Es ist nicht nur deine fachliche Klarheit und deine Souveränität, die mich von Anfang an inspiriert hat, sondern auch deine Loyalität und die Disziplin trotz aller Rückschläge weiterzumachen.
Lukas B., wirklich jedes einzelne Gespräch mit dir war bereichernd für mich. Ob es um fachliche Fragen ging, bei denen du mir so gut wie kein anderer eine Intuition vermitteln konntest, ob es politische Themen waren oder einfach das Austauschen persönlicher Empfindungen und Herausforderungen, ich habe jede einzelne Unterhaltung genossen.
Tobi S., ohne deine Hardware Expertise hätte ich meinen PC vermutlich bereits mehrfach versehentlich zurückgesetzt. Danke, dass du von Anfang an für sämtliche Themen ein offenes Ohr hattest und auch gegenüber offizieller Seite immer vehement für unsere Wünsche und Bedürfnisse während der Promotion eingestanden bist. Danke auch für

das Korrekturlesen meiner Arbeit und das wertvolle Feedback.
Auch bei allen anderen Kollegen und Kolleginnen, insbesondere **Dr. Marc Breisch**, **Dr. Lukas Rauscher**, **Dr. Katharina Kilgus**, **Dhanushka Bandara**, **Colin Heckmeyer** und **Dr. Katja Wurster** möchte ich mich von Herzen für alle die unterstützenden Gespräche und die wunderschönen gemeinsamen Momente innerhalb und außerhalb der Universität bedanken.

Diese Arbeit wäre nicht entstanden, wenn ich nicht jeden Tag seelische und moralische Unterstützung von Mitgliedern des **Tanz-Turnier Clubs Rot-Gold Tübingen** bekommen hätte. Dem aufmerksamen Leser werden die aus diesem Grund verwendeten tanzbezogenen Zitate zu Beginn jedes Kapitels nicht entgangen sein. Ich möchte an dieser Stelle insbesondere der **Latein-Gruppe** und dem **Präsidium** der TTC von Herzen für die Unterstützung und die Geduld in den letzten Jahren danken. Ganz besonders möchte ich hier meiner besten Freundin **Jule Merwitz** danken, die mir nicht nur durch regelmäßige Umarmungen, sondern auch durch persönliche Essenslieferungen so oft den Tag versüßt hat. Auch den O.G.s der Tübinger Lateingruppe **Arthur Ankerstein**, **Hendrik Laicher**, **Alexander Conzelmann**, **Lexie Böttcher**, **Dr. Tobias Heinz**, **Lukas Viestädt** sowie meinem Tanzpartner **Daniel Kanchev** möchte ich von Herzen danken, dass ihr mich physisch herausgefordert und emotional aufgefangen habt. Mein Dank geht auch an **Dr. Frank Gut** für das Korrekturlesen einzelner Kapitel meiner Arbeit und das wertvolle Feedback.

Die wichtigste Unterstützung habe ich von meiner Familie bekommen und ihnen kann ich dafür nicht genug danken. Ohne meine Eltern **Aljona und Alexander Eck**, die mir jeden Tag bedingungslose Liebe geschenkt haben und deren Glaube an mich zu keinem Moment gewankt ist, wäre ich wohl kaum in der Lage gewesen, diese Arbeit zu beenden. Meine Brüder **Jonathan Eck** und **Elias Eck** waren gemeinsam mit ihren Partnerinnen **Lea Scherl** und **Pia Voigtländer** jederzeit für mich da und hatten immer einen guten Ratschlag bereit. Meine Schwester **Susanne Eck** hat mich gemeinsam mit ihrem Partner **Fabian Hagen** nicht nur regelmäßig mit Kaffee und Essen versorgt, sondern war auch in jeder Lebenslage für mich da und ist gemeinsam mit mir durch dick und dünn gegangen. Danke euch allen für eure Unterstützung.

Ohne meinen Verlobten **Daniel Liermann** hätte ich diese Arbeit mit Sicherheit nicht fertiggestellt. **Dani**, du hast mich wirklich in jedem Aspekt dieser Arbeit begleitet, warst mein emotionaler Rückzugsort und mein moralischer Kompass. Du hast mich jeden Tag motiviert und inspiriert und ich kann dir gar nicht sagen, wie viel Kraft mir das gegeben hat. Danke für alles! `#sommerschlaf`

Und zu guter Letzt muss ich hier noch einer ganz besonderen Person danken, ohne die nicht nur diese Arbeit nie entstanden wäre, sondern ohne die ich wohl auch niemals Physik studiert hätte: **Dr. Lothar Diehl**. Wenn ich hier alle Punkte aufzählen würde, für die ich dir dankbar bin **Lothar**, dann würde die Danksagung wohl noch eine weitere Seite füllen. Angefangen hat alles mit einer Jugend-forscht-Arbeit 2013, zu der du mich ermutigt und fachlich begleitet hast. Seitdem bist du in jeder Phase meines Studiums mein Ratgeber und unterstützt mich aus der Ferne wie kein anderer. Danke, dass du an mich geglaubt hast und mir den Mut gegeben hast, diesen Weg zu gehen. Du bist in sehr vielen Aspekten zu meinem Vorbild geworden und ich danke dir für alles, was ich von dir lernen durfte.